Study of Nanoconfined Phases for the Rational Synthesis of Supported Catalysts

Studie van Nanobegrensde Fasen voor de Rationele Synthese van Gedragen Katalysatoren

(*met een samenvatting in het Nederlands*)

Proefschrift

ter verkrijging van de graad van doctor aan de Universiteit Utrecht op gezag van de rector magnificus, prof. dr. G. J. van der Zwaan, ingevolge het besluit van het college voor promoties in het openbaar te verdedigen op woensdag 16 mei 2012 des middags te 12.45 uur

door

Tamara Marijke Eggenhuisen

geboren op 7 september 1983 te Eindhoven

Promotor: Prof. dr. ir. K. P. de Jong
Co-promotor: Dr. P. E. de Jongh

Dit onderzoek werd gefinancierd door de Nederlandse Organisatie voor Wetenschappelijk Onderzoek (TOP/ECHO 700.57.341).

wanhoop niet - wanhoop niet
straks is het allemaal weer anders
en misschien wel beter dan ooit
dus wanhoop niet
wanhoop nooit

De Dijk

ISBN: 978-90-8891-408-9

Cover image by: Lonneke Boots, www.lonnekeboots.nl
Printed by: Proefschriftmaken.nl || Printyourthesis.com

Table of Contents

Chapter 1

General Introduction

1.1 Supported Catalysts

Catalysts are to the chemical industry what wheels are to a car: without these reaching your destination or performing chemical reactions would be cumbersome. As a logical consequence, the major fraction of all chemical production processes includes one or more catalyzed steps and this is even close to 100% for the production of transportation fuels.[1] Since there is an ever growing demand for more energy efficient production of chemicals, increasingly strict environmental legislation and diminishing fossil fuel sources, the crucial role that catalysts play will only increase. Supported catalysts are the most important class of heterogeneous catalysts. The active phase, often a metal, is dispersed over a support to maximize the metal surface area. Therefore, small particles are deposited in a porous support material with a large surface area. The support facilitates dispersion, accessibility of the active phase for the reactants and stability against sintering as well as mechanical stability of catalyst bodies. The structural requirements for a supported catalyst depend on the specific catalytic reaction as well as the conditions for industrial application. A rigorous understanding of the catalyst structure-activity relationship is essential for rational catalyst synthesis at the nanometer scale and aims for optimum activity, maximum selectivity and long-term stability.

1.1.1 Supported catalysts for the Fischer-Tropsch synthesis

Here, we will discuss supported catalyst requirements by the example of cobalt catalysts for the Fischer-Tropsch synthesis. By the Fischer-Tropsch reaction hydrocarbon chains are formed from a mixture of carbon monoxide and hydrogen, so-called synthesis gas, and it is catalyzed by iron, cobalt or ruthenium.[2-5] Depending on the carbon source used to produce the synthesis gas, the process is referred to as biomass-to-liquids (BTL), coal-to-liquids (CTL) or gas-to-liquids (GTL). The first CTL plant was operated in Germany and dates back to the 1930's, while the latest addition in industrial scale application of the Fischer-Tropsch reaction is Shell's GTL plant 'Pearl' in Qatar, set up to produce 140.000 barrels of transportation fuels and lubricants a day.[6, 7]

The activity of cobalt catalysts for the Fischer-Tropsch reaction has been studied extensively and a non-classical relation between particle size and activity was found. As expected, the catalyst activity increases for catalysts with smaller cobalt particles due to the larger available surface area. The intrinsic activity of metallic cobalt normalized tot the number of available surface atoms does not depend on the particle size above 10 nm.[2] However, an optimum cobalt particle size of ~6 nm on a carbon nanofiber support was found, as for smaller particles the intrinsic activity decreased due to a predominance of cobalt surface atoms with reduced coordination numbers.

[8, 9] On oxidic supports, an optimum of ~10 nm was observed.[10, 11] Catalyst stability is another important parameter and the reason of deactivation of cobalt Fischer-Tropsch catalysts has been a matter of debate since the employment in the 1940's. Pore blockage by long chain waxes, carbon deposition, sulfur poisoning and sintering were at that time identified as major deactivation pathways.[6] Although catalyst regeneration could be applied to reverse the effects of the first three pathways, for sintering no direct remedy was established. Currently, deactivation under industrially relevant conditions is ascribed to sintering, carbon deposition, carbidization and surface reconstruction of the active cobalt phase, while oxidation of metallic cobalt under reaction conditions has been a matter of debate.[12, 13] Deactivation by sintering is still intrinsically difficult to avoid, although an oxidation-reduction procedure has been proposed for catalyst regeneration.[12] The selectivity of supported cobalt catalysts towards hydrocarbons with chains of more than 5 carbon atoms, has been reported to depend on the cobalt particle size.[9, 14] However, diffusion of reactants, products and byproducts and other characteristics of the chemical reaction also play a dominant role.[3] Furthermore, promoters are commonly added to influence the selectivity or improve reducibility.

By these structure-property relationships of cobalt catalysts for the Fischer-Tropsch synthesis we can establish some general requirements for the preparation of the supported catalyst. To obtain maximum activity the metallic cobalt particle size should be close to the optimum one and the particle size distribution should be narrow. This demands particle size control by the synthesis procedure. Furthermore, it is desirable to maximize the nearest neighbor distance, as sintering of nanoparticles due to coalescence is a deactivation pathway. Therefore, the particles need to be distributed uniformly over the support, while a high volumetric metal weight loading is desirable. The catalyst preparation method is preferentially simple, cost-effective and environmentally friendly to be applicable for large scale production.

1.2 Supported Catalyst Preparation

In the past, supported catalyst preparation has been referred to as an art rather than a science. However, nowadays the limits and possibilities of the classical preparation routes are being studied at a fundamental level.[1, 15] Catalyst preparation has established itself as a field of research that combines materials science with surface and physical chemistry.[16-18] Nevertheless, control over metal nanoparticle size, distribution and even shape in order to maximize catalytic effectiveness persists as a motivation for designing new or improved preparation routes.[19, 20]

Three major routes exist for the synthesis of supported metal or metal oxide nanoparticles: 'deposition precipitation', ion-adsorption and 'impregnation and

drying' (see section 1.2.1), each with their own advantages and disadvantages. In all three preparation methods the metal precursor is contacted with a support using an, often aqueous, solution. Therefore, the interaction of the support with the metal-complex depends on the point-of-zero (PZC) charge of the support. For example, a silica support has a PZC at pH 2-4. Therefore, hydrated Ni^{2+} ions in a saturated aqueous $Ni(NO_3)_2$ solution with a pH of ~3 have only weak interaction with a silica surface, as the surface silanol groups are hardly (de-)protonated. However, using an alumina support with a higher PZC, adsorption of the hydrated Ni^{2+} ions is much stronger on the deprotonated surface hydroxyl groups. This principle is used to deposit monolayers of metal precursor complexes on support surfaces by strong electrostatic adsorption.[15, 21, 22] By adjusting the pH of the solution, the surface groups of the support are protonated or deprotonated such that the charge is opposite to that of the metal ion. The resulting metal loading is therefore limited by the support's surface area and adsorption capacity of the support at the applied pH.[23] Nevertheless, small metal particles with homogeneous distributions can be obtained. By deposition-precipitation, a controlled increase of the pH is used to induce deposition of the metal hydroxide onto a suspended support.[24, 25] This method is applicable to a wide variety of metals and small metal particles (<10 nm) at high metal loadings (e.g. up to 17 wt% Ni/SiO_2) can be achieved.[26] However, it involves large waste streams and the formation of difficult to reduce (hydro)silicate species.[27]

Alternative state-of-the-art methods use chemical vapor deposition,[28] atomic layer deposition,[29] glow discharge plasma,[30] or combinations of the more classical methods.[31] Also, colloidal metal particle provides an attractive method to actively control the nanoparticle size and obtain narrow particle size distributions and are especially suitable to study particle size-activity relations.[10, 32, 33] Nevertheless, for industrial, large scale applications environmentally friendly and simple preparation methods are preferable.

1.2.1 Preparation by impregnation and drying

Impregnation and drying is a seemingly simple synthesis method and is commonly applied in both academia and industry.[1, 34, 35] Figure 1.1 shows a scheme of the three elementary steps. A solution containing the metal precursor salt is contacted with a porous volume, upon which the capillary forces suck the solution into the pores. 'Incipient wetness', 'dry' or 'pore volume' impregnation involve the addition of a solution volume equal to the pore volume. For wet impregnation an excess of solution is added, which may be removed by filtration or drying. Upon drying, the salt should remain inside the pore system, where it is subsequently decomposed by a heat treatment referred to as calcination to form metal oxide nanoparticles. Transition metal catalysts are often prepared from nitrate precursors. These salts

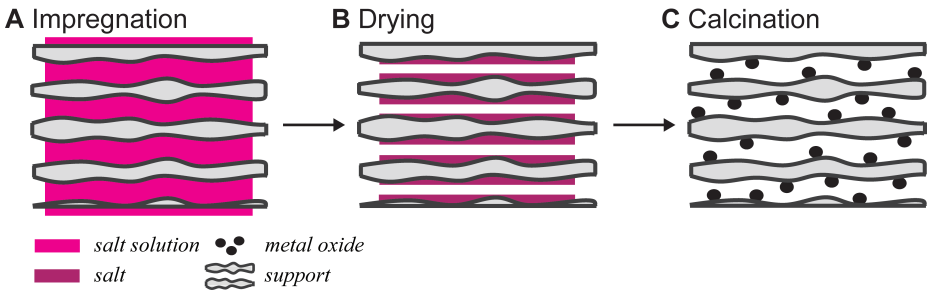

Figure 1.1. Supported catalyst preparation by impregnation and drying. Schematic representation of idealized distribution of phases after (A) a solution containing the metal precursor is absorbed by a porous support, (B) the metal salt is deposited inside the pores after solvent removal by a drying treatment and (C) the precursor salt is decomposed to from the metal oxide, which can be activated for catalysis by further reduction treatments.

have a high solubility in water, such that high metal loadings can be obtained in a single impregnation step. Furthermore, they are readily available and decompose into the pure metal oxide.

Nanoparticle dispersion and distribution

Although impregnation and drying is an advantageous catalyst preparation method for many reasons, the nanoparticles' sizes and their distribution over the support are difficult to control. Especially for transition metal nitrates on oxidic supports, often catalysts are obtained with an inhomogeneous metal dispersion and distribution. The examples in Figure 1.2 illustrate the wide range of catalytic systems for which this problem occurs. Low dispersions result from agglomeration of the metal oxide inside the pore systems, such as the ~200 nm large domains consisting of Co_3O_4 crystallites that appear in black in Figure 1.2A and Figure 1.2B. This can occur for catalysts with varying metal weight loadings or support pore morphology.[36-39] It is commonly observed for *ex*-nitrate transition metal oxides on silica supports, but occurs also with other precursor salts (Figure 1.2C)[40], on other oxidic supports (Figure 1.2D) [41, 42] and with various transition metals.[23, 43, 44] These agglomerates usually consist of smaller crystallites prone to sintering. Redistribution of the active phase can also occur towards the exterior of the support particle, which results in wide particle size distributions and low dispersions.[45-49] In Figure 1.2E for example, the large black particles are NiO particles on the exterior of an ordered mesoporous silica support.[43] Lastly, in some cases individual nanoparticles with high dispersion are obtained, but they occupy only a fraction of the available pores.[50, 51] For example, in Figure 1.2F only a few of the pores display bright dots indicating the presence of Fe nanoparticles in an ordered mesoporous silica support with otherwise empty pores.

[52] In this case, high dispersions were obtained but the support surface area is used inefficiently and the nearest neighbor distance is not maximized.

There has been much attention for the development of improved control over dispersion and distribution as there are many advantages to the use of impregnation and drying for supported catalyst preparation. This is illustrated by the large number of publications on catalyst preparation methods that involve some variation of impregnation and drying. The following section discusses several strategies to gain control over dispersion and distribution for the preparation of supported transition metal catalysts by impregnation and drying. The discussed approaches are often applicable to a wider range of materials than the reported application.

There are several approaches that involve adjustment of the impregnation step. For example, a second impregnation step can be used after calcination to fill the empty pores.[53, 54] However, in some catalyst systems this actually induces more redistribution due to solubility of the metal oxide in the impregnation solution. Furthermore, melt infiltration is an alternative precursor loading step.[49, 55] Under the right experimental conditions this method was effective to fill the pores of the support with the metal precursor, but it did not lead to improved metal oxide distribution

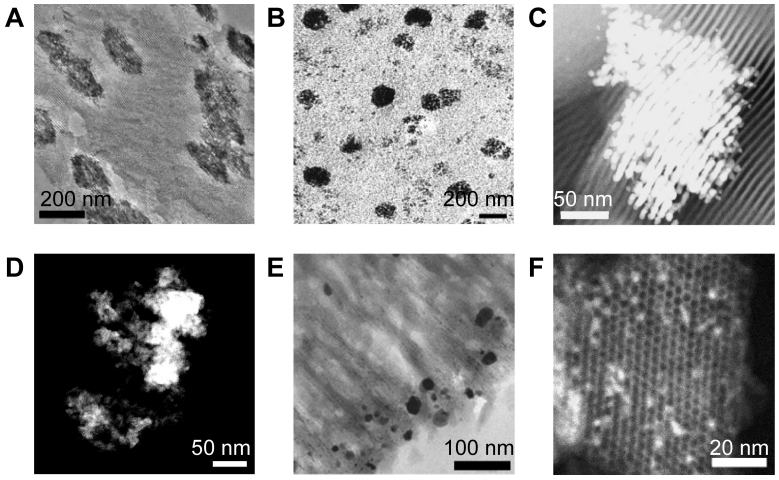

Figure 1.2. TEM micrographs of examples from literature showing cluster formation of various transition metals supported on mesoporous silica prepared by impregnation and drying with nitrate precursors; examples of large Co_3O_4 agglomerates on silica supports: (A) 11.5 wt% Co/SBA-15, adapted from [37], (B) 20 wt% Co/silica-gel, adapted from [39]; examples of agglomerates, redistribution and empty pores in catalysts prepared from various precursor salts, supports and transition metals: (C) 8 wt% Pt/SBA-15 (dark field image: bright rods indicate agglomeration of Pt nanorods), adapted from [40], (D) 20 wt% Co/γ-Al_2O_3 (HAADF-STEM image: bright areas indicate Co_3O_4 agglomerates), adapted from [42], (E) 5 wt% NiO/MCM-41, adapted from [43] (F) 5 wt% Fe/MCM-41 (HAADF-STEM image: bright dots indicate presence of Fe nanoparticles in mesopores), adapted from [52].

after calcination. The metal precursor can also be added during the synthesis of the oxidic support.[56, 57] However, the metal phase may be encapsulated in the support and thus become inaccessible for the reactant or the metal precursor can react with all the present components during further synthesis steps to form inactive metal-support compounds. Using organic solvents, such as ethanol or alkanes has been reported to improve the distribution of the salt over the support.[37-39, 58] However, in combination with hydrated transition metal nitrates, no significant improvement in the metal dispersion and distribution was obtained.

The interaction of the precursor salt with surface hydroxyl groups on an oxidic support affects the mobility of the precursor complex during drying and calcination treatments. Aqueous solutions of transition metal nitrates generally have weak interactions with silica supports. Using other transition metal salts, such as acetates, that are reasonably soluble in water at a higher pH favors the electrostatic interaction of the metal ion with the support surface groups.[43, 59-61] Although this is a successful approach to improve the dispersion and distribution, lower metal loadings are obtained than with nitrate precursors and the high dispersion causes a lower degree of reducibility of the metal oxides.[62] Alternatively, the supports surface acidity can be adjusted by forming mixed oxides.[63, 64] Nevertheless, even in systems with stronger support-metal complex interactions, such as for $Co(NO_3)_2$ (aq) on γ-Al_2O_3, agglomeration still occurred at high metal loadings due to limited adsorption capacity of the surface.[42] A more elaborate method is to introduce anchoring sites on the supports surface area by post-grafting[65, 66] or prenucleation of a transition metal hydroxide.[31]

Preventing redistribution during drying would allow control over the salt distribution. This can for example be achieved by using solutions with higher viscosity. For example with chelating ligands,[59] such as citrates,[67, 68] acetylacetonate[62] or ethylenediamine[69] high dispersion of metal particles can thus be obtained. However, since the solubility of these complexes in water is low, the resulting metal loadings are low. Furthermore, the high metal dispersions obtained lead to limited reducibility or the formation of undesirable metal-support compounds. The addition of ethylene glycol to the impregnation solution was also used to increase the metal dispersions.[14] Although the effect may result from an increased viscosity, the addition of organic components of the impregnation solution also affects the decomposition pathway.[70, 71] Lastly, immobilization of the precursor solution during drying can be achieved by freeze-drying.[72, 73]

The last step of supported catalyst preparation is decomposition of the precursor. Efficient removal of the decomposition products in combination with low heating rates are effective in increasing the dispersion and improving the distribution of metal oxides.[36, 47, 74, 75] Agglomeration or even redistribution of the metal oxide to

the exterior of the support particle has been ascribed to the high concentrations of gaseous decomposition products. In some cases redispersion of the metal precursor can be achieved with high gas flows during the decomposition.[44] Alternatively, decomposition of nickel nitrate under a reducing atmosphere led to the formation of smaller metal oxide particles as compared to an inert gas atmosphere.[76, 77]

Control over nanoparticle dispersion by the NO calcination method

The dispersion and distribution of nanoparticles for *ex*-nitrate supported silica catalysts is influenced by the decomposition atmosphere. In Figure 1.3 catalysts are shown that were prepared by impregnation and drying followed by calcination under different gas atmospheres.[47, 77] Indeed, when performed under stagnant conditions in air, i.e. by placing a crucible with lid in a muffle oven, calcination leads to severe redistribution of the precursor and even the formation of large NiO crystallites on the exterior of the support. It has been recognized that by the more rapid removal of gaseous decomposition products sintering and migration of the active phase can be reduced.[36, 75] Nevertheless, rodlike particles were still observed within the support's pore system after decomposition in a flow of helium (Figure 1.3B). In 2007 the effect of nitric oxide on the decomposition of transition metal nitrates was patented and

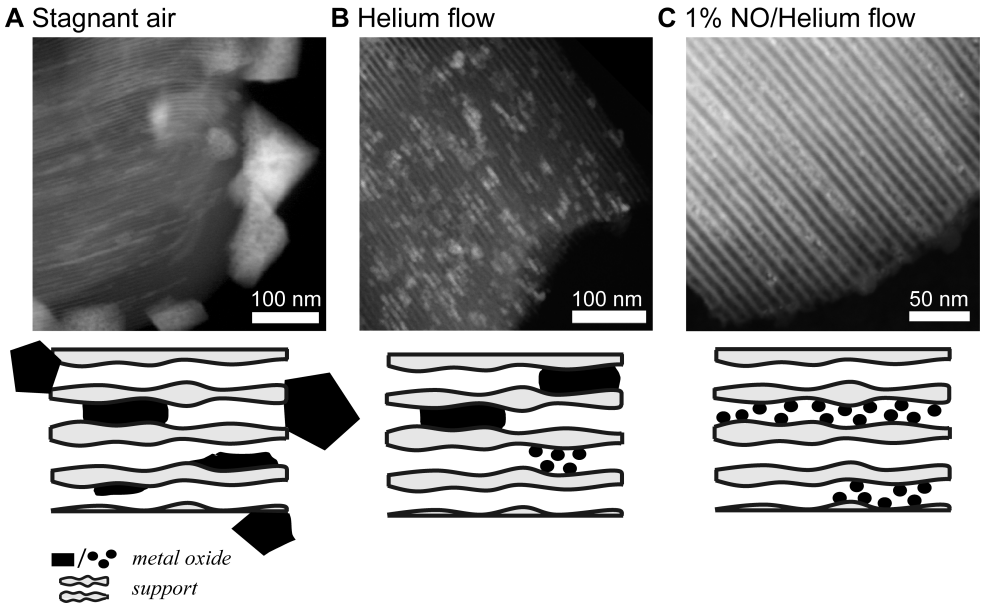

Figure 1.3. Effect of calcination conditions on dispersion and distribution of NiO on a mesoporous silica model support. HAADF-STEM dark field micrographs and cartoons of NiO on SBA-15 catalysts prepared by impregnation and drying with $Ni(NO_3)_2$ (aq) followed by calcination (A) in stagnant air, (B) helium flow and (C) a flow of 1% NO/He, adapted from [47, 78].

subsequently reported in open literature for the first time.[47] NiO nanoparticles of 2-6 nm were formed in the pores of the SBA-15 support after decomposition in a flow of an inert gas containing 1% v/v NO (Figure 1.3C).[50, 78]

Information on the mechanism of NO-assisted transition metal nitrate decomposition has been reported in several papers. First it was confirmed that after drying, basic nickel nitrate, $Ni_3(NO_3)_2(OH)_4$ was formed within the pores of a SBA-15 support.[77] Higher concentrations of NO_2 and O_2 were found to induce sintering, while decomposition under H_2 or 1% NO/He reduced sintering.[47, 77] By TGA/MS it was shown that O_2 was absent in the evolving gasstream when decomposition occurred in the presence of NO.[78] Indeed, by labeling studies NO was found to scavenge oxygen radicals by forming NO_2.[79] The reaction of NO with the nitrate ions is said to gradually convert the salt into NiO providing many nucleation sites for nanoparticle formation.[78] In absence of NO, decomposition occurs instantaneously with fewer nucleation sites and in the presence of mobile species, which causes the aggregation. Later it was found that NO also promoted the hydrolysis of hydrated $Ni(NO_3)_2$ to immobile basic nickel nitrate at low temperatures, reducing mobility of the active phase already during the first decomposition step.[80]

Generally, the decomposition of hydrated $Co(NO_3)_2$ follows the same decomposition pathway as nickel nitrate.[81] However, after drying at 60 ºC, $Co(NO_3)_2 \cdot 6H_2O$ forms instead of the basic nickel nitrate formed after drying $Ni(NO_3)_2$ (aq) at 120 ºC.[80] In absence of NO, cobalt nitrate is dehydrated and subsequently decomposed into large rodlike Co_3O_4 particles. Basic cobalt nitrate only forms in the presence of NO, which then decomposes to form small Co_3O_4 nanoparticles.[82] This has been applied for the synthesis of Co/SiO_2 catalysts with high activity for the Fischer-Tropsch synthesis.[55, 83, 84]

1.3 Toolbox

1.3.1 Ordered mesoporous silica supports

Ordered mesoporous silica (OMS) was first reported in the early 90's by the researchers of Mobil.[85] Since then it has found applications in adsorbents,[86] chromatography, drug delivery[87, 88] and catalysis.[49, 89-91] It is synthesized by the condensation of silica precursors in the presence of large organic template molecules as structure-directing agents that assemble into liquid crystals. For example, the triblock copolymer PEO_{20}-PPO_{70}-PEO_{20}, consisting of ethyleneoxide and propyleneoxide units, assembles into 2D hexagonal, lamellar or cubic structures depending on the concentration and temperature in acidic solutions.[92] By burning away the organic template, a silica matrix remains with an ordered pore system. The phase behavior of these and many other template molecules has allowed for

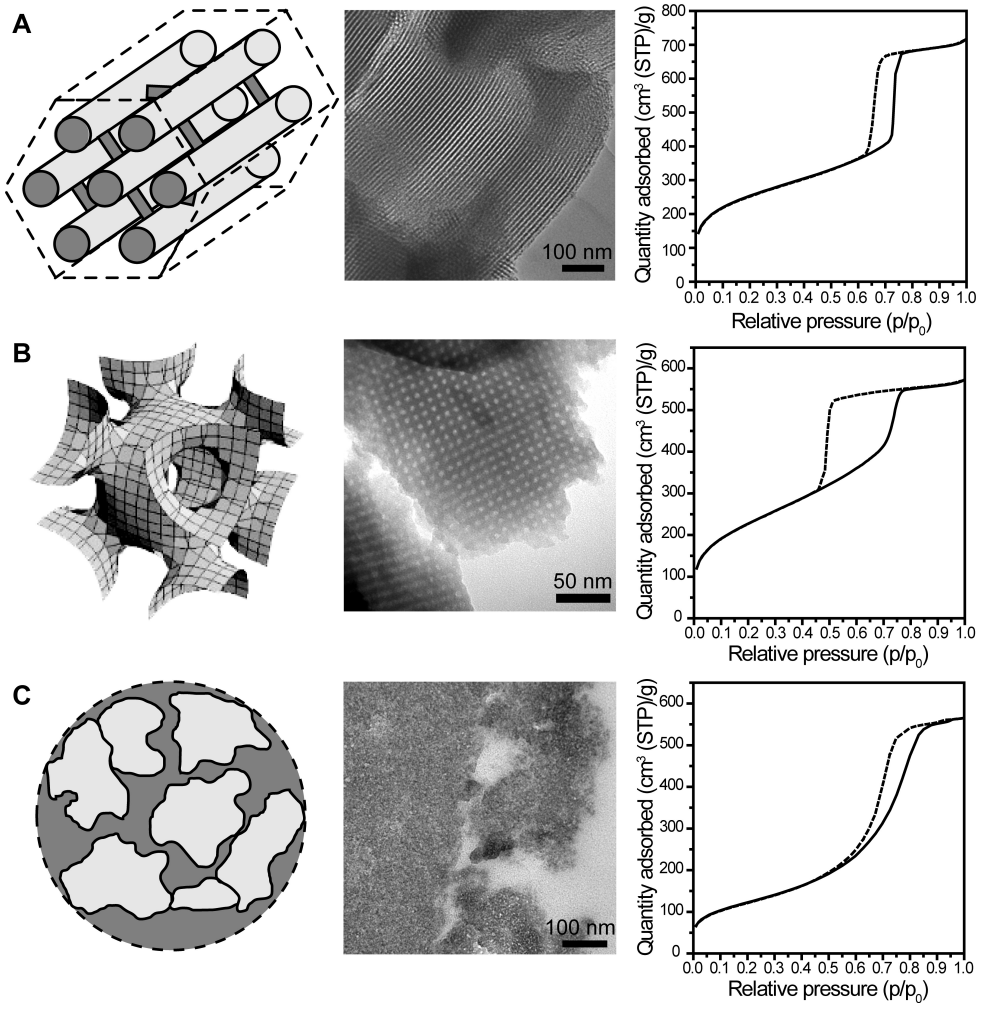

Figure 1.4. Mesoporous silica materials with different pore morphologies, from left to right: a schematic representation of the porous structure, a TEM micrograph and a typical N_2-physisorption isotherm. (A) SBA-15 with cylindrical pores with 2-D hexagonal ordering, silica surface is indicated in light grey, dark grey indicates pore openings and intrawall porosity, (B) SBA-16 with cage-like morphology, schematic displays cavity surface, adapted from [100], TEM by courtesy of G. Prieto and (C) disordered silica-gel, silica surface is indicated in light grey, dark grey indicates pore openings, TEM by courtesy of P. Munnik.

the synthesis of ordered mesoporous silica materials with different pore ordering, pore diameter and pore geometry.[93, 94] The enormous flexibility of these supports and their large surface area holds potential also for the field of supported catalyst preparation, as they can be used for example to vary the nanoparticle size inside the

pores.[82]

The use of OMS as supports has many advantages for the study of supported catalyst preparation and Figure 1.4 summarizes some of the typical properties of the rdered mesoporous silica materials and a typical silica-gel. Probably the most widely used OMS is SBA-15,[95] which consists of cylindrical straight pores with a 2-dimensional hexagonal ordering, as is illustrated by the schematic in Figure 1.4A. Depending on the synthesis temperature the average mesopore diameter can be varied between 6 – 15 nm.[96] Furthermore, intrawall porosity allows transport between the cylindrical pores.[97] The straight pores are easily identified in TEM and facilitate visualization of the location of for example metal oxide nanoparticles. The narrow pore size distribution results in typical capillary condensation and evaporation events expressed as parallel vertical features in nitrogen physisorption, which is also sensitive to the presence of guest phases in the pores. MCM-41 is another classical OMS with the same 2D hexagonal pore ordering as SBA-15.[85] Generally it has smaller pore diameters in the range of 2-6 nm, thinner pore walls and lack intrawall porosity.[98, 99] In Figure 1.4B, the characteristics of cage silica materials are illustrated. Here the symmetry of SBA-16 is indicated,[96, 100] which has a body-centered cubic ordering of cages which are connected to 8 nearest neighbors. Cage silica materials with many different symmetries exist and have cage sizes in the range of 6 – 30 nm.[101-104] The entrance size is substantially smaller than the cage size and therefore qualifies these materials for size selective applications and reduced mobility of a confined active phase. Physisorption for these materials shows a wide hysteresis loop, due to the delayed desorption through the narrow entrance size. Figure 1.4C illustrates the properties of an industrially more relevant support, silica-gel. It consists of amorphous silica agglomerates, where the pores are formed by interparticle voids. Due to its disordered nature, it is complicated to distinguish pore volume and silica material in TEM, even on 50 nm thin ultramicrotomed slices. Furthermore, due to the broad pore size distribution, the nitrogen physisorption isotherm becomes more gradual and the effect of guest phases on the porosity becomes less clear.

1.3.2 Electron tomography

Transmission electron microscopy is indispensable for the characterization of heterogeneous catalysts. The structure of catalysts supports and catalytic nanoparticles can be assessed with resolution even down to the atomic level.[105] Classically, it is used to obtain nanoparticle size distributions. However, more information is accessible, such as particle shape or elemental composition.[106] Furthermore, using environmental TEM the formation of nanoparticles during catalyst preparation[107, 108] has been visualized in-situ as well as the behavior of nanoparticles under reaction

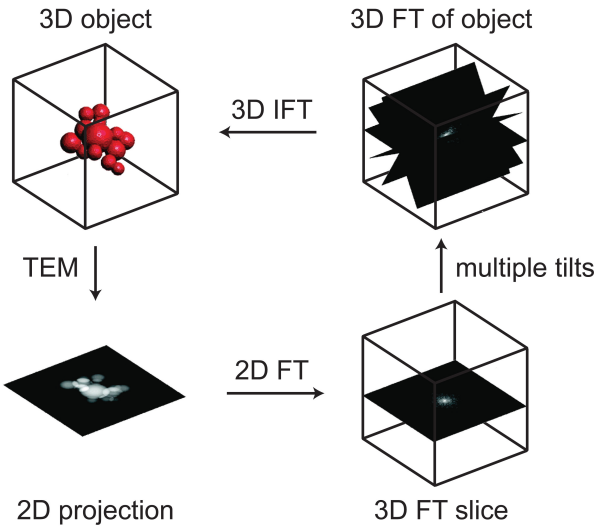

Figure 1.5. Electron tomography reconstruction scheme. Transmission electron micrographs are recorded at multiple tilt angles, building up the 3D Fourier transform (FT) of the object. The object is then reconstructed via inverse Fourier Transform (IFT), adapted from [113].

conditions.[109-111] Nevertheless, with TEM 3-dimensional (3D) objects are always projected onto a 2D plane, which makes it difficult to assess the nanoparticle distribution over a support particle, even though the use of ordered mesoporous supports facilitates the qualitative distribution analysis as the pore structure is clearly recognizable. More conventional disordered supports are commonly too thick as they usually have a primary particle size in the micrometer range. For these materials ultramicrotomy is a necessary tool to obtain thin slices down to 20 nm.

3-Dimensional information on the nanometer scale is accessible using electron tomography.[112, 113] The tomographic reconstruction of an object using TEM is illustrated in Figure 1.5. 2D projections of the object are acquired over a range of tilt angles. Using Fourier transform, the 3D Fourier space of the object is filled. Via inverse Fourier transform the object is reconstructed in 3 dimensions. Most commonly, tilt series are acquired using a single tilt axis, however, with a dual tilt axis a larger volume of the 3D Fourier space can be filled.[114] The resolution of the reconstruction parallel to the projection plane (d_{xy}) is can be estimated by the number of projections (N) and diameter of the reconstructed volume (D), eq. 1. The resolution perpendicular to the projection plane is mainly affected by the maximum tilt angle (α), eq. 2.

$$d_{xy} = \frac{\pi D}{N} \qquad \text{eq. 1}$$

$$d_z = d_{xy}\sqrt{\frac{\alpha + sin(\alpha)cos(\alpha)}{\alpha - sin(\alpha)cos(\alpha)}} \qquad \text{eq. 2}$$

The tilt range is commonly restricted by experimental conditions, as at high tilt angles shadowing by the TEM grid, grid holder and other particles can occur, or the particle of study may become too thick under high tilt angles. By these criteria, a typical tilt series of particle with 100 nm diameter obtained from ± 70º with 2º intervals, would result in a resolution of 2 nm both parallel and perpendicular to the projection plane. However, in practice higher resolutions have been realized.[113, 115] The resolution is based on theoretical considerations, but assumes a perfect alignment of the tilt series as well as the absence of shrinkage from the supporting film or the object itself.

Electron tomography was pioneered in biological sciences for the reconstruction of complete cell structures in the late sixties.[116] However, during the last decade it has been developed for the analysis of complex nanostructures.[117] The ability to determine the three dimensional distribution of nanoparticles in porous supports has stirred the field of catalyst preparation. Indeed, the first report of ET for catalyst characterization showed the presence of Ag particles inside a zeolite support.[117] Not much later ET using HAADF-STEM was also introduced.[118] Since then, ET has been applied to evaluate the location of catalytic nanoparticles inside e.g. mesoporous supports or carbon nanotubes.[56, 119, 120] Furthermore, image analysis has allowed the determination of nanoparticle size distribution and nearest neighbour distances[50] as well as assessment of preferential locations for nanoparticles in 3 dimensional porous supports.[121] Increasing computing powers and advanced image analyses processes are applied to assess not only particle size distribution but also their shape and orientation with respect to the support.[122, 123] Furthermore it allows quantitative assessment of the sintering of individual nanoparticles[124] or quantitative analysis of catalytic structures that perform under industrially relevant reaction conditions. ET has also brought forward the understanding of the morphology of commonly used porous supports.[125-127] By performing ET at cryogenic temperatures (cryo-ET), hydrated structures can be studied in detail.[128] Cryo-ET has been applied to determine the structures of large biological systems or polymer vesicles and to unravel the mechanisms of biomineralization.[129-132] Imaging of nanostructures

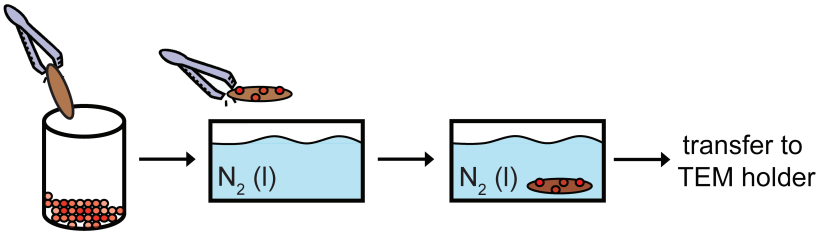

Figure 1.6. Sample preparation of hydrated nanostructures for imaging with cryo-ET. A small amount of sample is deposited onto a TEM grid, which is subsequently dipped into liquid nitrogen.

in solvated state requires sample preparation by plunge freezing to vitrify a thin solution layer on a TEM grid supported carbon film.[133] The preparation method for hydrated nanostructured materials, such as impregnated mesoporous silica particles, is illustrated in Figure 1.6. Here, the particles under study are not embedded in a vitrified amorphous layer to avoid interactions of the embedding solution with the impregnation solution. Rather, impregnated particles are deposited on a TEM grid after which the grid is dipped into liquid nitrogen.

To illustrate the value of ET for the study of supported catalysts, Figure 1.7 shows the results obtained for a rodlike SBA-15 particle containing Co_3O_4 nanoparticles. Figure 1.7A and Figure 1.7B show conventional TEM micrographs recorded under different tilt angles. Depending on the orientation of the hexagonal pore lattice, the pores are projected as a double lattice (Figure 1.7A) or a single lattice (Figure 1.7B). From these micrographs it can be tentatively concluded that the nanoparticles reside inside the pore system. Furthermore, a heterogeneous distribution of nanoparticles is most clearly observed from Figure 1.7A. The reconstruction obtained with ET provides a visualization of the nanoparticles inside the pore system of the same

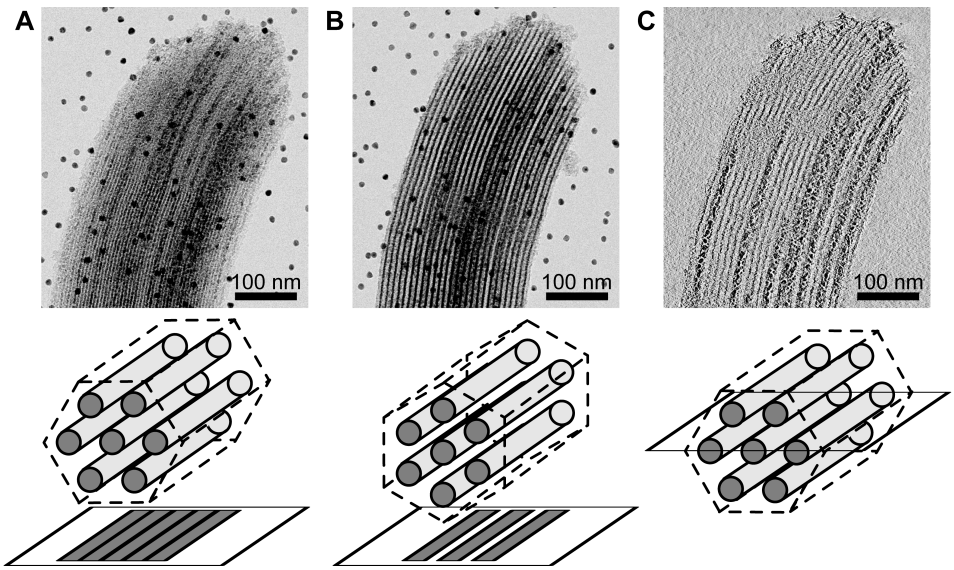

Figure 1.7. Comparison of TEM and electron tomography to visualize Co_3O_4 nanoparticles inside a rodlike SBA-15 particle. (A) 2D projection of Co_3O_4/SBA-15 particle tilted such that the [1 1] axis of the hexagonal pore lattice is aligned with the electron beam, 10 nm black circles are gold fiducials used to align the tilt series, (B) 2D projection of Co_3O_4/SBA-15 particle tilted such that the [1 0] axis of the hexagonal pore lattice is aligned with the electron beam, 10 nm black circles are gold fiducials used to align the tilt series, (C) 0.54 nm thick slice through 3D reconstruction obtained by electron tomography of the same Co_3O_4/SBA-15 particle showing 5 nm Co_3O_4 nanoparticles in individual pores.

SBA-15 catalyst particle. The slice through the reconstruction parallel to the pores in Figure 1.7C shows that few pores are filled with nanoparticles. Moreover, the nanoparticles inside the pores are actually in very close proximity of each other. In addition to the qualitative assessment of nanoparticle distribution, it is possible to obtain parameters as nanoparticle size distribution, shape distribution and nearest neighbor distances using image analysis on this tomographic reconstruction.[50]

1.3.3 Differential scanning calorimetry

A tool that is less prevailing in the field of catalyst preparation is differential scanning calorimetry (DSC). DSC is sometimes applied to study the decomposition of catalyst precursors[78] or their reduction behavior.[134] However, with DSC also the phase behavior of confined salts and salt solutions in mesoporous supports can be studied. This provides valuable information for supported catalyst preparation, as the major preparation routes for supported metal catalysts (ion-adsorption, deposition-precipitation and impregnation-drying) are altogether based on contacting a porous support with the metal-precursor in a liquid phase.

Thermoporometry

The curvature or size of a confined phase can be determined on the basis of the melting or freezing point depression by thermoporometry.[135] The influence of surface curvature on phase transitions plays a role in many characterization techniques, such as physisorption,[136] mercury porosimetry[137] or cryo-porometry by ^{1}H-NMR[138] and is essential for the characterization of mesoporous materials.[139] Therefore there are strong analogies between thermoporometry and N_2-physisorption.[140] Like the relative pressure of capillary condensation, the melting temperature is associated with the mesopore size. As freezing is a nucleation controlled process, it is comparable to evaporation and is sensitive to pore size but also pore connectivity. The melting point depression, ΔT, is inversely related to the pore radius, r, and is described by the Gibbs-Thomson equation, eq 3[141]

$$\Delta T = T_0 - T_m(r) = \frac{2T_0(\gamma_{sw} - \gamma_{lw})v_l}{\Delta H_f r} \qquad \text{eq.3}$$

where γ is the surface tension, ν is the molar volume of the liquid, T_0 is the bulk transition temperature and ΔH_f the enthalpy of fusion. With DSC the melting and freezing point of confined liquids is accurately determined.[142, 143] Although thermoporometry is classically performed using water as adsorptive,[135, 144, 145] confined organic liquids including cyclohexane, nitrobenzene and various aromatic

molecules[146-149] are also used to determine pore size dependent phase transition temperatures. For water in silica mesopores, a lower pore diameter limit of ~2 nm has been observed, below which the formation of ice was no longer detectable. [150, 151] For thermoporometry using benzene or cyclohexane this limit was higher at 4.7 nm[147] and 3.5 nm respectively[149], which could be related to the molecular dimensions of the adsorptive. However, for these molecules a larger melting point depression as a function of the pore radius as compared to water was observed, which can be used for increased resolution at larger pore diameters. The adsorptive of choice is dependent on the range of pore diameters under study and the nature of the porous material.

For water wetting a silica mesopore and having a contact angle $\theta = 0º$, $\gamma_{ws} - \gamma_{wl} = \gamma_{sl}$ and the Gibbs-Thomson equation can be simplified to eq. 4,

$$\Delta T = \frac{C_{GT}}{R - t} \qquad \text{eq. 4}$$

with C_{GT} a constant in ºC·nm and R the mesopore radius and *t* a non-freezing layer in nm.[152] In this case the surface tension γ_{sl}, the enthalpy of fusion ΔH_f and the molar volume ν are considered to be independent of the temperature. This equation provides a good description of experimental data, although it is known that for instance the enthalpy of fusion for water decreases with decreasing temperature. However many functions describing the temperature dependency of the enthalpy of fusion or surface tension can be found.[135, 141, 153-155] Furthermore, a non-freezing layer with thickness *t* is taken into account.[145, 156, 157] The existence of a layer of molecules between the pore wall and ice core that does not crystallize has been demonstrated,[158, 159] however, there is no real consensus on the actual thickness, as values between 0.20 and 1.05 nm are reported.[160, 161] The introduction of ordered mesoporous silica materials has

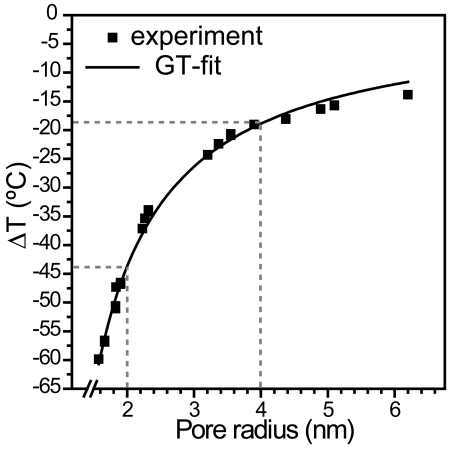

Figure 1.8. Melting point depression as function of the pore radius. Symbols are experimental values for the melting point onset temperature of water confined in OMS impregnated with a two-fold excess of H_2O determined with DSC at a heating rate of 1 ºC/min. The solid line represents best fit for the Gibbs-Thomson equation with $C_{GT} = 66.5$ ºC·nm and t = 0.48 nm. Grey dashed lines indicate melting point depression for a typical MCM-41 material with a pore radius of 2.0 nm and a typical SBA-15 material with a pore radius of 4.0 nm.

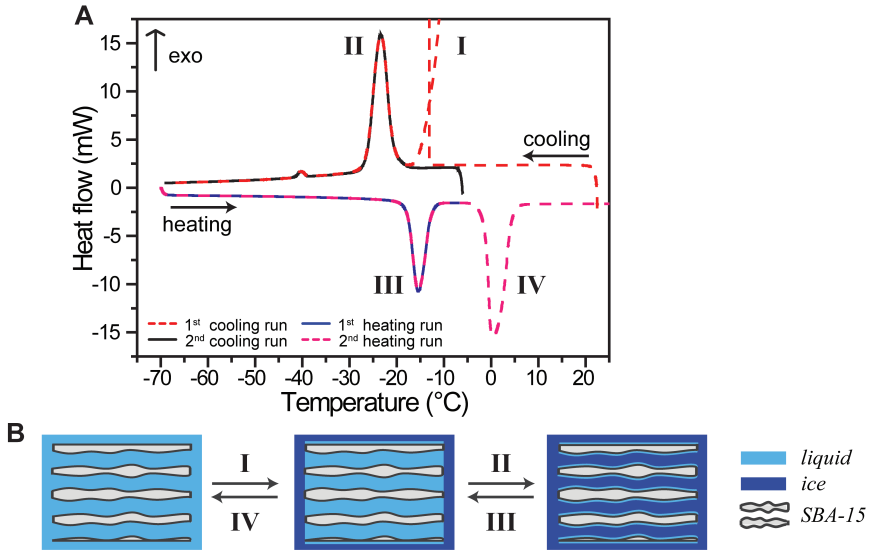

Figure 1.9. Freezing and melting of water confined in a mesoporous silica material. (A) DSC thermogram recorded for SBA-15 impregnated with an excess of water, roman numbers indicate different transitions illustrated by scheme in (B), I: freezing of extraporous water, II: freezing of water confined in pores, III: melting of water in pores, IV: melting of extraporous water. Heating rate 5 ºC/min.

allowed a practical approach to determine the melting point depression as a function of mesopore size.[157]

Figure 1.8 shows the experimental data and corresponding fit to the Gibbs-Thomson equation of a series of OMS materials spanning pore radii from 1.5 to 6.2 nm. It shows that water confined in a typical SBA-15 material with a pore radius of 4 nm melts at -16 ºC, while water confined in a typical MCM-41 with a pore radius of 2 nm has a melting point depression of even 43 ºC.

A typical DSC recording to determine the depressed melting and freezing point of water is shown in Figure 1.9. The porous material is typically impregnated with an excess of high purity water such that there is an extraporous bulk phase surrounding the pore system. During the first cooling ramp a large exothermic peak with a sharp onset (I) is observed, which corresponds to the freezing of supercooled extraporous water. The water confined in the mesopores subsequently freezes by heterogeneous nucleation at a temperature controlled by the mesopore radius (II). During heating melting of confined water (III) can be observed at slightly higher temperatures than the freezing, due to a hysteretic effect. By recooling the sample, from -5 ºC to -70 ºC the correlation between the freezing (II) and melting (III) of confined water can be

confirmed. Furthermore, the freezing point depression is more accurately determined from this second cooling cycle, as there is no overlap with the large exotherm peak (I). Finally, heating to room temperature melts both confined water and extraporous water.

1.4 Thesis Outline and Scope

The research in this thesis focuses on the rationalization of supported catalyst preparation by fundamental insights into the phase behavior of nanoconfined phases. Ultimately, catalysts with equally sized nanoparticles and a controlled distribution over the support are prepared by the simple impregnation and drying method. Challenges lie in the use of hydrated transition metal nitrate precursors and high metal loadings on silica supports.

The first step of supported catalyst preparation by 'impregnation and drying' was quantified using DSC. In **Chapter 2** we show that 85-100 % of the pores of mesoporous silica supports are filled by a single impregnation step with water or an aqueous salt solution. Therefore, a by and large homogeneous solution distribution is obtained by aqueous impregnation. Subsequently, the effect of drying on the salt distribution is discussed in **Chapter 3**. Using cryo-electron tomography (cryo-ET) the distribution of phases during the elementary preparation steps is visualized in 3D and with nanometer resolution. We demonstrated within a single SBA-15 particle that conventional drying caused a non-uniform salt deposition, while after impregnation the solution had been homogeneously distributed. On the other hand, by freeze-drying a uniform salt distribution was obtained as it successfully restricted the solution mobility. After thermal treatment this resulted in a more uniform nanoparticle distribution.

Fundamental insight into freeze-drying was obtained using DSC and is described in **Chapter 4**. The freezing point depression of the impregnated salt solution and the melt infiltration precursor salt were used to develop different freeze-drying methods. We were able to manipulate the nanoparticle distribution on industrially relevant silica-gel supports to form clusters, an egg-shell configuration or a uniform distribution. These catalysts for the Fischer-Tropsch synthesis form the starting point for investigations into the effect of nanoparticle spacing on deactivation by sintering under industrially relevant conditions.

Chapter 5 describes melt infiltration as an alternative preparation method to impregnation and drying. The melting of $Co(NO_3)_2 \cdot 6H_2O$ in the presence of mesoporous silica matrices was followed *in situ* using DSC. After decomposition of the nitrates highly dispersed Co_3O_4 nanoparticles formed with a distribution over the support similar to what is obtained by conventional impregnation and drying. After

reduction the catalysts showed high activity for the Fischer-Tropsch reaction.

Two applications of thermoporometry for mesoporous materials with catalytic relevance are described in **Chapters 6** and **7**. First differential scanning calorimetry is used to detect and quantify nanoparticle blockages in supported model hydrogenation catalysts. Together with argon physisorption, DSC showed to be more sensitive to detection of pore constrictions as compared to the classically applied technique, nitrogen physisorption. Second, DSC was applied to determine entrance sizes and entrance size distributions of cage silica materials. Here, DSC provided information that was inaccessible by nitrogen as well as argon physisorption techniques.

References

[1] K. P. de Jong, ed. *Synthesis of Solid Catalysts*. 2009, Wiley-VCH: Weinheim.
[2] E. Iglesia, S. L. Soled and R. A. Fiato, *J. Catal.* **1992**, *137*, 212.
[3] E. Iglesia, *Appl. Catal.- A Gen.* **1997**, *161*, 59.
[4] A. Y. Khodakov, W. Chu and P. Fongarland, *Chem. Rev.* **2007**, *107*, 1692.
[5] E. de Smit and B. M. Weckhuysen, *Chem. Soc. Rev.* **2008**, *37*, 2758.
[6] J. L. Casci, C. M. Lok and M. D. Shannon, *Catal. Today* **2009**, *145*, 38.
[7] shell.com. [cited 2011 October 21]; Available from: http://www.shell.com/home/content/aboutshell/our_strategy/major_projects_2/pearl/overview/.
[8] G. L. Bezemer, J. H. Bitter, H. P. C. E. Kuipers, H. Oosterbeek, J. E. Holewijn, X. D. Xu, F. Kapteijn, A. J. van Dillen and K. P. de Jong, *J. Am. Chem. Soc.* **2006**, *128*, 3956.
[9] J. P. den Breejen, P. B. Radstake, G. L. Bezemer, J. H. Bitter, V. Froseth, A. Holmen and K. P. de Jong, *J. Am. Chem. Soc.* **2009**, *131*, 7197.
[10] A. Martinez and G. Prieto, *J. Catal.* **2007**, *245*, 470.
[11] G. Prieto, A. Martinez, P. Concepcion and R. Moreno-Tost, *J. Catal.* **2009**, *266*, 129.
[12] A. M. Saib, D. J. Moodley, I. M. Ciobica, M. M. Hauman, B. H. Sigwebela, C. J. Weststrate, J. W. Niemantsverdriet and J. van de Loosdrecht, *Catal. Today* **2010**, *154*, 271.
[13] N. E. Tsakoumis, M. Ronning, O. Borg, E. Rytter and A. Holmen, *Catal. Today* **2010**, *154*, 162.
[14] O. Borg, P. D. C. Dietzel, A. I. Spjelkavik, E. Z. Tveten, J. C. Walmsley, S. Diplas, S. Eri, A. Holmen and E. Rytter, *J. Catal.* **2008**, *259*, 161.
[15] J. R. Regalbuto, ed. *Catalyst Preparation - Science and Engineering*. 2007, CRC Press: Boca Raton.
[16] L. Espinosa-Alonso, A. M. Beale and B. M. Weckhuysen, *Acc. Chem. Res.* **2010**, *43*, 1279.
[17] K. Bourikas, C. Kordulis, J. Vakros and A. Lycourghiotis, *Adv. Colloid Interfac.* **2004**, *110*, 97.
[18] P. L. J. Gunter, J. W. Niemantsverdriet, F. H. Ribeiro and G. A. Somorjai, *Catal. Rev. - Sci. Eng.* **1997**, *39*, 77.
[19] A. T. Bell, *Science* **2003**, *299*, 1688.
[20] G. A. Somorjai, F. Tao and J. Y. Park, *Top. Catal.* **2008**, *47*, 1.
[21] M. Schreier and J. R. Regalbuto, *J. Catal.* **2004**, *225*, 190.
[22] J. T. Miller, M. Schreier, A. J. Kropf and J. R. Regalbuto, *J. Catal.* **2004**, *225*, 203.
[23] L. Jiao and J. R. Regalbuto, *J. Catal.* **2008**, *260*, 329.
[24] K. P. de Jong, *Deposition Precipitation*, in *Synthesis of solid catalysts*, K. P. de Jong, Editor. 2009, Wiley-VCH: Weinheim.
[25] M. K. van der Lee, A. J. van Dillen, J. H. Bitter and K. P. de Jong, *J. Am. Chem. Soc.* **2005**, *127*, 13573.
[26] P. Burattin, M. Che and C. Louis, *J. Phys. Chem. B* **1999**, *103*, 6171.
[27] P. Burattin, M. Che and C. Louis, *The Journal of Physical Chemistry B* **1998**, *102*, 2722.
[28] P. Serp, P. Kalck and R. Feurer, *Chem. Rev.* **2002**, *102*, 3085.
[29] J. L. Lu and P. C. Stair, *Angew. Chem., Int. Ed.* **2010**, *49*, 2547.
[30] W. Chu, L. N. Wang, P. A. Chernavskii and A. Y. Khodakov, *Angew. Chem., Int. Ed.* **2008**, *47*, 5052.

[31] M. Che, Z. X. Cheng and C. Louis, *J. Am. Chem. Soc.* **1995**, *117*, 2008.
[32] N. F. Zheng and G. D. Stucky, *J. Am. Chem. Soc.* **2006**, *128*, 14278.
[33] J. V. I. Timonen, E. T. Seppala, O. Ikkala and R. H. A. Ras, *Angew. Chem., Int. Ed.* **2011**, *50*, 2080.
[34] A. V. Neimark, L. I. Kheifez and V. B. Fenelonov, *Ind. Eng. Chem. Prod. Res. Dev.* **1981**, *20*, 439.
[35] A. Lekhal, B. J. Glasser and J. G. Khinast, *Chem. Eng. Sci.* **2004**, *59*, 1063.
[36] G. Prieto, A. Martinez, R. Murciano and M. A. Arribas, *Appl. Catal.- A Gen.* **2009**, *367*, 146.
[37] J. van der Meer, I. Bardez, F. Bart, P. A. Albouy, G. Wallez and A. Davidson, *Micropor. Mesopor. Mat.* **2009**, *118*, 183.
[38] F. Jiao and H. Frei, *Angew. Chem., Int. Ed.* **2009**, *48*, 1841.
[39] Y. Zhang, Y. Liu, G. H. Yang, S. L. Sun and N. Tsubaki, *Appl. Catal.- A Gen.* **2007**, *321*, 79.
[40] L. Jiao and J. R. Regalbuto, *J. Catal.* **2008**, *260*, 342.
[41] O. Borg, J. C. Walmsley, R. Dehghan, B. S. Tanem, E. A. Blekkan, S. Eri, E. Rytter and A. Holmen, *Catal. Lett.* **2008**, *126*, 224.
[42] I. Arslan, J. C. Walmsley, E. Rytter, E. Bergene and P. A. Midgley, *J. Am. Chem. Soc.* **2008**, *130*, 5716.
[43] E. Marceau, M. Che, J. Cejka and A. Zukal, *ChemCatChem* **2010**, *2*, 413.
[44] P. Munnik, M. Wolters, A. Gabrielsson, S. D. Pollington, G. Headdock, J. H. Bitter, P. E. de Jongh and K. P. de Jong, *J. Phys. Chem. C* **2011**, *115*, 14698.
[45] M. Imperor-Clerc, D. Bazin, M. D. Appay, P. Beaunier and A. Davidson, *Chem. Mater.* **2004**, *16*, 1813.
[46] V. Escax, M. Imperor-Clerc, D. Bazin and A. Davidson, *C. R. Chim.* **2005**, *8*, 663.
[47] J. R. A. Sietsma, J. D. Meeldijk, J. P. den Breejen, M. Versluijs-Helder, A. J. van Dillen, P. E. de Jongh and K. P. de Jong, *Angew. Chem., Int. Ed.* **2007**, *46*, 4547.
[48] T. Tsoncheva, J. Rosenholm, M. Linden, F. Kleitz, M. Tiemann, L. Ivanova, M. Dimitrov, D. Paneva, I. Mitov and C. Minchev, *Micropor. Mesopor. Mat.* **2008**, *112*, 327.
[49] F. Schuth, A. Wingen and J. Sauer, *Micropor. Mesopor. Mat.* **2001**, *44*, 465.
[50] H. Friedrich, J. R. A. Sietsma, P. E. de Jongh, A. J. Verkleij and K. P. de Jong, *J. Am. Chem. Soc.* **2007**, *129*, 10249.
[51] N. Ikawa, M. Yamada, A. Miyaki and A. Endo, *Chem. Comm.*, *46*, 4342.
[52] M. S. Moreno, M. Weyland, P. A. Midgley, J. F. Bengoa, M. V. Cagnoli, N. G. Gallegos, A. M. Alvarez and S. G. Marchetti, *Micron* **2006**, *37*, 52.
[53] J. Roggenbuck, T. Waitz and M. Tiemann, *Micropor. Mesopor. Mat.* **2008**, *113*, 575.
[54] J. Panpranot, J. G. Goodwin and A. Sayari, *Catal. Today* **2002**, *77*, 269.
[55] T. M. Eggenhuisen, J. P. den Breejen, D. Verdoes, P. E. de Jongh and K. P. de Jong, *J. Am. Chem. Soc.* **2010**, *132*, 18318.
[56] C. J. Gommes, K. de Jong, J. P. Pirard and S. Blacher, *Langmuir* **2005**, *21*, 12378.
[57] Y. M. Wang, Z. Y. Wu, L. Y. Shi and J. H. Zhu, *Adv. Mater.* **2005**, *17*, 323.
[58] H. Tuysuz, C. W. Lehmann, H. Bongard, B. Tesche, R. Schmidt and F. Schuth, *J. Am. Chem. Soc.* **2008**, *130*, 11510.
[59] A. J. van Dillen, R. J. A. M. Terorde, D. J. Lensveld, J. W. Geus and K. P. de Jong, *J. Catal.* **2003**, *216*, 257.
[60] J. Panpranot, S. Kaewkun, P. Praserthdam and J. G. Goodwin, *Catal. Lett.* **2003**, *91*, 95.
[61] J. S. Girardon, A. S. Lermontov, L. Gengembre, P. A. Chernavskii, A. Griboval-Constant and A. Y. Khodakov, *J. Catal.* **2005**, *230*, 339.
[62] A. Martinez, C. Lopez, F. Marquez and I. Diaz, *J. Catal.* **2003**, *220*, 486.
[63] A. Zukal, H. Siklova and J. Cejka, *Langmuir* **2008**, *24*, 9837.
[64] T. Klimova, J. Reyes, O. Gutierrez and L. Lizama, *Appl. Catal.- A Gen.* **2008**, *335*, 159.
[65] C. H. Tu, A. Q. Wang, M. Y. Zheng, X. D. Wang and T. Zhang, *Appl. Catal. A-Gen.* **2006**, *297*, 40.
[66] C. S. Chen, C. C. Chen, C. T. Chen and H. M. Kao, *Chem. Comm.* **2011**, *47*, 2288.
[67] L. van de Loosdrecht, M. van der Haar, A. M. van der Kraan, A. J. van Dillen and J. W. Geus, *Appl. Catal.- A Gen.* **1997**, *150*, 365.
[68] D. J. Lensveld, J. G. Mesu, A. J. van Dillen and K. P. de Jong, *Micropor. Mesopor. Mat.* **2001**, *44*, 401.
[69] E. Lira, C. M. Lopez, F. Oropeza, M. Bartolini, J. Alvarez, M. Goldwasser, F. L. Linares, J. F. Lamonier and M. J. P. Zurita, *J. Mol. Catal. A: Chem.* **2008**, *281*, 146.
[70] J. S. Girardon, E. Quinet, A. Griboval-Constant, P. A. Chernavskii, L. Gengembre and A. Y. Khodakov, *J. Catal.* **2007**, *248*, 143.
[71] J. P. Hong, E. Marceau, A. Y. Khodakov, A. Griboval-Constant, C. La Fontaine, F. Villain, V. Briois and

P. A. Chernavskii, *Catal. Today* **2011**, *175*, 528.
[72] T. Vergunst, F. Kapteijn and J. A. Moulijn, *Appl. Catal.- A Gen.* **2001**, *213*, 179.
[73] T. M. Eggenhuisen, H. Friedrich, F. Nudelman, J. Zecevic, N. A. J. M. Sommerdijk, P. E. de Jongh and K. P. de Jong, *In preparation* **2012**.
[74] J. van de Loosdrecht, S. Barradas, E. A. Caricato, N. G. Ngwenya, P. S. Nkwanyana, M. A. S. Rawat, B. H. Sigwebela, P. J. van Berge and J. L. Visagie, *Top. Catal.* **2003**, *26*, 121.
[75] X. Sun, Y. Shi, P. Zhang, C. Zheng, X. Zheng, F. Zhang, Y. Zhang, N. Guan, D. Zhao and G. D. Stucky, *J. Am. Chem. Soc.* **2011**, *133*, 14542.
[76] C. H. Bartholomew and R. J. Farrauto, *J. Catal.* **1976**, *45*, 41.
[77] J. R. A. Sietsma, J. D. Meeldijk, M. Versluijs-Helder, A. Broersma, A. J. van Dillen, P. E. de Jongh and K. P. de Jong, *Chem. Mater.* **2008**, *20*, 2921.
[78] J. R. A. Sietsma, H. Friedrich, A. Broersma, M. Versluijs-Helder, A. J. van Dillen, P. E. de Jongh and K. P. de Jong, *J. Catal.* **2008**, *260*, 227.
[79] M. Wolters, H. Daly, A. Goguet, F. C. Meunier, C. Hardacre, J. H. Bitter, P. E. de Jongh and K. P. de Jong, *J. Phys. Chem. C* **2010**, *114*, 7839.
[80] M. Wolters, P. Munnik, J. H. Bitter, P. E. de Jongh and K. P. de Jong, *J. Phys. Chem. C* **2011**, *115*, 3332.
[81] M. Wolters, I. C. A. Contreras Andrade, P. Munnik, J. H. Bitter, P. E. de Jongh and K. P. de Jong, *Stud. Surf. Sci. Catal.* **2010**, *175*, 69.
[82] M. Wolters, L. J. W. van Grotel, T. M. Eggenhuisen, J. R. A. Sietsma, P. E. de Jongh and K. P. de Jong, *Catal. Today* **2011**, *163*, 27.
[83] J. P. den Breejen, J. R. A. Sietsma, H. Friedrich, J. H. Bitter and K. P. de Jong, *J. Catal.* **2010**, *270*, 146.
[84] G. Jacobs, W. P. Ma, B. H. Davis, D. C. Cronauer, A. J. Kropf and C. L. Marshall, *Catal. Lett.* **2010**, *140*, 106.
[85] C. T. Kresge, M. E. Leonowicz, W. J. Roth, J. C. Vartuli and J. S. Beck, *Nature* **1992**, *359*, 710.
[86] K. Nakanishi and N. Tanaka, *Acc. Chem. Res.* **2007**, *40*, 863.
[87] M. Vallet-Regi, *Chem.-Eur. J.* **2006**, *12*, 5934.
[88] J. L. Vivero-Escoto, I. I. Slowing, B. G. Trewyn and V. S. Y. Lin, *Small* **2010**, *6*, 1952.
[89] A. Martinez and G. Prieto, *Top. Catal.* **2009**, *52*, 75.
[90] A. Corma, *Top. Catal.* **1997**, *4*, 249.
[91] A. Taguchi and F. Schuth, *Micropor. Mesopor. Mat.* **2005**, *77*, 1.
[92] P. C. A. Alberius, K. L. Frindell, R. C. Hayward, E. J. Kramer, G. D. Stucky and B. F. Chmelka, *Chem. Mater.* **2002**, *14*, 3284.
[93] Y. Wan and D. Y. Zhao, *Chem. Rev.* **2007**, *107*, 2821.
[94] V. Meynen, P. Cool and E. F. Vansant, *Micropor. Mesopor. Mat.* **2009**, *125*, 170.
[95] D. Y. Zhao, J. L. Feng, Q. S. Huo, N. Melosh, G. H. Fredrickson, B. F. Chmelka and G. D. Stucky, *Science* **1998**, *279*, 548.
[96] D. Y. Zhao, Q. S. Huo, J. L. Feng, B. F. Chmelka and G. D. Stucky, *J. Am. Chem. Soc.* **1998**, *120*, 6024.
[97] A. Galarneau, N. Cambon, F. Di Renzo, R. Ryoo, M. Choi and F. Fajula, *New J. Chem.* **2003**, *27*, 73.
[98] J. S. Beck, J. C. Vartuli, W. J. Roth, M. E. Leonowicz, C. T. Kresge, K. D. Schmitt, C. T. W. Chu, D. H. Olson, E. W. Sheppard, S. B. Mccullen, J. B. Higgins and J. L. Schlenker, *J. Am. Chem. Soc.* **1992**, *114*, 10834.
[99] M. Kruk, M. Jaroniec, Y. Sakamoto, O. Terasaki, R. Ryoo and C. H. Ko, *J. Phys. Chem. B* **2000**, *104*, 292.
[100] Y. Sakamoto, M. Kaneda, O. Terasaki, D. Y. Zhao, J. M. Kim, G. Stucky, H. J. Shim and R. Ryoo, *Nature* **2000**, *408*, 449.
[101] C. Z. Yu, Y. H. Yu and D. Y. Zhao, *Chem. Comm.* **2000**, 575.
[102] J. Fan, C. Z. Yu, T. Gao, J. Lei, B. Z. Tian, L. M. Wang, Q. Luo, B. Tu, W. Z. Zhou and D. Y. Zhao, *Angew. Chem., Int. Ed.* **2003**, *42*, 3146.
[103] J. R. Matos, M. Kruk, L. P. Mercuri, M. Jaroniec, L. Zhao, T. Kamiyama, O. Terasaki, T. J. Pinnavaia and Y. Liu, *J. Am. Chem. Soc.* **2003**, *125*, 821.
[104] T. W. Kim, R. Ryoo, M. Kruk, K. P. Gierszal, M. Jaroniec, S. Kamiya and O. Terasaki, *J. Phys. Chem. B* **2004**, *108*, 11480.
[105] J. M. Thomas and P. A. Midgley, *ChemCatChem* **2010**, *2*, 783.
[106] H. L. Xin, J. A. Mundy, Z. Liu, R. Cabezas, R. Hovden, L. F. Kourkoutis, J. Zhang, N. P. Subramanian, R. Makharia, F. T. Wagner and D. A. Muller, *Nano Lett.* **2011**, DOI:10.1021/nl203975u.
[107] P. Li, J. Y. Liu, N. Nag and P. A. Croziers, *J. Phys. Chem. B* **2005**, *109*, 13883.
[108] P. Li, J. Liu, N. Nag and P. A. Crozier, *J. Catal.* **2009**, *262*, 73.

[109] E. D. Boyes and P. L. Gai, *Ultramicroscopy* **1997**, *67*, 219.
[110] J. F. Creemer, S. Helveg, G. H. Hoveling, S. Ullmann, A. M. Molenbroek, P. M. Sarro and H. W. Zandbergen, *Ultramicroscopy* **2008**, *108*, 993.
[111] S. R. Challa, A. T. Delariva, T. W. Hansen, S. Helveg, J. Sehested, P. L. Hansen, F. Garzon and A. K. Datye, *J. Am. Chem. Soc.* **2011**, DOI:10.1012/ja208324n.
[112] P. A. Midgley and R. E. Dunin-Borkowski, *Nat. Mater.* **2009**, *8*, 271.
[113] H. Friedrich, P. E. de Jongh, A. J. Verkleij and K. P. de Jong, *Chem. Rev.* **2009**, *109*, 1613.
[114] I. Arslan, J. R. Tong and P. A. Midgley, *Ultramicroscopy* **2006**, *106*, 994.
[115] U. Ziese, K. P. de Jong and A. J. Koster, *Appl. Catal.- A Gen.* **2004**, *260*, 71.
[116] V. Lucic, F. Forster and W. Baumeister, *Structural studies by electron tomography: From cells to molecules*, in *Annual Review of Biochemistry*. 2005, Annual Reviews: Palo Alto. p. 833.
[117] A. J. Koster, U. Ziese, A. J. Verkleij, A. H. Janssen and K. P. de Jong, *J. Phys. Chem. B* **2000**, *104*, 9368.
[118] M. Weyland, P. A. Midgley and J. M. Thomas, *J. Phys. Chem. B* **2001**, *105*, 7882.
[119] A. H. Janssen, C. M. Yang, Y. Wang, F. Schuth, A. J. Koster and K. P. de Jong, *J. Phys. Chem. B* **2003**, *107*, 10552.
[120] O. Ersen, J. Werckmann, M. Houlle, M. J. Ledoux and C. Pham-Huu, *Nano Lett.* **2007**, *7*, 1898.
[121] E. P. W. Ward, T. J. V. Yates, J. J. Fernandez, D. E. W. Vaughan and P. A. Midgley, *J. Phys. Chem. C* **2007**, *111*, 11501.
[122] R. Grothausmann, G. Zehl, I. Manke, S. Fiechter, P. Bogdanoff, I. Dorbandt, A. Kupsch, A. Lange, M. P. Hentschel, G. Schumacher and J. Banhart, *J. Am. Chem. Soc.* **2011**, *133*, 18161.
[123] N. Tanaka, S. Sueda and K. Yoshida, *Ultramicroscopy* **2010**, *110*, 1120.
[124] Y. Yu, H. L. Xin, R. Hovden, D. Wang, E. D. Rus, J. A. Mundy, D. A. Muller and H. Abruna, *Nano Lett.* **2012**, DOI:10.1021/nl203920s.
[125] O. Ersen, J. Parmentier, L. A. Solovyov, M. Drillon, C. Pham-Huu, J. Werckmann and P. Schultz, *J. Am. Chem. Soc.* **2008**, *130*, 16800.
[126] C. J. Gommes, H. Friedrich, M. Wolters, P. E. de Jongh and K. P. de Jong, *Chem. Mater.* **2009**, *21*, 1311.
[127] K. P. de Jong, J. Zecevic, H. Friedrich, P. E. de Jongh, M. Bulut, S. van Donk, R. Kenmogne, A. Finiels, V. Hulea and F. Fajula, *Angew. Chem., Int. Ed.* **2010**, *49*, 10074.
[128] F. Nudelman, G. de With and N. A. J. M. Sommerdijk, *Soft Matter* **2011**, *7*, 17.
[129] E. I. Tocheva, Z. Li and G. J. Jensen, *Cold Spring Harb. Perspect. Biol.* **2010**, *2*, a003442.
[130] E. M. Pouget, P. H. H. Bomans, J. A. C. M. Goos, P. M. Frederik, G. de With and N. A. J. M. Sommerdijk, *Science* **2009**, *323*, 1455.
[131] A. Dey, P. H. H. Bomans, F. A. Muller, J. Will, P. M. Frederik, G. de With and N. A. J. M. Sommerdijk, *Nat. Mater.* **2010**, *9*, 1010.
[132] F. Nudelman, K. Pieterse, A. George, P. H. H. Bomans, H. Friedrich, L. J. Brylka, P. A. J. Hilbers, G. de With and N. A. J. M. Sommerdijk, *Nat. Mater.* **2010**, *9*, 1004.
[133] H. Friedrich, P. M. Frederik, G. de With and N. A. J. M. Sommerdijk, *Angew. Chem., Int. Ed.* **2010**, *49*, 7850.
[134] B. P. C. Hereijgers, T. M. Eggenhuisen, K. P. de Jong, H. Talsma, A. M. J. van der Eerden, A. M. Beale and B. M. Weckhuysen, *J. Phys. Chem. C* **2011**, *115*, 15545.
[135] M. Brun, A. Lallemand, J.-F. Quinson and C. Eyraud, *Thermochim. Acta* **1977**, *21*, 59.
[136] S. J. Gregg and K. S. W. Sing, *Adsorption, Surface Area and Porosity*. 2nd ed. 1982, London: Academic Press.
[137] A. Galarneau, B. Lefevre, H. Cambon, B. Coasne, S. Vallange, Z. Gabelica, J. P. Bellat and F. Di Renzo, *J. Phys. Chem. C* **2008**, *112*, 12921.
[138] O. V. Petrov and I. Furo, *Prog. Nucl. Magn. Reson. Spectrosc.* **2009**, *54*, 97.
[139] R. Denoyel, P. Llewellyn, I. Beurroies, J. Rouquerol, F. O. Rouquerol and L. Luciani, *Part. Part. Syst. Char.* **2004**, *21*, 128.
[140] I. Beurroies, R. Denoyel, P. Llewellyn and J. Rouquerol, *Thermochim. Acta* **2004**, *421*, 11.
[141] R. Defay, I. Prigogine, A. Bellemans and D. H. Everett, *Surface Tension and Adsorption*. 1966, London: Longmans, Green & Co LTD.
[142] M. R. Landry, *Thermochim. Acta* **2005**, *433*, 27.
[143] A. M. Kjeldsen and M. R. Geiker, *Mater. Struct.* **2008**, *41*, 213.
[144] J. F. Quinson, J. Dumas and J. Serughetti, *J. Non-Cryst. Solids* **1986**, *79*, 397.
[145] K. Ishikiriyama and M. Todoki, *Thermochim. Acta* **1995**, *256*, 213.

[146] C. L. Jackson and G. B. McKenna, *J. Chem. Phys.* **1990**, *93*, 9002.
[147] G. Dosseh, Y. D. Xia and C. Alba-Simionesco, *J. Phys. Chem. B* **2003**, *107*, 6445.
[148] N. Billamboz, M. Baba, M. Grivet and J. M. Nedelec, *J. Phys. Chem. B* **2004**, *108*, 12032.
[149] S. Amanuel, H. Bauer, P. Bonventre and D. Lasher, *J. Phys. Chem. C* **2009**, *113*, 18983.
[150] K. Morishige and K. Kawano, *J. Chem. Phys.* **1999**, *110*, 4867.
[151] S. Jahnert, F. V. Chavez, G. E. Schaumann, A. Schreiber, M. Schonhoff and G. H. Findenegg, *Phys. Chem. Chem. Phys.* **2008**, *10*, 6039.
[152] G. H. Findenegg, S. Jahnert, D. Akcakayiran and A. Schreiber, *ChemPhysChem* **2008**, *9*, 2651.
[153] K. Ishikiriyama and M. Todoki, *J. Colloid Inter. Sci.* **1995**, *171*, 103.
[154] E. W. Hansen, H. C. Gran and E. J. Sellevold, *J. Phys. Chem. B* **1997**, *101*, 7027.
[155] S. Kittaka, S. Ishimaru, M. Kuranishi, T. Matsuda and T. Yamaguchi, *Phys. Chem. Chem. Phys.* **2006**, *8*, 3223.
[156] R. K. Rennie and J. Clifford, *J. Chem. Soc., Farad. T 1* **1977**, *73*, 680.
[157] A. Schreiber, I. Ketelsen and G. H. Findenegg, *Phys. Chem. Chem. Phys.* **2001**, *3*, 1185.
[158] K. Overloop and L. Vangerven, *J. Magn. Reson. Ser. A* **1993**, *101*, 179.
[159] J. B. W. Webber, J. C. Dore, J. H. Strange, R. Anderson and B. Tohidi, *Journal of Physics-Condensed Matter* **2007**, *19*.
[160] T. Yamamoto, A. Endo, Y. Inagi, T. Ohmori and M. Nakaiwa, *J. Colloid Inter. Sci.* **2005**, *284*, 614.
[161] A. Endo, T. Yamamoto, Y. Inagi, K. Wakabe and T. Ohmori, *J. Phys. Chem. C* **2008**, *112*, 9034.

Chapter 2

Impregnation of Mesoporous Silica for Catalyst Preparation Studied with Differential Scanning Calorimetry

Abstract

The effectiveness of impregnation as precursor loading step was quantified using DSC. 85-100% Of the pores of porous silica supports were filled by a single impregnation step with water or an aqueous salt solution. Therefore, aqueous impregnation yielded a largely homogeneous distribution of salt solution over the support.

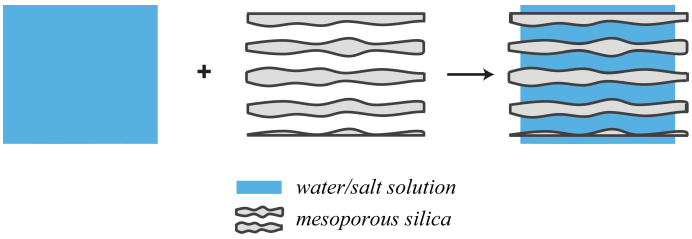

2.1 Introduction

Confinement can influence physico-chemical properties of liquids, such as the freezing point, solubility and self-diffusion. Understanding these properties is of fundamental interest,[1] but is also important for practical applications such as preserving biological materials[2] or predicting the stability of building materials at low temperatures[3] and the characterization of porous materials.[4, 5] Confined liquids can be used in drug delivery systems[6-8], nanoreactors[9] and for catalysis.[10] Moreover, they are important for catalyst synthesis, as the major preparation routes for supported metal catalysts (ion-adsorption[11-13], deposition-precipitation[14-17] and impregnation-drying[18-20]) are altogether based on contacting a porous support with the metal-precursor in a liquid phase.

Supported metal catalysts generally rely for their activity on a highly dispersed active phase. However, redistribution of the metal phase during one of the preparation steps is rather common, especially with the impregnation-drying route. For ordered mesoporous silica supports, undesired large metal particles are observed on the exterior surface of the mesoporous particles.[21-24] In addition, nanoparticle aggregates are found inside the pore network.[25-27] Therefore, it is important that the solution containing the metal precursor is distributed homogeneously over the mesoporous support by impregnation in the first place. Although this is generally assumed, there are indications otherwise. Empty pores were observed in a freshly impregnated SBA-15 in a cryoSTEM experiment.[28] In addition, inhomogeneous wetting of the support by the impregnation solution was suspected in relation to the synthesis of mesoporous metaloxides.[29] Others also suggested non-uniform pore filling by impregnation, but could only indirectly assess the actual filling.[22, 30]

Extra-porous and intra-porous phases in impregnated porous supports can be distinguished due to the melting point depression of confined liquids compared to bulk liquids.[31] With differential scanning calorimetry, the melting enthalpies and temperatures of pore and bulk liquids can be determined accurately. However, direct quantification of pore liquids from the melting enthalpy is complicated as the specific melting enthalpy of confined fluids depends on the temperature, the confinement, the specific crystal structure and liquid-wall interactions.[4, 32, 33] Although these effects are relatively well-studied for water, this is not the case for confined salt solutions. The bulk phase, on the other hand, can be quantified directly from DSC measurements using the specific melting enthalpy. This approach has been used to study for example the drug loading in porous media,[34] pore filling and wetting of organic liquids in porous glass [35] and also has been a starting point for modeling thermoporometry.[5, 36, 37]

In this work a rigorous approach is described to accurately determine the amount

of confined fluid in mesoporous media. This method is applied to evaluate a key step in catalyst preparation by quantifying the bulk phase present after impregnation of mesoporous silica. The effectiveness of the impregnation step is determined by calculating the extent of pore filling. Impregnation with water and a potassium chloride solution are used as model systems, a $Ni(NO_3)_2$ solution is used as a show case for catalyst preparation. Differential scanning calorimetry is introduced as a tool to give insight in fundamental steps of catalyst preparation.

2.2 Experimental Methods

2.2.1 Materials

$PEO_{20}PPO_{70}PEO_{20}$ triblockcopolymer (P123), HCl (37 wt%), tetraethylorthosilicate (TEOS, 98%), cetyltrimethylammoniumbromide (CTAB), tetramethylammonium-hydroxide (TMAOH, 25 wt% in water), $Ni(NO_3)_2 \cdot 6H_2O$ and KCl were all purchased from Aldrich and used as received. Aerosil 380 silica was obtained from Degussa. Davicat 1404 (D1404) and 1351 (D1351) silica gels were used as received from Grace-Davidson. For the impregnations, purified MilliQ water was used.

2.2.2 Support preparation

SBA-15 was synthesized according to the procedure described by Zhao *et al*. using P123 as template and TEOS as silica source.[38] A gel with a molar composition of 1 SiO_2 : 0.0143 P123 : 5.05 HCl : 144 H_2O was aged under stirring at 40 °C for 20 h, after which it was treated at 80 °C for 48 h under static conditions. The precipitated white product was filtered, washed, dried at 80 °C and subsequently calcined at 550 °C for 6 hours (heating rate 1 °/min).

MCM-41 was synthesized following the procedure described by Cheng *et al*. using a reaction mixture with a molar composition of 1 SiO_2 : 0.25 CTAB : 0.20 TMAOH : 40 H_2O with Aerosil 380 as silica source.[39] The gel was stirred for 1 hour at 40 °C after which it was kept static for 20 hours. The gel was treated at 140 °C or 150 °C for 48 hours in teflon-lined steel autoclaves to obtain different pore diameters. The product was filtered, washed extensively and dried at 60 °C for 12 hours and 120 °C for 9 hours. The product was calcined at 550 °C for 8 hours (heating rate of 1 °/min). The two different samples are designated MCM-140 and MCM-150.

2.2.3 Characterization

N_2-Physisorption measurements were performed at -196 °C using a Micromeretics Tristar 3000. The samples were dried prior to the measurement under an N_2 flow at 300 °C for at least 12 hours. The total pore volume (V_{tot}) was defined as the single

point pore volume at $p/p_0 = 0.95$. The microporous (V_{micro}) and the sum of the micro- and mesoporous volume (V_p) were determined using the t-plot method.[40] The pore size distribution was calculated from the adsorption branch of the isotherm by a NL-DFT method designed for cylindrical pores.[41] The pore diameter was taken at the maximum of the differential pore volume. The average pore diameter of the silica gels was determined at the maximum in the pore size distribution calculated from BJH analysis of the desorption branch. Ordering of the pores in the silica was confirmed with small angle X-ray diffraction. Patterns were obtained at room temperature from 0.5 to 8° 2θ with a Bruker-AXS D8 Advance X-ray Diffractometer using Co-$K_{\alpha 12}$ radiation.

2.2.4 Differential scanning calorimetry

The crystallization and melting behavior of impregnated silica samples was studied with DSC (Q2000, TA instruments). The temperature and heat flow were calibrated using a certified indium sample. Measurements were performed in the temperature range of -90 – 30 ˚C under a nitrogen flow of 50 mL/min. Samples were hermetically sealed in aluminum pans to avoid any drying effects during measurements. A scanning rate of 5 °/min was applied for the water impregnated samples. This allowed sufficient accuracy to determine the bulk phase melting enthalpy. A scanning rate of 1 °/min was used for the samples impregnated with salt solutions to improve the resolution. Melting and crystallization peaks were reproducible and did not depend on the time between sample preparation and the measurement, indicating that no additional equilibration time was needed. Impregnated samples which endured several cooling-heating cycles were washed and dried and subsequently analyzed by N_2-physisorption. The pore volumes and surface area of the retrieved silica were close to values for the untreated silica. Therefore, it was concluded that the silica pore structures were not damaged by crystallization of water or the salt solutions.

The silica was stored under ambient conditions in closed vials and not dried prior to the measurements. The silica was considered to be in equilibrium with the air humidity, as stable readings were achieved on the balance. Samples were prepared under ambient conditions by adding the appropriate volume of liquid to a weighed amount of silica with a micropipette in a glass vial. The sample was then homogenized with a spatula and transferred to a 40 μL aluminum pan. The sample pan was hermetically sealed, after which the sample mass for the DSC measurement was determined. Sample masses were between 5-10 mg, using 3-5 mg silica. To test for gas occlusion, a test sample was prepared by impregnation under vacuum. Quantification of pore filling gave the same result as for the sample contacted with water at ambient pressure, confirming that for these powder supports, occlusion of gasses does not play a significant role in pore filling.

The bulk melting enthalpy was quantified during the heating ramp with a sigmoidal baseline using Universal Analysis 2000 software (TA Instruments). To facilitate quantification of the bulk phase, eutectic concentrations were used for the salt solutions, i.e. 19.7 wt% KCl and 36.0 wt% $Ni(NO_3)_2$.[42] The specific enthalpy of fusion, ΔH_f = 334 J/g for bulk water and ΔH_f = 305 J/g for the eutectic KCl solution were then used to determine the bulk mass. Using the single point indium calibration, 1-2% accuracy was found in the bulk melting enthalpy of water. This is within the range of the instrumental specifications.

2.2.5 Thermogravimetric analysis

The total amount of liquids and silica present in the samples was determined after the DSC measurement by thermal gravimetric analysis (Q50, TA instruments). The DSC sample pan lids were pierced multiple times after which the samples were heated in a 60 mL/min N_2 flow to 150 °C for the water and KCl containing samples to remove all the water. The $Ni(NO_3)_2$ impregnated samples were heated to 500 °C to remove the water and decompose the nickel nitrate to NiO. The weight loss after 1 or 2 hours, for the water and salt containing samples respectively, was used to calculate the masses of solution and silica. For the samples impregnated with salt solution, an additional correction was applied for the physisorbed and chemisorbed water. This water, present in the silica prior to the impregnation, contributes to the mass loss but should be distinguished from the eutectic salt solution volume. The amount of physisorbed and chemisorbed water was estimated by the average weight loss over three TGA measurements from unimpregnated silica. The corrections for the KCl impregnated samples was measured by heating the silica supports to 150 ˚C for 2 hours, while for the $Ni(NO_3)_2$ impregnated samples the weight loss for physisorbed and chemisorbed water was measured by heating at 500 ˚C for 2 hours.

The filling factor, f, is used to indicate the total amount of impregnation liquid relative to the total silica pore volume and is calculated using equation 1,

$$f = (m_l / \rho) / (m_s * V_{tot}) \qquad \text{eq. 1}$$

where m_l is the impregnation liquid mass determined with TGA, ρ is the density of the impregnation liquid, m_s is the total silica mass in the sample and V_{tot} the total single point pore volume per gram of silica. The degree of pore filling was determined by the amount of pore liquid relative to V_{tot} (total single point pore volume) or V_p (micro- and mesoporous volume) of the silica using equation 2.

$$\text{pore filling} = [(m_l - m_b) / \rho\ ] / (m_s * V) \qquad \text{eq. 2}$$

The amount of pore liquid is defined as the difference between the total amount

of liquid found by TGA (m_l) and the amount of bulk liquid determined with DSC (m_b). Taking all analysis methods into account, the overall error in the pore filling is estimated at 5%.

2.3 Results

Different mesoporous silica supports were used for the impregnation studies to study possible effects of pore diameter and architecture. All supports were characterized with N_2-physisorption and the structural parameters are listed in Table 2.1. Three ordered supports from the MCM-41 and SBA-15 families with cylindrical pores were synthesized and had narrow pore size distributions. Their structural ordering was confirmed by a well-defined XRD pattern that could be indexed to a 2-dimensional hexagonal lattice. For comparison two disordered commercial silica-gels were included.

Increased pore filling by impregnation with larger amounts of water was deduced from the DSC heating thermograms. Figure 2.1 shows the thermograms recorded during heating for SBA-15 samples impregnated with increasing amounts of water. At low fillings, only one melting event occurred with a peak maximum at –15 ˚C. Since the amount of water is much lower than the total pore volume, indeed no bulk water is expected. The peak area gradually increased with an increasing amount of water. At filling factors above f = 0.82, a second endothermic event appeared at 0 ˚C, corresponding to the melting of bulk water. Then, for larger excesses added, the bulk melting peak increased, while the pore melting endotherm remained constant.

The amount of bulk and pore water was quantified using TGA and the melting enthalpy of the bulk water at 0 ˚C, and a maximum pore filling was determined. The pore and bulk water volumes are presented in Figure 2.2 as a function of the total amount of added water. When no bulk water was observed, the amount of pore water

Table 2.1. Structural parameters of (ordered) mesoporous silica supports.

Silica supports	V_{tot} [a] (cm^3/g)	V_p [b] (cm^3/g)	V_{micro} [c] (cm^3/g)	S_{BET} [d] (m^2/g)	d_{DFT} [e] (nm)	d_{BJH} [f] (nm)
MCM-140	0.83	0.77	0.00	1092	3.2	2.6
MCM-150	0.99	0.94	0.01	827	6.4	3.7
SBA-15	0.72	0.66	0.08	628	8.4	5.3
Silica-gel D1404	0.87	0.78	0.00	458	-	7.8
Silica-gel D1351	1.2	1.2	0.01	328	-	16

[a] total pore volume at $p/p_0 = 0.95$, [b] micro- and mesopore volume determined by the t-method, [c] micropore volume determined by the t-plot method, [d] BET surface area, [e] pore diameter from NL-DFT analysis, [f] pore diameter from BJH analysis.

increased according to the amount of added water. At a filling factor f ~ 0.82, the first bulk water appeared. Further increase in added water led to a linear increase of the bulk water, while the pore water volume remained constant. At a filling factor of f = 1.22, the peak areas in the thermogram for the silica impregnated suggest an equal amount of water outside and inside the porous system. However, the specific melting enthalpy of the water inside the pores is lower than for the bulk water.[32] In addition, part of the water inside the pores does not crystallize due to interactions with the silica pore wall. This explains the relatively low energy release for the intraporous water. The maximum pore filling was averaged at 86.7% of total pore volume; this corresponded to 94.4% of the micro- and mesoporous volume.

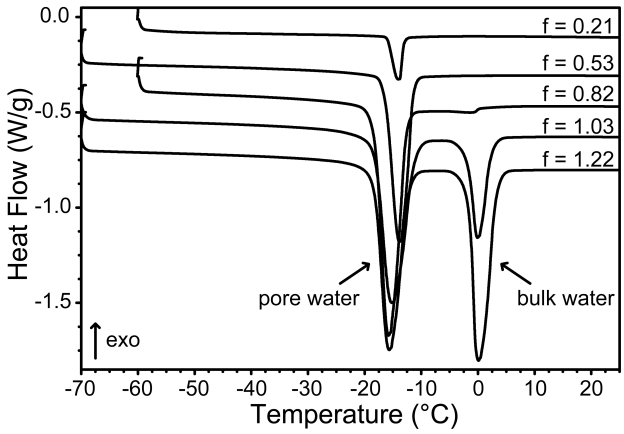

Figure 2.1. DSC curves of SBA-15 impregnated with different amounts of H_2O recorded during heating at 5 ºC/min, f = $V_{H2O}/V_{tot, SiO2}$, curves are offset for clarity.

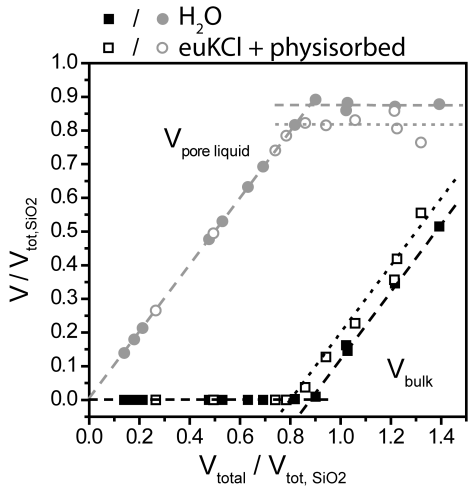

Figure 2.2. Pore filling of SBA-15 in terms of as a function of added H_2O (solid symbols) and euKCl (open symbols). The lines are added as guides for the eye.

SBA-15 samples impregnated with a eutectic KCl solution (euKCl) showed similar DSC curves to the water impregnated samples, as is shown in Figure 2.3. Only one melting peak was observed up to a certain maximum filling. Above this maximum filling, a bulk melting peak appeared. The bulk melting occurred at -11 ˚C, due to the freezing point depression of the bulk salt solution. The melting of the solution inside the pores occurred at -26 ˚C, leading to a $\Delta T_m = T_{m,\,bulk} - T_{m,\,pore} = 15$ ˚C. This freezing point depression due to the pore confinement is similar to that observed for water. The fact that only one melting peak is observed for the pore melting and one for the bulk melting indicates that the concentration of the solution is uniform throughout the pore system. The quantification of pore filling could be performed as the specific melting enthalpy of the eutectic KCl solution could be established with DSC.

Although the DSC thermograms for filling with euKCl (Figure 2.3) follow a similar pattern as with water, already at f = 0.77 the maximum pore filling seems to be reached. However, this pore filling was calculated for the salt solution in completely dry silica, while the samples were prepared under ambient conditions. The volume of physisorbed water present in the silica prior to impregnation should be taken into account when evaluating the degree of pore filling. The amount of physisorbed water was estimated by TGA measurements by heating to 150 ˚C for 2 hours. Figure 2.3 shows the results for the pore filling with euKCl and physisorbed water. The average maximum pore filling was 89% of the micro- and mesoporous volume. When the physisorbed water was removed prior to impregnation, by impregnating under vacuum, the micro- and mesopore filling was also 89%.

The pore filling with water and euKCl was determined for four different silica supports with different pore diameters and pore structures. Table 2.2 summarizes the results. Water filled 80-95% of the total pore volume of the different silica. This accounts for up to 90-100% of the micro- and mesopore volumes. The highest value was obtained for the commercial silica gel, D1404. The silica gel probably has a

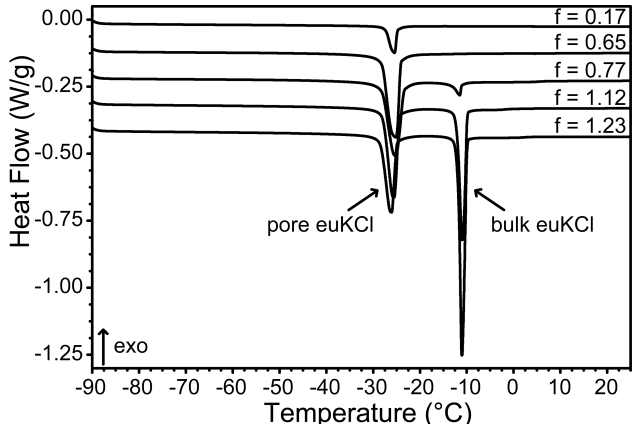

Figure 2.3. DSC curves of SBA-15 impregnated with different amounts of euKCl, recorded during heating at 1 ºC/min, $f = V_{euKCl}/V_{tot,\,SiO2,}$ curves are offset for clarity.

Table 2.2. Maximum degree of pore filling with H_2O and euKCl for different silica supports.

Silica supports	H_2O		euKCl		
	Total filling (% V_{tot})[a]	Pore filling (% V_p)[b]	Total filling (% V_{tot})[a]	Pore filling (% V_p)[b]	Pore filling (% V_p) corrected[c]
MCM-140	83.2	90.0	70.5	76.3	86.5
MCM-150	89.4	94.0	81.1	85.2	89.6
SBA-15	86.7	94.4	72.7	79.3	89.1
Silica-gel D1404	97.2	99.3	82.3	84.0	91.8

[a] volume of pore liquid relative to the total silica pore volume, [b] volume of pore liquid relative to the micro- and mesopore volume of the silica, [c] pore filling by combined volume of physisorbed water and pore solution relative to the micro- and mesopore volume of the silica.

higher surface –OH group density than the ordered mesoporous silica supports and therefore has a more hydrophilic surface.[43] Nevertheless, the difference with the ordered silica supports is within the error of the measurements. With euKCl, micro- and mesopore filling is in the range of 75-85%. When the estimated volume physisorbed water was taken into account, the total average micro- and mesopore volume filling for the different silica is 85-95%. Water almost completely fills the pores of the different silica supports, while with euKCl the maximum pore filling seems slightly lower.

Impregnation with a eutectic $Ni(NO_3)_2$ solution ($euNi(NO_3)_2$) was performed as a case study for catalyst preparation. Figure 2.4 shows the DSC curves of SBA-15 impregnated with different amounts of solution measured during heating. At low degrees of filling no heat flow was observed, indicating that the solution had entered the pores, but did not crystallize upon cooling. Crystallization was prevented either by confinement and/or by interactions with the silica pore wall. At a higher degree of filling, one large endotherm at -34 ˚C and two smaller peaks at -28 ˚C and ~ -20 ˚C are observed and assigned to bulk transitions. From the pure bulk solution, the specific enthalpy for eutectic melting at -28 ºC could be determined. Therefore, as the other transition enthalpies are not known, it is in this case not possible to quantify the bulk phase. However, the occurrence of bulk melting transitions at a certain filling factor indicates that the maximum pore filling has been reached, as was observed for the impregnation with water and euKCl. The highest filling factor that did not show bulk transitions was taken as the maximum pore filling. For SBA-15, this corresponded to 82% of the micro- and mesopore volume. Similar to the impregnations with euKCl, the pore filling was based on the salt solution volume and dry silica. When again the estimated volume of physisorbed water in the silica was included, 94% of the micro- and mesopore volume was filled.

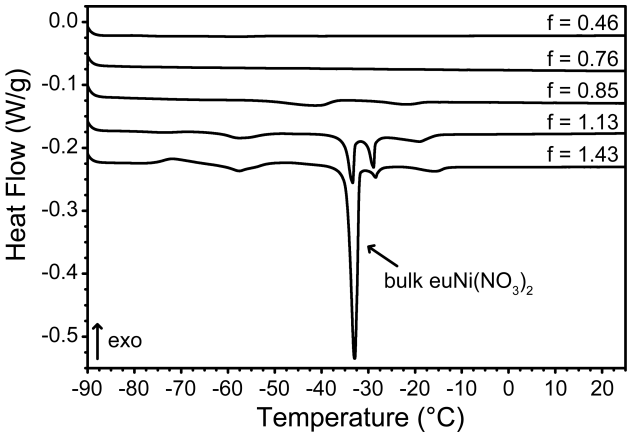

Figure 2.4. DSC curves of SBA-15 impregnated with different amounts of $euNi(NO_3)_2$ recorded during heating at 1 ºC/min, f = $V_{euNi(NO3)3}$/ $V_{tot,\ SiO2}$, curves are offset for clarity.

Table 2.3 shows the results for impregnation of the different silica supports with $euNi(NO_3)_2$. The highest degree of pore filling without bulk transitions was observed at 80-90% of the specific micro- and mesopore volumes of the different silica. This corresponds to a filling of more than 90%, when the volume of physisorbed water estimated for the different silica supports was included. Although the pore filling was not determined by quantification of the bulk phase, the degree of pore filling was similar to the results obtained with water and euKCl. It therefore confirms that with aqueous impregnation a largely homogeneous distribution of the solution over the support is achieved.

Pore liquid crystallization in SBA-15 could be detected only at filling factors above the maximum filling as very weak and broad peaks in the thermogram. To test if the lack of crystallization was the result of a strong confinement effect on the hydrated nickel nitrate complexes, a large pore silica gel D1351 (d = 16 nm) was also impregnated with $euNi(NO_3)_2$. The DSC curves recorded for these samples are shown in Figure 2.5. At low filling factors, crystallization during heating and two melting transitions were observed. The crystallization indicated that the

Table 2.3. Highest pore fillings observed without bulk melting transitions after impregnation with $euNi(NO_3)_2$ for different silica supports.

Silica supports	Pore filling (% V_p)[a] corrected
MCM-140	99
MCM-150	91
SBA-15	94
Silica-gel D1404	97
Silica-gel D1351	100

[a] pore filling by combined volume of physisorbed water and $euNi(NO_3)_2$ relative to the micro- and mesopore volume of the silica.

pore solution had probably formed a glass upon previous cooling, but eventually crystallizes during heating, although no glass transitions were observed under these measurement conditions. Bulk transitions were observed neither during cooling nor heating up to filling factors as high as 1.0, corresponding to 100% pore filling and in line with the hydrophilic nature of the silica gel. Crystallization during heating was not observed for samples with bulk solution present, showing that a crystallized bulk phase facilitates pore liquid crystallization. In contrast to SBA-15, the bulk solution present with D1351 showed only one transition at the expected -28 ˚C of the eutectic bulk solution.

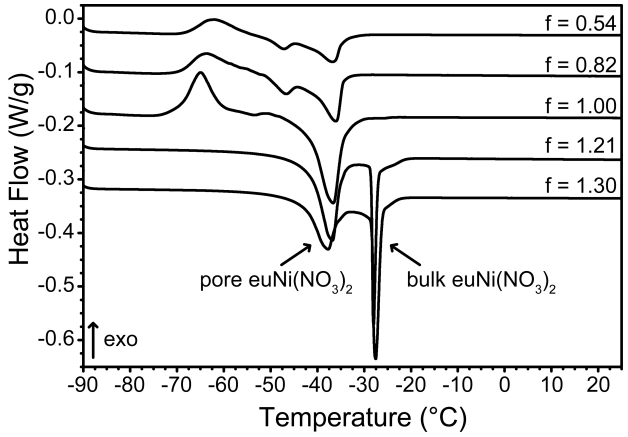

Figure 2.5. DSC curves of silica gel D1351 with different amounts of $euNi(NO_3)_2$ recorded during heating at 1 ºC/min, $f = V_{euNi(NO3)2} / V_{tot, SiO2}$, curves are offset for clarity.

2.4 Discussion

In this method, we derive the degree of pore filling from the amount of bulk liquid that undergoes a melting transition. The basis for this approach is that the specific enthalpy of water, or any liquid, inside a porous system is not constant. Firstly, the specific enthalpy of bulk water is temperature dependent.[44] Secondly, inside a porous system the presence of a non-freezing layer should also be taken into account.[36] Dispersed values for the actual thickness of this layer are found in literature (between 0.38 and 1.05 nm have been reported)[45, 46] and the dependence of the layer thickness on the surface morphology of the silica should be considered.[47, 48] In addition, the presence of micropores will increase the volume of non-freezing water inside the pores. In fact, in literature many different values are found for the temperature and confinement dependence of the specific enthalpy of water in mesoporous silica.[4, 5, 32, 33, 49, 50] Lastly, for the impregnations with salt solutions, the interactions of solutes with surface silanol groups will even further complicate the assessment of the specific melting enthalpy for an adsorbed salt solution. For all these reasons, the pore melting peak observed in the DSC thermograms cannot be used to directly quantify

the extent of pore filling without extensive study of the properties of the confined liquid.

The application of an ambiguous ΔH_f value for the confined liquid is avoided by using the bulk melting transition for the calculations of pore liquid volumes. The extra-porous liquid can be quantified directly from the bulk melting peak in the DSC thermogram and is not affected by the pore and inner surface morphologies. An important assumption in this approach is that all remaining liquid occupies the porous volume of the silica and has a density close to that of the bulk liquid. However, this reasoning is generally accepted in thermoporometry studies.[5, 36, 37] The bulk solution that does not undergo a melting transition causes an error in the pore filling results. The first one or two monolayers adsorbed on the exterior silica surface likely remain in a mobile state and therefore do not contribute to the crystallization/melting phase. However, since the external surface areas of the silica used in this report are small, the error is less than 3%. Furthermore, the impregnated samples consist volumetrically mainly of poor heat conducting silica. α-Al_2O_3 was used to test the influence of a low surface area filler in the sample pan. The detected bulk water volume was within 2% of the added value. Therefore, the detection limit of the bulk water should lie within 3% of the actual values.

A freezing point depression of 15 ºC was observed for the pore water in SBA-15. This corresponds well to calculations based on the Gibbs-Thomson equation for an average pore diameter of 8.4 nm determined by the NL-DFT method.[50] Recently, pore corrugation in SBA-15 was imaged[51] and this may account for the broadness of the melting peak. However, the freezing point depression of 15 ºC is well approximated by the average pore diameter based on a cylindrical model. A small increase of the pore melting temperature of water in SBA-15 is observed when the maximum pore filling is reached. This is likely an effect of the change of pore ice-air to pore ice-bulk ice interface at the pore mouth. A similar freezing point depression was observed for euKCl, even though ΔH_f and the solid-liquid surface tension are different. This has also been observed for NaCl and KI solutions, where the freezing point depression caused by the solution itself could be simply added to the confinement effect.[52, 53]

No melting transitions could be observed for euNi$(NO_3)_2$ in the pores of SBA-15, indicating a lack of crystallization. This is likely due to the larger crystallization volume needed for the formed crystal lattice. Depending on the solution, there exists a lower limit for the pore diameter to allow crystallization of the liquid.[54] Apparently, this diameter is much larger for euNi$(NO_3)_2$ than for water and euKCl. Indeed, pore crystallization was observed in D1351 with larger pores. The freezing point depression expected for water in the 16 nm diameter pores is roughly 8 ˚C, close to the observed 9 ˚C for the euNi$(NO_3)_2$ solution.

Three bulk melting peaks were observed for SBA-15 samples impregnated with

an excess of euNi$(NO_3)_2$. The expected melting point of the 36 wt% Ni$(NO_3)_2$ solution is -28 ˚C due to the melting of a eutectic mixture of Ni$(NO_3)_2 \cdot 9H_2O$ and ice.[42] A 39 wt% Ni$(NO_3)_2$ solution forms a solid phase of Ni$(NO_3)_2 \cdot 6H_2O$ and ice which melts at -34 ˚C. The peak at ~ -20 ˚C may be attributed to a diluted fraction. The melting bulk phase seems to be affected by local concentration changes enhanced by the presence of a porous solid and/or surface silanol groups. Quantification of the different fractions is not possible as the specific enthalpies are not known. In addition, recrystallization during heating cannot be excluded. Therefore, the local concentration of the bulk and adsorbed phase in the impregnated samples cannot be determined from the data obtained with DSC. Similar behavior was observed for the MCM-41 samples, but the bulk melting transitions showed different ratios. For the impregnations with euKCl, the thermograms suggested a uniform concentration of the salt solution in the intra-porous and extra-porous solution. Further investigations into the different present solid phases of the euNi$(NO_3)_2$ impregnated samples are needed to confirm the local concentration of the solution.

The micro- and mesoporous volumes of the silica supports were found to be almost completely filled, which is likely due to the hydrophilic nature of the supports. For more hydrophobic supports, such as carbon, incomplete wetting may be expected. The salt solution impregnated samples only showed slightly lower maximum fillings than the water impregnated samples. The decreased pore filling can be due to a higher surface tension of the solutions compared to water. However, the difference in maximum filling for euKCl and water is within the expected experimental error of the combined techniques. The maximum pore filling after impregnation with euNi$(NO_3)_2$ is based on the highest filling without bulk crystallization. The maximum filling obtained by this method is less accurate than for euKCl and water as it depends on one measurement. In this work, the degree of pore filling is discussed relative to the pore volume determined with N_2-physisorption. Shrinkage or swelling due to capillary condensation during gas adsorption measurements or during impregnation may affect the maximum pore filling. However, these deformations were found to cause volume changes of ~0.02% for microporous carbon materials.[55] Even though the mesoporous silica supports studied in this work may exhibit larger deformations, likely it does not account for the 0-10% empty pores. Therefore, the comparison of the intraporous water volume to the N_2-physisorption pore volume confirms that only a low fraction of the pores (up to 10%) may be empty after impregnation. Thus, a largely homogeneous distribution of the precursor solution is obtained. This is in line with previously obtained cryo-TEM results, where some empty pore sections were visualized after impregnating SBA-15.[28] These are probably the result of heterogeneities introduced by the mixing process.

2.5 Conclusions

The degree of pore filling of impregnated mesoporous silica was determined by differential scanning calorimetry measurements on wet samples. By calculating the amount of bulk liquid from the melting enthalpy and by determining the total amount of liquid with TGA, the pore filling was quantified. Results showed that water filled pores for ~95% of the micro- and mesopore volume. The salt solutions filled around 75-85% of the pores, but at least 90% of the pores were filled when the presence of physisorbed water was taken into account.

Two conclusions follow from these results. The largely inhomogeneous distribution of the metal phase over a support that is often observed in final catalysts is most likely not caused by the impregnation step. Although a small percentage of the pore volume may remain empty, the solution and therefore the precursor of the metal phase is distributed by and large over the whole support. Secondly, differential scanning calorimetry has proven to be a useful tool in studying the fundamentals of catalyst preparation. The degree of pore filling can be determined with DSC for any porous support and impregnation solution, as long as a bulk phase transition can be resolved. The application of DSC in the development of supported metal catalysts preparation is further explored in current research.

Acknowledgments

Mies van Steenbergen and Herre Talsma (Utrecht University) are acknowledged for the technical support and useful discussions on thermal analysis.

References

[1] E. Tombari, G. Salvetti, C. Ferrari and G. P. Johari, *J. Chem. Phys.* **2005**, *122*, 104712.
[2] J. P. Acker and L. E. McGann, *Cryo-lett.* **2001**, *22*, 241.
[3] G. W. Scherer, *Cem. Concr. Res.* **1999**, *29*, 1347.
[4] M. Brun, A. Lallemand, J.-F. Quinson and C. Eyraud, *Thermochim. Acta* **1977**, *21*, 59.
[5] K. Ishikiriyama and M. Todoki, *Thermochim. Acta* **1995**, *256*, 213.
[6] R. Mellaerts, J. A. G. Jammaer, M. Van Speybroeck, H. Chen, J. Van Humbeeck, P. Augustijns, G. Van den Mooter and J. A. Martens, *Langmuir* **2008**, *24*, 8651.
[7] M. Beiner, G. T. Rengarajan, S. Pankaj, D. Enke and M. Steinhart, *Nano Lett.* **2007**, *7*, 1381.
[8] H. Talsma, M. J. van Steenbergen and D. J. A. Crommelin, *Cryobiology* **1992**, *29*, 80.
[9] D. G. Shchukin and D. V. Sviridov, *J. Photoch. Photobio. C* **2006**, *7*, 23.
[10] F. Goettmann and C. Sanchez, *J. Mater. Chem.* **2007**, *17*, 24.
[11] M. Hartmann, A. Poppl and L. Kevan, *J. Phys. Chem.* **1996**, *100*, 9906.
[12] M. Schreier and J. R. Regalbuto, *J. Catal.* **2004**, *225*, 190.
[13] L. Jiao and J. R. Regalbuto, *J. Catal.* **2008**, *260*, 329.
[14] M. Che, Z. X. Cheng and C. Louis, *J. Am. Chem. Soc.* **1995**, *117*, 2008.
[15] P. Burattin, M. Che and C. Louis, *J. Phys. Chem. B* **1999**, *103*, 6171.

[16] M. K. van der Lee, A. J. van Dillen, J. H. Bitter and K. P. de Jong, *J. Am. Chem. Soc.* **2005**, *127*, 13573.
[17] G. L. Bezemer, P. B. Radstake, V. Koot, A. J. van Dillen, J. W. Geus and K. P. de Jong, *J. Catal.* **2006**, *237*, 291.
[18] A. V. Neimark, L. I. Kheifez and V. B. Fenelonov, *Ind. Eng. Chem. Prod. Res. Dev.* **1981**, *20*, 439.
[19] A. J. van Dillen, R. J. A. M. Terorde, D. J. Lensveld, J. W. Geus and K. P. de Jong, *J. Catal.* **2003**, *216*, 257.
[20] A. Lekhal, B. J. Glasser and J. G. Khinast, *Chem. Eng. Sci.* **2004**, *59*, 1063.
[21] M. Imperor-Clerc, D. Bazin, M. D. Appay, P. Beaunier and A. Davidson, *Chem. Mater.* **2004**, *16*, 1813.
[22] M. S. Moreno, M. Weyland, P. A. Midgley, J. F. Bengoa, M. V. Cagnoli, N. G. Gallegos, A. M. Alvarez and S. G. Marchetti, *Micron* **2006**, *37*, 52.
[23] T. Tsoncheva, J. Rosenholm, M. Linden, F. Kleitz, M. Tiemann, L. Ivanova, M. Dimitrov, D. Paneva, I. Mitov and C. Minchev, *Micropor. Mesopor. Mat.* **2008**, *112*, 327.
[24] J. R. A. Sietsma, J. D. Meeldijk, J. P. den Breejen, M. Versluijs-Helder, A. J. van Dillen, P. E. de Jongh and K. P. de Jong, *Angew. Chem., Int. Ed.* **2007**, *46*, 4547.
[25] V. Escax, M. Imperor-Clerc, D. Bazin and A. Davidson, *C. R. Chim.* **2005**, *8*, 663.
[26] O. Borg, P. D. C. Dietzel, A. I. Spjelkavik, E. Z. Tveten, J. C. Walmsley, S. Diplas, S. Eri, A. Holmen and E. Rytter, *J. Catal.* **2008**, *259*, 161.
[27] H. Friedrich, J. R. A. Sietsma, P. E. de Jongh, A. J. Verkleij and K. P. de Jong, *J. Am. Chem. Soc.* **2007**, *129*, 10249.
[28] J. R. A. Sietsma, J. D. Meeldijk, M. Versluijs-Helder, A. Broersma, A. J. van Dillen, P. E. de Jongh and K. P. de Jong, *Chem. Mater.* **2008**, *20*, 2921.
[29] J. Roggenbuck, T. Waitz and M. Tiemann, *Micropor. Mesopor. Mat.* **2008**, *113*, 575.
[30] H. Gies, S. Grabowski, M. Bandyopadhyay, W. Grunert, O. P. Tkachenko, K. V. Klementiev and A. Birkner, *Micropor. Mesopor. Mat.* **2003**, *60*, 31.
[31] R. Defay, I. Prigogine, A. Bellemans and D. H. Everett, *Surface Tension and Adsorption*. 1966, London: Longmans, Green & Co LTD.
[32] S. Kittaka, S. Ishimaru, M. Kuranishi, T. Matsuda and T. Yamaguchi, *Phys. Chem. Chem. Phys.* **2006**, *8*, 3223.
[33] T. Yamamoto, A. Endo, Y. Inagi, T. Ohmori and M. Nakaiwa, *J. Colloid Inter. Sci.* **2005**, *284*, 614.
[34] V. P. Lehto, K. Vaha-Heikkila, J. Paski and J. Salonen, *J. Therm. Anal. Calorim.* **2005**, *80*, 393.
[35] C. L. Jackson and G. B. McKenna, *Chem. Mater.* **1996**, *8*, 2128.
[36] R. K. Rennie and J. Clifford, *J. Chem. Soc., Farad. T 1* **1977**, *73*, 680.
[37] M. J. Bommel, d. C. W. Engelsen and v. J. C. Miltenburg, *J. Porous. Mat.* **1997**, *4*, 143.
[38] D. Y. Zhao, J. L. Feng, Q. S. Huo, N. Melosh, G. H. Fredrickson, B. F. Chmelka and G. D. Stucky, *Science* **1998**, *279*, 548.
[39] C. F. Cheng, D. H. Park and J. Klinowski, *J. Chem. Soc., Faraday T* **1997**, *93*, 193.
[40] B. C. Lippens and J. H. de Boer, *J. Catal.* **1965**, *4*, 319.
[41] M. Jaroniec, M. Kruk, J. P. Olivier and S. Koch, *Proceedings of COPS-V, Heidelberg, Germany* **1999**.
[42] W. F. Linke, *A Compilation of Solubility Data from the Periodical Literature*. 4 ed. Vol. II, page 1216. 1965, Washington D.C.: American Chemical Society.
[43] S. Ek, A. Root, M. Peussa and L. Niinisto, *Thermochim. Acta* **2001**, *379*, 201.
[44] R. J. Speedy, *J. Phys. Chem.* **1987**, *91*, 3354.
[45] A. Schreiber, I. Ketelsen and G. H. Findenegg, *Phys. Chem. Chem. Phys.* **2001**, *3*, 1185.
[46] J. F. Quinson, J. Dumas and J. Serughetti, *J. Non-Cryst. Solids* **1986**, *79*, 397.
[47] K. Ishikiriyama and M. Todoki, *J. Colloid Inter. Sci.* **1995**, *171*, 103.
[48] A. Endo, T. Yamamoto, Y. Inagi, K. Wakabe and T. Ohmori, *J. Phys. Chem. C* **2008**, *112*, 9034.
[49] A. H. Janssen, H. Talsma, M. J. van Steenbergen and K. P. de Jong, *Langmuir* **2004**, *20*, 41.
[50] S. Jahnert, F. V. Chavez, G. E. Schaumann, A. Schreiber, M. Schonhoff and G. H. Findenegg, *Phys. Chem. Chem. Phys.* **2008**, *10*, 6039.
[51] C. J. Gommes, H. Friedrich, M. Wolters, P. E. de Jongh and K. P. de Jong, *Chem. Mater.* **2009**, *21*, 1311.
[52] A. M. Kjeldsen and M. R. Geiker, *Mater. Struct.* **2008**, *41*, 213.
[53] M. Lemercier, M. Brun and J. F. Quinson, *J. Therm. Anal.* **1992**, *38*, 887.
[54] G. Dosseh, Y. D. Xia and C. Alba-Simionesco, *J. Phys. Chem. B* **2003**, *107*, 6445.
[55] P. Kowalczyk, A. Ciach and A. V. Neimark, *Langmuir* **2008**, *24*, 6603.

Chapter 3

Controlling the Aqueous Synthesis of Functional Nanoparticles in Porous Materials

Abstract

Using (cryo-) electron tomography, the redistribution of phases throughout the elementary steps of impregnation and drying and using different drying procedures was imaged at the nanometer level. A direct comparison of the solution and salt distribution before and after a drying treatment in the same support particle revealed that freeze-drying was essential to obtain a homogeneous salt distribution. This strategy was demonstrated for the synthesis of catalysts with uniform Co_3O_4 and NiO nanoparticle distributions in a mesoporous silica support.

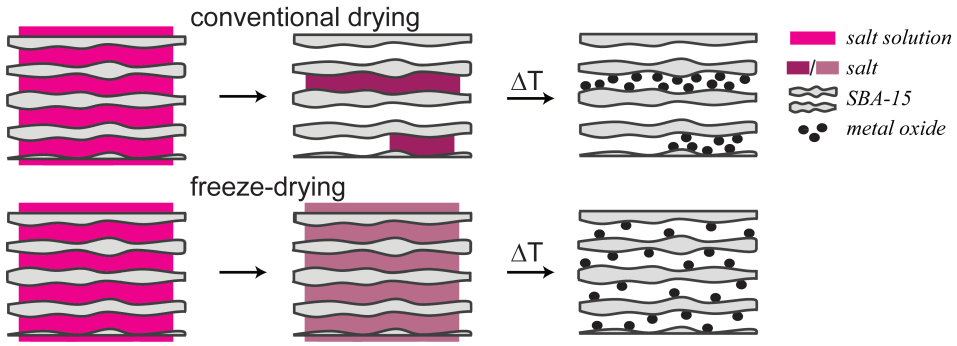

3.1 Introduction

The synthesis of functional nanostructures by simple, cost-effective and environmentally friendly methods is crucial for their large scale application[1, 2]. For the preparation of deactivation resistant heterogeneous catalysts, the deposition of equally-sized and maximally-spaced sub-10 nm particles within a porous support material is considered "the holy grail"[3-5]. However, controlling the aqueous synthesis of nanoparticles by the classical "impregnation and drying" method remains a challenge[6-8]. Here, we show that immobilization of the liquid during solvent removal by freeze-drying is essential to achieve monodisperse particle sizes and homogeneous distributions in supports. Using (cryo-) electron tomography, the redistribution of phases throughout the elementary steps and using different drying procedures was visualized at the nanometer level. Our strategy was demonstrated for the synthesis of catalysts with uniform Co_3O_4 and NiO nanoparticle distributions in a mesoporous silica support but is applicable to a much broader range of catalytic nanoparticles and carriers. Moreover, we anticipate its use in the controlled synthesis of many other nanostructured materials.

Nanoparticles play a key role in many present day applications such as catalysis, biomedical imaging, fuel cells, solar cells and electrochemistry. To exploit the exceptional properties of nanoparticles in multiphase systems, they are often stabilized within carriers that warrant their function and accessibility[9, 10]. Supported nanoparticles are for example widely studied for the energy efficient production of fuels and chemicals[11, 12]. For applications relying on the surface properties of these nanoparticles their controlled, equally-spaced deposition within a porous carrier is of paramount importance.[13-15] However, the controlled deposition of a high density of 1-10 nm particles as required e.g. in heterogeneous catalysts is difficult to achieve.

Although state-of-the-art preparation routes that apply lithography[16] or printing[17], or use metal-organic frameworks[18] and single crystal surfaces[19] can be used for small scale model systems, for large scale application in the petrochemical industry, oil refining, fuel cell technology, or solar cells, simple and environmentally viable methods need to be employed[20-22]. Within the field of heterogeneous catalysis, impregnation and drying is a seemingly simple bottom-up method to prepare supported transition metal or metal oxide nanoparticles and is commonly applied in both academia and industry[23]. This procedure which uses aqueous transition metal nitrate precursor solutions produces little waste, but control over particle size, shape and distribution during the consecutive synthesis steps is problematic[24, 25].

Here we demonstrate control over the nanoparticle distribution employing impregnation and freeze-drying in model catalyst systems consisting of a mesoporous silica carrier (SBA-15) and a cobalt or nickel nitrate precursor. For this we used

insight on the 3-dimensional distribution of phases obtained from the (cryo-) electron tomographic analysis[26, 27] of the system in the solute state, dried state, and after nitrate decomposition applying different modes of drying. The derived approach was successfully applied yielding model catalysts with significantly improved structural characteristics by rational design.

3.2 Experimental Methods

3.2.1 Catalyst preparation

SBA-15 with rodlike morphology was prepared according to the procedure described by Sayari *et al.*[28] 4.0 g P123 was dissolved in 130 mL dematerialized H_2O and 20 mL HCl (37 wt%, Aldrich) at 39 ºC. After addition of 7.5 g tetraethylorthosilicate (98%, Aldrich), the solution was stirred for 6 minutes and subsequently kept static at 39 ºC for 24 hours. After a hydrothermal treatment at 100 ºC for 48 hours, the white product was filtered, washed and dried at 60 ºC for 3 hours and 120 ºC for 6 hours. Calcination was performed at 550 ºC for 6 hours (heating rate 1 ºC/min). The structural properties of the different batches of SBA-15 were determined using N_2-physisorption at -196 ºC (Tristar 3000, Micromeritics): d_p = 11 nm, V_p = 1.15 cm^3/g and S_{BET} = 845 m^2/g (see Appendix 3 for porosity characterization of individual batches).

Catalyst preparation was performed by incipient wetness impregnation with a saturated aqueous $Co(NO_3)_2$ solution (4.2 M, $Co(NO_3)_2 \cdot 6H_2O$ >99 %, Sigma-Aldrich) leading to a cobalt metal loading of 18 wt%, or with a saturated aqueous solution of $Ni(NO_3)_2$ (4.3 M, $Ni(NO_3)_2 \cdot 6H_2O$ 99%, Acros) leading to a nickel metal loading of 19 wt%.

Conventional drying was performed in a preheated muffle oven for 16 hours at 60 ºC for the cobalt catalysts and 120 ºC for the nickel catalyst. Freeze-drying for NiO and Co_3O_4-Pt catalysts was performed using an Epsilon 2-4 Lyophilizer (Martin Christ). Samples were frozen with liquid nitrogen, after which the sample vials were placed on a precooled shelf at -55 ºC. Primary drying was performed at a pressure of 0.02 mbar and a shelf temperature of -50 ºC for 4.5 days. The temperature was increased stepwise to 20 ºC over 8 hours, during which the pressure did not increase. Freeze-dried samples were transferred and stored under a dry N_2 atmosphere to prevent rehydration.

The dried catalysts were thermally treated to decompose the nitrate salt in a plug-flow reactor at 350 ºC (1 ºC/min, 1 hour) in a flow of 1% NO/N_2 or N_2 (100 mL / 50 mg catalyst).

3.2.2 Catalyst characterization

Thermogravimetric analysis (TGA, Q50 TA Instruments) measured the weight loss after heating to 500 ºC at 10 ºC/min for 30 min. The weight loss was corrected for the loss of water from a pure silica reference sample between 150 ºC and 500 ºC, while water lost below 150 ºC was considered to be included in the precursor phase. The residual water was expressed in moles H_2O/mole metal. XRD patterns were recorded for all catalysts between 10 and 60 º2θ with a Bruker-AXS D2 Phaser X-ray Diffractometer using Co-$K_{\alpha 12}$ radiation (λ = 1.790 Å). The volume averaged Co_3O_4 and NiO crystallite sizes were determined using line broadening analysis by a fitting procedure in Eva2 software (Bruker AXS) and the Scherrer equation with shape factor k = 0.9. Line broadening was not corrected for strain effects. TEM microscopy was performed using a Tecnai 12 operated at 120 kV.

3.2.3 Cryo-electron tomography: in-situ and lab scale drying experiments

The effect of drying on the cobalt nitrate salt distribution was visualized in two sets of experiments. For the *in-situ* drying experiment, tilt series were acquired of the same support particle as impregnated and after subsequent drying. SBA-15 was impregnated to incipient wetness with a saturated aqueous $Co(NO_3)_2$ solution and applied on a TEM grid, which was subsequently immersed into liquid nitrogen. For the conventional drying experiment finder grids (Cu, 200 mesh, type F1 Electron Miscroscopy Sciences) were used. After acquisition of the tilt series of an impregnated particle, the grid was removed from the microscope sample holder and heated to 60 ºC for 16 hours on a hot plate. The grid was then re-immersed in liquid nitrogen and reinserted into the microscope sample holder. The same particle was located on the finder grid to acquire the second tilt series. *In-situ* freeze-drying was performed on a Quantifoil R2/2 carbon film supported on square mesh grids (Cu, 200 mesh). A tilt series was acquired of an impregnated SBA-15 particle and subsequently the temperature of the grid holder inside the ultra-high vacuum microscope column was allowed to rise to room temperature over night. Prior to acquiring the tilt series of the freeze-dried particle, the system was cooled again to ~ -170 ºC. Image analysis was performed on 14.8 nm thick slices through the reconstructions perpendicular through the body of the particle. Empty or partially empty pores were detected by a gray value intensity upper limit integrated over 10 nm circular areas fixed on an hexagonal array.[29] For clarity of the 3 dimensional reconstructions, empty pore detections at the rim of the particle were cut-off.

Samples prepared on lab scale were impregnated and conventionally dried in an oven as described in the catalyst preparation section. Freeze-drying for cryo-ET on lab scale the sample was performed using a Sublimator 400 Freeze-dryer (Zirbus). Samples were frozen by cooling to -45 ºC (1 ºC/min, 3 hours) and were dried at

0.02-0.03 mbar for 4 days on a shelf with a temperature of -30 ºC. The temperature was increased to -10 ºC for 1 hour and to 20 ºC for 1 day at 0.01-0.02 mbar. A small amount of powder was deposited on a TEM grid, which was then immersed in liquid nitrogen and transferred to the cryo-holder of the CryoTitan microscope (FEI, www.cryoTEM.nl) to perform cryo-electron tomography. The freeze-dried sample was handled under a dry N_2 atmosphere at all times.

TEM grids were glow discharged prior to sample preparation using a Cressington 208 carbon coater. Tomography labels were added by applying 10 nm sized colloidal gold particles (Aurion, PAG conjugated) from aqueous suspension. The calcined catalysts were applied onto a 2/2 Quantifoil grid from a suspension in ethanol. The other samples were prepared by depositing a small amount of powder on the grid, after which the excess was shaken off. FD-$Co(NO_3)_2$/SBA-15 was applied under a dry N_2 atmosphere in a N_2-drybox. Cryo-tomography was performed on the TU/e CryoTitan (FEI) equipped with a field emission gun and operated at 300 kV acceleration voltage. Cryo-TEM images were acquired on a Gatan a 2k x 2k Gatan CCD camera usinmg zero-loss energy filtering with a slit width of 20 eV. Tilt series were recorded from ±65º at 1º tilt increments at a nominal magnification of 24k resulting in a pixel size of 0.37 nm. Electron tomography of calcined catalysts was performed on a Tecnai 20 microscope operated at 200 kV. Tilt series were recorded from ±75º at 2º tilt increments at a nominal magnification of 29k with a 2k x 2k Gatan CCD camera resulting in a pixel size of 0.27 nm and 0.54 nm after binning by a factor of 2. Alignment of the TEM tilt series and 3D reconstructions were performed in IMOD software.[30]

3.3 Results & Discussion

Particle filling before and after drying was studied with cryo-electron tomography directly within the same SBA-15 carrier particle using *in-situ* drying on a transmission electron microscope grid. Rodlike SBA-15 particles[28] with a narrow pore size distribution and a uniform morphology (~1 μm x 0.3 μm) were used as model supports to exclude transport effects induced by variations in pore length or diameter. 3D reconstructions of the tomograms revealed the pore-filling directly after impregnation (Figs. 3.1a, c) and after either conventional drying (Fig. 3.1b) or freeze-drying (Fig. 3.1d) within the same carrier particle. The pores of the SBA-15 particle in Figure 3.1a were homogeneously filled after impregnation with cobalt nitrate solution. However, after conventional drying, many open or partially open pore sections were present throughout the particle (Fig. 3.1b). The SBA-15 particle in Figure 3.1c contained some empty pores after impregnation, which were ascribed to local deficiency of impregnation solution, in line with our previous report.[31]

Nevertheless, in this case, after freeze-drying the salt distribution perfectly matched the solution distribution after impregnation (Figs 3.1c, d). This demonstrates the successful immobilization of precursor phase during the sublimation of the water in contrast to the redistribution occurring during conventional drying.

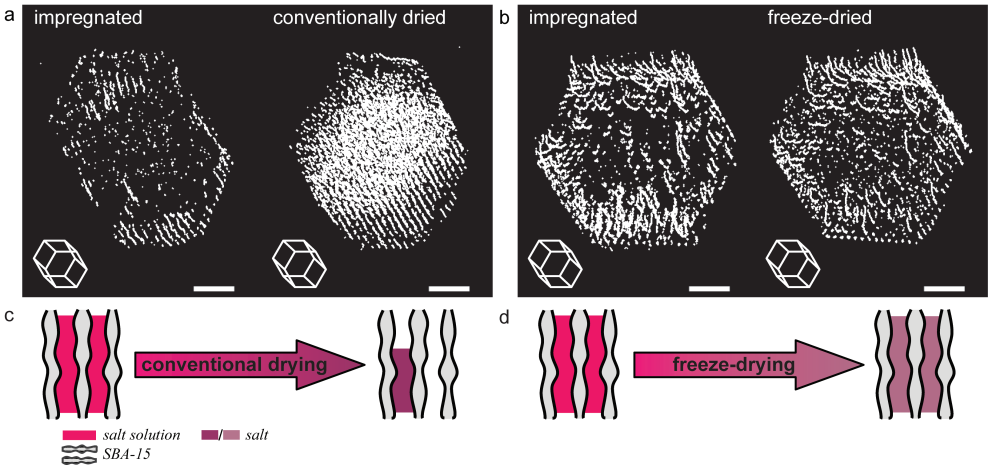

Figure 3.1. 3D reconstruction showing empty pore sections present in a single mesoporous silica particle after impregnation and after *in-situ* drying. a, *In-situ* conventional drying at 60 ºC in oven. Scale bars: 200 nm. b, *In-situ* freeze-drying. Scale bars: 200 nm. c, d, Cartoon showing local pore filling after impregnation and drying treatments. Please refer to the movie Figure1_3D-insitu.mov for the 3D reconstruction models (see Appendix A1, for details on image analysis see Appendix A2).

Preparation on the lab scale of quantities employable for preparation of functional materials yielded similar results (Fig. 3.2). After conventional drying the pores were partially filled with plugs of cobalt nitrate salt with empty and filled pore sections occurring randomly throughout the particle (Fig. 3.2a). Furthermore, by comparing the pores in the rectangular and triangular areas marked in slices B and C of Figure 3.2a it becomes clear that both empty and filled areas exist within a single pore. In contrast, freeze-drying (Fig. 3.2b) led to a uniform salt distribution. The tomogram shows that the pore system was homogeneously filled, with exception of the pores at the outer rim of the particle.

Cryo-ET analysis of several SBA-15 particles prepared by conventional lab-scale *ex-situ* drying showed a significant variance in the level of salt redistribution, which was attributed to variations in the local drying rate (see Appendix A3, Figure A4). Indeed, in some cases plug-wise filling was observed (*cf.* Fig. 3.2a), while other cases showed deposition of small aggregates throughout the pore system (*cf.* Fig. 3.1b). In contrast, lab-scale prepared freeze-dried SBA-15 particles all showed the same uniform salt distribution. Notably, the hydration state of the nitrate precursor

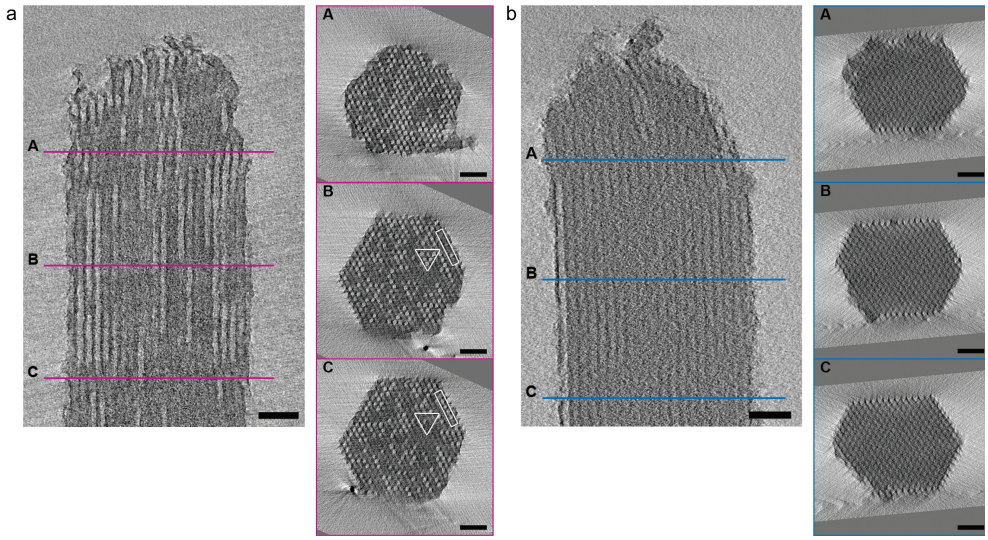

Figure 3.2. $Co(NO_3)_2$ salt distribution in mesoporous silica particles after impregnation and different drying treatments visualized by cryo-electron tomography. a, Prepared on mg scale by conventional drying at 60 ºC in oven, open triangle and rectangle in slices B and C indicate pores with alternating filling. b, Prepared on mg scale by freeze-drying. a, b, All scale bars are 50 nm. 2.2 nm Thick slices from cryo-ET reconstructions parallel to the pores. Lines A, B and C indicate positions of the 14.8 nm thick cross sections perpendicular to the pore direction. The 3D distribution of salt within the pores is best appreciated by the illustrating movies Figure2a_Conv.mov and Figure2b_Freeze.mov (see Appendix A1).

was found to be directly dependent on the applied drying method. For cobalt nitrate 3 - 7 H_2O molecules per mole of Co remained after conventional drying, depending on the details of handling. However, samples freeze-dried contained only 0.3 residual water molecules per mole of cobalt. So, after conventional drying, cobalt nitrate retained crystal water, while freeze-dried samples were almost fully dehydrated.

Rational synthesis of catalysts with controlled nanoparticle distribution was performed by combining freeze-drying for a uniform salt distribution with an NO-assisted nitrate decomposition method.[24] As opposed to more standard procedures which use N_2 or air, calcination in an NO/N_2 gas flow restricts mobility of the precursor phase during decomposition, allowing more control over the final nanoparticle distribution.[32] Figure 3.3 shows the 3D nanoparticle distribution in a platinum promoted cobalt catalyst, which is an industrially relevant catalyst system for the Fischer-Tropsch synthesis.[8] After conventional drying and cobalt nitrate decomposition in NO/N_2, the Co_3O_4 nanoparticles concentrated within several pores (Fig. 3.3a) leaving the remaining pores empty as is typical for hydrated transition metal nitrates calcined in a NO-containing atmosphere.[6] After freeze-drying, the distribution of cobalt oxide nanoparticles was more uniform (Fig. 3.3b), even though

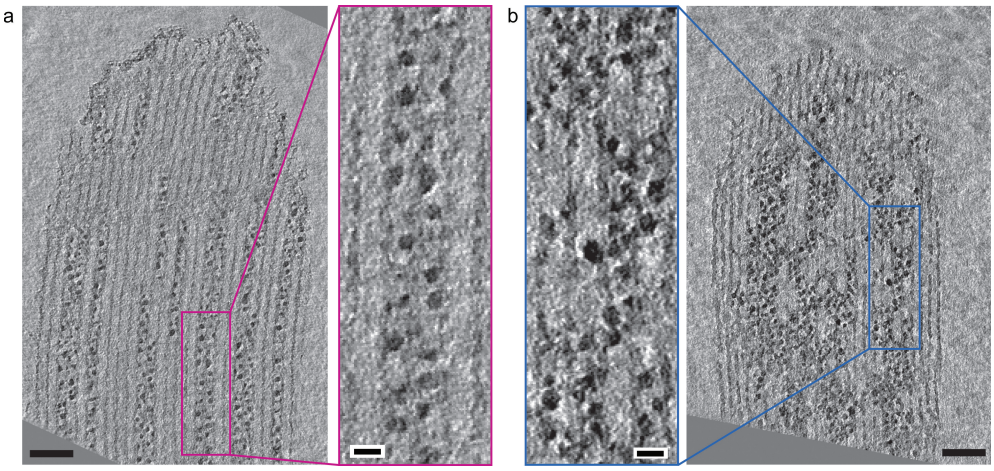

Figure 3.3. Effect of drying on Co_3O_4 nanoparticle distribution in a Co-Pt on mesoporous silica catalyst after calcination in a flow of 1% NO/N_2. a, Prepared via conventional drying at 60 ºC. b, Prepared via freeze-drying. a,b, Scale bar: 50 nm, close-up of boxed area: scale bar: 10 nm. 2.7 nm thick slices through reconstructions obtained by electron tomography.

a few pores at the outer rim of the particle were empty. This clearly demonstrates the potential of freeze-drying for the preparation of more sintering resistant *ex*-nitrate prepared cobalt Fischer-Tropsch catalysts.

The versatility of the method was demonstrated by *ex*-nitrate preparation of NiO nanoparticles via the same synthesis route. Significantly, ET showed that an even smaller average particle size was obtained for NiO (2.6 - 3.6 nm) than for Co_3O_4 (5.1 - 5.5 nm) (Fig. 3.4, Table 3.1). The particle sizes corresponded very well to the average crystallite size determined by XRD, while the formation of some nickel or cobalt (hydro)silicates during calcination cannot be excluded.[33, 34] The hydration

Table 3.1. Average crystallite and average particle sizes as determined with XRD and electron tomography (ET) respectively for nickel oxide and platinum promoted cobalt oxide catalysts after calcination in a flow of 1% NO/N_2 or in a flow of N_2 via impregnation and conventional drying (CD) or freeze-drying (FD).

	Calcination in 1% NO/N_2		Calcination in N_2
Catalyst	d_{XRD} (nm)	d_{ET} (nm)	d_{XRD} (nm)
CD-NiO/SBA-15	3.4	3.6	8.4
FD-NiO/SBA-15	2.4	2.6	6.5
CD-Co_3O_4-Pt/SBA-15	5.2	5.5[a]	9.7
FD-Co_3O_4-Pt/SBA-15	4.6	5.1[a]	7.4

[a] ET particle size determined after reduction at 450 ºC and passivation.

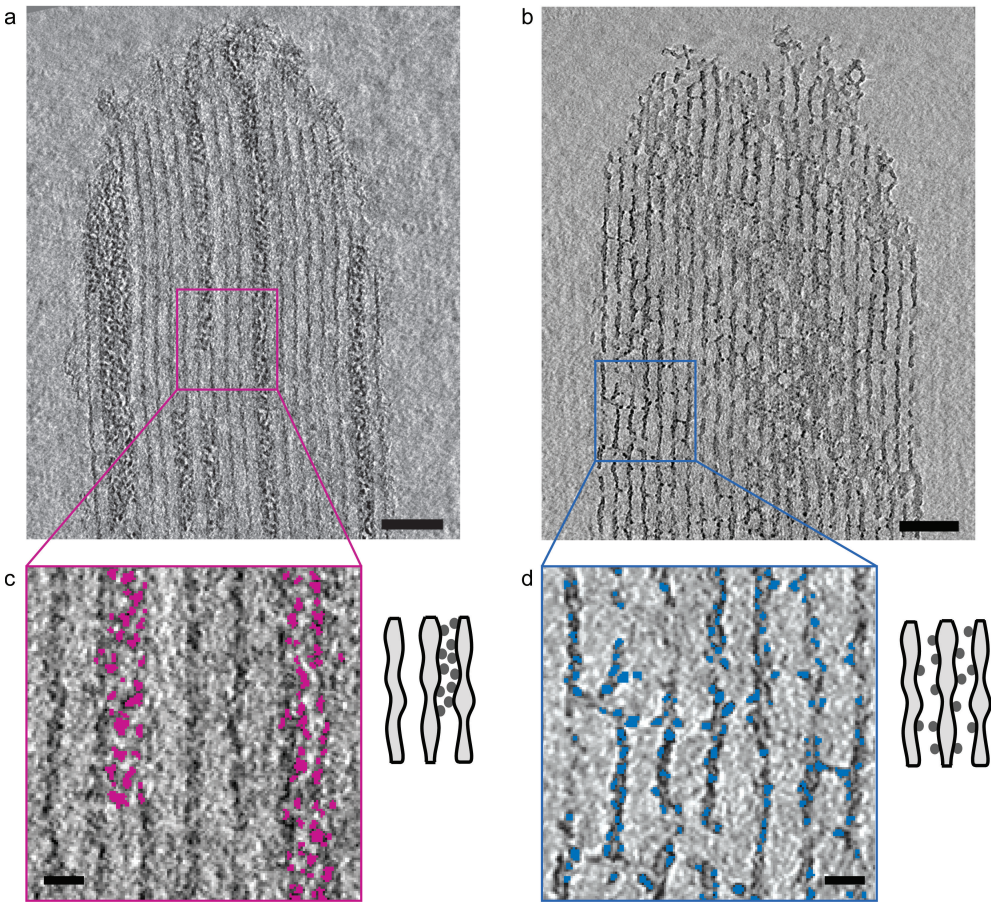

Figure 3.4. Effect of drying on NiO nanoparticle distribution in mesoporous silica after calcination in a flow of 1% NO/N_2. a, Prepared via conventional drying at 120 ºC in oven. b, Prepared via freeze-drying. c, Close-up of boxed area in a, NiO nanoparticles are accentuated in pink for clarity. d, Close-up of boxed area in b, NiO nanoparticles are accentuated in blue for clarity. a-d, 2.7 nm Thick slices through reconstructions obtained by electron tomography. Scale bars are 50 nm (a,b) and 10 nm (c,d). Please refer to movies Figure4a_NiOconv.mov and Figure4b_NiOfreeze.mov to observe the 3D distribution of nanoparticles (Appendix A1).

state of the precursor after drying again depended on the applied drying treatment. For $Ni(NO_3)_2$ - which is known to partially decompose to $Ni_3(NO_3)_2(OH)_4$ at 120 ºC - the observed residual weight loss corresponded to ~75% $Ni_3(NO_3)_2(OH)_4$ and ~25% $Ni(NO_3)_2 \cdot 6H_2O$, in line with previously reported results.[32] However, after freeze-drying only 0.7 residual molecules of water remained. Considering the low salt-support interaction in nitrate-silica systems[25], the small nanoparticles sizes obtained by calcination in NO/N_2 are remarkable.

Also here the use of freeze-drying yielded a more homogeneous distribution of the nanoparticles compared to the conventional drying method (Fig. 3.4). Moreover, substantially smaller crystallites were obtained; in fact, freeze-drying reduced the nanoparticle volume by a factor of three. Figure 3.4d suggests gaps in the silica pore walls, this was found not to be representative for the SBA-15 pore structures after freeze-drying (see Appendix A4, Table A1).

Where freeze-drying and NO-assisted calcination led to a very efficient dispersion of small NiO nanoparticles (Figs. 4b,d) over the entire SBA-15 particle, standard calcination in N_2 after freeze-drying led to the formation of larger crystallites as compared to NO/N_2 (6.5 nm *vs*. 2.4 nm, Table 3.1). It is known that in N_2 some aggregation of the active phase occurs during the decomposition of hydrated $Co(NO_3)_2$ and $Ni(NO_3)_2$.[24, 32, 35] Still, both the nickel as well as the Pt promoted cobalt catalyst prepared by freeze-drying showed a lesser extent of clustering as compared to conventional drying, see Figure 3.5. Clearly, freeze-drying improves the nanoparticle distribution in the carrier, even when standard calcination conditions induce more mobility of the active phase.

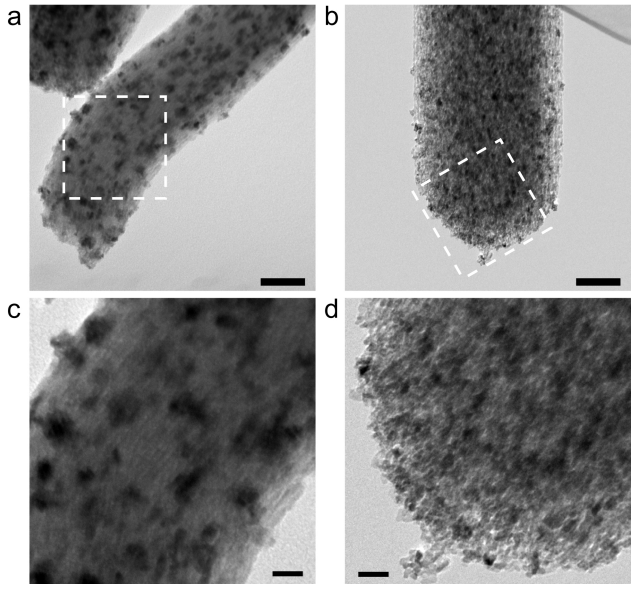

Figure 3.5. TEM micrographs of NiO nanoparticles on SBA-15 after calcination in an N_2 flow. a, Prepared via conventional drying at 120 ºC Scale bar: 100 nm. b, Prepared via freeze-drying. Scale bar: 100 nm. c, Close-up of boxed area in a. Scale bar: 25 nm. d, Close-up of boxed area in b. Scale bar: 25 nm.

3.4 Conclusions

A unique insight into the elementary steps of the aqueous synthesis of supported nanoparticles was obtained with (cryo-) electron tomography. It allowed for the first time a direct comparison of the impact of drying on the local salt distribution within a single support particle. While conventional drying led to a non-uniform deposition of salt, freeze-drying immobilized the precursor phase leading to a uniform distribution. This concept was confirmed by lab scale experiments. Based on these findings a rational synthesis approach for catalysts with uniform nanoparticle distributions was composed. By combining freeze-drying with the NO-assisted decomposition method, 3 nm NiO particles were obtained with a uniform distribution over the carrier. In contrast, conventional procedures utilize only a fraction of the pores of the carrier. The potential and versatility of freeze-drying was illustrated by the preparation of platinum promoted cobalt catalysts for the Fischer-Tropsch synthesis and a nickel based hydrogenation catalyst. Our results not only have implications for the field of catalysis, they also open an avenue to exploit the exceptional properties of supported nanoparticles for applications in other fields of materials science.

Acknowledgements

Heiner Friedrich (Utrecht University) is acknowledged for his contributions in the data evaluation, the experiments and the manuscript. Fabio Nudelman and Heiner Friedrich (Eindhoven University of Technology) are acknowledged for the cryo-ET experiments, Jovana Zečević (Utrecht University) is acknowledged for the ET experiments. Nico Sommerdijk (Eindhoven University of Technology) is acknowledged for his contributions to the manuscript and useful discussions. The Electron Microscopy Unit at Utrecht University is acknowledged for their excellent facilities. Mies van Steenbergen and Herre Talsma (Utrecht University) and Hans de Waard (University of Groningen) are acknowledged for their technical support and useful discussions on freeze-drying. Jan Hilhorst (Utrecht University) is acknowledged for the image analysis performed for figure 1.

References

[1] B. C. H. Steele and A. Heinzel, *Nature* **2001**, *414*, 345.
[2] F. Raimondi, G. G. Scherer, R. Kotz and A. Wokaun, *Angew. Chem., Int. Ed.* **2005**, *44*, 2190.
[3] A. T. Bell, *Science* **2003**, *299*, 1688.
[4] G. A. Somorjai and J. Y. Park, *Top. Catal.* **2008**, *49*, 126.
[5] H. M. Torres Galvis, J. H. Bitter, C. B. Khare, M. Truitenbeek, A. I. Dugulan and K. P. de Jong, *Science* **2012**, Accepted.
[6] H. Friedrich, J. R. A. Sietsma, P. E. de Jongh, A. J. Verkleij and K. P. de Jong, *J. Am. Chem. Soc.* **2007**, *129*, 10249.
[7] I. Arslan, J. C. Walmsley, E. Rytter, E. Bergene and P. A. Midgley, *J. Am. Chem. Soc.* **2008**, *130*, 5716.
[8] J. P. den Breejen, J. R. A. Sietsma, H. Friedrich, J. H. Bitter and K. P. de Jong, *J. Catal.* **2010**, *270*, 146.
[9] D. Astruc, F. Lu and J. R. Aranzaes, *Angew. Chem., Int. Ed.* **2005**, *44*, 7852.
[10] A. H. Lu, E. L. Salabas and F. Schuth, *Angew. Chem., Int. Ed.* **2007**, *46*, 1222.
[11] Y. Lei, F. Mehmood, S. Lee, J. Greeley, B. Lee, S. Seifert, R. E. Winans, J. W. Elam, R. J. Meyer, P. C. Redfern, D. Teschner, R. Schlogl, M. J. Pellin, L. A. Curtiss and S. Vajda, *Science* **2010**, *328*, 224.
[12] M. Turner, V. B. Golovko, O. P. H. Vaughan, P. Abdulkin, A. Berenguer-Murcia, M. S. Tikhov, B. F. G. Johnson and R. M. Lambert, *Nature* **2008**, *454*, 981.
[13] C. H. Bartholomew, *Appl. Catal.- A Gen.* **2001**, *212*, 17.
[14] A. M. Saib, D. J. Moodley, I. M. Ciobica, M. M. Hauman, B. H. Sigwebela, C. J. Weststrate, J. W. Niemantsverdriet and J. van de Loosdrecht, *Catal. Today* **2010**, *154*, 271.
[15] H. L. Xin, J. A. Mundy, Z. Liu, R. Cabezas, R. Hovden, L. F. Kourkoutis, J. Zhang, N. P. Subramanian, R. Makharia, F. T. Wagner and D. A. Muller, *Nano Lett.* **2011**, DOI:10.1021/nl203975u.
[16] J. A. Chai, F. W. Huo, Z. J. Zheng, L. R. Giam, W. Shim and C. A. Mirkin, *Proc. Natl. Acad. Sci. U. S. A.* **2010**, *107*, 20202.
[17] T. Kraus, L. Malaquin, H. Schmid, W. Riess, N. D. Spencer and H. Wolf, *Nature Nanotech.* **2007**, *2*, 570.
[18] R. J. T. Houk, B. W. Jacobs, F. El Gabaly, N. N. Chang, A. A. Talin, D. D. Graham, S. D. House, I. M. Robertson and M. D. Allendorf, *Nano Lett.* **2009**, *9*, 3413.
[19] R. Subbaraman, D. Tripkovic, D. Strmcnik, K.-C. Chang, M. Uchimura, A. P. Paulikas, V. Stamenkovic and N. M. Markovic, *Science* **2011**, *334*, 1256.
[20] G. Wu, K. L. More, C. M. Johnston and P. Zelanay, *Science* **2011**, *332*, 443.
[21] W. J. E. Beek, M. M. Wienk and R. A. J. Janssen, *Adv. Mater.* **2004**, *16*, 1009.
[22] T. M. Eggenhuisen, J. P. den Breejen, D. Verdoes, P. E. de Jongh and K. P. de Jong, *J. Am. Chem. Soc.* **2010**, *132*, 18318.
[23] A. V. Neimark, L. I. Kheifez and V. B. Fenelonov, *Ind. Eng. Chem. Prod. Res. Dev.* **1981**, *20*, 439.
[24] J. R. A. Sietsma, J. D. Meeldijk, J. P. den Breejen, M. Versluijs-Helder, A. J. van Dillen, P. E. de Jongh and K. P. de Jong, *Angew. Chem., Int. Ed.* **2007**, *46*, 4547.
[25] L. Jiao and J. R. Regalbuto, *J. Catal.* **2008**, *260*, 329.
[26] F. Nudelman, K. Pieterse, A. George, P. H. H. Bomans, H. Friedrich, L. J. Brylka, P. A. J. Hilbers, G. de With and N. A. J. M. Sommerdijk, *Nat. Mater.* **2010**, *9*, 1004.
[27] F. Nudelman, G. de With and N. A. J. M. Sommerdijk, *Soft Matter* **2011**, *7*, 17.
[28] A. Sayari, B. H. Han and Y. Yang, *J. Am. Chem. Soc.* **2004**, *126*, 14348.
[29] J. C. Crocker and D. G. Grier, *J. Colloid Inter. Sci.* **1996**, *179*, 298.
[30] J. R. Kremer, D. N. Mastronarde and J. R. McIntosh, *J. Struct. Biol.* **1996**, *116*, 71.
[31] T. M. Eggenhuisen, M. J. van Steenbergen, H. Talsma, P. E. de Jongh and K. P. de Jong, *J. Phys. Chem. C* **2009**, *113*, 16785.
[32] M. Wolters, P. Munnik, J. H. Bitter, P. E. de Jongh and K. P. de Jong, *J. Phys. Chem. C* **2011**, *115*, 3332.
[33] C. Louis, Z. X. Cheng and M. Che, *J. Phys. Chem.* **1993**, *97*, 5703.
[34] R. Trujillano, J. F. Lambert and C. Louis, *J. Phys. Chem. C* **2008**, *112*, 18551.
[35] J. R. A. Sietsma, H. Friedrich, A. Broersma, M. Versluijs-Helder, A. J. van Dillen, P. E. de Jongh and K. P. de Jong, *J. Catal.* **2008**, *260*, 227.

Chapter 4

Freeze-Drying for Controlled Nanoparticle Distribution in Co/SiO_2 Fischer-Tropsch Catalysts

Abstract

The phase behavior of confined cobalt nitrate precursor phases in a porous silica matrix was investigated using differential scanning calorimetry to develop suitable freeze-drying methods for solution impregnation and melt infiltration. The nanoparticle distribution was successfully manipulated by varying the (freeze-)drying conditions for the preparation of Co/SiO_2 Fischer-Tropsch catalysts using a commercial silica-gel support. The catalysts thus synthesized form an excellent platform for future studies of catalyst stability under industrially relevant Fischer-Tropsch conditions.

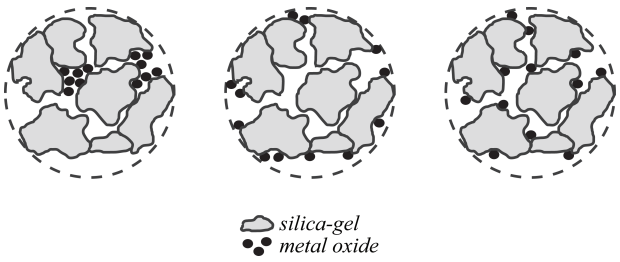

Tamara Eggenhuisen and Peter Munnik contributed equally to this chapter and therefore it is part of both PhD theses.

4.1 Introduction

Coalescence and sintering of nanoparticles is an irreversible deactivation pathway with detrimental effects on the activity and life time of supported catalysts.[1, 2] Therefore, many innovative pathways have been developed to improve stability of heterogeneous catalysts, such as encapsulation by a metal oxide shell around colloidal nanoparticles[3, 4] or by a porous metal oxide layer covering supported nanoparticles[5], and restriction of nanoparticle mobility by using cagelike support materials[6] or by alloying with a metal with a higher melting point.[7] Nevertheless, for supported nanoparticles maximizing nearest neighbor distances or, in other words, achieving a uniform nanoparticle distribution is essential to improve catalytic stability. Indeed, non-uniform nanoparticle distributions have been observed in many metal-support systems and showed to be prone to sintering.[8, 9] On the other hand, a non-uniform distribution of the active phase over microns or even millimeters in macroscopic catalyst bodies may be preferred depending on the catalysis conditions.[10] For example, deposition of the active phase in the outer rim of a macroscopic support body, a so-called egg-shell configuration, is favorable for fast reactions combined with diffusion constrictions of substrates and products.[11] Therefore, active control over metal or metal oxide nanoparticle distribution on a support on different lengths scales is crucial to the rational synthesis of supported catalysts.

Impregnation and drying is a convenient catalyst preparation method and is commonly applied in industry and academia. With the use of highly soluble transition metal nitrate salts, waste streams are low and high metal loadings can be obtained in a single impregnation step. Nevertheless, controlling dispersion and distribution by this synthesis route has remained challenging.[12-15] Especially at high metal loadings[16] and low support-salt interactions[17], agglomeration and cluster formation of nanoparticles after calcination is difficult to prevent. Drying has been recognized as a major influence on the distribution of the active phase over macroscopic bodies.[18-20] And although alternatives have been developed[21-24], a method preserving the advantages of impregnation and drying is desirable. Here, we will explore in detail the potential of freeze-drying for controlled nanoparticle distribution on an industrially relevant silica-gel support for the preparation of Co/SiO_2 Fischer-Tropsch catalysts.

Freeze-drying is a drying method often encountered in food-processing[25, 26] as well as in the pharmaceutical industry[27-29] usually for preservation purposes. By freeze-drying a solvent can be removed without exposing the matrix to tensile forces of a receding meniscus. Therefore, it is a suitable drying technique for the cryo-preservation of biological tissues[30, 31] or to develop porous aerogels based on soft templates from polymeric materials.[32, 33] For catalyst preparation, freeze-drying has been suggested to reduce precursor solution mobility during drying and

therefore control the location of deposition of the precursor phase. Nevertheless, few applications have been reported.[34-37]

Freeze-drying generally consists of three steps: freezing, primary drying and secondary drying.[38, 39] Freeze-drying processes for complex solutions most often result from experimentally based considerations and seems an art rather than a science.[40] Freezing is actually the most important step, as it determines the ice crystalline structure, which is affected by the cooling rate, degree of supercooling and annealing.[41-43] During primary drying, ice sublimates due to the reduced pressure. The rate depends on the heat transfer determined mainly by the ice structure, pressure and temperature.[44] However, several experimental details have a large influence on this step, even the sample vial configuration.[45] Finally, non-freezing or amorphous water can be removed in the secondary drying step, during which the temperature is raised under reduced pressure.[46]

Due to its long history and industrial relevance, literature on freeze-drying of (bio)pharmaceutical formulations and food is extensive. Here we aim to obtain the first fundamental insight into freeze-drying for the preparation of Co/SiO_2 Fischer-Tropsch catalysts. To develop a suitable freeze-drying method, The phase behavior of $Co(NO_3)_2$ (aq) solution and $Co(NO_3)_2 \cdot 6H_2O$ salt confined within a mesoporous silica matrix was studied with DSC. The phases present after freeze-drying were identified and compared to those resulting from conventional drying treatments. Detailed assessment of the distribution of the cobalt oxide nanoparticles after decomposition of the nitrates was done using ultramicrotomy and TEM. The fundamental insights on precursor phase behavior combined with freeze-drying led to control over the nanoparticle distribution on an industrially relevant silica gel support. Thus a platform was created for future investigation of the effect of uniform, clustered or egg-shell configurations on catalyst stability.

4.2 Experimental Methods

4.2.1 Catalyst synthesis

Co/SiO_2 catalysts were prepared using a commercially available silica gel as support (Davicat 1404, Grace-Davidson). The support was sieved to a fraction of 38 - 75 μm and the porous properties were characterized with N_2-physisorption at -196 ºC (Tristar 3000, Micromeritics): $V_p = 0.87$ cm^3/g, $S_{BET} = 443$ m^2/g, $d_p = 8$ nm. Solution impregnation (SI) was performed to incipient wetness using a saturated $Co(NO_3)_2$ (aq) solution (4.2 M, $Co(NO_3)_2 \cdot 6H_2O$, >99% Sigma-Aldrich), leading to a nominal cobalt metal loading of 17 wt%. For melt infiltration (MI), for example, 929 mg of $Co(NO_3)_2 \cdot 6H_2O$ and 754 mg of SiO_2-gel were physically mixed in a mortar with a pestle. The physical mixture was then heated overnight at 60 ºC in a Teflon-lined

steel autoclave (~6 mL). A nominal cobalt metal loading of 20 wt% was obtained.

Different drying treatments were applied to the as-prepared SiO_2-SI and SiO_2-MI precursor loaded catalysts. Conventional drying (CD) for SiO_2-SI was performed in a crucible in a preheated muffle oven at 60 ºC overnight, after which the sample was handled under ambient conditions. Melt infiltrated samples were used as-prepared. Freeze-drying (FD) was performed using a Sublimator 400 Freeze-dryer (Zirbus) and using the conditions summarized in Table 4.1. Samples were freeze-dried in 2 mL glass vials. The two freeze-drying procedures are denoted by their freezing temperature and the shelf temperature during the primary drying step. In the method FD(-45/-30), samples were frozen on the shelf by cooling to -45 ºC (~1 ºC/min, 5 hours). Primary drying was started by reducing the chamber pressure, after which the shelf temperature was increased to -30 ºC. For FD(LN_2/-45), quench freezing with liquid N_2 was applied. The glass vials containing the samples were cooled down in a reservoir containing liquid nitrogen, after which the reservoir was placed on the precooled shelf at -45 ºC in the freeze-dryer. Subsequently, the chamber pressure was reduced to start the primary drying step. Both methods included secondary drying by step-wise heating to 20 ºC under reduced pressure. The condenser temperature was between -65 and -70 ºC and the condenser chamber pressure was 0.02-0.03 mbar.

Calcination of all precursor loaded catalysts was performed by heating to 350 ºC (1 ºC/min, 1 hour) in a flow of N_2 or 1% v/v NO/N_2 (100 mL/min/100 mg catalyst). Freeze-dried pre-catalysts were transferred under dry nitrogen atmosphere to a fluidized-bed reactor.

Table 4.1. Summary of freeze-drying conditions.

	FD(-45/-30)	FD(LN_2/-45)
freezing temperature (time)	-45 ºC (5 h)	~ -170 ºC (15 min)
primary drying temperature (time)	-30 ºC (82 h)	-45 ºC (48 h)
primary drying pressure	0.02-0.03 mbar	0.02-0.03 mbar
secondary drying temperature (time)	-10 ºC (3 h), 20 ºC	-30 ºC (12 h), -15 ºC (12 h), 20 ºC
secondary drying pressure	<0.02 mbar	<0.02 mbar

4.2.2 Catalyst characterization

The phase behavior of cobalt nitrate present during the different stages of catalyst preparation was analyzed using differential scanning calorimetry (DSC, Q2000, TA Instruments). The temperature and heat flow were calibrated with a certified indium sample and measurements were performed with hermetically sealed aluminum pans (~40 μL, Tzero, TA Instruments) under a flow of N_2 (50 mL/min). Sample masses

were typically between 5 - 15 mg and heat flows were recorded between -90 ºC and 75 ºC at a rate of 1 ºC/min.

Thermogravimetric analysis (TGA, Q50 TA Instruments) was used to determine the residual water after different drying treatments by measuring the weight loss after heating to 500 ºC for 30 min (heating rate 10 ºC/min). The weight loss was corrected for the loss of water from the pristine silica gel between 150 ºC and 500 ºC, while water lost below 150 ºC was considered to be included in the precursor phase. The amount of residual water was calculated in moles H_2O/mole Co from the resulting corrected weight loss (m_{loss}), which was ascribed to the loss of residual water and the decomposition of the $Co(NO_3)_2$ precursor to Co_3O_4.

Diffuse Reflectance Spectroscopy (DRS) was used to obtain the UV/VIS absorption spectra of dried samples. Measurements were obtained on a Varian Cary 500 spectrophotometer from 800 to 250 nm in diffuse reflectance mode. Samples were held in an air tight sample holder with a quartz window to prevent rehydration during measurements.

XRD patterns were recorded between 30 and 60 º2θ with a Bruker-AXS D2 Phaser X-ray Diffractometer using Co-$K_{\alpha 12}$ radiation (λ = 1.790 Å). The volume averaged Co_3O_4 crystallite size was determined using the Scherrer equation with a shape factor k = 0.9 and line broadening analysis on the (110), (111) and (200) peaks by a fitting procedure in Eva2 software (Bruker AXS).

The catalyst particles were embedded in a two component epoxy resin (Epofix, EMS) and cured at 60 °C overnight. The embedded catalysts were then cut into thin sections with a nominal thickness of 50 nm using a Diatome Ultra 35° diamond knife mounted on a Reichert-Jung Ultracut E microtome and collected on a TEM grid. Bright field TEM images were obtained on a Tecnai 12, operated at 120 keV. High angle annular dark field (HAAFD) STEM was performed on a Tecnai 20 equipped with a field emission gun and operated at 200 keV.

4.2.3 Catalytic testing

Fischer-Tropsch synthesis was performed at 220 ºC and 1 bar with a H_2/CO ratio of 2 v/v. Typically, a plug-flow reactor was loaded with 10 mg of catalyst diluted with 200 mg SiC (200 μm). The catalysts were reduced *in-situ* at 500 ºC for 2 hrs (heating rate 5 ºC/min) under a flow or H_2/Ar (20/40 mL/min). C_1-C_{15} products were analyzed by online gas chromatography (Varian 430 GC, CP sil-5). The catalytic activity, expressed as cobalt-time-yield (10^{-5} $mol_{CO}/g_{Co}/s$) and C_1/C_{5+} selectivity, expressed in wt%, were determined after 20 hrs reaction time and a CO conversion of 2%.

4.3 Results & Discussion

4.3.1 Freeze-drying methods for confined $Co(NO_3)_2$ (aq) and $Co(NO_3)_2 \cdot 6H_2O$

To develop suitable freeze-drying methods, the phase behavior of cobalt nitrate confined in the mesoporous silica gel support was studied with differential scanning calorimetry (DSC). Figure 4.1 shows the freezing and melting behavior observed for silica gel after solution impregnation (SI) with $Co(NO_3)_3$ (aq) and after melt infiltration (MI) with $Co(NO_3)_2 \cdot 6H_2O$. Different freezing and melting point depressions were observed for the confined cobalt nitrate solution and for the cobalt nitrate salt. For SiO_2-MI, a single freezing and a single melting event were detected, indicating a uniform composition and structure of the confined salt. Bulk $Co(NO_3)_2 \cdot 6H_2O$ melts at 55 ºC, therefore, the confinement in the silica matrix caused a melting point depression of 35 ºC. The solution impregnated on silica gel displayed more complex phase behavior with several crystallization and melting events. A saturated aqueous $Co(NO_3)_2$ solution melts at -31 ºC. Therefore, the broad melting peak with a maximum at -35 ºC was ascribed to residual extraporous solution. The melting peak with maximum at -54 ºC was tentatively attributed to the confined solution, which would correspond to a melting point depression of 23 ºC. The melting peak at 10 ºC as well as the freezing peak at -30 ºC were tentatively ascribed to melting and freezing of confined $Co(NO_3)_2 \cdot 6H_2O$, indicating that some phase separation of the solution occurred inside the pore system. The different amounts of water present after SI or MI, caused a 55 ºC difference in the absolute freezing and melting point.

Two freeze-drying conditions can be deduced from the DSC thermograms. Firstly, the closed arrows in Figure 4.1 indicate the minimum freezing temperature to solidify all cobalt nitrate. The confined solution was frozen below -85 ºC, while for MI -30 ºC would suffice as freezing temperature. Second, the sample temperature during drying should not exceed the melting point. Therefore, as indicated by the open arrows, freeze-drying conditions should be chosen such that SiO_2-SI remains below 65 ºC and SiO_2-MI below -10 ºC.

Based on the results from DSC, two freeze-drying methods were developed within the boundaries set by experimental equipment. The first method, denoted by FD(LN_2/-45) involved quench freezing by liquid nitrogen, which should solidify both the confined cobalt nitrate solution (SI) as well as the salt (MI). Samples were then placed on a precooled shelf at -45 ºC for the primary drying step. In the second freeze-drying method, FD(-45/-30) a higher freezing temperature (-45 ºC) and a higher shelf temperature during primary drying (-30 ºC) were applied. By this method, the confined cobalt nitrate solution will not freeze, but the cobalt nitrate salt will. In both methods, the pressure range during primary drying was 0.02-0.03 mbar, which corresponds to an ice (I_h) equilibrium temperature of -55 ºC to -53 ºC. The

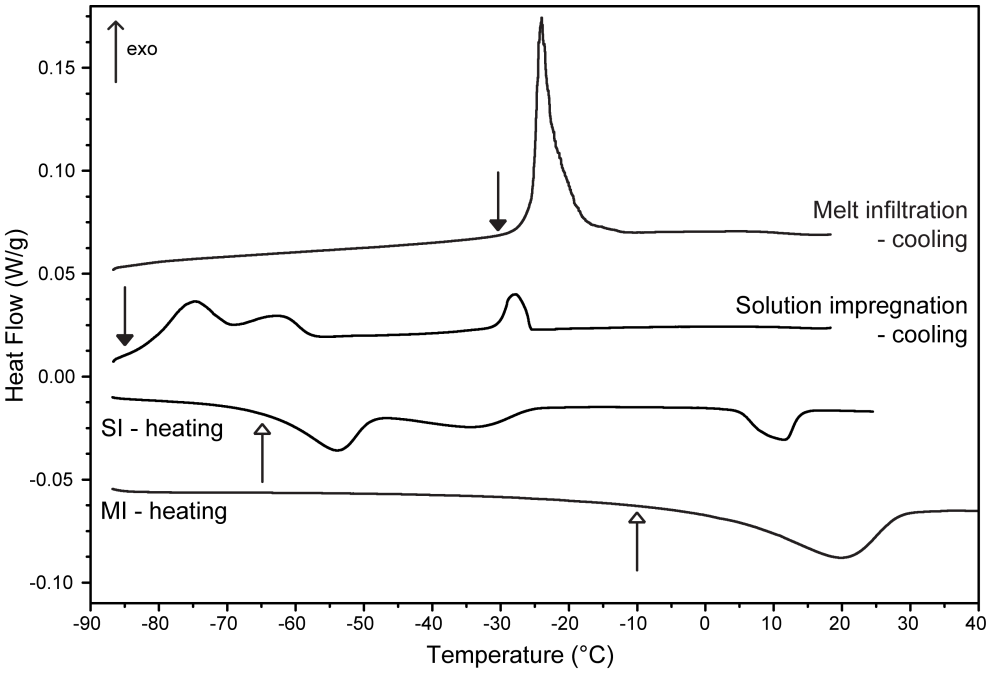

Figure 4.1. DSC thermograms recorded for precursor loaded silica gel prepared via solution impregnation (SI) with $Co(NO_3)_2$ (aq) or melt infiltration (MI) with $Co(NO_3)_2 \cdot 6H_2O$. Closed arrows indicate minimum freezing temperature and open arrows indicate maximum sample temperature during freeze-drying. Cooling/heating rate 1 ºC/min, thermograms are offset for clarity.

temperature is low enough during primary drying in both methods to keep SiO_2-MI frozen, while SiO_2-SI will only remain frozen in FD(LN_2/-45) by self-cooling at sufficiently high freeze-drying rates. Thus, the mobility of the precursor phase is expected to be restricted by FD(LN_2/-45) for both SiO_2-SI and SiO_2-MI. With FD(-45/-30), precursor immobilization is expected for SiO_2-MI, while for SiO_2-SI mobility of the solution is likely.

4.3.2 Cobalt nitrate precursor phase after drying

The precursor phase present after the different drying treatments was assessed by TGA, DSC and UV/VIS and the results are summarized in Table 4.2. The residual water was quantified using TGA analysis. After conventional drying, 6.5 and 7.8 moles of H_2O per mole of cobalt remained for SI and MI respectively. The samples were handled under ambient air conditions, and therefore rehydration of the salt could have occurred. Indeed, for SI-CD a sample transferred directly from the muffle oven at 60 ºC to the drybox contained only 4.9 residual water molecules per mole of Co. Therefore, some re-adsorption had occurred due to the hydrophilic nature of

cobalt nitrate. After melt infiltration, the water to cobalt ratio was slightly higher than for the $Co(NO_3)_2 \cdot 6H_2O$ from stock. This is partly due to the presence of physisorbed water in the silica gel, as the support was not dried prior to melt infiltration. After both freeze-drying treatments, water contents between 0.1 and 0.9 H_2O/Co were found for SI and MI. The different hydration states of cobalt nitrate depended on the drying method. This was also clearly observed in the derivative weight change profiles during decomposition, see Figure 4.2. For Si-CD, decomposition occurred largely in two steps: dehydration and decomposition of the nitrate which corresponds to results reported earlier.[47] For the samples obtained after freeze-drying, dehydration was virtually absent and decomposition occurred in a single step.

Further information on the precursor phase after drying was deduced from the phase behavior observed with DSC. Figure 4.3 shows the melting behavior of the precursor loaded silica gel after the different drying treatments. SI-CD and MI showed a single melting peak at 20 ºC, which has been ascribed to confined cobalt nitrate hexahydrate before.[48] Thus, both SI-CD and MI resulted in confined, liquid cobalt nitrate hexahydrate salt at room temperature. No melting transitions were observed after freeze-drying. The hydration state was also studied by UV/VIS spectroscopy, as after conventional drying both SI and MI samples were pink, while after freeze-drying they had turned purple. Indeed, the main UV/VIS absorption band shifted from 510 nm, which corresponds to octahedral cobalt nitrate hexahydrate, to 540

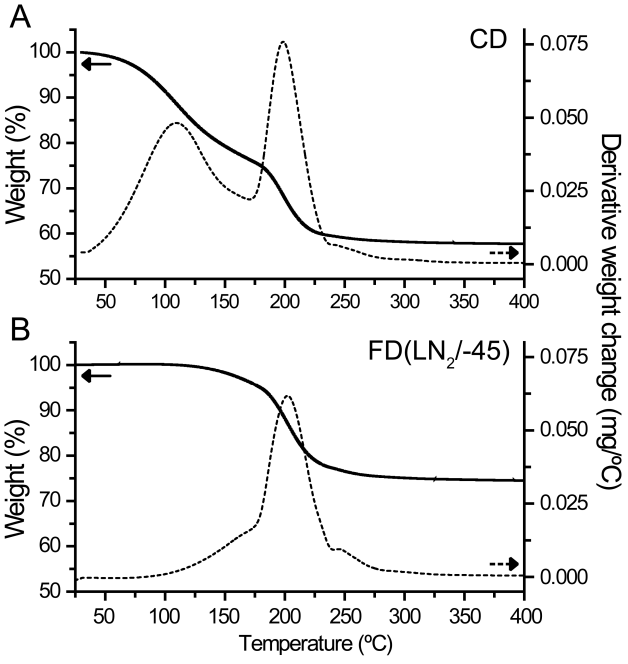

Figure 4.2. Weight loss determined with TGA (5 ºC/min) for precursor loaded silica gel prepared via solution impregnation (SI) with $Co(NO_3)_2$ (aq) (A) after conventional drying at 60 ºC (CD) and (B) after freeze-drying ($FD(LN_2/-45)$).

Table 4.2. Hydration state of precursor loaded silica gel prepared via solution impregnation (SI) with $Co(NO_3)_2$ (aq) and melt infiltration (MI) with $Co(NO_3)_2 \cdot 6H_2O$ after conventional drying (CD) or freeze-drying (FD).

Precursor loading	Drying method	Residual water [a] (moles H_2O /mole Co)	DSC melting peak maximum (ºC)	UV-VIS absorption maximum (nm)
SI	CD	6.5	19	514
SI	FD(-45/-30)	0.1	none	540
SI	FD(LN_2/-45)	0.7	none	538
MI	none	7.8	20	510
MI	FD(-45/-30)	0.9	none	539
MI	FD(LN_2/-45)	0.7	none	542

[a] determined by TGA

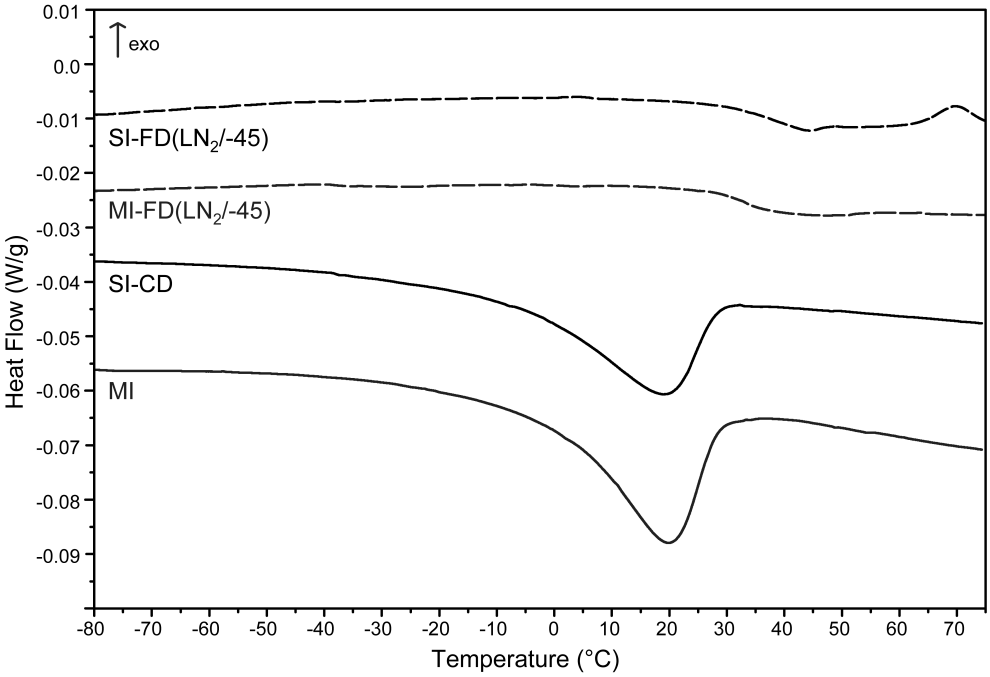

Figure 4.3. DSC thermograms (heating rate 1 ºC/min) recorded for precursor loaded silica gel prepared via solution impregnation (SI) with $Co(NO_3)_2$ (aq) and melt infiltration (MI) with $Co(NO_3)_2 \cdot 6H_2O$ after conventional drying at 60 ºC (CD) and after freeze-drying (FD(LN_2/-45)).

nm for freeze-dried samples (Table 4.2). This suggests exchange of H_2O ligands for NO_3^- or a surface hydroxyl group, which both have a smaller ligand-field splitting parameter and therefore cause a shift of the absorption to lower energy.[49]

4.3.3 Effect of drying on Co_3O_4 distribution at the micrometer length scale

The effect of the precursor distribution on the cobalt oxide distribution after calcination was imaged. Preparation of ~50 nm thick slices by ultramicrotomy allowed detailed TEM analysis of nanoparticle size and distribution over the support. First, the distribution of Co_3O_4 over the silica gel particle on the micrometer scale will be discussed, while the next section addresses the dispersion and distribution of individual Co_3O_4 nanoparticles on the nanometer scale. Figure 4.4 shows micrographs recorded for catalysts prepared by different drying treatments followed by calcination in a flow of N_2. In most cases clusters were observed with sizes ranging from 10 to 40 nm. Please note that the clusters appeared to consist of a (large) number of individual nanoparticles of about 8 nm in size (*vide infra*). Three types of cobalt oxide distribution over the support particles were identified. After conventional treatment of both SI and MI (Figure 4.4A and D), ~40 nm clusters

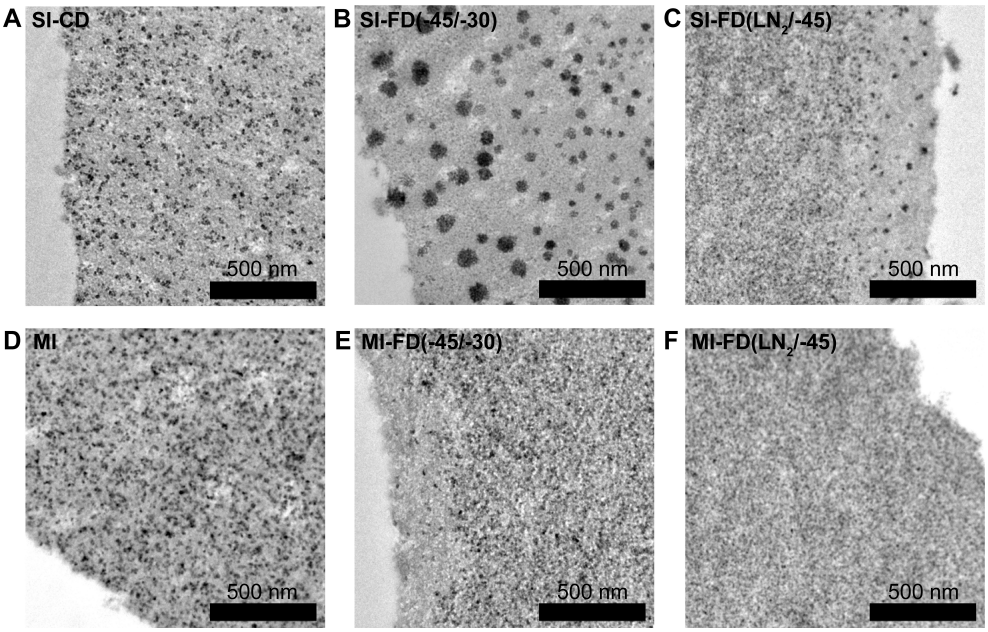

Figure 4.4. TEM micrographs of ultramicrotomed slices of Co_3O_4/SiO_2 prepared via different drying treatments followed by calcination in a flow of N_2 prepared via solution impregnation (SI, top row) or melt infiltration (MI, bottom row) and conventional drying (left column, CD), freeze-drying (middle column, FD(-45/-30)) and freeze-drying (right column, FD(LN_2/-45)).

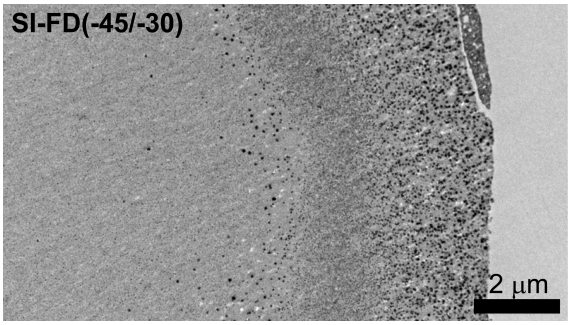

Figure 4.5. TEM micrograph of ultramicrotomed slice of Co_3O_4/SiO_2 prepared via solution impregnation (SI) and freeze-drying (FD(-45/-30)) followed by calcination in a flow of N_2.

were distributed homogeneously over the whole support. Second, freeze-drying by liquid nitrogen freezing (Figure 4.4C and F) as well as FD(-45/-30) for MI (Figure 4.4E) led to a homogeneous distribution of very small Co_3O_4 clusters below 20 nm. Last, by solution impregnation and FD(-45/-30) shown in Figure 4.4B, clusters up to 140 nm were observed. Surprisingly, an egg-shell configuration was apparent for this catalyst at lower magnification and cobalt clusters were only observed in the ~5 µm outer rim, while the body of the particle was mostly empty (Figure 4.5). Thus, FD(-45/-30) caused extensive redistribution of the cobalt nitrate solution to the surface of the macroscopic support particle, while for the sample melt infiltrated with $Co(NO_3)_2 \cdot 6H_2O$ this drying method led to a homogeneous distribution after calcination.

By calcination in a flow of N_2, mobility of cobalt during decomposition is expected.[50] By the addition of 1% v/v NO during calcination, aggregation is mostly

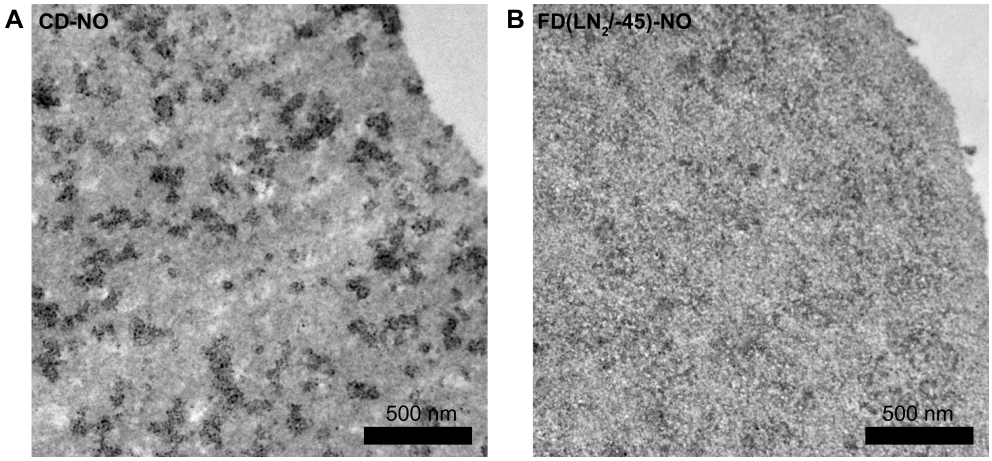

Figure 4.6. TEM micrographs of ultramicrotomed slices of Co_3O_4/SiO_2 prepared via solution impregnation (SI) and different drying treatments followed by calcination in a flow of 1% NO/N_2: (A) conventional drying (CD) or (B) freeze-drying ($FD(LN_2/-45)$).

prevented during decomposition of hydrated transition metal nitrates.[13, 51] Here NO calcination was applied to confirm the footprint of the salt distribution obtained after different drying treatments. TEM showed that the Co_3O_4 cluster distribution followed the same general trend as was observed after calcination in N_2 flow. Both SI and MI resulted in similar cobalt oxide cluster distributions after conventional drying or after freeze-drying starting at liquid nitrogen temperatures. By FD(-45/-30), solution impregnation again led to an egg-shell configuration. Therefore, the cobalt distribution on the micrometer length scale was mainly determined by the precursor phase distribution after drying. Figure 4.6A illustrates the difference in Co_3O_4 cluster size obtained by NO-assisted calcination after conventional drying as compared to calcination in a flow of N_2. Clusters of 20 nm up to 400 nm consisting of individual Co_3O_4 nanoparticles (*vide infra*). These clusters are significantly larger than those observed after calcination in N_2 (~10-40 nm, Figure 4.4A). The details of the effect of the calcination atmosphere on cluster formation from hydrated transition metal nitrate salts is beyond the scope of this paper and e. Regardless, it is clear that after conventional drying the cobalt distribution is very inhomogeneous. In contrast, freeze-drying starting at liquid nitrogen temperatures (Figure 4.6B) again led to a homogeneous distribution of cobalt oxide.

Table 4.3. Average crystallite size determined with XRD and average particle size determined with HAADF STEM for catalysts after calcination in a flow of N_2 or a flow of 1% NO/N_2, prepared via solution impregnation (SI) with $Co(NO_3)_2$ (aq) and melt infiltration (MI) with $Co(NO_3)_2 \cdot 6H_2O$ and conventional drying at 60 ºC (CD) or after freeze-drying (FD).

	Calcination in flow of N_2		Calcination in flow of 1% NO/N_2	
Catalyst	d_{XRD} (nm)	d_{TEM} (nm)	d_{XRD} (nm)	d_{TEM} (nm)
Co_3O_4/SiO_2-SI-CD	8.0	7.9 ± 1.9	5.4	6.4 ± 1.7
Co_3O_4/SiO_2-SI-FD(-45/-30)	7.9	7.4 ± 1.8	4.7	5.5 ± 1.5
Co_3O_4/SiO_2-SI-FD(LN_2/-45)	7.8	6.6 ± 1.5	4.4	4.2 ± 0.8
Co_3O_4/SiO_2-MI	7.9	6.8 ± 1.5	6.2	6.0 ± 1.3
Co_3O_4/SiO_2-MI-FD(-45/-30)	7.9	7.3 ± 1.5	6.0	5.0 ± 1.1
Co_3O_4/SiO_2-MI-FD(LN_2/-45)	7.9	6.8 ± 1.4	4.2	4.6 ± 1.1

4.3.4 Effect of drying on Co_3O_4 nanoparticle distribution at nanometer scale

For a more detailed analysis of the nanoparticle size and local distribution, micrographs at higher magnifications are shown in Figure 4.7 for catalysts prepared by solution impregnation. In this case, the cobalt nanoparticles were imaged in dark field mode, and appear as light spots on the darker background of the silica matrix. Furthermore, Table 4.3 shows the results for average crystallite size as determined by XRD and average particle size from analysis of high angle annular dark field (HAADF) STEM images. After calcination in a flow of N_2, SI-CD led to the formation of 10-40 nm large clusters as can be seen in Figure 4.7A. However, the clusters appeared to consist 8 nm nanoparticles, which corresponded to the average crystallite size from XRD. After calcination in 1% NO/N_2, larger clusters up to 400 nm were formed by SI-CD (Figure 4.6A). However, in Figure 4.7C it is clear that the large clusters consisted of ~6 nm individual nanoparticles. By freeze-drying (Figure 4.7B and D), nanoparticles were found distributed uniformly over the support. Furthermore, by both calcination methods smaller Co_3O_4 nanoparticles formed after freeze-drying, i.e ~7 nm by N_2 calcination and ~4 nm by NO calcination.

4.3.5 Co/SiO_2 catalysts for the Fischer-Tropsch synthesis

The Co_3O_4/SiO_2 catalysts prepared by different drying methods were tested for the Fischer-Tropsch synthesis. Table 4.4 shows the results of the catalytic tests at 1 bar and 2% conversion. The catalysts prepared by calcination in N_2 were activated by reduction at 450 ºC. The smaller particles obtained after calcination in NO/N_2 were reduced at 550 ºC, as these are more difficult to reduce than larger particles.[52, 53] They showed catalytic activities comparable to earlier reported highly active catalysts treated at the same reduction temperature.[53] The N_2 calcined catalysts exhibited a slightly lower Fischer-Tropsch activity, which is ascribed to the larger Co_3O_4 nanoparticle size.[54] The freeze-dried catalysts showed slightly higher activity as compared to the catalysts prepared by conventional drying. This indicates that the cobalt oxides formed after calcination and different drying treatments had similar reducibility and excludes the formation of large amounts of cobalt (hydro)silicates. Due to the mild reaction conditions catalyst deactivation during reaction was not significant. Therefore, industrially relevant reaction conditions should be applied to study the effect of the Co_3O_4 nanoparticle distribution on deactivation by sintering, i.e. high pressures and high conversion. Nevertheless, the observed comparable activities for catalysts with similar particle sizes, but various nanoparticle spacings qualify these materials to study a structure-performance relation for deactivation.

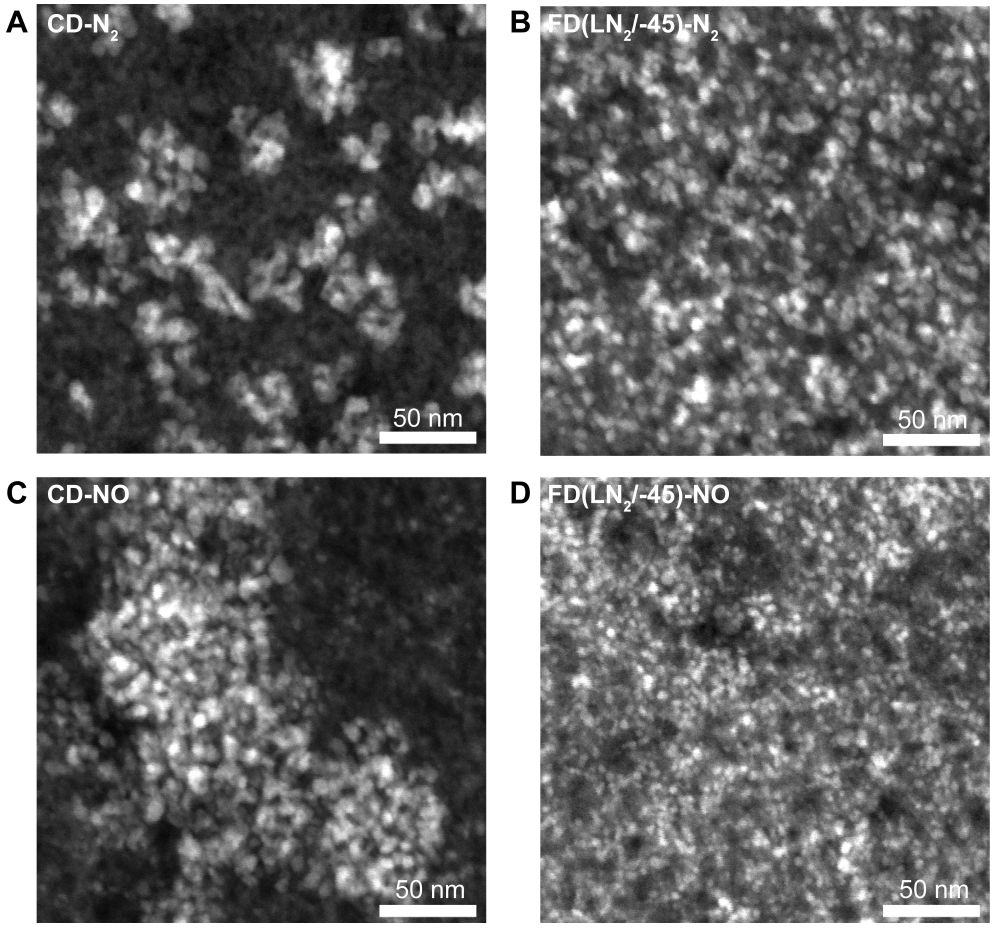

Figure 4.7. HAADF-STEM micrographs of ultramicrotomed slices of Co_3O_4/SiO_2 prepared via solution impregnation (SI) and conventional drying (left column) or freeze-drying (right column) followed by calcination in a flow of N_2 (top row) or a flow of 1% NO/N_2 (bottom row): (A) CD-N_2, (B) FD(LN_2/-45)-N_2, (C) CD-NO, (D) FD(LN_2/-45)-NO.

Table 4.4. Catalytic activity for the Fischer-Tropsch synthesis at 220 ºC and 1 bar of various catalysts prepared by solution impregnation (SI) and conventional drying (CD) or freeze-drying (FD) and calcination in different gas flows.

Catalyst	Calcination atmosphere	reduction temperature (ºC)	CTY[a,b]	C_1[a,c] (wt%)	C_{5+}[a,c] (wt%)
Co_3O_4/SiO_2-SI-CD	N_2	450	3.70	19.9	51.5
Co_3O_4/SiO_2-SI-FD(LN_2/-45)	N_2	450	4.09	23.0	44.9
Co_3O_4/SiO_2-SI-CD	NO/N_2	550	5.20	20.9	49.9
Co_3O_4/SiO_2-SI-FD(LN_2/-45)	NO/N_2	550	6.20	23.3	44.0

[a] catalytic properties were determined after 20 hrs time-on-stream, [b] cobalt-time-yield in 10^{-5} $mol_{CO}/g_{Co}/s$, [c] selectivity.

4.4. Conclusions

The cobalt oxide nanoparticle distribution in Co/SiO_2 Fischer-Tropsch catalysts was successfully manipulated by varying the drying treatments. More specifically, this was achieved for a system with weak support-precursor interaction and at high metal loadings, using a commercially available silica-gel support and cobalt nitrate as precursor. Freeze-drying was applied to restrict precursor mobility during the drying step. Based on the different freezing point depressions of confined cobalt nitrate solution and cobalt nitrate hexahydrate salt, two freeze-drying methods were developed. DSC showed that by freezing at liquid nitrogen temperatures, both solution and salt solidified, while by freezing at -45 ºC only the confined cobalt nitrate salt crystallized. The Co_3O_4 distribution after decomposition of the nitrate largely represented the distribution of the precursor phase obtained by drying. Conventional drying led to the formation of clusters of individual nanoparticles, while freeze-drying starting at liquid nitrogen temperatures led to a uniform distribution of nanoparticles over the support. An egg-shell catalyst was obtained after solution impregnation and freeze-drying starting at -45 ºC, which is above the crystallization temperature of confined cobalt nitrate solution. An average particle size of 8 nm was obtained after calcination in a flow of N_2 and 4-6 nm particles were obtained by decomposition in 1% NO/N_2. All catalysts showed high activity for the Fischer-Tropsch reaction at 1 bar, showing similar reducibility of the oxides formed after the different drying treatments and calcination. The catalysts thus synthesized comprise an excellent platform to test the effect of nanoparticle spacing on deactivation by sintering under industrially relevant reaction conditions.

Acknowledgements

P. Munnik contributed equally to this work. Mies van Steenbergen and Herre Talsma (Utrecht University) are acknowledged for technical support and useful discussions on freeze-drying as well as thermal analysis. Hans de Waard (University of Groningen) and Foppe Bakker (MSD) are acknowledged for providing access to freeze-drying equipment and sharing their expertise. Mw. E. van Donselaar (Utrecht University) is acknowledged for ultramicrotomy instructions. The Electron Microscopy Unit at Utrecht University is acknowledged for their excellent facilities.

References

[1] C. H. Bartholomew, *Appl. Catal.- A Gen.* **2001**, *212*, 17.
[2] P. Forzatti and L. Lietti, *Catal. Today* **1999**, *52*, 165.
[3] P. M. Arnal, M. Comotti and F. Schuth, *Angew. Chem., Int. Ed.* **2006**, *45*, 8224.
[4] S. H. Joo, J. Y. Park, C. K. Tsung, Y. Yamada, P. D. Yang and G. A. Somorjai, *Nat. Mater.* **2009**, *8*, 126.
[5] W. F. Yan, S. M. Mahurin, Z. W. Pan, S. H. Overbury and S. Dai, *J. Am. Chem. Soc.* **2005**, *127*, 10480.
[6] L. Y. Li, D. L. King, J. Liu, Q. S. Huo, K. K. Zhu, C. M. Wang, M. Gerber, D. Stevens and Y. Wang, *Chem. Mater.* **2009**, *21*, 5358.
[7] A. Cao and G. Veser, *Nat. Mater.* **2010**, *9*, 75.
[8] S. L. Soled, A. Malek, S. Miseo, J. Baumgartner, C. Kliewer, M. Afeworki and P. A. Stevens, *Scientific Bases for the Preparation of Heterogeneous Catalysts, Proceedings of the 9th International Symposium* **2006**, *162*, 103.
[9] A. M. Saib, D. J. Moodley, I. M. Ciobica, M. M. Hauman, B. H. Sigwebela, C. J. Weststrate, J. W. Niemantsverdriet and J. van de Loosdrecht, *Catal. Today* **2010**, *154*, 271.
[10] A. V. Neimark, L. I. Kheifez and V. B. Fenelonov, *Ind. Eng. Chem. Prod. Res. Dev.* **1981**, *20*, 439.
[11] E. Iglesia, S. L. Soled, J. E. Baumgartner and S. C. Reyes, *J. Catal.* **1995**, *153*, 108.
[12] O. Borg, J. C. Walmsley, R. Dehghan, B. S. Tanem, E. A. Blekkan, S. Eri, E. Rytter and A. Holmen, *Catal. Lett.* **2008**, *126*, 224.
[13] J. R. A. Sietsma, J. D. Meeldijk, J. P. den Breejen, M. Versluijs-Helder, A. J. van Dillen, P. E. de Jongh and K. P. de Jong, *Angew. Chem., Int. Ed.* **2007**, *46*, 4547.
[14] A. Martinez, C. Lopez, F. Marquez and I. Diaz, *J. Catal.* **2003**, *220*, 486.
[15] J. van der Meer, I. Bardez, F. Bart, P. A. Albouy, G. Wallez and A. Davidson, *Micropor. Mesopor. Mat.* **2009**, *118*, 183.
[16] I. Arslan, J. C. Walmsley, E. Rytter, E. Bergene and P. A. Midgley, *J. Am. Chem. Soc.* **2008**, *130*, 5716.
[17] E. Marceau, M. Che, J. Cejka and A. Zukal, *ChemCatChem* **2010**, *2*, 413.
[18] A. Lekhal, B. J. Glasser and J. G. Khinast, *Chem. Eng. Sci.* **2001**, *56*, 4473.
[19] X. Liu, J. G. Khinast and B. J. Glasser, *Ind. Eng. Chem. Res.* **2010**, *49*, 2649.
[20] M. Komiyama, R. P. Merrill and H. F. Harnsberger, *J. Catal.* **1980**, *63*, 35.
[21] M. Che, Z. X. Cheng and C. Louis, *J. Am. Chem. Soc.* **1995**, *117*, 2008.
[22] W. Chu, L. N. Wang, P. A. Chernavskii and A. Y. Khodakov, *Angew. Chem., Int. Ed.* **2008**, *47*, 5052.
[23] A. J. van Dillen, R. J. A. M. Terorde, D. J. Lensveld, J. W. Geus and K. P. de Jong, *J. Catal.* **2003**, *216*, 257.
[24] N. F. Zheng and G. D. Stucky, *J. Am. Chem. Soc.* **2006**, *128*, 14278.
[25] A. Reyes, R. Vega, R. Bustos and C. Araneda, *Dry. Technol.* **2008**, *26*, 1272.
[26] V. Kirmaci, H. Usta and T. Menlik, *Dry. Technol.* **2008**, *26*, 1570.
[27] G. H. Chen and W. Wang, *Dry. Technol.* **2007**, *25*, 29.
[28] C. J. Chen, D. D. Han, C. F. Cai and X. Tang, *J. Control. Release* **2010**, *142*, 299.
[29] W. Wang, *Int. J. Pharm.* **2000**, *203*, 1.
[30] D. C. Portner, R. G. K. Leuschner and B. S. Murray, *Cryobiology* **2007**, *54*, 265.

[31] C. Schwab, R. Vogel and M. G. Ganzle, *Cryobiology* **2007**, *55*, 108.
[32] L. Qian and H. Zhang, *J. Chem. Technol. Biotechnol.* **2010**, *86*, 172.
[33] K. Kraiwattanawong, N. Sano and H. Tamon, *Carbon* **2011**, *49*, 3404.
[34] T. Vergunst, F. Kapteijn and J. A. Moulijn, *Appl. Catal.- A Gen.* **2001**, *213*, 179.
[35] X. L. Xi, Z. R. Nie, Y. B. Jiang, X. Y. Xu and T. Y. Zuo, *Powder Technol.* **2009**, *191*, 107.
[36] H. J. Kim, S. M. Choi, S. H. Nam, M. H. Seo and W. B. Kim, *Appl. Catal.- A Gen.* **2009**, *352*, 145.
[37] X. Carrier, J. F. Lambert, S. Kuba, H. Knozinger and M. Che, *J. Mol. Struct.* **2003**, *656*, 231.
[38] J. D. Mellor, *Fundamentals of freeze-drying*. 1978, London New York San Fransisco: Academic Press.
[39] E. W. Flosdorf, *Freeze-drying. Drying by sublimation*. 1949, New York: Reinhold Publishing corporation.
[40] X. L. Tang and M. J. Pikal, *Pharm. Res.* **2004**, *21*, 191.
[41] J. C. Kasper and W. Friess, *Eur. J. Pharm. Biopharm.* **2011**, *78*, 248.
[42] J. Beirowski, S. Inghelbrecht, A. Arien and H. Gieseler, *J. Pharm. Sci.* **2011**, *100*, 1958.
[43] J. A. Searles, J. F. Carpenter and T. W. Randolph, *J. Pharm. Sci.* **2001**, *90*, 872.
[44] B. G. Malmstrom, *Exp. Cell Res.* **1951**, *2*, 688.
[45] K. H. Gan, R. Bruttini, O. K. Crosser and A. I. Liapis, *Dry. Technol.* **2004**, *22*, 1539.
[46] M. J. Pikal, S. Shah, M. L. Roy and R. Putman, *Int. J. Pharm.* **1990**, *60*, 203.
[47] M. Wolters, I. C. A. Contreras Andrade, P. Munnik, J. H. Bitter, P. E. de Jongh and K. P. de Jong, *Stud. Surf. Sci. Catal.* **2010**, *175*, 69.
[48] T. M. Eggenhuisen, J. P. den Breejen, D. Verdoes, P. E. de Jongh and K. P. de Jong, *J. Am. Chem. Soc.* **2010**, *132*, 18318.
[49] J. Vakros, K. Bourikas, S. Perlepes, C. Kordulis and A. Lycourghiotis, *Langmuir* **2004**, *20*, 10542.
[50] J. R. A. Sietsma, H. Friedrich, A. Broersma, M. Versluijs-Helder, A. J. van Dillen, P. E. de Jongh and K. P. de Jong, *J. Catal.* **2008**, *260*, 227.
[51] M. Wolters, P. Munnik, J. H. Bitter, P. E. de Jongh and K. P. de Jong, *J. Phys. Chem. C* **2011**, *115*, 3332.
[52] G. Jacobs, T. K. Das, Y. Q. Zhang, J. L. Li, G. Racoillet and B. H. Davis, *Appl. Catal.- A Gen.* **2002**, *233*, 263.
[53] J. P. den Breejen, J. R. A. Sietsma, H. Friedrich, J. H. Bitter and K. P. de Jong, *J. Catal.* **2010**, *270*, 146.
[54] J. P. den Breejen, P. B. Radstake, G. L. Bezemer, J. H. Bitter, V. Froseth, A. Holmen and K. P. de Jong, *J. Am. Chem. Soc.* **2009**, *131*, 7197.

Chapter 5

Fundamentals of Melt Infiltration for the Preparation of Supported Metal Catalysts. The Case of Co/SiO_2 for Fischer-Tropsch Synthesis

Abstract

Melt infiltration was investigated as an alternative preparation method for supported catalysts. Melting of $Co(NO_3)_2 \cdot 6H_2O$ in the presence of silica supports was studied *in-situ* with differential scanning calorimetry. The dispersion and distribution of Co_3O_4 after calcination could be controlled using the same toolbox as for preparation via solution impregnation: confinement and the calcination gas atmosphere. After reduction the Co/SiO_2 catalysts showed high activity for the Fischer-Tropsch synthesis, illustrating the versatility of melt infiltration for supported catalyst preparation.

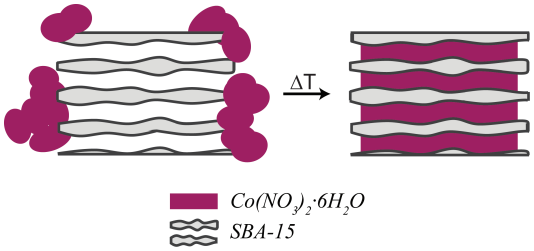

5.1 Introduction

In the past, supported catalyst preparation has been referred to as an art rather than science. However, nowadays the limits and possibilities of the classical preparation routes are being studied at a fundamental level.[1, 2] The literature on impregnation and drying,[3-5] deposition-precipitation[6-8] and ion-adsorption[9-11] is extensive. Nevertheless, control over metal nanoparticle size, distribution and even shape in order to maximize catalytic effectiveness persists as a motivation for designing new or improved preparation routes.[12, 13] Many alternative methods, such as chemical vapor deposition,[14] atomic layer deposition,[15] surface functionalization[16, 17] or combined approaches have been developed. Still, impregnation and drying with metal nitrate salts as a precursor is the most widely applied preparation method. It is favored because of its convenience and the use of highly soluble, low cost precursors that readily decompose. Unfortunately, often catalysts are obtained with an inhomogeneous metal dispersion and distribution, due to low support-precursor interactions.[18-21]

Melt infiltration can be considered as an alternative to impregnation and drying. Metal salts that melt before they decompose can be introduced to a porous support via capillary forces without the use of a solvent. Hydrated transition metal nitrates are particularly suitable, since they have low melting points coined to dissolution in crystal water.[22] Melt infiltration appears in literature under various names, such as the solvent-free method,[23, 24] solid-state grinding[25] or the solid-liquid route.[22, 26] In the field of catalyst preparation, it has been applied to obtain highly dispersed copper species on SBA-15[23, 27] as well as on ZSM-5.[28] On the other hand, melt infiltration of MCM-41 with iron nitrate resulted in large extraporous crystallites.[29] Melt infiltration with cobalt nitrate salt has been used with extrudates to obtain an egg-shell catalyst, where the high viscosity of the nitrate melt was used to obtain an inhomogeneous precursor distribution.[30] In the field of nanocasting,[31] this procedure was used to obtain mesoporous silica with a high loading and after calcination a highly agglomerated metal oxide to form mesoporous single crystals.[25, 26, 32] Melt infiltration with metals is applied in materials science for the preparation of ceramic composites or hydrogen storage materials.[33-35]

Although melt infiltration has been applied to prepare supported metal oxides, the fundamental phenomena have remained obscure and erratic results were sometimes obtained. Insights relied on information obtained after calcination or the disappearance of the precursor diffraction pattern after heat treatment. In addition, the potential of melt infiltration to tune the dispersion and distribution of the metal oxide for catalytic applications has not been studied.

Differential scanning calorimetry (DSC) gives direct information on the melting

behavior of the precursor salt and its interaction with a porous support. Salt confined in a mesoporous system can be distinguished from extraporous phases due to the depressed melting point.[36] This technique has been applied to study water or aqueous solutions confined in mesoporous silica,[37, 38] and the melting point depression of confined salt hydrates was also studied with ^{1}H NMR.[39] In addition, the phases can be quantified through the specific melting enthalpy. This allows direct evaluation of precursor infiltration.

In this chapter, the applicability of melt infiltration to obtain highly loaded supported catalysts with controllable nanoparticle size is discussed. The extent of pore-filling as well as effects of the melt infiltration conditions on the precursor loading was studied with DSC. In addition, low and high angle XRD and TEM were used to determine the precursor distribution. The versatility of melt infiltration for supported catalyst preparation was illustrated by the preparation of a series of Co/SiO_2 catalysts for the Fischer Tropsch synthesis with ordered mesoporous silica as model supports and a commercial silica gel as example of an industrial support. The same preparation toolbox was employed as for solution impregnation to control dispersion and distribution of the cobalt oxide particles, i.e. via confinement and calcination.[40]

5.2 Experimental Methods

5.2.1 Support preparation

SBA-15 was synthesized according to the procedure described by Zhao *et al*. using P123 as template and tetraethylorthosilicate (98%, Aldrich) as silica source.[41] A gel with molar ratio of 1 SiO_2:0.0143 P123:5.05 HCl:144 H_2O was aged under stirring at 40 ºC for 20 h after which it was treated at 50, 100 or 120 ºC in a Teflon-lined steel autoclave for 48 h under static conditions. After filtration and washing the samples were dried at 120 ºC and subsequently calcined at 550 ºC (1 ºC/min, 6 h). Samples prepared at different temperatures are denoted as S50, S100 and S120.

Large pore MCM-41 was synthesized using a procedure described by Cheng *et al.* with cetyltrimethylammoniumbromide (CTAB, Aldrich) as template, Aerosil 380 (Degussa) as silica source and tetramethyl ammonium hydroxide (TMAOH, 25% Aldrich) as base.[42] All reactants were mixed at room temperature for 30 min until a homogeneous gel was obtained with the molar ratio 1 SiO_2 : 0.25 CTAB : 0.20 TMAOH : 40 H_2O. The gel was aged in a Teflon-lined steel autoclave at 80 ºC for 24 h and subsequently crystallized at 150 ºC for 24 h. The product was filtered, washed with water and acetone, dried at 120 ºC and subsequently calcined at 550 ºC (1 ºC/min, 8 h).

A commercial silica gel, Davicat 1404 (Grace-Davidson) was used as obtained.

5.2.2 Catalyst preparation

To prepare a typical catalyst, 802 mg $Co(NO_3)_2 \cdot 6H_2O$ (>99.0%, Aldrich) and 592 mg of the support (S100), corresponding to a theoretical Co loading of 22 wt% in the reduced catalyst, were physically mixed in a mortar with a pestle for several minutes under ambient conditions until the powder was homogeneously pink. Mixtures of $Co(NO_3)_2 \cdot 6H_2O$ and support are denoted by the mass loading of $Co(NO_3)_2 \cdot 6H_2O$ in $g/g_{support}$, e.g. $Co(NO_3)_2 \cdot 6H_2O$/S100 with 1.4 g/g_{S100} loading. In the same manner other supports were mixed with $Co(NO_3)_2 \cdot 6H_2O$ to obtain the following catalysts Co/MCM (1.2 g/g_{MCM}, 19.9 wt% Co), Co/S50 (0.58 g/g_{S50}, 10.5 wt% Co), Co/S120 (1.3 g/g_{S120}, 21.2 wt% Co) and Co/silica gel (1.1 g/g_{SiO2}, 17.6 wt% Co). The reported cobalt loadings coincided with the maximum precursor loading that was determined with DSC (*vide infra*). Melt infiltration was performed at 60 ºC for 24 h in a Teflon-lined steel autoclave (Ø 1 cm, height 3 cm). After melt infiltration samples were stored under ambient atmosphere in Teflon sealed vials. The infiltrated sample was transferred to a fluidized-bed reactor and calcined by heating to 350 ºC (1 ºC/min, 1 h) in a flow of N_2 or 1% v/v NO/N_2 (150 mL/min for 150 mg precursor loaded catalyst). An N_2 flow was used to prevent extensive redistribution and agglomeration of Co_3O_4 during calcination, while an NO/N_2 flow was applied to achieve a high metal oxide dispersion, as has been reported by Sietsma *et al*.[43]

5.2.3 Support characterization

N_2-Physisorption measurements were performed at -196 °C using a Micromeritics Tristar 3000. The samples were dried prior to the measurement under an N_2 flow at 250 °C for at least 12 hours. The total microporous and mesoporous volume (V_p) was determined using the t-plot method at thicknesses in the range of 1.0 – 1.4 nm.[44] For the ordered mesoporous silica supports, the pore size distribution was calculated from the adsorption branch of the isotherm by a NL-DFT method designed for N_2 in cylindrical pores.[45] The pore size distribution of the silica gel was calculated from the desorption branch by BJH analysis. The maximum of the pore size distribution was taken as the average pore diameter.

Long range pore ordering was confirmed with low-angle X-ray diffraction. Patterns were obtained at room temperature from 0.5 to 8° 2θ with a Bruker-AXS D8 Advance X-ray Diffractometer using Co-$K_{\alpha 12}$ radiation.

5.2.4 Differential scanning calorimetry

The melting behavior of $Co(NO_3)_2 \cdot 6H_2O$ in the presence of mesoporous silica was

studied with DSC (Q2000, TA instruments). The temperature and heat flow were calibrated with a certified indium sample and measurements were performed with hermetically sealed aluminum pans (Tzero, ~40 µL) under a flow of N_2 (50 mL/min). Sample masses were typically between 3 - 10 mg. To study the pore loading of S100 with $Co(NO_3)_2 \cdot 6H_2O$, mixtures of 0.45, 0.92, 1.4, 1.6, 1.8 and 2.7 g/g_{S100} were prepared. To determine maximum precursor loading of different supports, mixtures of $Co(NO_3)_2 \cdot 6H_2O$/support were prepared with the same salt volume/pore volume ratio as the maximum loading of S100. Melt infiltration was followed *in situ* for the $Co(NO_3)_2 \cdot 6H_2O$/support physical mixtures by a heat-cool-heat cycle to 75, -90 and 75 ºC, respectively, at 2.5 ºC/min with 5 minute isothermal steps at each temperature extreme. The melting behavior of $Co(NO_3)_2 \cdot 6H_2O$ in samples that were melt infiltrated in an autoclave was followed during a single heating run to 75 ºC. To detect the depressed melting point of intraporous salt, the samples were first cooled to -90 ºC.

The amount of residual extraporous $Co(NO_3)_2 \cdot 6H_2O$ was calculated from the bulk melting enthalpy of $Co(NO_3)_2 \cdot 6H_2O$ in the second heating run for the *in situ* experiments or during the single heating run for the melt infiltrated samples. The melting enthalpy of $Co(NO_3)_2 \cdot 6H_2O$ at ~55 ºC was measured by integration using Universal Analysis 2000 (TA instruments) with a sigmoidal baseline. The mass of extraporous $Co(NO_3)_2 \cdot 6H_2O$ was subsequently calculated with the specific melting enthalpy (ΔH_m = 142.9 J/g).[46] The degree of pore-loading was expressed as the amount of intraporous $Co(NO_3)_2 \cdot 6H_2O$ ($=m_{added\ CoN} - m_{extrap\ CoN}$) in $g/g_{support}$.

5.2.5 Catalyst characterization

Thermal gravimetric analysis (TGA, Q50 TA Instruments) was used to determine the weight loss of melt infiltrated samples by heating to 500 ºC at 10 º/min for 60 min. XRD patterns were recorded for all catalysts between 30 and 60 º2θ with a Bruker-AXS D8 Advance X-ray Diffractometer using Co-$K_{\alpha 12}$ radiation. The volume averaged Co_3O_4 crystallite size was determined for calcined catalysts using line broadening analysis on the (110), (111) and (200) peaks by a fitting procedure in Eva2 software (Bruker AXS) and the Scherrer equation with a shape factor k = 0.9. Long range pore ordering of the supports was confirmed with low-angle XRD. Transmission electron microscopy was performed on a Technai 20 FEG microscope operated at 200 keV as well as on a Technai 12 microscope operated at 120 keV.

5.2.6 Catalytic testing

Fischer Tropsch synthesis was performed at 220 ºC and 1 bar with an H_2/CO ratio of 2 v/v (3.0/1.5 mL/min). Typically, a plug-flow reactor was loaded with 15 mg of

catalyst diluted with 200 mg SiC (200 μm). The catalysts were reduced *in situ* at 500 ºC (5 ºC/min, 2 h) under a flow of H_2/Ar (20/40 mL/min). Online gas chromatography analysis (C_1-C_{16}, CP sil-5, Varian) was performed during the FT reaction to determine the activity expressed as cobalt time yield (10^{-5} $mol_{CO}/g_{Co}/s$) and the C_1/C_{5+} selectivity (in wt%). The reported data were obtained after 15 h reaction time at CO conversions below 10%.

5.3 Results & Discussion

Ordered mesoporous silica supports with different pore sizes and a commercially available silica gel were used for this study of melt infiltration. A large pore MCM-41 was synthesized as well as SBA-15 at different crystallization temperatures to vary the pore diameters. The total microporous and mesoporous volume and pore diameters as characterized with N_2-physisorption are listed in the first two columns of Table 5.1.

The extent of pore loading of mesoporous silica with cobalt nitrate salt by melt infiltration was determined with DSC by quantifying the residual extraporous $Co(NO_3)_2 \cdot 6H_2O$ after melt infiltration. Ordered mesoporous silica S100 was mixed with increasing amounts of $Co(NO_3)_2 \cdot 6H_2O$, indicated by the mass loading in g/g_{S100}. The heat flows recorded during two subsequent heating cycles are shown in Figure 5.1. In the first heating cycle, a melting peak was observed at ~53 ºC for all mixtures, which corresponded to the melting of crystalline, extraporous $Co(NO_3)_2 \cdot 6H_2O$. For loadings above 1.4 g/g_{S100}, a melting peak remained at ~53 ºC in the second heating run indicating the presence of residual extraporous $Co(NO_3)_2 \cdot 6H_2O$. However, melting of $Co(NO_3)_2 \cdot 6H_2O$ at ~53 ºC vanished for loadings at 1.4 g/g_{S100} and lower, implying all salt had entered the pores. During the second heating run, melting was also observed between 5 and 20 ºC which was ascribed to melting of confined or intraporous $Co(NO_3)_2 \cdot 6H_2O$.

The energy released by the melting of residual $Co(NO_3)_2 \cdot 6H_2O$ at ~53 ºC in the second heating run was used to calculate the amounts of extraporous and intraporous cobalt nitrate. In Figure 5.2, the amount of intraporous salt in g/g_{S100} is plotted as a function of the amount of $Co(NO_3)_2 \cdot 6H_2O$ present. In these *in situ* melt infiltration experiments the pore-loading reached a plateau at 1.4 g/g_{S100} which corresponds to 22 wt% Co, indicating the pores were maximally filled. Samples prepared *ex situ* by melt infiltration at 60 ºC in an autoclave were also analyzed, to determine if the same maximum was obtained. The melting of surplus $Co(NO_3)_2 \cdot 6H_2O$ after the lab heat treatment was quantified during a single heating run with DSC. The pore-loading is plotted in Figure **5.2** and reached the same plateau at 1.4 g/g_{S100}. Furthermore, the degree of pore-filling could not be improved by additional mixing or remelting the

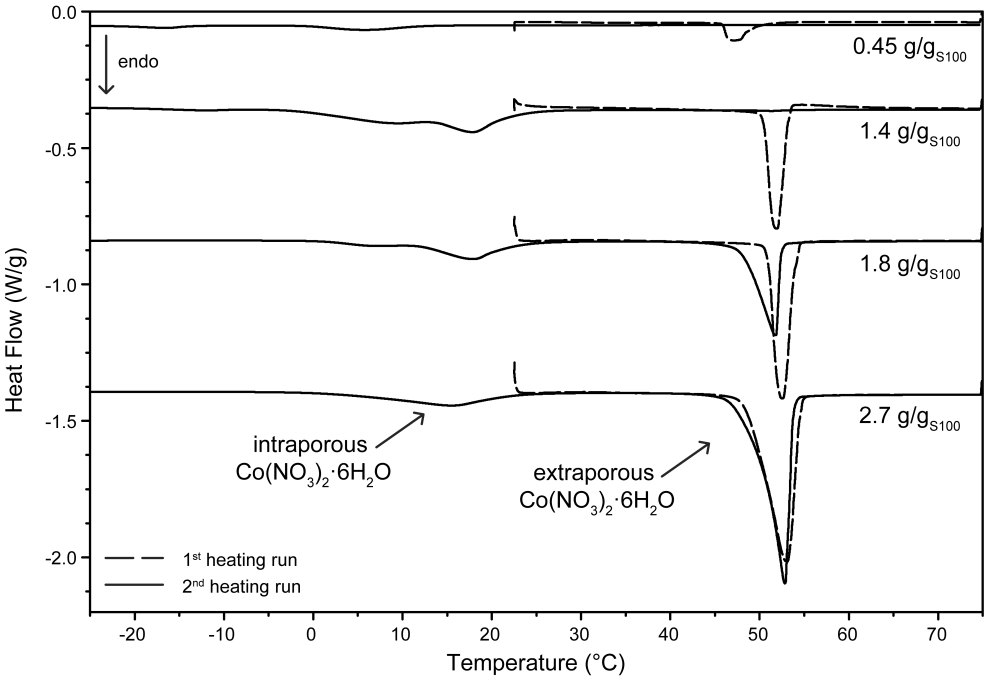

Figure 5.1. DSC thermograms of $Co(NO_3)_2 \cdot 6H_2O$/S100 physical mixtures with increasing amounts of $Co(NO_3)_2 \cdot 6H_2O$ (g/g_{S100}) recorded during heating at 2.5 ºC/min, thermograms are offset for clarity.

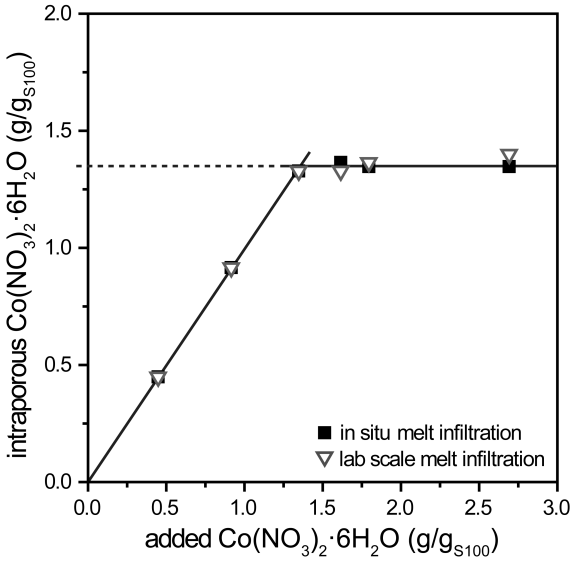

Figure 5.2. Amount of intraporous salt in $Co(NO_3)_2 \cdot 6H_2O$/S100 mixtures with increasing amounts of $Co(NO_3)_2 \cdot 6H_2O$ (g/g_{S100}) obtained with DSC after in situ melt infiltration and after melt infiltration in an autoclave at 60 ºC for 24 h. Lines are added as guide for the eye.

samples. Therefore, 1.4 g/g_{S100} or 22 wt% Co was the practical loading limit for S100. If the intraporous phase would be considered to be crystalline $Co(NO_3)_2 \cdot 6H_2O$ with a density of 1.88 g/cm^3 this would correspond to a filling of 75% of the pore volume.

The quantification of pore-filling was based on the melting enthalpy of residual extraporous $Co(NO_3)_2 \cdot 6H_2O$. However, wetting of the external surface of the mesoporous silica by extraporous $Co(NO_3)_2 \cdot 6H_2O$ caused broadening and a slight shift to lower temperatures of the melting peak at ~53 ºC. Nevertheless, since the mesoporous silica supports have low external surface areas, the effect on the calculated degree of pore-filling was expected to be within the error of the measurements and therefore neglected. Furthermore, the energy released in the first heating run was much lower than the enthalpy expected from melting of all present $Co(NO_3)_2 \cdot 6H_2O$. This was also observed for other infiltration experiments[47] and indicated that wetting and infiltration into the pores is an exothermic process occurring simultaneously with the endothermic melting of extraporous $Co(NO_3)_2 \cdot 6H_2O$.

To study the effect of pore size on melt infiltration and the extent of pore-filling, mesoporous silica supports with different pore radii and pore geometries were infiltrated with $Co(NO_3)_2 \cdot 6H_2O$ at 60 ºC for 24 h in an autoclave. The maximum loading of S100 corresponded to a theoretical pore volume filling of 75%, if the intraporous phase was considered to be crystalline $Co(NO_3)_2 \cdot 6H_2O$. Therefore, an intended loading of 75% V_{CoN}/V_p was used for the other supports. After melt infiltration, the pore-filling was studied with DSC during a single heating run from -90 to 75 ºC and Figure 5.3 shows the recorded thermograms. The maximum precursor loading for the different supports was calculated in $g/g_{support}$ and is listed in Table 5.1, together with the corresponding cobalt weight loadings. If the intraporous phase is considered to be crystalline $Co(NO_3)_2 \cdot 6H_2O$, the pore-filling ranged from 70% to 80% of the microporous and mesoporous volume and was slightly dependent on the pore diameters. For MCM, a melting peak remained at ~53 ºC corresponding to a practical filling lower than 75%. Since the specific melting enthalpy of extraporous $Co(NO_3)_2 \cdot 6H_2O$ is at least an order of magnitude larger than for intraporous $Co(NO_3)_2 \cdot 6H_2O$, the bulk melting peak appeared to be relatively large compared to other pore melting peaks. Nevertheless, the melting peak at ~53 ºC corresponds to only 7 wt% of the total amount of $Co(NO_3)_2 \cdot 6H_2O$ added. For all samples the weight loss determined with TGA confirmed the composition of $Co(NO_3)_2 \cdot 6H_2O$. In a control experiment all $Co(NO_3)_2 \cdot 6H_2O$ was dissolved after melt infiltration. The pore volume of MCM was recovered within 5% of the parent pore volume, indicating that the physical mixing and melt infiltration did not significantly damage the pore structure.

The melting transitions corresponding to intraporous $Co(NO_3)_2 \cdot 6H_2O$ were very broad and consisted of multiple peaks for the different supports, indicating

that inside the pores a single crystalline phase had not formed. They shifted to lower temperatures as the pore diameter decreased. Also, the melting enthalpy for intraporous $Co(NO_3)_2 \cdot 6H_2O$ decreased with decreasing pore diameter due an increasing ratio of $Co(NO_3)_2 \cdot 6H_2O$ in interacting with the silica pore wall with respect to the crystallizing intraporous $Co(NO_3)_2 \cdot 6H_2O$ phase.[48] A discrete melting transition is no longer observed for the MCM support since the pore diameter is only 3 times the $Co(NO_3)_2 \cdot 6H_2O$ crystal unit cell. These effects are known for confined fluids such as water or organic solvents.[49, 50] Based on the observations from melting of the intraporous salt, it can be concluded that the intraporous phase does not have a well-defined crystal structure and most likely does not have the density of crystalline $Co(NO_3)_2 \cdot 6H_2O$. Therefore, we propose that the extent of pore filling is actually close to 100% with a lower density disordered intraporous phase interacting with the silica surface.

The melting point of $Co(NO_3)_2 \cdot 6H_2O$ is close to its decomposition point, i.e. 55 ºC and 74 ºC respectively. Hence, decomposition could inhibit the melt infiltration process. To ensure ample time for the liquid phase to flow into the porous system, an equilibration step at 60 ºC was introduced and the effect of sample containment

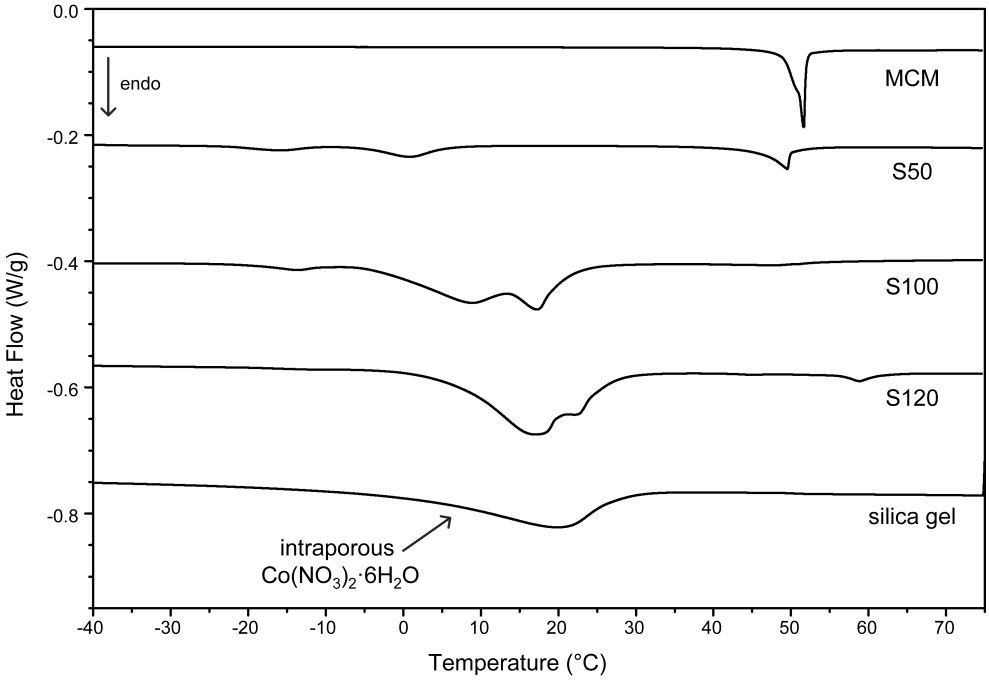

Figure 5.3. DSC thermograms of different silica supports melt infiltrated with $Co(NO_3)_2 \cdot 6H_2O$ (amount corresponding to practical filling limit S100) in an autoclave at 60 ºC for 24 h, recorded during heating at 2.5 ºC/min, thermograms are offset for clarity.

Table 5.1. Structural characterization of different mesoporous supports and $Co(NO_3)_2 \cdot 6H_2O$ pore-loading (g/gsupport) after melt infiltration at 60 ºC for 24 h in an autoclave and corresponding Co loading (wt%) of the reduced catalyst.

Support	pore diameter (nm)	V_p [a] (cm^3/g)	maximum loading	
			($g/g_{support}$)	(wt% Co)
MCM	4.5	0.87	1.2	19.5
S50	7.1	0.41	0.58	10.5
S100	11	0.96	1.4	22.1
S120	12	0.94	1.3	20.8
silica gel	12	0.80	1.1 [b]	18.2

[a] sum of microporous and mesoporous volume determined with t-plot method, [b] calculated from melt infiltration with 100% V_{CoN}/V_p.

was studied with XRD and TEM. Figure 5.4 shows the XRD patterns recorded after 12 hours at 60 ºC in an open crucible and in a closed autoclave. During open melt infiltration, $Co(NO_3)_2 \cdot 6H_2O$ had dehydrated to $Co(NO_3)_2 \cdot 4H_2O$. The sharp diffraction lines indicated that this phase was not confined within the pore system. After melt infiltration in the closed autoclave no crystalline phases were observed, but with TGA the presence of $Co(NO_3)_2 \cdot 6H_2O$ and a small amount of physisorbed water on the silica was confirmed.

XRD at low scattering angles was used to obtain complementary information to DSC on the pore-filling after open and closed melt infiltration. As shown in Figure 5.5, no diffraction lines were recorded after melt infiltration in an autoclave, but were present after open melt infiltration. Nevertheless, the long range ordering of the parent S100 was apparent in the physical mixture (data not shown) as well as after

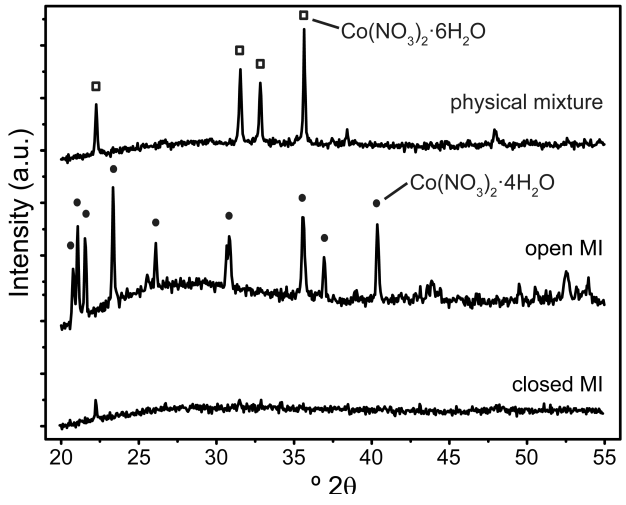

Figure 5.4. XRD patterns of $Co(NO_3)_2 \cdot 6H_2O$ (1.4 g/gS100) physical mixture and after open and closed melt infiltration at 60 ºC for 12 h.

closed melt infiltration and calcination in N_2 flow. Therefore, the hexagonal pore ordering of the SBA-15 support was not destroyed by the melt infiltration procedure. Rather, the loss of diffraction lines after closed melt infiltration was caused by filling of the pores with $Co(NO_3)_2 \cdot 6H_2O$. The diffraction lines for ordered mesoporous silica originate from the difference in electron density of the silica matrix and the contents of the pores, i.e. air in case of the parent material and the calcined sample. When the pores are filled with a material of comparable electron density to the silica matrix, e.g. amorphous $Co(NO_3)_2 \cdot 6H_2O$, the contrast diminishes and diffraction of the ordered pore system can no longer be observed. For that reason it can be concluded that the pores of S100 after melt infiltration with $Co(NO_3)_2 \cdot 6H_2O$ in a closed vessel are filled, such that there is no long range ordering of empty pores. The clear diffraction pattern after open melt infiltration indicated that a fraction of the pores remained empty. This is in line with the formation of extraporous tetra hydrate cobalt nitrate observed in XRD at higher angles.

The distribution of Co_3O_4 over the support particles after calcination in a N_2 flow was visualized with TEM and could be correlated to the precursor distribution after open and closed melt infiltration. Figure 5.6A shows a typical image for Co_3O_4/S100 infiltrated with cobalt nitrate in an autoclave. It shows aggregates of pluglike Co_3O_4 particles present in several neighboring pores (*vide infra*). These aggregates were observed throughout the support particle. Even though the distribution of Co_3O_4 over the support particle was inhomogeneous, it was all intraporous after calcination and all the support particles contained similar loadings. Therefore, the precursor had been present as intraporous phase in all the support particles prior to calcination.

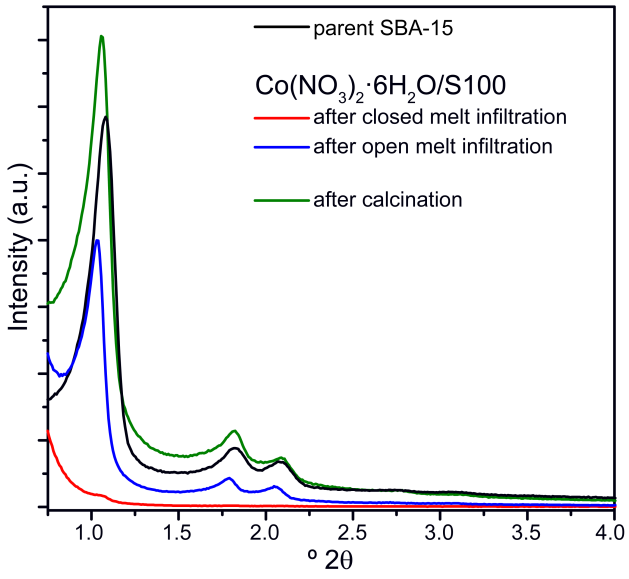

Figure 5.4. XRD patterns of $Co(NO_3)_2 \cdot 6H_2O$ (1.4 g/gS100) physical mixture and after open and closed melt infiltration at 60 ºC for 12 h.

Figure 5.6B and C show two micrographs of Co_3O_4/S100 prepared via open melt infiltration. In Figure 5.6B, a support particle is shown with intraporous aggregates similar to Figure 5.6A. However, also some extraporous aggregates were observed, which are indicated by the arrows in Figures 6B and 6C. In addition, Figure 5.6C shows some empty support particles, which illustrate the large variation of Co_3O_4 loading over the support particles in the sample. It suggested that the precursor had not infiltrated all the support particles and that open melt infiltration led to an inhomogeneous precursor distribution over the support. Therefore, to obtain a homogeneous distribution of the metal oxide over the support after calcination, decomposition of the precursor during melt infiltration should be prevented. Please note that although NO/N_2 calcination leads to high metal oxide dispersions (*vide infra*) it does not bring about redistribution of previously non-uniform cobalt nitrate distributions.

To prepare Co/SiO_2 catalysts for the Fischer Tropsch synthesis, different supports were melt infiltrated with $Co(NO_3)_2 \cdot 6H_2O$ at 60 ºC for 24 hours in an autoclave. After calcination in a N_2 flow, the Co_3O_4 loaded catalysts were characterized with XRD and TEM. The metal loadings ranged from 10 – 22 wt% depending on the support pore volume. The volume-average Co_3O_4 crystallite sizes, calculated with the Scherrer equation, were taken as a measure for the dispersion and are listed in Table 5.2. Their sizes ranged from 4 – 10 nm and generally followed the support pore diameters or were slightly smaller than the pore diameter for the larger pore systems. This showed that the average crystallite sizes could be well controlled through the mesoporous supports as was also reported for impregnated systems.[40] Also on the

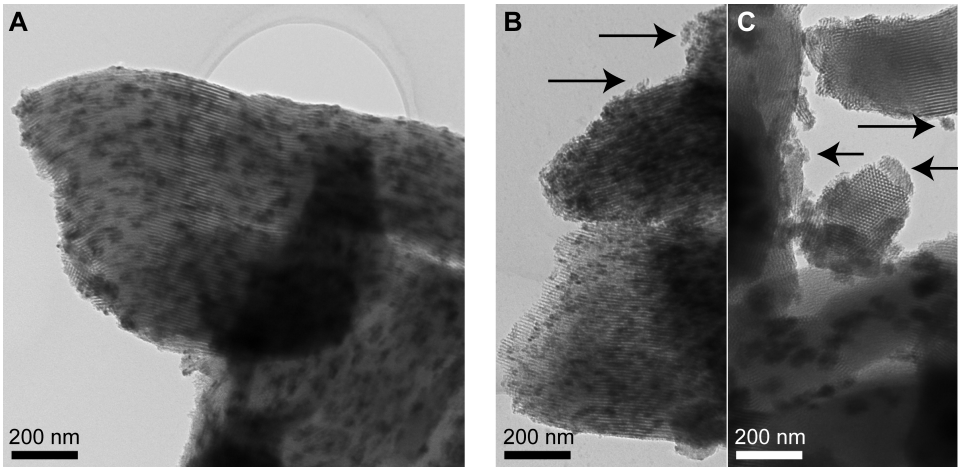

Figure 5.6. TEM micrographs of Co_3O_4/S100 after calcination in N_2 prepared via closed melt infiltration (A) and prepared via open melt infiltration (B and C). Arrows indicate extraporous Co_3O_4.

industrial silica gel support, highly dispersed Co_3O_4 was obtained, even though this support has a much broader pore size distribution than the ordered supports. Additional control over the Co_3O_4 crystallite size was obtained by using the modified calcination procedure in 1% NO/N_2,[40, 43] which resulted in a decrease of the average crystallite size from 9.5 nm to 4.3 nm on S100.

The Co_3O_4 nanoparticle distribution over the support was visualized with TEM. The high metal loadings hindered accurate particle size analysis with TEM, however, Co_3O_4 crystallites were typically observed confined within the pore system with sizes in the same range as the pore diameter. Figure 5.7 shows typical micrographs for Co_3O_4/S100 obtained via melt infiltration in an autoclave after calcination in N_2 (Figure 5.7A) or in 1% NO/N_2 (Figure 5.7B). N_2-calcination led to the formation of pluglike nanoparticles inside the pore system, which formed aggregates that spanned multiple pores. The formation of these pluglike nanoparticles after calcination in N_2 was visualized earlier with electron tomography for NiO on SBA-15[51] and similar intraporous aggregates have often been observed for Co/SiO_2 systems prepared via impregnation and calcination.[52-54] Calcination in 1% NO/N_2 led to the formation of individual Co_3O_4 nanoparticles, which has also been observed for NiO/SBA-15 and Co_3O_4/SBA-15 prepared via impregnation.[40, 43] This confirms that after melt infiltration the Co_3O_4 dispersion and distribution is affected strongly by the calcination conditions as well as confinement. The possibility to tune the nanoparticle size and distribution after melt infiltration is essential for its application in supported catalyst preparation.

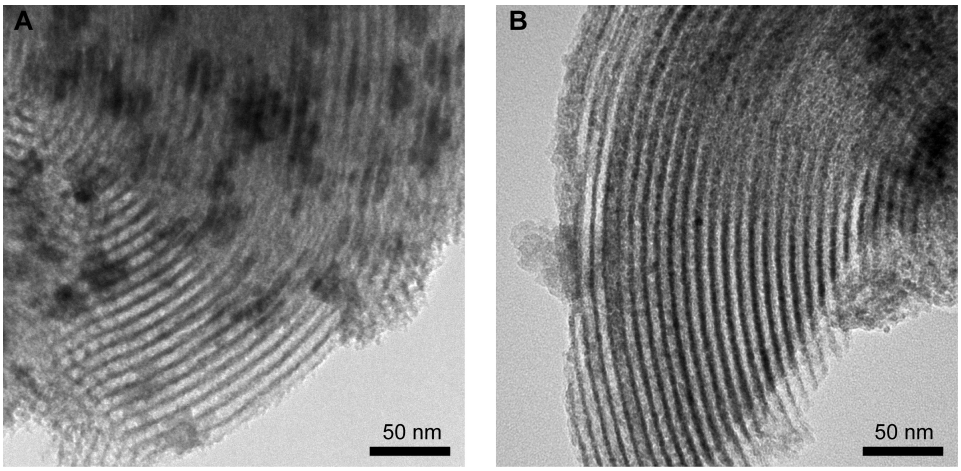

Figure 5.7. TEM micrographs of Co_3O_4/S100 prepared via melt infiltration and calcination (A) in a flow of N_2 or (B) a flow of 1 % v/v NO/N_2.

Table 5.2. Characterization and catalytic activity for Fischer Tropsch synthesis of catalysts prepared via melt infiltration in an autoclave at 60 ºC for 24 h and calcination in N_2.

Support	Co loading (wt%)	pore diameter (nm)	Co_3O_4 crystallite size[a] (nm)	CTY[b] (10^{-5} $mol_{CO}/g_{Co}/s$)	selectivity C_1/C_{5+} (wt%)
MCM	19.9	4.5	4.9	1.0	35/39
S50	10.5	7.1	7.8	1.8	29/44
S100	21.7	11	9.5	1.3	27/45
S120	21.2	12	8.3	2.7	28/43
silica gel	17.6	12	8.0	2.1	22/54
S100[c]	21.7	11	4.3	3.0	34/36

[a] determined with XRD line broadening analysis after calcination in N_2 flow, [b] catalytic properties determined after 15 h time on stream, [c] calcined in 1 % v/v NO/N_2 flow.

The activity of the catalysts for the Fischer Tropsch synthesis was tested after *in situ* reduction at 500 ºC at 220 ºC and 1 bar. The obtained cobalt weight normalized activities (CTY) and selectivity are listed in Table 5.2. For the N_2-calcined samples, moderate (MCM, S50) to high activities (S120) were observed, as compared to the most active Co/CNF catalyst (CTY reported 3.5 10^{-5} $mol_{CO}/g_{Co}/s$).[55, 56] For the Co/S100 N_2-calcined catalyst a dispersion of 7.2% was measured with chemisorption. This corresponds to a TOF of 11 $*10^{-3}$ s^{-1}, which is the value found for Co/CNF catalysts with particle sizes larger than 6 nm.[55, 56] Based on the different pore diameters, pore geometries and Co_3O_4 average crystallite sizes, differences in the observed CTY are expected. Previous XANES analysis of a Co/SiO_2 catalyst with 5 nm Co particles has shown that a reduction degree of 90% is obtained after reduction at 450 ºC and 2 hours reaction time.[57] The catalysts presented in this chapter were reduced at 500 ºC and had degrees of reduction close to 100%. Nevertheless, the catalytic activity can be optimized by changing for example the calcination conditions, which was shown recently by den Breejen *et al*.[57] Indeed, the Co/S100 NO calcined catalyst showed a much higher activity than its N_2 calcined counterpart, due to less agglomeration, a higher dispersion and a narrow particle size distribution. With TEM sintering or redistribution of the active phase upon reduction and Fischer Tropsch synthesis were excluded (Appendix B, Figure B1). All catalysts showed a high methane selectivity, with the lowest value observed for the industrial silica support. The selectivity is mainly related to the low pressure applied, while also pore geometry can play a role. Optimization of support morphology or addition of promoters could be used to improve the selectivity.[53, 57]

5.4 Conclusions

We have studied in depth the physico-chemical aspects of melt infiltration for preparation of supported catalysts. To establish the effectiveness of melt infiltration as a precursor loading method, infiltration of mesoporous silica supports with $Co(NO_3)_2 \cdot 6H_2O$ was followed *in situ* with differential scanning calorimetry. The melting point depression of intraporous $Co(NO_3)_2 \cdot 6H_2O$ allowed detection of residual extraporous $Co(NO_3)_2 \cdot 6H_2O$. Maximum precursor loadings were expressed in $g/g_{support}$ and corresponded to 70 – 80% of the pore volume, if the intraporous phase was considered to be crystalline $Co(NO_3)_2 \cdot 6H_2O$. Nevertheless, after melt infiltration at 60 ºC in a closed vessel, no crystalline phases could be detected with XRD diffraction. In addition, the diffraction lines from the ordered mesoporous support at low scattering angles had disappeared. This led to the conclusion that the pores of the support were actually completely filled with an amorphous $Co(NO_3)_2 \cdot 6H_2O$ phase with a lower density than crystalline $Co(NO_3)_2 \cdot 6H_2O$. When the $Co(NO_3)_2 \cdot 6H_2O$ precursor decomposed by dehydration to $Co(NO_3)_2 \cdot 4H_2O$ during the infiltration process, melt infiltration was partly inhibited and an inhomogeneous distribution of the precursor over the support resulted.

Finally, melt infiltration was applied to prepare a series of Fischer Tropsch catalysts with controllable particles sizes and high metal loadings. By using supports with different pore diameters, Co_3O_4 crystallite sizes ranging from 4 to 10 nm at Co loadings ranging from 10 - 22 wt% were obtained. After calcination in N_2 flow, pluglike nanoparticles were obtained, while calcination in a gas flow of 1% NO/N_2 led to the formation of highly dispersed individual Co_3O_4 nanoparticles. The catalysts showed high activity for the Fischer Tropsch synthesis, with the highest activity observed for the catalyst calcined in NO/N_2 flow.

Acknowledgements

Johan den Breejen (Utrecht University) is acknowledged for sharing his expertise on supported cobalt catalysts for the Fischer-Tropsch reaction and help with the catalytic testing. Dirkjan Verdoes (Utrecht University) is thanked for his exploratory research on melt infiltration that formed the basis for this manuscript. The authors acknowledge Hans Meeldijk for performing TEM measurements and Mies van Steenbergen and Herre Talsma for providing access to thermal analyses equipment and useful discussions.

References

[1] J. R. Regalbuto, ed. *Catalyst Preparation - Science and Engineering*. 2007, CRC Press: Boca Raton.
[2] K. P. de Jong, ed. *Synthesis of Solid Catalysts*. 2009, Wiley-VCH: Weinheim.
[3] A. J. van Dillen, R. J. A. M. Terorde, D. J. Lensveld, J. W. Geus and K. P. de Jong, *J. Catal.* **2003**, *216*, 257.
[4] A. Lekhal, B. J. Glasser and J. G. Khinast, *Chem. Eng. Sci.* **2004**, *59*, 1063.
[5] J. A. Bergwerff, T. Visser, B. R. G. Leliveld, B. D. Rossenaar, K. P. de Jong and B. M. Weckhuysen, *J. Am. Chem. Soc.* **2004**, *126*, 14548.
[6] M. Che, Z. X. Cheng and C. Louis, *J. Am. Chem. Soc.* **1995**, *117*, 2008.
[7] P. Burattin, M. Che and C. Louis, *J. Phys. Chem. B* **1999**, *103*, 6171.
[8] M. K. van der Lee, A. J. van Dillen, J. H. Bitter and K. P. de Jong, *J. Am. Chem. Soc.* **2005**, *127*, 13573.
[9] M. Hartmann, A. Poppl and L. Kevan, *J. Phys. Chem.* **1996**, *100*, 9906.
[10] M. Schreier and J. R. Regalbuto, *J. Catal.* **2004**, *225*, 190.
[11] L. Jiao and J. R. Regalbuto, *J. Catal.* **2008**, *260*, 329.
[12] A. T. Bell, *Science* **2003**, *299*, 1688.
[13] G. A. Somorjai, F. Tao and J. Y. Park, *Top. Catal.* **2008**, *47*, 1.
[14] P. Serp, P. Kalck and R. Feurer, *Chem. Rev.* **2002**, *102*, 3085.
[15] J. L. Lu and P. C. Stair, *Angew. Chem., Int. Ed.* **2010**, *49*, 2547.
[16] C. H. Tu, A. Q. Wang, M. Y. Zheng, X. D. Wang and T. Zhang, *Appl. Catal. A-Gen.* **2006**, *297*, 40.
[17] M. G. Cutrufello, E. Rombi, C. Cannas, M. Casu, A. Virga, S. Fiorilli, B. Onida and I. Ferino, *J. Mater. Sci.* **2009**, *44*, 6644.
[18] B. Mile, D. Stirling, M. A. Zammitt, A. Lovell and M. Webb, *J. Catal.* **1988**, *114*, 217.
[19] J. Panpranot, J. G. Goodwin and A. Sayari, *Catal. Today* **2002**, *77*, 269.
[20] J. S. Girardon, A. S. Lermontov, L. Gengembre, P. A. Chernavskii, A. Griboval-Constant and A. Y. Khodakov, *J. Catal.* **2005**, *230*, 339.
[21] E. Marceau, M. Che, J. Cejka and A. Zukal, *ChemCatChem* **2010**, *2*, 413.
[22] W. Yue and W. Z. Zhou, *Chem. Mater.* **2007**, *19*, 2359.
[23] C. F. Zhou, Y. M. Wang, Y. Cao, T. T. Zhuang, W. Huang, Y. A. Chun and J. H. Zhu, *J. Mater. Chem.* **2006**, *16*, 1520.
[24] J. K. Shon, S. S. Kong, Y. S. Kim, J. H. Lee, W. K. Park, S. C. Park and J. M. Kim, *Micropor. Mesopor. Mat.* **2009**, *120*, 441.
[25] Y. M. Wang, Z. Y. Wu, H. J. Wang and J. H. Zhu, *Adv. Funct. Mater.* **2006**, *16*, 2374.
[26] M. B. Zheng, J. Cao, S. T. Liao, J. S. Liu, H. Q. Chen, Y. Zhao, W. J. Dai, G. B. Ji, J. M. Cao and J. Tao, *J. Phys. Chem. C* **2009**, *113*, 3887.
[27] Y. M. Wang, Z. Y. Wu and J. H. Zhu, *J. Solid State Chem.* **2004**, *177*, 3815.
[28] F. S. Xiao, S. Zheng, J. M. Sun, R. B. Yu, S. L. Qiu and R. R. Xu, *J. Catal.* **1998**, *176*, 474.
[29] F. Schuth, A. Wingen and J. Sauer, *Micropor. Mesopor. Mat.* **2001**, *44*, 465.
[30] E. Iglesia, S. L. Soled, J. E. Baumgartner and S. C. Reyes, *J. Catal.* **1995**, *153*, 108.
[31] F. Schuth, *Angew. Chem., Int. Ed.* **2003**, *42*, 3604.
[32] W. B. Yue, A. H. Hill, A. Harrison and W. Z. Zhou, *Chem. Comm.* **2007**, 2518.
[33] S. W. Lai and D. D. L. Chung, *J. Mater. Sci.* **1994**, *29*, 3128.
[34] J. W. Liu, Z. X. Zheng, J. M. Wang, Y. C. Wu, W. M. Tang and J. Lu, *J. Alloys Compd.* **2008**, *465*, 239.
[35] P. E. de Jongh, R. W. P. Wagemans, T. M. Eggenhuisen, B. S. Dauvillier, P. B. Radstake, J. D. Meeldijk, J. W. Geus and K. P. de Jong, *Chem. Mater.* **2007**, *19*, 6052.
[36] M. Brun, A. Lallemand, J.-F. Quinson and C. Eyraud, *Thermochim. Acta* **1977**, *21*, 59.
[37] A. Schreiber, I. Ketelsen and G. H. Findenegg, *Phys. Chem. Chem. Phys.* **2001**, *3*, 1185.
[38] T. M. Eggenhuisen, M. J. van Steenbergen, H. Talsma, P. E. de Jongh and K. P. de Jong, *J. Phys. Chem. C* **2009**, *113*, 16785.
[39] D. Vargas-Florencia, O. Petrov and I. Furo, *J. Phys. Chem. B* **2006**, *110*, 3867.
[40] M. Wolters, I. C. A. Contreras Andrade, P. Munnik, J. H. Bitter, P. E. de Jongh and K. P. de Jong, *Stud. Surf. Sci. Catal.* **2010**, *175*, 69.
[41] D. Y. Zhao, Q. S. Huo, J. L. Feng, B. F. Chmelka and G. D. Stucky, *J. Am. Chem. Soc.* **1998**, *120*, 6024.
[42] C. F. Cheng, W. Z. Zhou, D. H. Park, J. Klinowski, M. Hargreaves and L. F. Gladden, *J. Chem. Soc.,*

Faraday T **1997**, *93*, 359.
[43] J. R. A. Sietsma, J. D. Meeldijk, J. P. den Breejen, M. Versluijs-Helder, A. J. van Dillen, P. E. de Jongh and K. P. de Jong, *Angew. Chem., Int. Ed.* **2007**, *46*, 4547.
[44] B. C. Lippens and J. H. de Boer, *J. Catal.* **1965**, *4*, 319.
[45] M. Jaroniec, M. Kruk, J. P. Olivier and S. Koch, *Proceedings of COPS-V, Heidelberg, Germany* **1999**.
[46] J. Guion, J. D. Sauzade and M. Laugt, *Thermochim. Acta* **1983**, *67*, 167.
[47] P. Adelhelm, J. B. Gao, M. H. W. Verkuijlen, C. Rongeat, M. Herrich, P. J. M. van Bentum, O. Gutfleisch, A. P. M. Kentgens, K. P. de Jong and P. E. de Jongh, *Chem. Mater.* **2010**, *22*, 2233.
[48] K. Morishige and K. Nobuoka, *J. Chem. Phys.* **1997**, *107*, 6965.
[49] S. Kittaka, S. Ishimaru, M. Kuranishi, T. Matsuda and T. Yamaguchi, *Phys. Chem. Chem. Phys.* **2006**, *8*, 3223.
[50] S. Jahnert, F. V. Chavez, G. E. Schaumann, A. Schreiber, M. Schonhoff and G. H. Findenegg, *Phys. Chem. Chem. Phys.* **2008**, *10*, 6039.
[51] J. R. A. Sietsma, H. Friedrich, A. Broersma, M. Versluijs-Helder, A. J. van Dillen, P. E. de Jongh and K. P. de Jong, *J. Catal.* **2008**, *260*, 227.
[52] J. van der Meer, I. Bardez, F. Bart, P. A. Albouy, G. Wallez and A. Davidson, *Micropor. Mesopor. Mat.* **2009**, *118*, 183.
[53] G. Prieto, A. Martinez, R. Murciano and M. A. Arribas, *Appl. Catal.- A Gen.* **2009**, *367*, 146.
[54] F. Jiao and H. Frei, *Angew. Chem., Int. Ed.* **2009**, *48*, 1841.
[55] G. L. Bezemer, J. H. Bitter, H. P. C. E. Kuipers, H. Oosterbeek, J. E. Holewijn, X. D. Xu, F. Kapteijn, A. J. van Dillen and K. P. de Jong, *J. Am. Chem. Soc.* **2006**, *128*, 3956.
[56] J. P. den Breejen, P. B. Radstake, G. L. Bezemer, J. H. Bitter, V. Froseth, A. Holmen and K. P. de Jong, *J. Am. Chem. Soc.* **2009**, *131*, 7197.
[57] J. P. den Breejen, J. R. A. Sietsma, H. Friedrich, J. H. Bitter and K. P. de Jong, *J. Catal.* **2010**, *270*, 146.

Chapter 6

Quantitative Assessment of Pore Blockage in Supported Catalysts: Comparing Differential Scanning Calorimetry and Physisorption

Abstract

The quantification of blockages induced by nanoparticles in supported catalysts was assessed using nitrogen physisorption and two alternative techniques: differential scanning calorimetry (DSC) of the freezing and melting of confined water and physisorption of argon at 77 K. A set of well-defined model catalyst nanostructures with varying degrees of pore blockage was synthesized using ordered mesoporous supports and different nanoparticle sizes. DSC and argon physisorption both provided information which could not be accessed by standard nitrogen physisorption and are advocated for the analysis of complex porous structures.

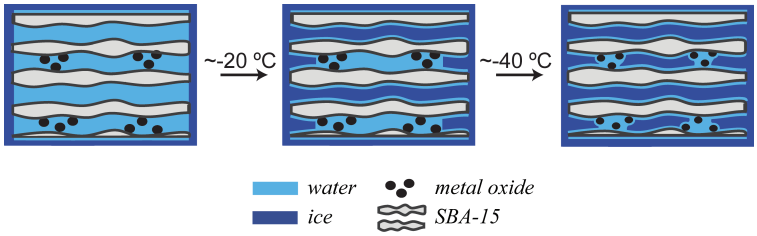

6.1 Introduction

Mesoporous oxides are used for a wide variety of applications, such as chromatography, adsorbents, drug delivery systems, catalysts or as catalytic supports.[1-6] The nature of the porosity is, understandably, of crucial importance. Parameters such as pore volume, surface area and pore diameter are routinely determined using nitrogen physisorption.[7] However, introduction of a guest phase, which can be for example nanoparticles, polymers, drug molecules or organometallic complexes, complicates analysis of the porosity. Specifically, the degree of pore blockage and size of constrictions are essential parameters as they indicate preservation of pore accessibility upon guest phase loading[8, 9] and the effectiveness of grafting or infiltration[10-12] Furthermore, pore constrictions with different sizes are purposely introduced in mesoporous silica to explore advantageous structural properties, such as improved mechanical stability.[13-15] However, pore blockage can also indicate pore destruction[16] or can have detrimental effects on, for example, the catalytic activity by diffusion limitations, altered condensation properties of gasses,[17] or size-selective mass transportation.[18, 19]

Synthesis of supported catalysts with controlled particle size and distribution is a holy grail for the field of heterogeneous catalysis.[20-24] For these materials, the degree of pore blockage contains valuable information on the size and 3-dimensional distribution of the catalyst particles over the support. Microscopic details on particle size and location are commonly obtained by electron microscopy techniques. For example, electron tomography allows visualization and quantification of nanoparticle distribution in porous supports on a nanometer scale in three dimensions.[25-29] Average crystallite sizes are determined from XRD line broadening analysis which, related to the support pore diameter, gives an indication of the crystallites location. However, particle size distributions or particle aggregate sizes are hardly detected by XRD. Small angle scattering techniques were recently used to provide quantitative information on average sizes and location of guest phases present in porous systems, but have not yet been applied to study supported nanoparticles.[30, 31] A proper structural characterization requires a toolbox comprising bulk statistical techniques and microscopic analyses. Bulk statistical information on porosity is classically obtained from nitrogen physisorption. Landau *et al.* proposed using the normalized surface area from nitrogen physisorption to identify four different particle agglomeration and distribution types.[32, 33] Furthermore, a two-step desorption in the hysteresis loop has been recognized as indicator for nanoparticles induced constrictions.[25, 34, 35] Nevertheless, the qualitative and quantitative assessment of pore blockage by interpretation of nitrogen physisorption isotherm of supported catalysts is not straightforward.

We discuss in this chapter two alternative techniques, i.e. differential scanning calorimetry (DSC) of the freezing and melting of confined water and physisorption of Ar at 77 K and compare their capabilities to the current standard, nitrogen physisorption. Gas desorption is controlled by the curvature (r) of the liquid meniscus in direct contact with the vapor phase and is related to the relative pressure (p/p_0) as described by the Kelvin equation (eq. 1),

$$ln(p/p_0) = \frac{C_K}{r} \quad , C_K = \frac{2\gamma_{lg}\nu_l}{RT} \qquad \text{eq. 1}$$

where γ_{lg} is the liquid-gas interfacial tension, ν_l is the molar volume, R the gas constant and T the absolute temperature.[7] In analogue, the freezing of a confined liquid is controlled by the curvature of the interface of the liquid and a heterogeneous nucleation source, such as a large crystal.[36] For water wetting a silica mesopore, the resulting freezing point depression (ΔT) can be described by the simplified Gibbs-Thomson equation (eq. 2),

$$\Delta T = \frac{C_{GT}}{r} \quad , C_{GT} = \frac{2T_0\gamma_{sl}\nu_l}{\Delta H_f} \qquad \text{eq. 2}$$

where γ_{sl} is the solid-liquid interfacial tension for complete wetting of the silica wall with water having a contact angle $\theta = 0º$, ν_l is the molar volume, T_0 the bulk transition temperature and ΔH_f the enthalpy of fusion.[36, 37] An increase of the curvature of the liquid-gas or liquid-solid interface by narrowed pore entrances causes a delay in both phase transitions. Whenever this delay is controlled by the entrance size, this is indicated by the term “pore blockage”. However, the sensitivity of gas desorption towards entrance sizes is limited by the spontaneous desorption of the adsorptive below certain relative pressures, referred to as “cavitation”. Pore entrances with sizes causing desorption below this limit cannot be distinguished. Water is known to spontaneously freeze by homogeneous nucleation at temperatures of -39 ºC and below,[38] which sets the lower limit for the range of detectable pore entrance sizes by DSC.

A liquid Ar meniscus remains stable at lower relative pressures as compared to N_2, which is an advantage for the analysis of pore constrictions by the gas desorption isotherm.[39-41] For example, plugged hexagonal silica showed full cavitation in nitrogen physisorption, while only partial blockage was found with argon physisorption at 77 K.[13, 42, 43] DSC of confined water, also referred to as thermoporometry is considered to provide similar data as nitrogen physisorption,[44] but it allows analysis of hydrated structures avoiding porosity changes due to drying effects.[45-47] Furthermore, it can also provide insight into pore connectivity, such as the presence of U-shaped pores

in modified SBA-15,[48] isolated cavities in zeolites,[49] or for the characterization of cagelike silica materials.[50, 51]

Here we use well-defined systems to explore the applicability of argon physisorption at 77 K and for the first time DSC of confined water for pore blockage characterization. A set of nickel hydrogenation catalysts with high relevance to the catalysis community was synthesized by using ordered mesoporous silica as supports with different pore diameters and NiO nanoparticles with different sizes. The varying degree of pore blockage was correlated to the nanoparticle distribution in the supported catalysts.

6.2 Experimental Methods

6.2.1 Materials

Block copolymer P123, tetraethylorthosilicate (TEOS, 98%), hydrochloric acid (HCl, 37 wt%), cetyltrimethylammoniumbromide (CTAB), tetramethylammoniumhydroxide (TMAOH) obtained from Sigma Aldrich and $Ni(NO_3)_2 \cdot 6H_2O$ (99%, Acros) were used as obtained.

6.2.2 Ordered mesoporous silica synthesis

SBA-15 was synthesized according to the procedure described by Zhao *et al*.[52] Different hydrothermal treatment temperatures were used to obtain supports with different pore diameters. A gel with a molar composition of 1 SiO_2 : 0.0143 P123 : 5.05 HCl : 144 H_2O with TEOS as silica source was aged under stirring at 40 °C for 20 h, after which it was treated at 50, 60 or 100 °C for 48 h under static conditions. The precipitated white product was filtered, washed, dried at 120 °C and subsequently calcined at 550 °C for 6 hours (heating rate 1 °/min). The supports are denoted by S, for SBA-15, and their expected relative pore size small, medium and large: SS (50 ºC), SM (60 ºC) and SL (100 ºC).

An MCM-41 with relatively large pores, was synthesized following the procedure described by Cheng *et al*. using a synthesis gel with a molar composition of 1 SiO_2 : 0.25 CTAB : 0.20 TMAOH : 40 H_2O with Aerosil 380 as silica source.[53] The gel was stirred for 1 hour at 40 °C after which it was kept static for 20 hours and subsequently heated at 150 °C for 48 hours in a teflon-lined steel autoclave. The product was filtered, washed extensively and dried at 60 °C for 12 hours and 120 °C for 9 hours. The product was calcined at 550 °C for 8 hours (heating rate 1 °/min). The support is denoted as MCM.

6.2.3 NiO catalyst synthesis

NiO catalysts were prepared via incipient wetness impregnation with $Ni(NO_3)_2$ (aq). The support was dried at ~80 ºC under dynamic vacuum for approximately 30 min and was impregnated with a saturated aqueous $Ni(NO_3)_2$ solution (4.3 M). The impregnated supports were dried overnight in a preheated oven at 120 ºC. Small, uniformly sized nanoparticles were obtained by decomposition of the hydrated nickel nitrate precursor in a flow of 1% NO/N_2,[22, 24, 54] while a flow of air induced the formation of larger, pluglike nanoparticles.[35, 54-56] Thermal decomposition or calcination was performed in a fluidized bed reactor at 350 ºC for 1 hour (heating rate 1 ºC/min) under either a flow of 1% NO/N_2 or air at 100 mL / 100 mg catalyst. The catalysts contained a loading of 12, 18 and 23 wt% NiO for SS, SM and SL respectively and 24 wt% NiO for MCM. Catalysts calcined in a flow of NO/N_2 contained nanoparticles and are denoted by the support followed by –part: SX-part or MCM-part, catalysts containing larger, rodlike NiO particles are denoted SX-rod or MCM-rod.

6.2.4 Catalyst characterization

XRD patterns were recorded between 15 and 60 º2θ with using Co-$K_{\alpha 12}$ radiation (λ = 1.790 Å) on a Bruker-AXS D2 Phaser X-ray Diffractometer. The volume averaged NiO crystallite size was determined using line broadening analysis by a fitting procedure in Eva2 software (Bruker AXS) and the Scherrer equation with a shape factor k = 0.9. Transmission electron microscopy was performed on a Tecnai 12 microscope operated at 120 keV. Electron tomography was performed on a Tecnai 20 microscope equipped with a LaB_6 electron source operated at 200 kV. Tilt series were recorded from ±75º at 2º tilt increments and TEM images were acquired at a nominal magnification of 29k with a 2k x 2k TVIPS CCD camera. Alignment of the TEM tilt series and 3D reconstruction was performed in IMOD software[57] and using binning by 2 resulted in a pixel size of 0.54 nm.

6.2.5 Physisorption

Physisorption measurements were performed with N_2 or Ar at 77 K (-196 ºC) using a Micromeritics Tristar 3000. The samples were dried prior to the measurement under an N_2 flow at 250 °C for 16 hours. From nitrogen physisorption, the total pore volume (V_{tot}) was defined as the single point pore volume at p/p_0 = 0.95. The microporous volume (V_{micro}) was determined using the t-plot method.[58] The pore size distribution was calculated from the adsorption branch of the N_2 isotherm by a NL-DFT method designed for cylindrical pores.[59] The maximum of the pore size distribution was considered as the average mesopore diameter. The pore size distribution from the

N_2 desorption isotherm was calculated using the BJH method using the Harkins-Jura reference curve and KJS correction.[60] To calculate the pore size distribution from the Ar desorption branch, the corrected BJH model as determined by Kruk *et al.* was used.[61] The reported thickness reference curve for Ar at 77 K on a macroporous silica (Li-Chrospher Si-1000) was found to be accurately represented in the relative pressure range of 0.10 to 0.95 by the following form of the Harkins-Jura equation (eq. 3),

$$t\,(p/p_0)\,[nm] = \left(\frac{0.1605}{0.1156 - \log(-0.06199 + p/p_0)}\right)^{0.5085} \qquad \text{eq. 3}$$

where t is the statistical film thickness in nm.

6.2.6 Differential scanning calorimetry

The freezing and melting behavior of water confined in the empty mesoporous silica supports and catalysts was recorded using differential scanning calorimetry (DSC, TA instruments Q2000). The temperature and heat flow were calibrated using a certified indium sample. Measurements were performed in the range of -70 ºC – 25 ºC under a flow of 50 mL/min N_2. 3-5 mg of solids was mixed with a 2-fold excess of H_2O (Millipore, R = 18 MΩcm) based on the pore volume determined by nitrogen physisorption. The impregnated sample was hermetically sealed in an aluminum pan (40 µL, Tzero, TA Instruments) to prevent water evaporation during the measurement. A heating/cooling rate of 5 ºC/min and 5 minutes isothermal periods at -70 ºC were used for all measurements. The enthalpy of melting and freezing were integrated using linear baselines in Universal Analysis 2000 software (TA Instruments). The amount of water and support or catalyst was determined afterwards using thermogravimetric analysis (TGA, TA Instruments Q50). The weight loss was measured after heating at 150 ºC for 15 min (heating rate 10 ºC/min). From DSC and TGA the amounts of extraporous and intraporous water were calculated. The amount of extraporous water was calculated from the DSC thermogram by the enthalpy of water melting at 0 ºC ($\Delta H_{m,\,bulk}$) and the specific melting enthalpy of water (ΔH_f = 334 J/g). The amount of pore water as well as the degree of pore filling (f) were determined as follows: $m_{pore,\,water} = m_{total,\,water\,TGA} - (\Delta H_{m,\,bulk}/\Delta H_f)$, $f = (m_{pore\,water} / \rho_{H2O}) / (m_{solid,\,TGA} * V_{tot})$.

6.2.7 Pore blockage quantification

The percentage of blocked mesopores in the catalysts was determined using DSC and gas sorption by quantification of the open mesopore volume with respect to the total accessible mesopore volume. With DSC, open pores in catalysts were defined as pores where water crystallizes by heterogeneous nucleation from extraporous bulk ice

at the same temperature as water confined in the parent support. This was quantified by selectively freezing this water and comparing the released melting enthalpy at the mesopore melting temperature to the total enthalpy released after the sample had been cooled to -70 ºC and all water confined in the mesopores had been frozen. The selective freezing of water was done by cooling to -34 ºC, -29 ºC or -26 ºC for SS, SM and SL supported catalysts, respectively, and -38.5 ºC for MCM supported catalysts. Pore blockage was quantified by gas sorption using BJH analysis of the desorption isotherm. Open pore volume was defined as the volume of gas desorbing at the same relative pressures of desorption as the empty support. Their relative amount was calculated by compared to the total cumulative mesopore volume from 3 – 10 nm. From nitrogen physisorption open pore volume was determined from 4.5 – 10, 4.7 – 10 and 5.5 – 10 nm for SS, SM and SL supported catalysts, respectively. Open pores were determined from the argon desorption isotherm by comparing the cumulative mesopore volume between 4.1 – 8, 5.0 – 8, 5.5 – 8 and 3.8 - 8 nm for SL, SM, SS and MCM supported catalysts respectively.

6.3. Results and Discussion

6.3.1 Mesoporous model catalysts

A set of well-defined model supported NiO catalysts was prepared to study pore blockage with DSC and sorption. Figure 6.1 illustrates the varying degrees of pore blockage that were created. On the one hand, the supports pore diameters were varied, while on the other hand, the NiO nanoparticle size was varied by using different decomposition atmospheres during preparation.[22, 24] Typical mesoporous silica supports, SBA-15 and a MCM were synthesized with pore diameters between 6.4 to 9.6 nm (Table 6.1), and are denoted by their relative pore size: large, medium and small for the SBA-15 supports, or MCM. NiO nanoparticles of ~3 nm were deposited on all supports by catalyst preparation using calcination in a flow of 1%NO/N_2 (Table 6.1, catalysts indicated with –part). These nanoparticles are expected to create partial pore blockages in case the difference between the support pore diameter and average crystallite size ranges between 3 nm for MCM to 7 nm for SL. Alternatively, larger, elongated nanoparticles (catalysts indicated by –rod) were formed by calcination in a flow of air and the average crystallite size was close or equal to the support pore diameter.

Information on the distribution of the nanoparticles over the support was obtained with TEM. Figure 6.2A and C show typical micrographs for the 3 nm NiO nanoparticles on MCM and SM supports, respectively. The individual nanoparticles could not be distinguished due to the overlap of multiple mesopores and the high metal loading. However, it was clear that nanoparticles were confined within the

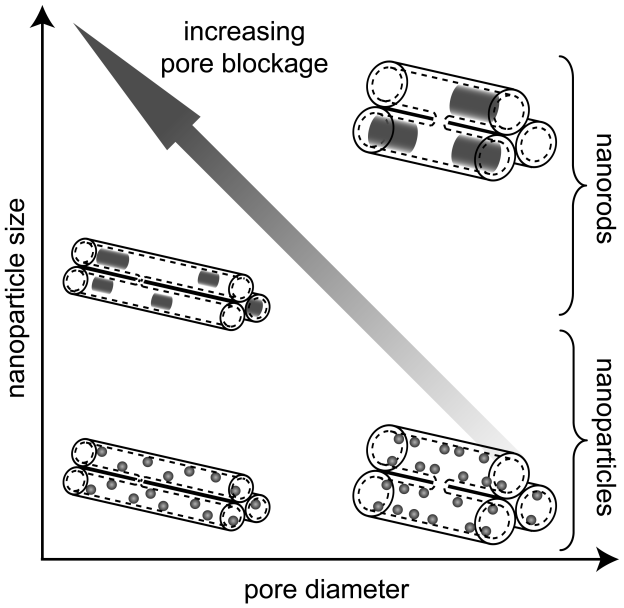

Figure 6.1. Cartoon illustrating the expected degree of pore blockage our in model catalytic systems.

pore system. For catalysts prepared by this method, an inhomogeneous distribution of nanoparticles has been visualized by various electron tomography studies. They showed that several pores were filled with closely packed individual nanoparticles, while the remainder of the pores was empty.[26, 54] The presence of a striping pattern, best illustrated in Figure 6.2C, indicated the presence of empty and filled pores. Larger nanoparticles were observed within the pore system for MCM-rod (Figure 6.2B) and NiO/SS-rod, while in both SM-rod (Figure 6.2D) and SL-rod more elongated nanorods were present. Some larger extraporous particles were also observed for SM-rod as well as for MCM-rod.

6.3.2 Nitrogen physisorption

Classically, micro- and mesoporosity are characterized using nitrogen physisorption and the results are summarized in Table 6.1. The surface areas of the catalysts ranged from 0.87 and 1.01 relative to the parent surface areas, after normalization to the silica weight. Following the ensemble assessment described by Landau *et al*. this would indicate pore blockage by particles with large dimensions relative to the pore diameter.[32] Indeed, some pore volume in the catalysts was aparently completely blocked. A loss of 6-14% of the total pore volume was calculated, after normalization to the silica weight and correcting for the occupied volume (~5%) by the NiO nanoparticles. Nevertheless, the pore structure was not destroyed significantly by the synthesis of the supported NiO nanoparticles as the average pore diameter of

Table 6.1. Structural characterization of ordered mesoporous silica supports and model catalysts with NiO nanoparticles (-part) or nanorods (-rod).

Support/ catalyst	d_{pore} (nm)	V_{tot} (cm^3/g_{SiO2})	Volume loss[a] ($\%/V_{tot,parent}$)	V_{micro}[b] (cm^3/g_{SiO2})	S_{BET} (m^2/g_{SiO2})	d_{NiO}[c] (nm)
MCM	6.4	1.0	-	0.03	849	
MCM-part		0.90	12	0.00	861	2.7
MCM-rod		0.95	6.6	0.05	810	5.5[d]
SBA-small	7.1	0.44	-	0.04	410	
SS-part		0.39	11	0.02	386	2.9
SS-rod		0.39	12	0.03	359	4.4
SBA-medium	8.3	0.65	-	0.10	606	
SM-part		0.57	12	0.04	570	2.7
SM-rod		0.61	5.9	0.10	570	9.2[d]
SBA-large	9.6	0.90	-	0.08	730	
SL-part		0.84	7.4	0.05	659	2.9
SL-rod		0.78	14	0.08	632	8.7

[a] total pore volume loss after correction for the occupied volume of NiO, [b] micropore volume determined by fitting the t-plot in thickness range of 0.35-0.50 nm, [c] average NiO crystallite size determined with XRD, [d] peaks displayed a bimodal crystallite size distribution indicating presence of larger extraporous crystals.

the catalysts corresponded to the parent's. Preservation of the structure has also been confirmed before by TEM and low angle XRD.[34] Interestingly, the catalysts containing nanorods also showed only a small pore volume loss. Apparently, the pores were not completely blocked by the nanorods, even though their crystallite sizes were close to or equal to the pore diameters.

More detailed information on pore entrance sizes can be extracted from the desorption branch of the hysteresis loop. Desorption from open mesopores leads to an isotherm branch parallel with the adsorption, while a two-step desorption occurs when part of the mesopore volume is constricted. Depending on the size of the constrictions, in this case the nanoparticles or nanorods, desorption can occur via entrance size controlled pore blocking or by forced desorption at $p/p_0 \approx 0.42$-0.50 due to cavitation. Figure 6.3A and B show the N_2 sorption isotherms for the model catalysts containing the nanoparticles and rodlike particles, respectively. In Figure 6.3A, it is clear that the small NiO nanoparticles did not cause significant

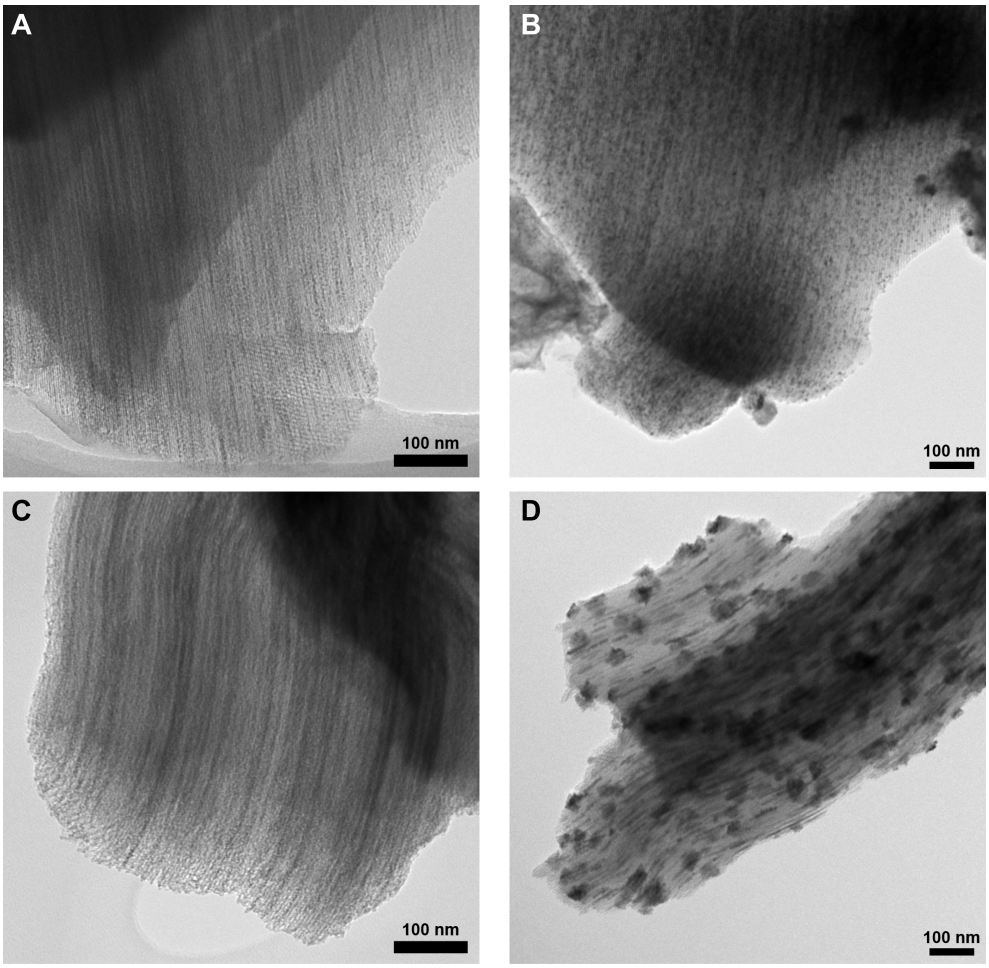

Figure 6.2. TEM micrographs for model catalysts with small NiO nanoparticles (left) and larger rodlike nanoparticles (right) on MCM and SM supports, (A) MCM-part, (B) MCM-rod, (C) SM-part and (D) SM-rod.

pore blockage. On the other hand, a clear two-step desorption was observed for the SBA-15 catalysts containing the larger nanoparticles or nanorods (Figure 6.3B) with a steep desorption step closing the hysteresis loop at $p/p_0 \approx 0.44$ - 0.46. This corresponds to the lower limit of stability of a liquid N_2 meniscus,[7] and indicates desorption brought about by cavitation. Therefore, although it can be concluded that a fraction of the pores is constricted, the pore entrance sizes cannot be deduced from the desorption branch obtained by nitrogen physisorption. Furthermore, the volume desorbing by cavitation increased going from SS to SL, but in all cases part of the mesopore volume remained open. Surprisingly, the isotherms for both MCM

supported catalysts showed hystereses with parallel branches and closure at relative pressures of 0.42-0.44. This was also observed for the parent support and indicates that pore blockage is absent for these catalysts. More likely however, it suggests that nitrogen physisorption cannot detect pore blockage within these catalysts.

6.3.2 Differential scanning calorimetry

DSC was used to follow the altered freezing and melting behavior of water confined in the pores of the catalysts. According to the Gibbs-Thomson equation, the depressed melting and freezing point of confined water is related to the mesopore radius.[36, 62] There are strong analogies between thermoporometry by DSC and physisorption and generally, the process of melting is compared to gas adsorption, while freezing is compared to gas desorption.[44] Therefore, freezing of confined water is expected to be sensitive to the presence of pore blockages. Freezing is controlled by nucleation and heterogeneous nucleation indicates freezing by the propagation of a solid front induced by a preformed crystal, such as extraporous ice. [37] The temperature at which this occurs depends on the pore entrance radius and is delayed by pore constrictions, such as nanoparticles. However, water that is isolated

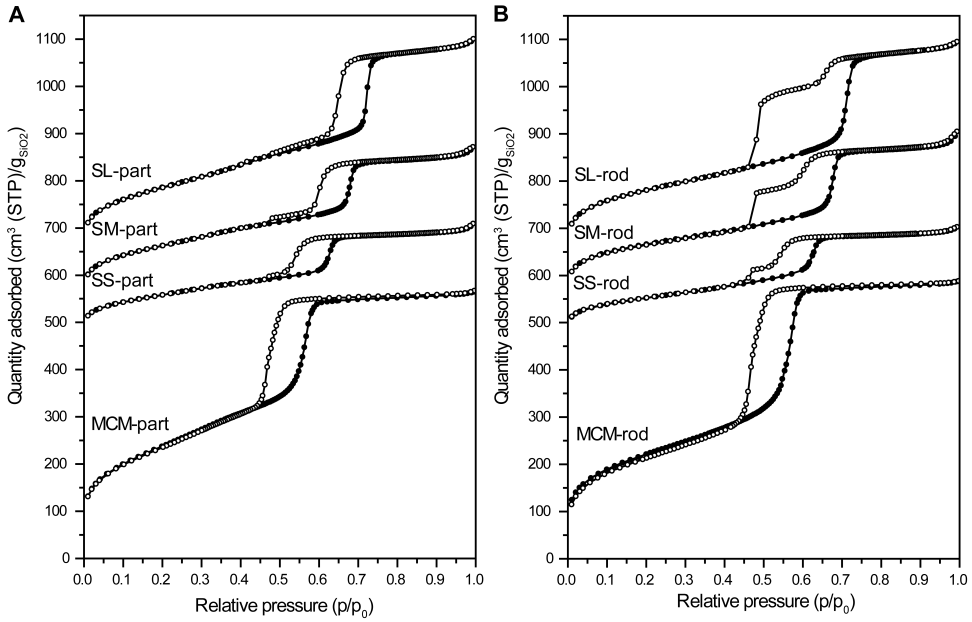

Figure 6.3. N_2 isotherms for model catalysts with different support pore diameters containing (A) small NiO nanoparticles or (B) larger NiO rodlike particles, isotherms are offset for clarity with 450, 500 and 600 cm^3 (STP)/g_{SiO2} respectively.

from extraporous bulk ice and is e.g. only accessible through micropores or narrow entrances freezes at -39 ºC by homogeneous nucleation.[38, 49-51, 63] This is similar to the cavitation effect in gas desorption. According to the relation between temperature and pore radius derived by Jahnert *et al*.,[64] -39 ºC corresponds to a radius of 4.6 nm or 4.2 nm based on cylindrical mesopore sizes calculated from N_2 adsorption isotherms with a DFT model or BJH model, respectively. Therefore, depending on the size of the nanoparticles, water confined in mesopores containing nanoparticles freezes by delayed heterogeneous nucleation, comparable to a pore blocking effect, or freezes at -39 ºC by homogeneous nucleation.

To demonstrate first the effect of confinement on the freezing behavior of water, Figure 6.4 shows the thermograms recorded for the mesoporous silica supports. Samples were impregnated with an excess of water such that all water in open mesopores is in contact with extraporous bulk ice and freezes by heterogeneous nucleation. Cool-heat cycles were recorded after samples were cooled to -70 ºC and reheated to -5 ºC. For some supports a small peak at ~-39 ºC was observed, which corresponds to the homogeneous nucleation of water. The main freezing peak of the water confined in these mesoporous materials corresponds to the heterogeneous nucleation of water in open mesopores. Indeed, the onset of freezing of the confined water decreased from -17.8 ºC to -27.6 ºC with decreasing pore diameter going from SL to MCM.

Figure 6.5 shows the distinct effect of the presence of nanoparticles in the model catalysts on the freezing behavior of confined water. In addition to freezing at the heterogeneous nucleation temperature corresponding to the parent support, a significant second freezing peak occurred at -39 ºC. As we report the freezing of water in supported catalysts for the first time, other possible causes for the delayed freezing need to be excluded. Firstly, the cooling rate did not affect the freezing

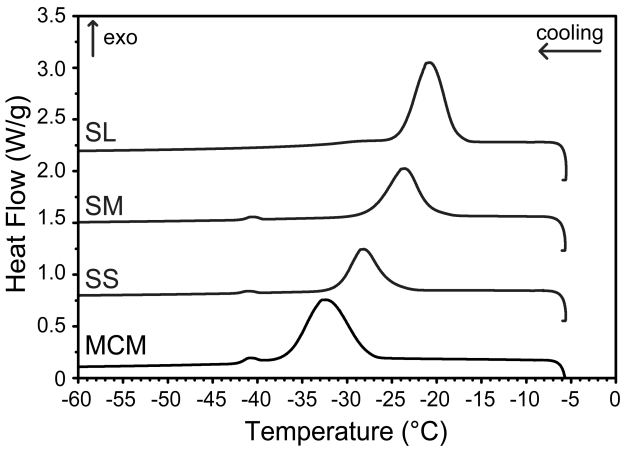

Figure 6.4. DSC thermograms water freezing in mesoporous silica supports. Samples were impregnated with an excess of H_2O, thermograms recorded during cooling at 5 ºC/min, thermograms are offset for clarity.

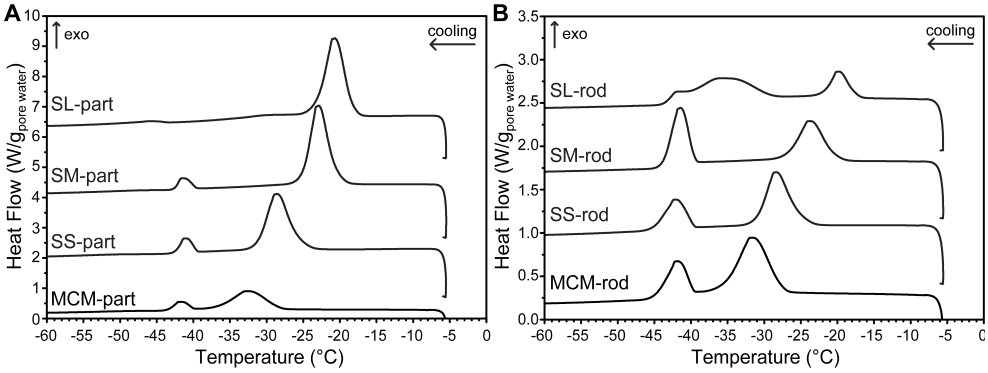

Figure 6.5. DSC thermograms for model catalysts with different support pore diameters containing (A) small NiO nanoparticles or (B) larger NiO rodlike particles. Samples are impregnated with an excess of H_2O, thermograms are recorded during cooling at 5 ºC/min, heat flow is normalized to quantity of pore water, thermograms are offset for clarity.

behavior significantly, as the same peaks were observed at a cooling rate of 1 ºC/min. Secondly, in all cases, all water melted in one single event at the same temperature as water impregnated in the parent support (thermograms recorded during heating not shown). Therefore, all the water freezing in Figure 6.5 was present in mesopores with the same average diameter as the mesopores of the support. Then, the degree of pore filling with water is reported to influence the freezing behavior considerably.[51, 65] By a method described earlier,[66] the impregnation effectiveness was determined with TGA and pore filling in the range of 87 – 100% was confirmed. Furthermore, the effect of dissolution of the silica matrix or NiO particles was found to be negligible. The structural integrity of the materials after DSC analysis was confirmed by nitrogen physisorption. The recovered pore volume was within 87-100% of the original pore volume and no significant changes in the hysteresis shapes were observed. Hence, the different freezing peaks can be ascribed to constrictions caused by nanoparticles.

The small NiO crystallites caused a small percentage of the water in the catalysts to freeze by homogeneous nucleation (Figure 6.5A), while in Figure 6.5B, the peaks of pore water freezing by homogeneous nucleation are much larger in the case of NiO nanorods. Clearly, the ratio of the peak areas depends on the nanoparticle size and pore diameter of the support, and its relation to the degree of pore blockage is discussed in detail in section 3.4. Interestingly, the rods in the SL support caused an intermediate freezing peak with an onset of ~-27 ºC, which was also observed at lower cooling rates. This indicated freezing of water by delayed heterogeneous nucleation controlled by the pore entrance size. In contrast, with nitrogen physisorption cavitation was observed for this catalyst (Figure 6.3B) from which it is only possible to deduce an upper limit of the entrance size. Strikingly, both

MCM supported catalysts displayed clear pore blockage effects in DSC, while these showed no delayed desorption in nitrogen physisorption. This illustrates that by DSC more detailed information on pore blockage is obtained than with the standard nitrogen physisorption.

6.3.3 Argon physisorption

Argon as adsorptive at 77 K is expected to provide a significant extension as compared to nitrogen physisorption for the study of pore blockages. As the forced closure of the hysteresis loop is shifted to lower relative pressures, the pressure range in which desorption of Ar occurs by pore blockage is extended.[39, 40] Figure 6.6A and B show the argon physisorption isotherms for all catalysts. A two-step desorption was now observed for all catalysts, including the MCM supported catalysts. Where nitrogen physisorption did not detect pore blockage for these catalysts, delayed desorption is clear in the extended range for the hysteresis loop of argon. Another striking difference is observed for desorption from the SL-rod catalyst (Figure 6.6B). The gradual desorption indicates a pore blocking mechanism, while with nitrogen physisorption desorption occurred by cavitation. By calculating the pore size distribution from the desorption branch, entrance sizes can be determined (Figure 6.7). Applying the BJH model allows a fair comparison to nitrogen physisorption data, even though it is known that BJH underestimates the absolute pore sizes by at least 1 nm.[67] Note that the non-zero baseline in Figure 6.7B causes some inaccuracy in the blocked pore volume quantification and is likely related to the used t-plot reference curve. The entrance sizes created by the nanorods in the SL support are in the range of 3.5 - 5.0 nm based on the BJH model for argon physisorption at 77 K.[61] In contrast, the pore size distribution calculated from N_2 desorption in Figure 6.7A shows a narrow peak at 4.7 nm, which is a typical result for desorption by cavitation. Figure 6.7 nicely illustrates the extended detection of pore blockages for the MCM supported catalysts by application of argon as compared to nitrogen.

6.3.4 Quantification of pore blockage and nanoparticle distribution

The percentage of blocked pores in the model catalysts was quantified by DSC and by physisorption. Figure 6.8A illustrates our method to extract quantitative information with DSC on pore blockage from the freezing and melting behavior of confined water. The total accessible mesopore volume is derived from the melting enthalpy released at the depressed melting point of the confined pore water after cooling to -70 ºC. The open mesopore volume is then derived from the melting enthalpy released after selectively freezing water by heterogeneous nucleation at the temperature corresponding to freezing of water confined in the parent support. The percentage of open pores follows from the ratio of the measured enthalpies. Using

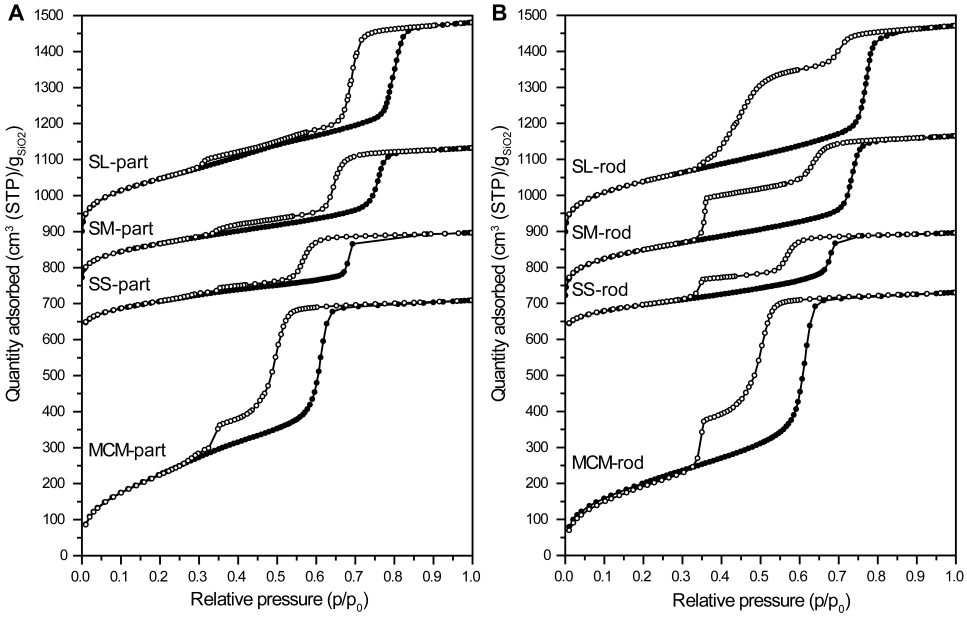

Figure 6.6. Ar physisorption isotherms obtained at 77 K for model catalysts with different support pore diameters containing (A) small NiO nanoparticles or (B) larger NiO rodlike particles, isotherms are offset for clarity with 600, 750 (-part)/700 (-rod) and 875 cm^3 (STP)/g_{SiO2}, respectively.

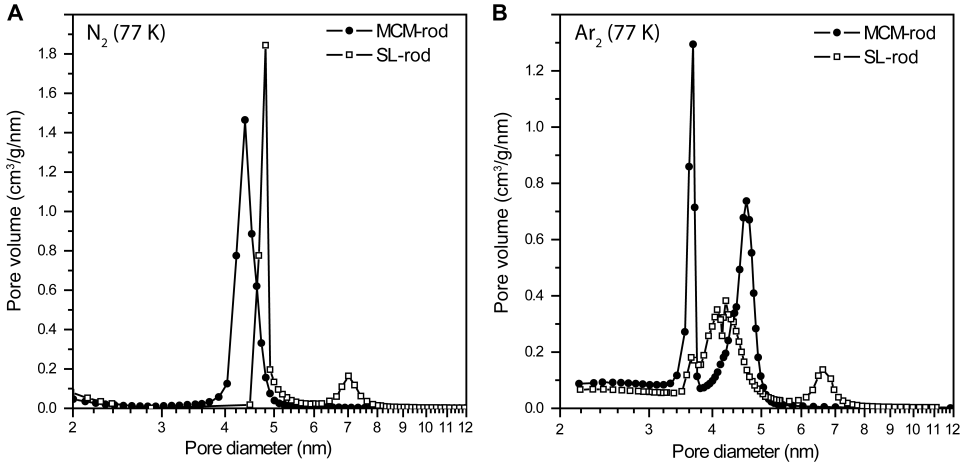

Figure 6.7. BJH pore size distribution calculated from desorption isotherms obtained by (A) nitrogen physisorption or (B) argon physisorption (77 K) for MCM-rod and SL-rod.

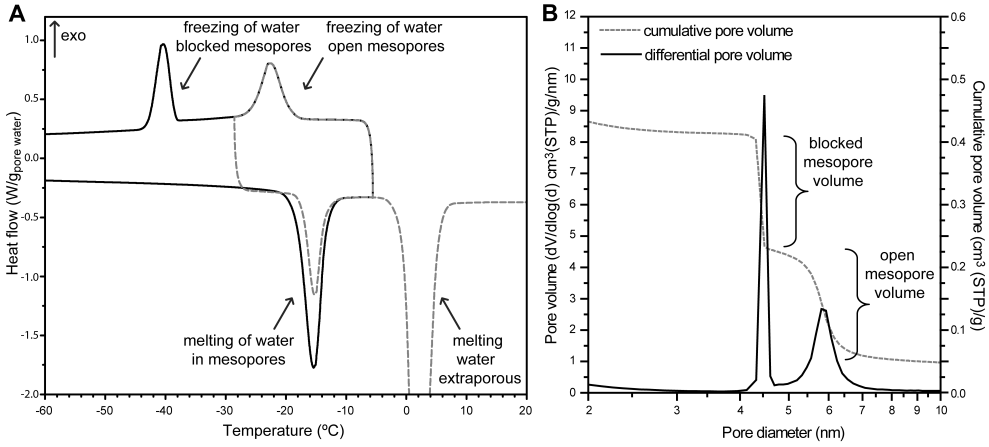

Figure 6.8. Quantification of pore blockage in SM-rod (A) by selective freezing of water in open pores recorded by DSC or (B) by BJH analysis of the desorption isotherm obtained with N_2-physisorption.

physisorption (see Figure 6.8B), the amount of open mesopore volume relative to the total accessible mesopore volume was calculated from the cumulative pore volume as a function of the pore size distribution determined from the desorption branch. Here, the pore size distribution was based on the BJH model,[34] but quantification can also be performed using an NL-DFT method.[13, 68]

Figure 6.9A shows the percentages of blocked mesopore volume that follow from the quantification by DSC. In Figure 6.9B the results are compared to the quantification by physisorption and they correspond well. This validates the new method for pore blockage quantification by selective water freezing with DSC. By argon physisorption systematically, a higher percentage of blocked pores was detected for the catalysts containing nanoparticles than by DSC and nitrogen physisorption. As seen in Figure 6.9A, the nanoparticles caused 10-15% of the mesopore volume to be blocked. Even in the 6 nm pores of the MCM supported catalysts, only 20% of the pores was blocked according to DSC, this is further discussed in detail in section 3.5. A larger degree of pore blockage was created by the larger nanoparticles or nanorods. The blocked mesopore volume increased from 42% for MCM to 73% for SL. For MCM, SS and SM, the blocked mesopore volumes were accessible through narrow openings between the nanorods and pore walls or via intrawall porosity, as was inferred from freezing by homogeneous nucleation in DSC and cavitation in both argon and nitrogen physisorption. Notably, although the percentage of blocked pores by the nanorods in SL is the highest, they are accessible by larger pore openings. As the average NiO crystallite size approaches the average pore diameter, it is postulated that the blocked pore volume is accessible through intrawall porosity,

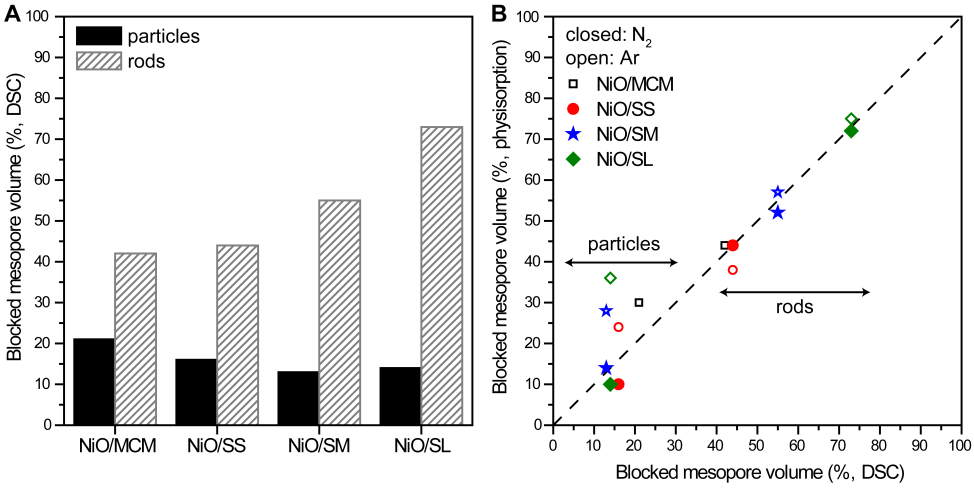

Figure 6.9. Blocked mesopore volume of model NiO catalysts on different mesoporous silica supports (A) as determined by DSC and (B) comparison of quantification by DSC to nitrogen and argon physisorption, dashed line is added as guide to the eye.

which is known to persist in SBA-15 materials synthesized at high temperatures.[69] Interestingly, both DSC and argon physisorption indicate entrance sizes of ~5 nm or 3.5 – 5 nm, respectively, based on cylindrical pore models, which is substantially larger than the proposed 1-2 nm intrawall porosity present in similar mesoporous silica supports.[69]

The 3 nm NiO crystallites caused only up to 20% of blocked mesopore volume as determined by DSC and nitrogen physisorption, even in the 6 nm pores of the MCM support. If the nanoparticles had been distributed randomly over the support, a much larger fraction of the mesopore volume was have been blocked by the constrictions. Therefore, this statistical result of less than 20% blocked mesopore volume by bulk techniques gives a strong indication that the nanoparticles are not distributed homogeneously. Indeed, this is illustrated by the nanoparticle distribution as visualized using electron tomography in Figure 6.10A. It agrees with earlier results[26, 54] that by calcination in NO/N_2 the nanoparticles were densely packed in several pore sections and part of the mesopore system remains empty. Between the nanoparticle filled pore sections enclosed voids were observed, as indicated by the white arrows in Figure 6.10A. These pore sections are only accessible through intrawall porosity or through the narrow path created by the dense nanoparticle packing. Actually, the nearest neighbor distance between these closely packed nanoparticles was measured to be in the range of 1 - 2 nm.[26] By the definitions used in this paper, the volume between the nanoparticles does not contribute to the total accessible mesopore volume. By physisorption the accessible mesopore volume ranges from 3 - 10 nm, as the BJH

model is not applicable for pores sizes below 2 nm.[7] Also, water in confinement with diameters below 2 nm does not freeze[37] and therefore does not contribute to the melting peaks. Therefore, the small cavitation features in Figures 3A and 6A as well as the homogeneous freezing of water in Figure 5A for NO/N_2 calcined catalysts is not attributed to single nanoparticle constrictions. Rather it corresponds to the voids enclosed by nanoparticle filled pore sections, as indicated with the white arrows in Figure 6.10A. The presence of secondary microporosity between the nanoparticles was confirmed by a detailed analysis of the t-plot. The micropore volume obtained as listed in Table 6.1 was determined by fitting the t-plot between 0.35 and 0.50 nm. However, a secondary micropore volume is obtained by fitting the t-plot just before the capillary condensation at a statistical film thickness between 0.7 - 0.8 nm. As indicated by the dashed lines in Figure 6.10B, the secondary micropore volume was larger for the SL catalyst with nanoparticles, i.e. 0.17 cm^3/g_{SiO2} *versus* 0.10 cm^3/g_{SiO2} for the catalyst containing nanorods. As the sum of the micropore and mesopore volume was the same for the two catalysts, the nanoparticles clearly created additional microporosity.

6.3.5 Comparison of pore blockage analysis by DSC and physisorption

Pore blockage analysis by physisorption is limited by the forced closure of the hysteresis loop in nitrogen physisorption at $p/p_0 \approx 0.42$-0.48 and in argon physisorption

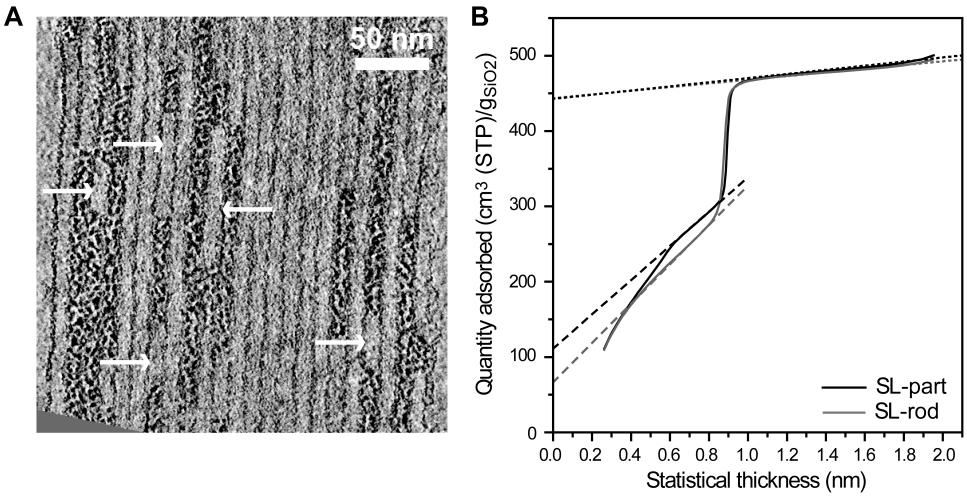

Figure 6.10. (A) NiO nanoparticles prepared by calcination in NO/N_2 in pores of SBA-15, white arrows indicate voids enclosed by pore sections filled with nanoparticles. Slice through 3D reconstruction obtained by electron tomography. (B) t-Plot analysis calculated from N_2 adsorption isotherm of SL-part and SL-rod. Dashed lines indicate fitting in the thickness range of 0.70 - 0.80 nm, dotted lines indicate fitting to obtain the sum of micropore and mesopore volume.

(77 K) at $p/p_0 \approx 0.3$,[39] which corresponds to cylindrical pore entrances of ~4.5 nm and ~3.6 nm respectively based on the BJH model.[60, 61] In DSC, homogeneous nucleation of water at ~-39 ºC limits analysis of entrance sizes to ~4.2 nm based on a calibration using cylindrical mesopores and their BJH pore diameters.[64] Therefore, both physisorption with argon at 77 K as well as DSC provide information on an extended range of pore constrictions. However, it is important to note that these pore size distributions are based on cylindrical pore models. Therefore, desorption by pore blocking or freezing by heterogeneous nucleation contains information on the pore entrance size, but cannot be used for absolute calculations of pore constrictions. The extended sensitivity of argon physisorption and DSC was evidenced by the case of the MCM supported catalysts. Desorption of N_2 occurred in a single event, due to coincidence of capillary evaporation and forced closure of the hysteresis loop, while pore blockage was clearly distinguished by the two other techniques. Furthermore, both DSC and Ar (77 K) detected pore blocking caused by the nanorods in SL, while with nitrogen physisorption cavitation was observed. Both the gradual desorption of Ar as well as the broad freezing peak in DSC indicated that constricted pore volume was accessible via openings corresponding to a cylindrical pore size of 4-6 nm. A choice for either of the techniques depends on the material being analyzed, as e.g. DSC allows the characterization of materials without the need of a drying step or can be applied with organic liquids for a favorable liquid-solid interaction. Regardless, both DSC and argon physisorption provided additional information on pore blockage to nitrogen physisorption.

6.4 Conclusions

The introduction of guest phases into mesoporous supports can greatly affect their porous properties and in this work we have shown that both DSC and argon sorption at 77 K supplement N_2 sorption in the characterization of complex mesoporous structures. A set of catalysts with varying degrees of pore blockage was assembled by depositing NiO nanoparticles with varying sizes in the pores of ordered mesoporous silica supports. Quantitative information on the number of pores blocked by nanoparticles obtained by argon physisorption and DSC was validated by comparison to results from nitrogen physisorption. Furthermore, by both techniques, a larger size range of pore constrictions can be analyzed as compared to nitrogen physisorption. By combining bulk statistical quantification with microscopic observations, the pore blockage was correlated to the nanoparticle distribution over the support, an essential parameter for supported catalysts.

Acknowledgements

Jovana Zečević (Utrecht University) is acknowledged for performing electron tomography. Mies van Steenbergen and Herre Talsma (Utrecht University) are acknowledged for technical support of thermal analysis equipment and useful discussions. The Electron Microscopy Unit at Utrecht University is acknowledged for their excellent facilities.

References

[1] A. Taguchi and F. Schuth, *Micropor. Mesopor. Mat.* **2005**, *77*, 1.
[2] K. Nakanishi and N. Tanaka, *Acc. Chem. Res.* **2007**, *40*, 863.
[3] M. Vallet-Regi, *Chem.-Eur. J.* **2006**, *12*, 5934.
[4] J. L. Vivero-Escoto, I. I. Slowing, B. G. Trewyn and V. S. Y. Lin, *Small* **2010**, *6*, 1952.
[5] A. Martinez and G. Prieto, *Top. Catal.* **2009**, *52*, 75.
[6] A. Stein, *Adv. Mater.* **2003**, *15*, 763.
[7] S. J. Gregg and K. S. W. Sing, *Adsorption, Surface Area and Porosity*. 2nd ed. 1982, London: Academic Press.
[8] C. K. Krishnan, T. Hayashi and M. Ogura, *Adv. Mater.* **2008**, *20*, 2131.
[9] F. Schuth, A. Wingen and J. Sauer, *Micropor. Mesopor. Mat.* **2001**, *44*, 465.
[10] B. S. Tian and C. Yang, *J. Phys. Chem. C* **2009**, *113*, 4925.
[11] A. Zukal, H. Siklova and J. Cejka, *Langmuir* **2008**, *24*, 9837.
[12] T. M. Eggenhuisen, J. P. den Breejen, D. Verdoes, P. E. de Jongh and K. P. de Jong, *J. Am. Chem. Soc.* **2010**, *132*, 18318.
[13] P. Van Der Voort, P. I. Ravikovitch, K. P. De Jong, A. V. Neimark, A. H. Janssen, M. Benjelloun, E. Van Bavel, P. Cool, B. M. Weckhuysen and E. F. Vansant, *Chem. Comm.* **2002**, 1010.
[14] V. Meynen, E. Beyers, P. Cool, E. F. Vansant, M. Mertens, H. Weyten, O. I. Lebedev and G. Van Tendeloo, *Chem. Comm.* **2004**, 898.
[15] Z. Y. Wu, H. J. Wang, T. T. Zhuang, L. B. Sun, Y. M. Wang and J. H. Zhu, *Adv. Funct. Mater.* **2008**, *18*, 82.
[16] S. Chytil, L. Haugland and E. A. Blekkan, *Micropor. Mesopor. Mat.* **2008**, *111*, 134.
[17] C. Jang and B. Han, *J. Chem. Phys.* **2010**, *132*.
[18] V. Meynen, Y. Segura, M. Mertens, P. Cool and E. F. Vansant, *Micropor. Mesopor. Mat.* **2005**, *85*, 119.
[19] E. Beyers, E. Biermans, S. Ribbens, K. De Witte, M. Mertens, V. Meynen, S. Bals, G. Van Tendeloo, E. F. Vansant and P. Cool, *Appl. Catal.-B Environ.* **2009**, *88*, 515.
[20] W. Chu, L. N. Wang, P. A. Chernavskii and A. Y. Khodakov, *Angew. Chem., Int. Ed.* **2008**, *47*, 5052.
[21] O. Borg, P. D. C. Dietzel, A. I. Spjelkavik, E. Z. Tveten, J. C. Walmsley, S. Diplas, S. Eri, A. Holmen and E. Rytter, *J. Catal.* **2008**, *259*, 161.
[22] J. R. A. Sietsma, J. D. Meeldijk, J. P. den Breejen, M. Versluijs-Helder, A. J. van Dillen, P. E. de Jongh and K. P. de Jong, *Angew. Chem., Int. Ed.* **2007**, *46*, 4547.
[23] J. P. den Breejen, J. R. A. Sietsma, H. Friedrich, J. H. Bitter and K. P. de Jong, *J. Catal.* **2010**, *270*, 146.
[24] M. Wolters, L. J. W. van Grotel, T. M. Eggenhuisen, J. R. A. Sietsma, P. E. de Jongh and K. P. de Jong, *Catal. Today* **2011**, *163*, 27.
[25] A. H. Janssen, C. M. Yang, Y. Wang, F. Schuth, A. J. Koster and K. P. de Jong, *J. Phys. Chem. B* **2003**, *107*, 10552.
[26] H. Friedrich, J. R. A. Sietsma, P. E. de Jongh, A. J. Verkleij and K. P. de Jong, *J. Am. Chem. Soc.* **2007**, *129*, 10249.
[27] I. Arslan, J. C. Walmsley, E. Rytter, E. Bergene and P. A. Midgley, *J. Am. Chem. Soc.* **2008**, *130*, 5716.
[28] O. Ersen, J. Werckmann, M. Houlle, M. J. Ledoux and C. Pham-Huu, *Nano Lett.* **2007**, *7*, 1898.
[29] H. Friedrich, P. E. de Jongh, A. J. Verkleij and K. P. de Jong, *Chem. Rev.* **2009**, *109*, 1613.

[30] C. J. Gommes, B. Goderis and J. P. Pirard, *J. Phys. Chem. C* **2007**, *111*, 11150.
[31] T. G. Shin, D. Muter, J. Meissner, O. Paris and G. H. Findenegg, *Langmuir* **2011**, *27*, 5252.
[32] L. Vradman, M. V. Landau, D. Kantorovich, Y. Koltypin and A. Gedanken, *Micropor. Mesopor. Mat.* **2005**, *79*, 307.
[33] M. V. Landau, L. Vradman, A. Wolfson, P. M. Rao and M. Herskowitz, *C. R. Chim.* **2005**, *8*, 679.
[34] J. R. A. Sietsma, J. D. Meeldijk, M. Versluijs-Helder, A. Broersma, A. J. van Dillen, P. E. de Jongh and K. P. de Jong, *Chem. Mater.* **2008**, *20*, 2921.
[35] G. Prieto, A. Martinez, R. Murciano and M. A. Arribas, *Appl. Catal.- A Gen.* **2009**, *367*, 146.
[36] R. Defay, I. Prigogine, A. Bellemans and D. H. Everett, *Surface Tension and Adsorption*. 1966, London: Longmans, Green & Co LTD.
[37] G. H. Findenegg, S. Jahnert, D. Akcakayiran and A. Schreiber, *ChemPhysChem* **2008**, *9*, 2651.
[38] C. A. Angell, *Supercooled Water*, in *Water and aqueous solutions at subzero temperatures*, F. Franks, Editor. 1982, Plenum Press: New York.
[39] P. I. Ravikovitch and A. V. Neimark, *Langmuir* **2002**, *18*, 9830.
[40] M. Kruk and M. Jaroniec, *Chem. Mater.* **2003**, *15*, 2942.
[41] M. Thommes, B. Smarsly, M. Groenewolt, P. I. Ravikovitch and A. V. Neimark, *Langmuir* **2006**, *22*, 756.
[42] M. Kruk, M. Jaroniec, S. H. Joo and R. Ryoo, *J. Phys. Chem. B* **2003**, *107*, 2205.
[43] E. B. Celer, M. Kruk, Y. Zuzek and M. Jaroniec, *J. Mater. Chem.* **2006**, *16*, 2824.
[44] I. Beurroies, R. Denoyel, P. Llewellyn and J. Rouquerol, *Thermochim. Acta* **2004**, *421*, 11.
[45] A. M. Kjeldsen and M. R. Geiker, *Mater. Struct.* **2008**, *41*, 213.
[46] P. Luukkonen, T. Maloney, J. Rantanen, H. Paulapuro and J. Yliruusi, *Pharm. Res.* **2001**, *18*, 1562.
[47] S. Park, R. A. Venditti, H. Jameel and J. J. Pawlak, *Carbohydr. Polym.* **2006**, *66*, 97.
[48] J. Riikonen, J. Salonen, M. Kemell, N. Kumar, D. Y. Murzin, M. Ritala and V. P. Lehto, *J. Phys. Chem. C* **2009**, *113*, 20349.
[49] A. H. Janssen, H. Talsma, M. J. van Steenbergen and K. P. de Jong, *Langmuir* **2004**, *20*, 41.
[50] K. Morishige, H. Yasunaga, R. Denoyel and V. Wernert, *J. Phys. Chem. C* **2007**, *111*, 9488.
[51] S. Kittaka, Y. Ueda, F. Fujisaki, T. Iiyama and T. Yamaguchi, *Phys. Chem. Chem. Phys.* **2011**, *13*, 17222.
[52] D. Y. Zhao, J. L. Feng, Q. S. Huo, N. Melosh, G. H. Fredrickson, B. F. Chmelka and G. D. Stucky, *Science* **1998**, *279*, 548.
[53] C. F. Cheng, D. H. Park and J. Klinowski, *J. Chem. Soc., Faraday T* **1997**, *93*, 193.
[54] J. R. A. Sietsma, H. Friedrich, A. Broersma, M. Versluijs-Helder, A. J. van Dillen, P. E. de Jongh and K. P. de Jong, *J. Catal.* **2008**, *260*, 227.
[55] J. van der Meer, I. Bardez, F. Bart, P. A. Albouy, G. Wallez and A. Davidson, *Micropor. Mesopor. Mat.* **2009**, *118*, 183.
[56] E. Marceau, M. Che, J. Cejka and A. Zukal, *ChemCatChem* **2010**, *2*, 413.
[57] J. R. Kremer, D. N. Mastronarde and J. R. McIntosh, *J. Struct. Biol.* **1996**, *116*, 71.
[58] B. C. Lippens and J. H. de Boer, *J. Catal.* **1965**, *4*, 319.
[59] M. Jaroniec, M. Kruk, J. P. Olivier and S. Koch, *Proceedings of COPS-V, Heidelberg, Germany* **1999**.
[60] M. Kruk, M. Jaroniec and A. Sayari, *Langmuir* **1997**, *13*, 6267.
[61] M. Kruk and M. Jaroniec, *J. Phys. Chem. B* **2002**, *106*, 4732.
[62] M. Brun, A. Lallemand, J.-F. Quinson and C. Eyraud, *Thermochim. Acta* **1977**, *21*, 59.
[63] H. Talsma, M. J. van Steenbergen and D. J. A. Crommelin, *Cryobiology* **1992**, *29*, 80.
[64] S. Jahnert, F. V. Chavez, G. E. Schaumann, A. Schreiber, M. Schonhoff and G. H. Findenegg, *Phys. Chem. Chem. Phys.* **2008**, *10*, 6039.
[65] A. Schreiber, I. Ketelsen and G. H. Findenegg, *Phys. Chem. Chem. Phys.* **2001**, *3*, 1185.
[66] T. M. Eggenhuisen, M. J. van Steenbergen, H. Talsma, P. E. de Jongh and K. P. de Jong, *J. Phys. Chem. C* **2009**, *113*, 16785.
[67] P. I. Ravikovitch and A. V. Neimark, *Langmuir* **2002**, *18*, 1550.
[68] C. Vercaemst, H. Friedrich, P. E. de Jongh, A. V. Neimark, B. Goderis, F. Verpoort and P. Van Der Voort, *J. Phys. Chem. C* **2009**, *113*, 5556.
[69] A. Galarneau, N. Cambon, F. Di Renzo, R. Ryoo, M. Choi and F. Fajula, *New J. Chem.* **2003**, *27*, 73.

Chapter 7

Thermoporometry of Cage Silica Materials for Entrance Size Analysis

Abstract

The entrance size of cage mesoporous materials is a crucial, but a notoriously difficult parameter to asses. Here we present differential scanning calorimetry (DSC) as a technique to quantify the entrance sizes in a series of mesoporous silica materials with different cage and neck sizes. We show that DSC extends the range of classical physisorption techniques and is a powerful tool for the determination of entrance sizes and entrance size distributions in mesoporous materials.

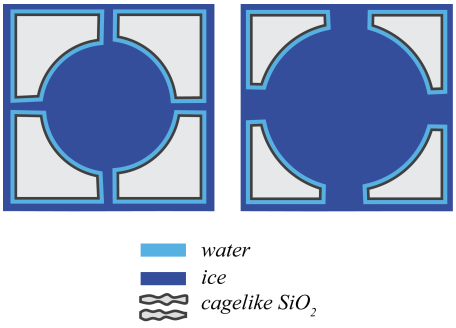

7.1 Introduction

Cage silica materials form a unique class within the ordered mesoporous materials family. They possess a 3-dimensional highly ordered arrangement of spherical cages interconnected by 6 up to 12 windows, with varying cage size, entrance size and symmetry depending on the synthesis conditions applied.[1-4] Applications are in catalysis,[5] drug delivery,[6] separation via size selection or as template for the synthesis of other mesoporous materials via nanocasting.[7-9] Cage silica are of particular interest as catalyst supports, as the necks help to confine the catalytically active phase to the cage, while the 3-dimensional connectivity provides transport for substrates and products. They are applied to reduce sintering of supported metal nanoparticles[10, 11] or prevent leaching of homogeneous catalysts.[12, 13]

The entrance and cage size are crucial structural parameters. Although *cage sizes* can be derived from gas physisorption,[14] extracting *entrance sizes* has remained a challenge. Different approaches have been employed, such as advanced electron microscopy,[15-17] diffraction and scattering techniques,[18-21] synthesis of negative replicas,[3, 22] size selective adsorption,[23] and anchoring organic moieties to the surface with gradually increasing molecular sizes.[24-26] Nevertheless, all these methods involve specific material requirements and have limited applicability. Gas physisorption is a common analysis technique to analyze mesoporosity and does not require structural ordering of the material.[27-29] The adsorption isotherm is used to determine the cage size, while the entrance size is extracted from the desorption branch as long as evaporation is controlled by the pore restriction.[3, 16] The use of the desorption isotherm is limited due to the cavitation effect, but using alternative adsorptives as argon or krypton at different temperatures stretches the forced closure of the hysteresis loop.[30-32] For example, argon physisorption at 77 K has shown to provide a modest extension towards entrance sizes of ~4 nm as compared to the limit of ~5 nm in classical nitrogen physisorption.[26, 33-35] Alternative approaches use consecutive adsorption of H_2O and N_2,[36, 37] quantification of intrawall porosity from the adsorption isotherm[4, 38] and pore size distribution analysis with a combined cylindrical and spherical pore model.[19, 39]

Thermoporometry by differential scanning calorimetry (DSC) of confined water is an alternative characterization technique that provides information on mesoporosity.[40] The melting point of a material inside a mesopore depends on the pore size, similar to capillary adsorption in gas sorption.[41-45] Freezing of a liquid in a mesopore shows similarities to gas desorption and contains information on pore connectivity or entrance sizes.[43, 46, 47] Earlier reports of thermoporometry by DSC on mesoporous cage materials showed that the freezing of water confined within the cages was dominated by homogeneous nucleation of ice at ~-39 ºC.[48-52] Similar to cavitation

in gas desorption, homogeneous nucleation of water induces a lower limit for the entrance size range that can be analyzed. Although the limits of nitrogen and argon physisorption have been discussed extensively,[24, 31, 53-55] the sensitivity of DSC towards entrance and cages size has not been reported in detail.

Here we explore thermoporometry by DSC of confined water for entrance size analysis of mesoporous cage materials. Series of SBA-16[26, 56, 57] and FDU-12[16] silica materials were synthesized with a range of entrance sizes such that the desorption isotherms in nitrogen physisorption varied between pore blocking controlled and full cavitation. The quantification of cage and entrance sizes obtained by DSC are validated by physisorption with N_2 and Ar at 77 K, for those materials where data are available. We report a fair comparison between the techniques by analysis of entrance sizes using the same BJH based approach for the sorption techniques[30, 58] as well as for the freezing temperature-pore radius calibration for the DSC. To demonstrate the advantage of DSC, the cage and entrance sizes of FDU-12 with ultralarge cages were analyzed that were inaccessible by both physisorption techniques. To exploit the full potential of DSC we developed a new method to derive the entrance size distribution.

7.2 Experimental Methods

7.2.1 Synthesis of ordered mesoporous cage silicas

Block-copolymers Pluronic F127 ($EO_{106}PO_{70}EO_{106}$) and Pluronic P123 ($EO_{20}PO_{70}EO_{20}$) from Sigma-Aldrich, 1-butanol (p.a., Acros), 1,3,5-trimethylbenzene (99%, Acros), KCl (p.a., Acros) and tetraethyl ortosilicate (TEOS, ≥99%, Sigma-Aldrich) were used as received. The synthesis conditions employed for the individual SBA-16 and FDU-12 samples are summarized in Table 1.

SBA-16 silica materials with small cages were synthesized following the procedure reported by Kim et al.[26] The synthesis gel had the following molar composition: 0.0016 P123 : 0.0037 F127 : 1.0 TEOS: 4.4 HCl : 140 H_2O, in Table 7.1 labeled as (1). The copolymers were dissolved at room temperature in HCl/H_2O. TEOS was subsequently added drop-wise under fast magnetic stirring and the gel was aged in an oven at 35 ºC for 20 hours under static conditions. The mixture was transferred to a Teflon-lined steel autoclave and further treated for 24 hours at 100 ºC. The different materials are denoted by their gel composition (1) and hydrothermal treatment temperature (T) and time in hours (t): SBA1-T/t.

Large cage SBA-16 silica materials were prepared using 1-butanol (BuOH) as a swelling agent at low-acid concentrations as described by Kleitz et al.[56] A synthesis gel with the following molar ratios was used: 0.0035 F127 : 1.79 BuOH : 1.0 TEOS :

0.91 HCl : 120 H_2O, in Table 7.1 labeled as (2). After dissolving the block-copolymer in HCl/H_2O, 1-butanol was added and the mixture stirred at 35 ºC for 1 hour. Then, TEOS was added drop-wise under fast magnetic stirring and the gel was aged in an oven at 35 ºC for 20 hours under static conditions. The mixture was transferred to a Teflon-lined steel autoclave and further treated for 24-72 hours at 90-120 ºC. The temperature and duration of the last hydrothermal treatment were adjusted to obtain SBA-16 silica materials with varying cage and neck sizes. The different materials are denoted by their gel composition (2) and hydrothermal treatment temperature (T) and time in hours (t): SBA2-T/t.

A series of ultralarge cage FDU-12 silica materials was synthesized employing 1,3,5-trimethylbenzene (TMB) as swelling agent according to the procedure reported by Yu et al.[16] Pluronic F127 and KCl were dissolved in HCl/H_2O at room temperature. TMB was subsequently added and the mixture stirred at 14 ºC for 24 hours. Then TEOS was added drop-wise under fast magnetic stirring and the mixture further stirred at 14 ºC for 20 hours. The final synthesis gel molar composition was: 0.004 F127 : 1.7 KCl : 0.93 TMB : 1.0 TEOS : 6.1 HCl : 157 H_2O, in Table 7.1 labeled as (3). Subsequently, the mixture submitted to a final thermal treatment at a temperature of 35-130 ºC for 24-48 hours in an oven. For thermal treatments at 90 ºC or higher temperatures the gel was transferred to Teflon-lined steel autoclaves. The temperature

Table 7.1. Synthesis conditions for SBA-16 and FDU-12 with varying cage and neck sizes.

Sample	Synthesis gel[a]	Hydrothermal treatment		Additional heat treatment
		T (ºC)	Time (h)	
SBA1-60-24	(1)	60	24	
SBA1-100/24	(1)	100	24	
SBA2-90/48	(2)	90	48	
SBA2-120/24_II	(2)	120	24	800 ºC, 3 hrs
SBA2-120/24_I	(2)	120	24	650 ºC, 3 hrs
SBA2-120/24	(2)	120	24	
SBA2-100/72	(2)	100	72	
FDU-35/24	(3)	35	24	
FDU-60/48	(3)	60	48	
FDU-100/48	(3)	100	48	
FDU-110/48	(3)	110	48	
FDU-120/48	(3)	120	48	
FDU-130/48	(3)	130	48	

and duration of this treatment were adjusted to obtain FDU-12 silicas with different cage and neck sizes. FDU-12 materials are denoted by their hydrothermal treatment temperature (T) and time in hours (t), FDU-T/t.

In all cases, after the hydrothermal treatment, the white solid was filtered, extensively washed with double deionized water and dried at 120 ºC for 10 hours. Finally, the product was calcined at 540 ºC in a muffle oven in order to remove the copolymer template. An additional thermal treatment was applied to selected calcined silicas in order to controllably shrink the porous structure.[57] This additional thermal treatment was performed in static air at a temperature of 650 ºC or 800 ºC for 3 hours.

7.2.2 Structural characterization

To perform transmission electron microscopy, the samples were embedded in an epoxy resin (Epofix, EMS) and cured at room-temperature for 72 hours. The embedded materials were then cut into ultrathin sections with 50 nm nominal thickness using a Diatome 35º diamond knife mounted on a Reichert-Jung Ultracut E microtome, and the sections were collected on a carbon-coated Ni grid (200 mesh). Transmission electron micrographs were acquired using a Tecnai 12 microscope (FEI company) operated at 120 keV. The volume averaged cage diameter was determined over *ca*. 50 mesocages on different micrographs of ~50 nm thick ultramicrotomed slices. The cages were distinguished from the silica pore walls by image thresholding and the individual cage diameter was determined from the area-equivalent circle.

Low angle X-ray diffraction patterns (LA-XRD) were recorded for the calcined silica mesostructures with a Bruker-Nonius D8 Advance X-ray diffractometer using Co-$K_{\alpha 12}$ radiation (λ=1.79026 Å). The diffraction patterns were recorded in the 2θ range of 0.7º-2.5º using a scanning step size 0.08˚ and acquisition time 140 s·step^{-1}.

7.2.3 Porosity characterization

N_2 and Ar physisorption isotherms were measured at -196 ºC (77 K) (Micromeritics, TriStar 3000). Prior to the measurements, samples (50-100 mg) were dried under flowing N_2 at 250 ºC for 12 h. The average cage size was defined as the maximum value in the pore size distribution (PSD) obtained by applying a NL-DFT model for cylindrical pores to the adsorption branch of the N_2 isotherm.[59] The PSD for the entrance size from the N_2 desorption data was calculated using the BJH model modified according to the Kruk-Jaroniec-Sayari (KJS) correction and using the empirical from of the Harkin-Jura equation as thickness reference curve as displayed in equation 1 and 2.[58]

$$r\,(p/p_0)\,[nm] = \frac{-0.959}{0.434\,\log(p/p_0)} + t(p/p_0) + 0.3 \qquad \text{eq. 1}$$

$$t\,(p/p_0)\,[nm] = 0.1\left(\frac{60.65}{0.03071 - \log(p/p_0)}\right)^{0.3968} \qquad \text{eq. 2}$$

The PSD from the Ar desorption branch was calculated using the BJH model with empirically established corrections as published by Kruk *et al*., equation 3.[60]

$$r\,(p/p_0)\,[nm] = \frac{-0.5393}{\log(0.8259\,p/p_0)} + t(p/p_0) + 0.343 \qquad \text{eq. 3}$$

The thickness reference curve reported therein was obtained using a macroporous silica (LiChrospher Si-1000)[60] and was found to be accurately represented in the relative pressure range of 0.1 to 0.95 by the empirical formula displayed in equation 4.

$$t\,(p/p_0)\,[nm] = \left(\frac{0.1605}{0.1156 - \log(-0.06199 + p/p_0)}\right)^{0.5085} \qquad \text{eq. 4}$$

The average entrance sizes were defined as the peak maximum in the thus obtained PSDs from N_2 and Ar desorption.

Differential scanning calorimetry (DSC) was used to analyze the freezing and melting behavior of water in mesoporous silica materials (TA instruments, Q2000). The temperature and heat flow were calibrated using a certified indium sample. Measurements were performed in the range of -70 ºC – 25 ºC under a flow of 50 mL/min N_2. 3-5 mg silica was mixed with a 2-fold excess of H_2O (Millipore, R = 18 MΩ·cm) based on the pore volume determined by N_2-physisorption. The impregnated sample was hermetically sealed in an aluminum pan (40 µL, Tzero, TA Instruments) to prevent water evaporation during the measurement. A heating/cooling rate of 1 ºC/min and 5 min isothermal periods at -70 ºC were used for all measurements. The melting and freezing peaks were integrated using linear baselines in Universal Analysis 2000 software (TA Instruments).

To derive an empirical temperature-pore radius relation, the onset temperature (T_{ons}) for freezing and melting of water/ice in ordered mesoporous silica materials with cylindrical were determined and fitted to a simplified Gibbs-Thomson equation, eq 5:

$$\Delta T = 0\ ºC - T_{ons} = \frac{C_{GT}}{r} \quad , C_{GT} = \frac{2T_0\gamma_{sl}v_l}{\Delta H_f} \qquad \text{eq. 5}$$

with r the pore radius in nm, C_{GT} a constant in ºC·nm and t a correction for a non-freezing layer in nm.[40, 61] Table 7.2 lists the fitting results, while the experimental data and corresponding fits are included in the supplementary information (Appendix C, Figures C1 and C2). The melting point onset temperature (T_m) was related to pore sizes of the cylindrical mesoporous silica derived as the maximum in the PSD calculated from the N_2 adsorption isotherm with an NL-DFT model.[59] The freezing point onset was related to the pore radii determined with the BJH model.[58] For freezing, a good fit was only obtained excluding the correction for a non-freezing layer.

Table 7.2. Gibbs-Thomson fitting parameters for the melting point depression (T_m) and freezing point depression (T_f) for H_2O impregnated cylindrical OMS using pore radii from nitrogen physisorption determined with an NL-DFT method or BJH model respectively.

Gibbs-Thomson fitting parameters	T_m (ºC)	T_f(ºC)
C_{GT} (ºC·nm)	66.4	80.0
t (nm)	0.48	0

To determine the entrance and cage sizes, the onset freezing and melting point were averaged over three samples for each cage silica material. The onset temperatures of freezing and melting were determined with a heating/cooling rate of 1 ºC/min in the presence of extraporous ice after first cooling the sample to -70 ºC and heating to -5 ºC (for SBA-16 materials) or -3 ºC (for FDU-12 materials). The standard error was ≤0.04 ºC. The entrance size distribution was determined by equilibrating for 10 min at temperatures between -45 ºC and -10 ºC with 1 ºC or 0.5 ºC intervals and subsequently heating to -5 ºC (for SBA-16 materials) or -3 ºC (for FDU-12 materials). The percentage of cages accessible through entrances freezing at the equilibration temperature was determined by the ratio of the released melting enthalpy compared to the melting enthalpy released after cooling to -70 ºC.

7.3 Results & Discussion

7.3.1 Structural characterization of SBA-16 and FDU-12 silicas

Thermoporometry for cagelike silica materials was evaluated on a series of SBA-16 and FDU-12 materials. SBA-16 materials display a body-centered cubic ordering of cages with 8 connecting entrances (*Im-3m* symmetry).[15] In FDU-12 (*Fm-3m*), cages have a face-centered cubic close-packing and are connected to 12 nearest neighbors.[16] Here, SBA-16 with cages ranging from 7 – 10 nm as well as some ultra-large cage FDU-12 materials (17-25 nm) were used. Transmission electron microscopy confirmed large ordered porosity domains for the selected SBA-16 and FDU-12 materials (Figure 7.1). The views recorded along the [1 0 0] and [1 1 1] crystallographic directions agree with the cubic *Im-3m* and *Fm-3m* symmetries for the SBA-16 and FDU-12 samples, respectively. For the SBA-16 materials, the use of 1-butanol as a swelling agent, as well as the increase in the hydrothermal treatment temperature and time led to an increase in the cage diameter and a concurrent decrease in the wall thickness (*cf.* SBA1-60/24 in Figure 7.1A and B and SBA2-90/48 in Figure 7.1C). Similar trends were observed for the series of FDU-12 materials (Figure 7.1D to F), for which an increased hydrothermal treatment temperature from 60 ºC (FDU-60/48) to 120 ºC (FDU-120/48) led to an enlargement of the cage diameter at the expense of the wall thickness. Long range structural ordering was confirmed by low angle X-ray

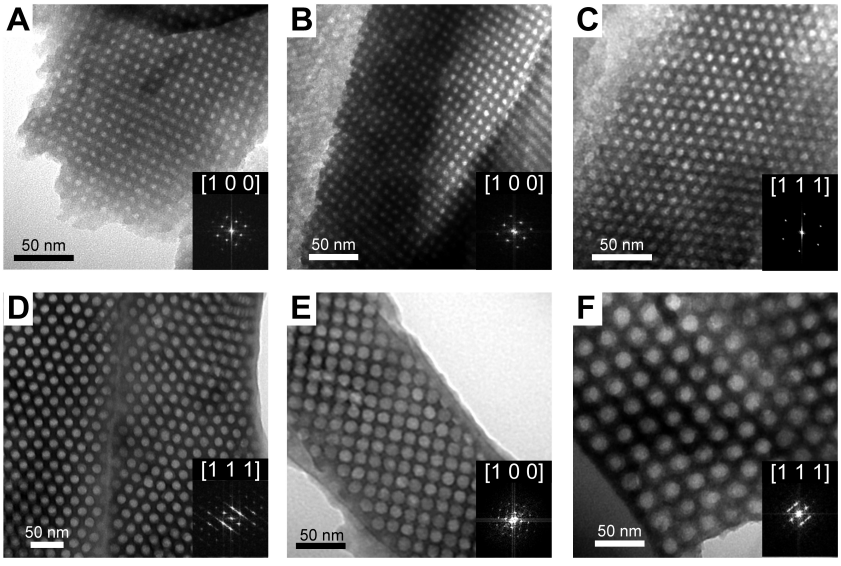

Figure 7.1. TEM micrographs for SBA-16 silicas (A) SBA1-60/24, (B,C) SBA2-90/48, FDU-12 silicas (D,E) FDU-60/48 and (F) FDU-120/48 along the [1 0 0] or the [1 1 1] crystallographic planes as indicated. Insets show corresponding Fourier diffractograms.

diffraction (Appendix C, Figure C3). For the SBA-16 materials, the XRD patterns were in agreement with the expected the *Im-3m* symmetry. However, the (200) and (220) diffraction lines were difficult to observe for the materials with the largest unit cells.[38] For the ultralarge cage FDU-12 silica materials, the very large unit cell prevented recording of the (110) diffraction peak and indexing of higher diffractions. Finally, the particle morphology was visualized with SEM and depended on the synthesis gel composition (Appendix C, Figure C4).

7.3.2 Cage size analysis by differential scanning calorimetry

The depressed melting and freezing point of confined water was determined with 0.04 ºC accuracy using differential scanning calorimetry. Analogous to adsorption in physisorption, the depressed melting point of confined water is related to the cage sizes, while freezing is correlated to the entrance size. We first discuss the use of DSC to evaluate the cage sizes of the SBA-16 and FDU-12 series. Figure 7.2 shows the melting of water impregnated in selected SBA-16 and FDU-12 materials. The DSC thermograms recorded during heating showed single, narrow melting peaks, confirming uniform cage sizes. Only for SBA2-100/72 a bimodal melting peak was observed, which agrees with the observation of a two-step adsorption in nitrogen physisorption (*vide infra*). The depressed melting point is inversely related to the cage diameter according to the Gibbs-Thomson equation.[40] For the selected SBA-16 materials shown in Figure 7.2A, the onset melting point varied between -16.8 ºC and -21.3 ºC as a result of the varying cage diameters. The additional heat treatment of SBA2-100/24_I and SBA2-100/24_II was expected to cause cage shrinkage and this was indeed reflected by the lower melting points as compared to SBA2-100/24. For the FDU-12 materials, roughly two cage sizes were observed with melting points

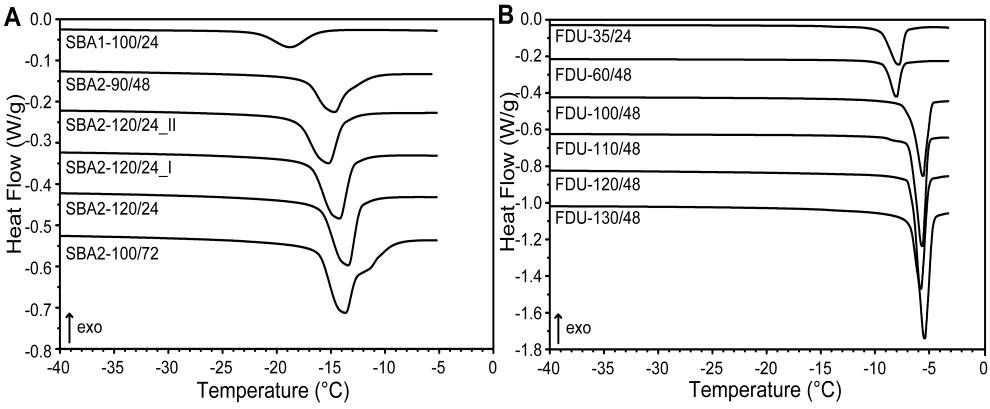

Figure 7.2. DSC thermograms recorded during heating at 1 ºC/min of (A) selected SBA-16 and (B) selected FDU-12 silica materials impregnated with a twofold excess of H_2O as compared to the pore volume, thermograms are off-set for clarity.

around -9 ºC and around -6 ºC. Nevertheless, as can be seen in Table 7.3 the small differences in cage sizes resulted in significantly distinguishable melting point onsets highlighting the exceptional accuracy of DSC.

The cage sizes calculated form the melting point onsets using cylindrical ordered mesoporous silica materials as references are listed in Table 7.3. The correlation of the cage diameters calculated from DSC and nitrogen physisorption is illustrated in Figure 7.3. Especially the cage sizes of the SBA-16 materials are in good agreement. It has been reported earlier that the melting depression is independent of the pore shape,[49, 51] confirming the validity of cylindrical mesoporous materials as reference. However, a larger melting point depression has also been reported for the spherical cages of SBA-16 as compared to cylindrical pores with similar pore radii.[50] As seen in Figure 7.3 the FDU-12 cage sizes obtained by physisorption exceeded the values obtained by DSC cage size with 5 - 20%. Although this may result from a pore shape effect on the melting point depression, it is more likely due to underestimation of the cage sizes from nitrogen physisorption as they were calculated using an NL-DFT model for cylindrical pores.[14, 19] For selected SBA-16 and FDU-12 materials, the

Table 7.3. Cage size analysis for selected SBA-16 and FDU-12 silica materials.

	onset melting point[a] (ºC)	cage diameter (nm)			
Sample		DSC[b]	N_2-phys[c]	XRD[d]	TEM[e]
SBA1-60/24	-26.4	6.0	6.3	9.0	4.5 ± 0.4
SBA1-100/24	-21.8	7.0	7.1	12.2	
SBA2-90/48	-17.5	8.5	9.6	12.6	7.5 ± 0.6
SBA2-120/24_II	-18.1	8.3	8.4	13.8	
SBA2-120/24_I	-17.0	8.8	9.6	13.7	
SBA2-120/24	-16.1	9.2	10.1		
SBA2-100/72	-16.3	9.1	10.1		
FDU-35/24	-9.5	15.0	17.0		
FDU-60/48	-9.1	15.5	16.8		14.2 ± 0.5
FDU-100/48	-6.8	20.4	25.0		
FDU-110/48	-6.8	20.6	24.8		
FDU-120/48	-6.6	21.1	24.8		21.4 ± 1.3
FDU-130/48	-6.4	21.6	25.9		

[a] melting point determined by DSC by heating at 1 ºC/min, [b] cage size determined from the onset melting point by DSC using the Gibbs-Thomson equation with fitting parameters listed in Table 2, [c] cage size determined from adsorption isotherm using NL-DFT model, [d] determined from the [1 1 0] lattice distance by adopting the model for BCC arrangement of packed spheres[14, 38], [e] volume averaged cage diameter and volume averaged standard deviation.

cage size was also determined from the XRD pattern and from TEM micrographs. The cage diameters obtained with XRD exceeded both the cage diameters obtained by DSC and physisorption, which has been reported earlier.[14, 38] By image analysis of several TEM micrographs smaller cage diameters were obtained that were closer to the sizes determined by DSC than physisorption. However, they are determined from 2D projections of multiple overlaying cages and assume spherical geometry. Also shrinkage and shear forces due to ultramicrotomy may affect the obtained value. Nevertheless, significant variations in the onset melting temperature of the confined water with DSC clearly distinguished the different cage sizes.

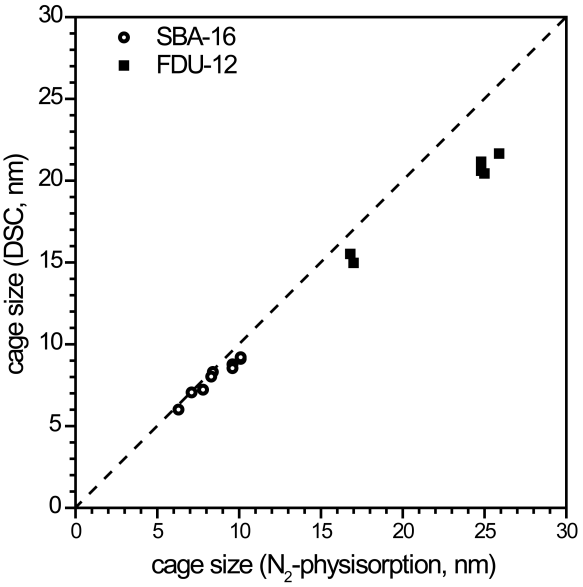

Figure 7.3. Cage sizes of selected SBA-16 and FDU-12 silicas as determined by N_2-physisorption (NL-DFT PSD of adsorption branch) and calculated from the onset temperature of melting of confined water determined by DSC. Line is added as guide to the eye.

7.3.3 Entrance size analysis by physisorption

The silica materials are expected to display a range of cage sizes and cage entrance sizes. The isotherms obtained with N_2 and Ar for selected SBA-16 materials are shown in Figure 7.4A and B. Wide hysteresis loops were generally observed. This indicates a large difference between the cage diameters and entrance sizes as capillary condensation during adsorption is determined by the cage diameter. The relative pressure for capillary evaporation can either be determined by the entrance size or cavitation. In the first case entrance size information can be extracted from the relative pressure of gas evaporation from the cages. However, when forced desorption occurs due to the lower stability limit of the adsorptive, only an upper limit of the entrance size can be deduced. The lower relative pressure limit for forced closure of the hysteresis loop depends on the adsorptive and temperature and occurs

at p/p_0 ~0.42-0.50 for N_2 at 77 K and p/p_0 ~ 0.30 for Ar at 77 K.[30, 31] The selected samples in Figure 7.4A and B illustrate both desorption modes for N_2, as well as the extension of relative pressures of the hysteresis loop achieved by using Ar instead of N_2. SBA2-100/72 shows entrance controlled desorption in both nitrogen and argon physisorption (isotherm d). The desorption branch of Ar extends to lower relative pressures, indicating an entrance size distribution. Likely, this material consists of mixed mesophases due to the extended hydrothermal treatment time, as a dual cage size was observed from the adsorption branches. The sharp desorption observed for SBA1-100/24 (isotherm a) indicates cavitation during desorption of both N_2 and Ar, indicating an entrance size below the detection limit of both adsorptives. The desorption of N_2 from SBA2-120/24_II also occurred via cavitation (isotherm b), but a more gradual desorption was observed with argon physisorption. The additional thermal of SBA2-120/24_II caused shrinkage of the cages as compared to SBA2-100/24, see Table 7.3. From the sorption isotherms it is clear that also the entrance size has shrunken, as SBA2-120/24_II showed a very sharp onset of desorption in Figure 7.4A, while SBA2-100/24 displayed a more gradual onset. From argon physisorption it is clear that SBA2-100/24 likely has a wider entrance size distribution than SBA2-100/24_II.

For the SBA-16 materials, argon physisorption provided an essential extension of the detectable entrance size limit. However, argon physisorption at 77 K is limited to cage sizes up to 15 nm, due to the measurement temperature well below the bulk triple point of Ar.[53, 54] While this is circumvented by performing argon physisorption at its triple point, 87 K, the extension of the lower relative pressure limit would then

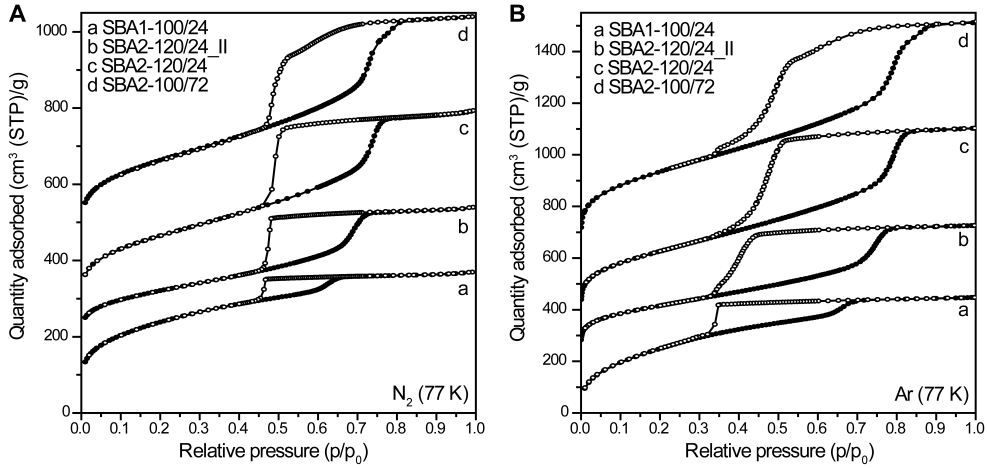

Figure 7.4. Physisorption isotherms for selected SBA-16 silica materials obtained by (A) N_2 and (B) Ar at 77 K, isotherms are offset for clarity with (A) 175, 260 and 450 cm^3 (STP)/g and (B) 275, 425 and 700 cm^3 (STP)/g.

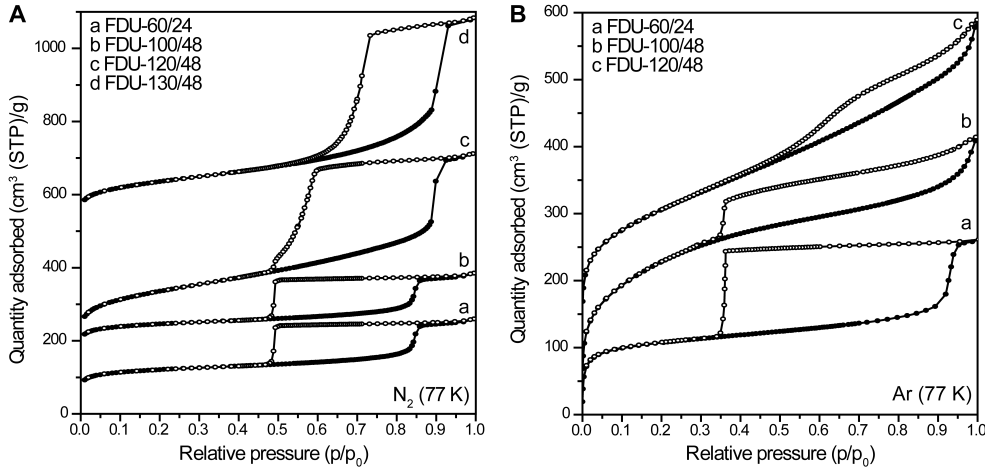

Figure 7.5. Physisorption isotherms for selected FDU-12 silica materials obtained by (A) N_2 and (B) Ar at 77 K, isotherms are offset for clarity with (A) 125, 175 and 525 and cm^3 (STP)/g and (B) 50 and 150 cm^3 (STP)/g.

be largely lost.[53] For the ultralarge cage FDU-12 materials indeed only FDU-60/24 showed capillary condensation of Ar at 77 K (Figure 7.5B, isotherm a). On the other hand, Figure 7.5A shows that capillary condensation/evaporation of N_2 occurred for all FDU-12 materials. Here, the FDU-12 materials with the highest hydrothermal treatment temperatures at 120 ºC and 130 ºC display desorption via pore blocking (isotherms c and d), while the entrance sizes of the other FDU-12 materials caused desorption via cavitation (isotherms a and b). Therefore, entrance size information can only be extracted from physisorption for 2 out of 6 FDU-12 materials.

7.3.4 Entrance size analysis by thermoporometry

Physisorption with N_2 and Ar confirmed that the synthesized materials formed series with varying cage and entrance sizes. Of a limited number of materials entrance sizes could be assessed with physisorption from the desorption branch. We now discuss the use of thermoporometry with DSC to determine the entrance sizes by the freezing point onsets of water confined in the cage materials. As the freezing of water is controlled by nucleation it is sensitive towards the entrance size. The freezing point depression is determined by the entrance size for water in contact with extraporous ice that freezes by heterogeneous nucleation. However, water freezing by homogeneous nucleation around -39 ºC limits the entrance size sensitivity, similar to the effect of cavitation in gas desorption.[62]

Figure 7.6A and B show the thermograms recorded during cooling for series of SBA-16 and FDU-12 materials, respectively, that were impregnated with an excess

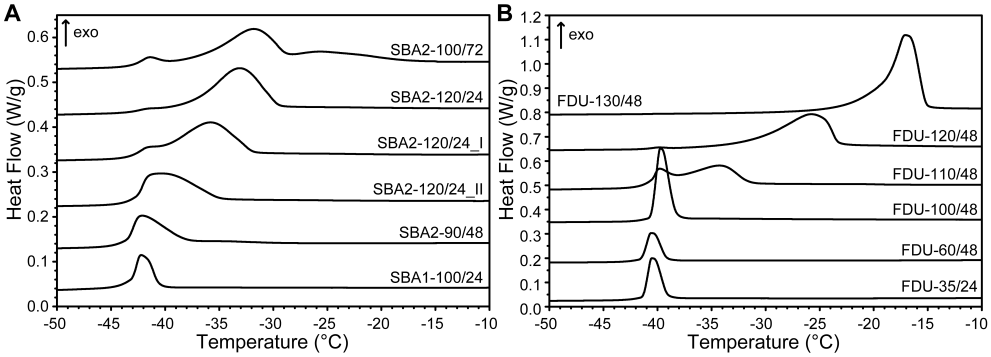

Figure 7.6. DSC thermograms of selected (A) SBA-16 and (B) FDU-12 silica materials impregnated with a twofold excess of water compared to the pore volume, recorded during cooling at 1 ºC/min, thermograms are offset for clarity.

of water. For the SBA-16 materials a gradual decrease in the freezing point onset is observed from SBA2-100/72 to SBA1-100/24. Clearly, the additional heat treatment of SBA2-120/24_I and SBA2-120/24_II at 650 ºC and 800 ºC resulted in a significant decrease of the onset freezing point as compared to their parent, SBA2-120/24. For the FDU-12 materials (Figure 7.6B), the samples FDU-35/24 and FDU-60/48 showed sharp freezing peaks with onsets of -39.1 ºC, while for the other FDU-12 samples higher freezing temperatures indicated significantly larger entrance sizes. Most samples exhibited a single freezing event, indicating uniformity of entrance sizes. As an exception, SBA2-100/72 displayed 3 freezing events, likely related to the presence of multiple mesophases which is in agreement with the desorption profile observed in argon physisorption (Figure 7.4B, isotherm d). A few other samples also displayed a minor additional peak of water freezing by homogeneous nucleation around -39 ºC, which indicated some cages with narrowed entrances. As the peak shapes persisted for thermograms recorded at heating rates as low as 0.2 º/min, peak broadening is ascribed to the pore entrance size distribution rather than the scanning rate of DSC. The freezing peaks of SBA1-100/24 (Figure 7.6A) and FDU-35/48 and FDU-60/48 (Figure 7.6B) were sharp, occurred at temperatures below -39 ºC, had a sharp onset and are hence likely controlled by homogeneous nucleation. The freezing peak for FDU-100/48 was slightly broader with an onset of -38.4 ºC and indicated freezing of water by heterogeneous nucleation. Therefore, onset freezing points below -38.5 ºC measured at 1 ºC/min are considered to be related to homogeneous nucleation and forms the lower limit for entrance size analysis.

The entrance sizes are calculated from the onset freezing point using the Gibbs-Thomson equation and cylindrical ordered mesoporous silica reference materials and are listed in Table 7.4. For the SBA-16 materials, only SBA1-60/24 and SBA1-100/24 showed freezing onset temperatures below -38.5 ºC, which means that with DSC the

entrance sizes of all the other SBA-16 materials can be determined. Freezing point onsets between -37.7 ºC and 28.8 ºC corresponded to entrance sizes between 4.2 nm and 5.7 nm. The increase in hydrothermal treatment temperature from 100 ºC to 130 ºC for the synthesis of FDU-12 materials led to an increase of the freezing point onset from -38.4 ºC to -15.2 ºC corresponding to an almost triple increase in entrance size from 4.5 nm to 11.0 nm. Interestingly, the homogeneous freezing temperature for selected SBA-16 materials seemed to be related to the cage diameter (see figure S5). A similar effect has been observed by other groups for the dependence of the relative pressure of cavitation on cage sizes below 8 nm.[19, 26, 31, 37, 39, 63] Significant increases in the onset freezing points which can be measured with high temperature accuracy corresponded to small increases in entrance sizes. DSC therefore provides high sensitivity and high resolution to distinguish entrance sizes.

Table 7.4. Entrance size analysis by DSC and physisorption with N_2 and Ar at 77 K.

	onset freezing point (ºC)[a]	entrance size (nm)		
Sample		DSC[b]	N_2-phys[c]	Ar-phys[c]
SBA1-60/24	-41.3	≤4.2	≤ 4.7	≤ 3.6
SBA1-100/24	-40.5	≤4.2	≤ 4.7	≤ 3.6
SBA2-90/48	-37.7	4.2	≤ 4.7	3.69
SBA2-120/24_II	-33.5	4.6	≤ 4.7	3.96
SBA2-120/24_I	-30.5	5.1	≤ 4.7	4.20
SBA2-120/24	-29.6	5.4	4.96	4.49
SBA2-100/72	-28.2	5.7	5.0/≤ 4.7	4.55
FDU-35/24	-39.1	≤4.2	≤ 4.9	≤ 3.7
FDU-60/48	-39.1	≤4.2	≤ 4.9	≤ 3.7
FDU-100/48	-38.4	4.4	≤ 4.9	-
FDU-110/48	-31.5	5.3	≤ 4.9	-
FDU-120/48	-23.2	7.2	5.85	-
FDU-130/48	-15.2	11.0	8.19	-

[a] freezing point determined by DSC by cooling at 1 ºC/min, [b] entrance size determined from the onset freezing point by DSC using the Gibbs-Thomson equation with fitting parameters listed in Table 2, [c] entrance size determined from pore size distribution calculated by BJH from the N_2 or Ar desorption branch.

7.3.5 Comparison of entrance size analyses by thermoporometry and physisorption

Entrance size of cage materials can only be determined by physisorption if desorption is controlled by pore blocking rather than cavitation. Similarly, with DSC the range of entrance sizes that can be analyzed is limited by the homogeneous nucleation of water. To directly compare DSC with both nitrogen and argon physisorption, we applied the BJH model to calculate the pore size distributions from desorption and used the BJH pore diameters of cylindrical silica reference materials to fit the Gibbs-Thomson equation. Although the BJH method is known to underestimate the absolute pore size by up to 1 nm,[14] it enables a fair comparison for different adsorptives. The entrance size analyses for both N_2 and Ar physisorption contain the same systematic error as we use the corrections for the Kelvin equation as published by Kruk *et al*. and thickness curves reported for macroporous silica materials.[58, 60] With nitrogen physisorption cavitation limits the entrance size analysis to 4.7 nm, while with Ar entrance sizes down to 3.6 nm were detected, which corresponds earlier reported lower limits.[30, 31] With DSC, freezing temperatures above -38.5 ºC were related to heterogeneous nucleation and therefore controlled by the pore entrance size. This

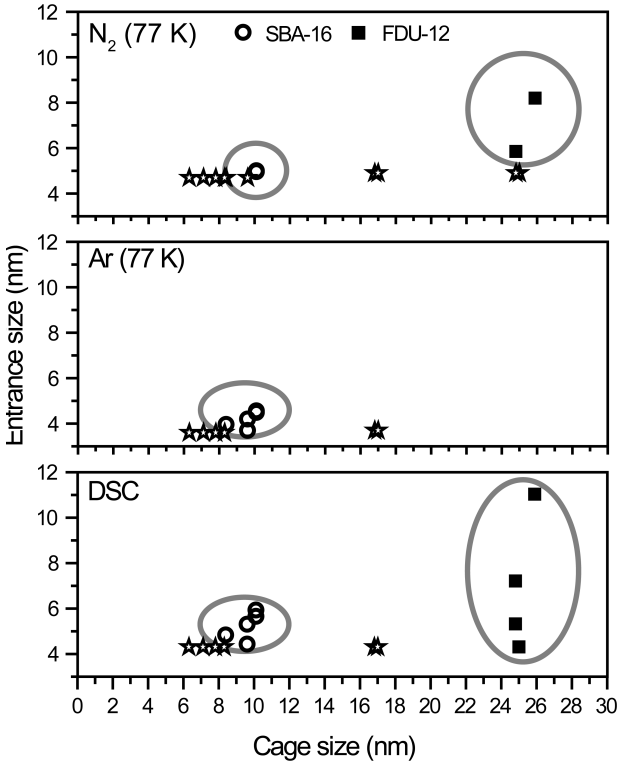

Figure 7.7. Entrance sizes versus cage size as determined by DSC, nitrogen physisorption and argon physisorption. Areas enclosed by solid grey lines indicate meaningful results. Stars indicate entrance sizes below the limit of the respective techniques.

corresponds to an entrance size limit of 4.2 nm, based on the BJH pore sizes of the cylindrical mesoporous silica references.

In Figure 7.7 the range of materials for which relevant results were obtained by thermoporometry and physisorption can be compared. The results are plotted as a function of the cage diameter as there is no readily available independent method to determine the entrance sizes. Comparison of the absolute entrance sizes obtained by the different techniques would benefit from an independent method such as electron tomography.[17, 64] Nevertheless, here we focus on a generalization of the range of materials that can be analyzed by thermoporometry as compared to physisorption. Although the entrance sizes of the cage materials are not assessed as a function of their cage diameter, the cage diameter turned out to be an important parameter that showed the added value of DSC for entrance size analysis. Specifically, entrance sizes of several ultra-large FDU-12 materials could only be analyzed with DSC as freezing by heterogeneous nucleation was observed as is indicated in Figure 7.7 . These materials displayed cavitation in nitrogen physisorption and had cages too large for argon condensation at 77 K. Furthermore, the entrance sizes of a large number of the SBA-16 materials was determined with DSC as well as argon physisorption, while with nitrogen physisorption for only one sample a meaningful result was obtained. In general, DSC resulted in larger entrance sizes than physisorption (Table 7.4). However, the application of the argon desorption branch to calculate absolute pore size distributions is under discussion,[60, 65] while the entrance sizes determined by DSC are based on the pore size distributions obtained from adsorption, which results in a more accurate freezing temperature-pore radius relation.

7.2.6 Entrance size distribution by thermoporometry

We developed a new analysis protocol that allowed determining the entrance size distribution with thermoporometry by DSC. It is based on quantification of the amount of water frozen after equilibration at different temperatures. Water in cages freezes at the temperature that corresponds to the heterogeneous nucleation temperature of the largest entrance size in the pathway that connects to the extraporous ice. The amount of frozen water is determined from the melting enthalpy released during heating. The total amount of water that could freeze in the cages was determined from the melting enthalpy released after freezing at -70 ºC. The cumulative amount of water freezing in the cages as a function of the temperature can be used to calculate the differential freezing cage volume. This plotted in Figure 7.8 and this curve represents the entrance size distribution. The top axis shows the entrance sizes corresponding to the temperature axis as calculated with the Gibbs-Thomson equation (Table 7.2). The shapes of the entrance size distributions in Figure 7.8A and B correspond to the peak shapes observed in the scanning experiments (Figure 7.6A and B), confirming that a

scanning rate of 1 ºC/min is sufficient to detect effects of entrance size distributions. Furthermore, the onset temperatures observed in the entrance size distribution agrees well with the onset temperatures obtained by scanning with 1 ºC/min. For comparison Figure 7.9 shows the pore size distribution calculated from the Ar desorption branch with the BJH model for selected SBA-16 materials. The entrance size distribution obtained for these materials by DSC (Figure 7.8A) agrees well with the results from argon desorption, which validates our new analysis protocol. The entrance size distribution for the FDU-12 materials (Figure 7.8B) was determined with DSC, but was inaccessible by any of the other physisorption techniques.

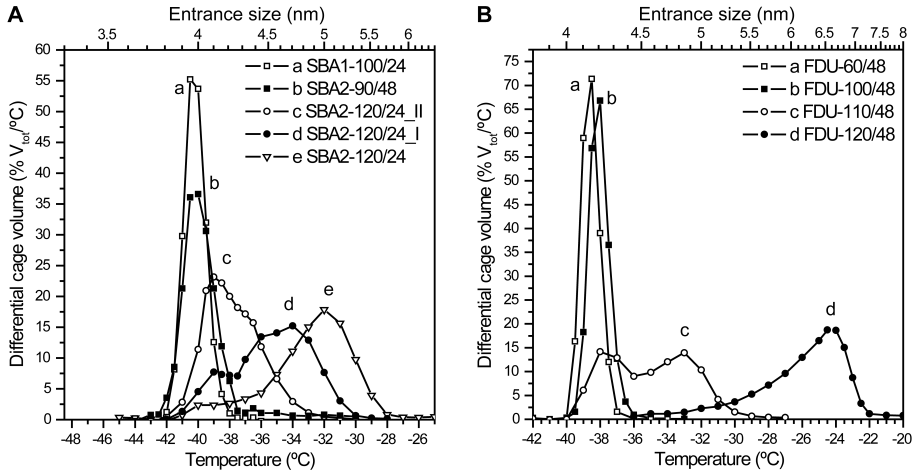

Figure 7.8. Entrance size distributions obtained by DSC for (A) selected SBA-16 materials and (B) selected FDU-12 materials.

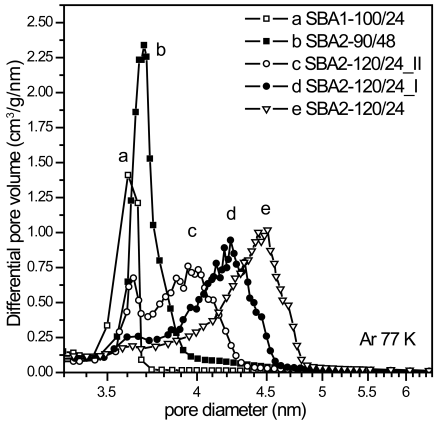

Figure 7.9. BJH pore size distributions for selected SBA-16 silica materials calculated with the BJH model from the Ar desorption isotherms.

7.4 Conclusions

The value of thermoporometry by differential scanning calorimetry for the quantitative analysis of entrance size analysis in mesoporous materials was demonstrated using series of SBA-16 and FDU-12 silica materials with varying cage and entrance sizes. A direct comparison with more conventional physisorption techniques using nitrogen and argon at 77 K was made. DSC extends the quantifiable range of entrance sizes. Due to the homogeneous nucleation of water, DSC could determine entrance sizes down to 4.2 nm (based on the BJH model). Cavitation limits argon physisorption at 77 K to entrance sizes down to 3.6 nm and nitrogen physisorption to 4.7 nm. However, DSC has an important advantage over argon physisorption for cages larger than 15 nm, which exceeded the condensation limit of argon. Furthermore, using DSC we were able to determine the cage entrance size distribution for materials that could not be analyzed using either of the physisorption techniques. We report here a first proof of principle that would profit from further development of the theory and modeling of the entrance size dependence of the freezing of water and independent techniques to study the entrance size (e.g. electron tomography[64]). These results clearly show that DSC is a powerful analysis technique for mesoporous materials and is potentially applicable a wide range of materials.

Acknowledgements

Gonzalo Prieto (Utrecht University) contributed equally to this work. The authors thank Mies van Steenbergen and Herre Talsma (Utrecht Univeristy) for technical support of thermal analysis equipment. Mw. E. van Donselaar (Utrecht University) is acknowledged for ultramicrotomy instructions. Mw. M. Versluijs-Helder is acknowledged for SEM analysis. The Electron Microscopy Unit at Utrecht University is acknowledged for their excellent facilities. The work of Gonzalo Prieto was supported as part of the Center for Atomic-Level Catalyst Design, an Energy Frontier Research Center funded by the U.S. Department of Energy, Office of Science, Office of Basic Energy Sciences under Award Number DE-SC0001058.

References

[1] D. Y. Zhao, Q. S. Huo, J. L. Feng, B. F. Chmelka and G. D. Stucky, *J. Am. Chem. Soc.* **1998**, *120*, 6024.
[2] C. Z. Yu, Y. H. Yu and D. Y. Zhao, *Chem. Comm.* **2000**, 575.
[3] J. Fan, C. Z. Yu, T. Gao, J. Lei, B. Z. Tian, L. M. Wang, Q. Luo, B. Tu, W. Z. Zhou and D. Y. Zhao, *Angew. Chem., Int. Ed.* **2003**, *42*, 3146.
[4] J. R. Matos, M. Kruk, L. P. Mercuri, M. Jaroniec, L. Zhao, T. Kamiyama, O. Terasaki, T. J. Pinnavaia and Y. Liu, *J. Am. Chem. Soc.* **2003**, *125*, 821.
[5] H. Q. Yang, L. Zhang, W. G. Su, Q. H. Yang and C. Li, *J. Catal.* **2007**, *248*, 204.

[6] Y. C. Hu, Z. Z. Zhi, Q. F. Zhao, C. Wu, P. Zhao, H. T. Jiang, T. Y. Jiang and S. L. Wang, *Micropor. Mesopor. Mat.* **2012**, *147*, 94.
[7] J. K. Shon, S. S. Kong, Y. S. Kim, J. H. Lee, W. K. Park, S. C. Park and J. M. Kim, *Micropor. Mesopor. Mat.* **2009**, *120*, 441.
[8] W. B. Yue, A. H. Hill, A. Harrison and W. Z. Zhou, *Chem. Comm.* **2007**, 2518.
[9] A. H. Lu and F. Schuth, *Adv. Mater.* **2006**, *18*, 1793.
[10] L. Y. Li, D. L. King, J. Liu, Q. S. Huo, K. K. Zhu, C. M. Wang, M. Gerber, D. Stevens and Y. Wang, *Chem. Mater.* **2009**, *21*, 5358.
[11] Z. C. Ma, H. Q. Yang, Y. Qin, Y. J. Hao and G. A. Li, *Journal of Molecular Catalysis a-Chemical* **2010**, *331*, 78.
[12] H. Q. Yang, J. Li, J. Yang, Z. M. Liu, Q. H. Yang and C. Li, *Chem. Comm.* **2007**, 1086.
[13] H. Q. Yang, L. Zhang, L. Zhong, Q. H. Yang and C. Li, *Angew. Chem., Int. Ed.* **2007**, *46*, 6861.
[14] P. I. Ravikovitch and A. V. Neimark, *Langmuir* **2002**, *18*, 1550.
[15] Y. Sakamoto, M. Kaneda, O. Terasaki, D. Y. Zhao, J. M. Kim, G. Stucky, H. J. Shim and R. Ryoo, *Nature* **2000**, *408*, 449.
[16] T. Yu, H. Zhang, X. W. Yan, Z. X. Chen, X. D. Zou, P. Oleynikov and D. Y. Zhao, *J. Phys. Chem. B* **2006**, *110*, 21467.
[17] O. Ersen, J. Parmentier, L. A. Solovyov, M. Drillon, C. Pham-Huu, J. Werckmann and P. Schultz, *J. Am. Chem. Soc.* **2008**, *130*, 16800.
[18] F. Kleitz, D. N. Liu, G. M. Anilkumar, I. S. Park, L. A. Solovyov, A. N. Shmakov and R. Ryoo, *J. Phys. Chem. B* **2003**, *107*, 14296.
[19] F. Kleitz, T. Czuryszkiewicz, L. A. Solovyov and M. Linden, *Chem. Mater.* **2006**, *18*, 5070.
[20] O. Sel, A. Brandt, D. Wallacher, M. Thommes and B. Smarsly, *Langmuir* **2007**, *23*, 4724.
[21] S. Mascotto, D. Wallacher, A. Brandt, T. Hauss, M. Thommes, G. A. Zickler, S. S. Funari, A. Timmann and B. M. Smarsly, *Langmuir* **2009**, *25*, 12670.
[22] T. W. Kim, R. Ryoo, K. P. Gierszal, M. Jaroniec, L. A. Solovyov, Y. Sakamoto and O. Terasaki, *J. Mater. Chem.* **2005**, *15*, 1560.
[23] K. Morishige and T. Yasuki, *J. Phys. Chem. C* **2010**, *114*, 10910.
[24] M. Kruk, V. Antochshuk, J. R. Matos, L. P. Mercuri and M. Jaroniec, *J. Am. Chem. Soc.* **2002**, *124*, 768.
[25] V. Antochshuk, M. Kruk and M. Jaroniec, *J. Phys. Chem. B* **2003**, *107*, 11900.
[26] T. W. Kim, R. Ryoo, M. Kruk, K. P. Gierszal, M. Jaroniec, S. Kamiya and O. Terasaki, *J. Phys. Chem. B* **2004**, *108*, 11480.
[27] H. I. Lee, G. D. Stucky, J. H. Kim, C. Pak, H. Chang and J. M. Kim, *Adv. Mater.* **2011**, *23*, 2357.
[28] J. Lee, J. Kim, J. Kim, H. F. Jia, M. I. Kim, J. H. Kwak, S. M. Jin, A. Dohnalkova, H. G. Park, H. N. Chang, P. Wang, J. W. Grate and T. Hyeon, *Small* **2005**, *1*, 744.
[29] P. Schmidt-Winkel, W. W. Lukens, D. Y. Zhao, P. D. Yang, B. F. Chmelka and G. D. Stucky, *J. Am. Chem. Soc.* **1999**, *121*, 254.
[30] M. Kruk and M. Jaroniec, *Chem. Mater.* **2003**, *15*, 2942.
[31] P. I. Ravikovitch and A. V. Neimark, *Langmuir* **2002**, *18*, 9830.
[32] K. Morishige, M. Tateishi, F. Hirose and K. Aramaki, *Langmuir* **2006**, *22*, 9220.
[33] M. Kruk, E. B. Celer, J. R. Matos, S. Pikus and M. Jaroniec, *J. Phys. Chem. B* **2005**, *109*, 3838.
[34] M. Kruk, M. Jaroniec, S. H. Joo and R. Ryoo, *J. Phys. Chem. B* **2003**, *107*, 2205.
[35] R. M. Grudzien and M. Jaroniec, *Chem. Comm.* **2005**, 1076.
[36] K. Morishige and Y. Kanzaki, *J. Phys. Chem. C* **2009**, *113*, 14927.
[37] K. Morishige and K. Yoshida, *J. Phys. Chem. C* **2010**, *114*, 7095.
[38] O. C. Gobin, Y. Wan, D. Y. Zhao, F. Kleitz and S. Kaliaguine, *J. Phys. Chem. C* **2007**, *111*, 3053.
[39] M. Thommes, B. Smarsly, M. Groenewolt, P. I. Ravikovitch and A. V. Neimark, *Langmuir* **2006**, *22*, 756.
[40] M. Brun, A. Lallemand, J.-F. Quinson and C. Eyraud, *Thermochim. Acta* **1977**, *21*, 59.
[41] K. Ishikiriyama and M. Todoki, *Thermochim. Acta* **1995**, *256*, 213.
[42] A. Schreiber, I. Ketelsen and G. H. Findenegg, *Phys. Chem. Chem. Phys.* **2001**, *3*, 1185.
[43] I. Beurroies, R. Denoyel, P. Llewellyn and J. Rouquerol, *Thermochim. Acta* **2004**, *421*, 11.
[44] T. M. Eggenhuisen, M. J. van Steenbergen, H. Talsma, P. E. de Jongh and K. P. de Jong, *J. Phys. Chem. C* **2009**, *113*, 16785.
[45] T. M. Eggenhuisen, J. P. den Breejen, D. Verdoes, P. E. de Jongh and K. P. de Jong, *J. Am. Chem. Soc.* **2010**, *132*, 18318.

[46] R. Denoyel and R. J. M. Pellenq, *Langmuir* **2002**, *18*, 2710.
[47] O. Petrov and F. I, *Physical Review E* **2006**, *73*.
[48] A. H. Janssen, H. Talsma, M. J. van Steenbergen and K. P. de Jong, *Langmuir* **2004**, *20*, 41.
[49] K. Morishige, H. Yasunaga, R. Denoyel and V. Wernert, *J. Phys. Chem. C* **2007**, *111*, 9488.
[50] S. Kittaka, Y. Ueda, F. Fujisaki, T. Iiyama and T. Yamaguchi, *Phys. Chem. Chem. Phys.* **2011**, *13*, 17222.
[51] K. Morishige, H. Yasunaga and Y. Matsutani, *J. Phys. Chem. C* **2010**, *114*, 4028.
[52] O. Petrov and I. Furo, *Phys. Chem. Chem. Phys.* **2011**, *13*, 16358.
[53] M. Thommes, R. Kohn and M. Froba, *Appl. Surf. Sci.* **2002**, *196*, 239.
[54] M. Kruk, J. R. Matos and M. Jaroniec, *Colloids Surf., A* **2004**, *241*, 27.
[55] C. Reichenbach, G. Kalies, D. Enke and D. Klank, *Langmuir* **2011**, *27*, 10699.
[56] F. Kleitz, L. A. Solovyov, G. M. Anilkumar, S. H. Choi and R. Ryoo, *Chem. Comm.* **2004**, 1536.
[57] M. Kruk and C. M. Hui, *J. Am. Chem. Soc.* **2008**, *130*, 1528.
[58] M. Kruk, M. Jaroniec and A. Sayari, *Langmuir* **1997**, *13*, 6267.
[59] M. Jaroniec, M. Kruk, J. P. Olivier and S. Koch, *Proceedings of COPS-V, Heidelberg, Germany* **1999**.
[60] M. Kruk and M. Jaroniec, *J. Phys. Chem. B* **2002**, *106*, 4732.
[61] S. Jahnert, F. V. Chavez, G. E. Schaumann, A. Schreiber, M. Schonhoff and G. H. Findenegg, *Phys. Chem. Chem. Phys.* **2008**, *10*, 6039.
[62] C. A. Angell, *Supercooled Water*, in *Water and aqueous solutions at subzero temperatures*, F. Franks, Editor. 1982, Plenum Press: New York.
[63] C. J. Rasmussen, A. Vishnyakov, M. Thommes, B. M. Smarsly, F. Kleitz and A. V. Neimark, *Langmuir* **2010**, *26*, 10147.
[64] H. Friedrich, P. E. de Jongh, A. J. Verkleij and K. P. de Jong, *Chem. Rev.* **2009**, *109*, 1613.
[65] M. Kruk and M. Jaroniec, *Chem. Mater.* **2000**, *12*, 222.

Chapter 8a

Summary

Catalysts are indispensable for modern day society since they are used in the production of transportation fuels, chemicals and materials. Understanding the structure-activity relation for a catalytic system allows the formulation of catalyst structure specifications that optimizes activity, selectivity and stability. For supported catalysts, size and shape of the catalytic nanoparticles and their distribution over the support are of paramount importance to achieve the desired catalytic properties. Nevertheless, catalyst preparation has long been considered an art rather than a science.

In this work, catalyst preparation is rationalized from the phase behavior of the precursor salt or salt solution and is mainly performed within the framework of silica supported cobalt catalysts for Fischer-Tropsch synthesis. The Fischer-Tropsch synthesis involves the conversion of CO and H_2 gas into longer chain hydrocarbons to produce transportation fuels and lubricants from feedstock other than crude oil, e.g. natural gas, coal or biomass. Therefore, this process has a high industrial and economic relevance. Supported cobalt catalysts require a controlled preparation method as there is an optimum cobalt nanoparticle size of ~6 nm. Furthermore, high metal loadings are needed to obtain high activity of the supported catalysts. At the same time, the nanoparticles should be distributed uniformly over the support such that their nearest neighbor distance is maximized and deactivation due to the coalescence of nanoparticles (sintering) is minimized. Finally, due the large scale of the application, a convenient preparation method producing little waste is desired.

Impregnation and drying is such a convenient preparation method and is commonly applied in industry and academia. However, it suffers from a lack of control over the nanoparticle dispersion and distribution, especially when using low cost transition metal nitrate salts with a high solubility in water. In this thesis we aim to acquire fundamental insight into this preparation method to reach the ultimate goal: equally-sized and maximally-spaced nanoparticles.

Chapter 2 is focused on the effectiveness of impregnation as the first step of

supported catalyst preparation via impregnation and drying. Confined liquids have a depressed melting point as compared to the bulk liquid. Therefore, with differential scanning calorimetry (DSC) the melting and freezing of water or aqueous salt solutions absorbed in the pores of a mesoporous silica is distinguished from melting of extraporous liquid. By quantification of the melting enthalpy released by extraporous liquid and thermogravimetric analysis, a pore-filling of 85-100% was determined after a single impregnation step with water or aqueous salt solutions.

Cryo-electron tomography (cryo-ET) was used to image the distribution of the solution after impregnation, the salt after drying and the metal oxide after salt decomposition which is described in **Chapter 3**. Cryo-ET confirmed that the pores of rodlike SBA-15 support particles were by and large homogeneously filled with the salt solution after impregnation. By an *in-situ* drying experiment, it was shown that freeze-drying is essential to restrict mobility of the solution during drying. Freeze-drying yielded a homogeneous salt distribution, whereas by conventional drying a heterogeneous deposition of the salt was obtained. Rational syntheses of catalysts were performed by combining freeze-drying with the NO-assisted decomposition method, which is known to restrict precursor mobility during decomposition. Indeed, platinum promoted cobalt catalysts and nickel based catalysts were synthesized with much more uniform nanoparticle distributions.

The fundamentals of freeze-drying for supported catalyst preparation with controlled nanoparticle distribution are described in detail in **Chapter 4**. The phase behavior of a cobalt nitrate solution and a cobalt nitrate salt in a mesoporous silica matrix was investigated with DSC. Based on the depressed freezing and melting points, two different freeze-drying methods were developed. Catalyst synthesis by freeze-drying starting from liquid nitrogen temperatures resulted in uniform nanoparticle distributions using both the solution and salt as precursors, while by conventional drying extensive nanoparticle clustering was observed. Due to its higher freezing and melting point, the catalyst prepared via melt infiltration of the cobalt nitrate salt was also successfully freeze-dried starting from -45 ºC. However, this freeze-drying procedure caused extensive redistribution of the cobalt nitrate solution which resulted in a catalyst with an egg-shell configuration. The synthesized catalysts were highly active for the Fischer-Tropsch reaction at 1 bar. They form an excellent platform for the future study of the effect of nanoparticle spacing on catalyst deactivation by sintering under industrially relevant conditions.

Chapter 5 describes supported catalyst preparation by melt infiltration as an alternative to impregnation. Using DSC, infiltration of a mesoporous silica matrix with hydrated cobalt nitrate salt is studied *in-situ*. It was shown that by melt infiltration the precursor salt was successfully deposited inside the pore system and after decomposition led to highly dispersed cobalt nanoparticles. The nanoparticles

size and distribution were similar to that obtained by preparation via impregnation and drying and the catalysts showed high activity for the Fischer-Tropsch reaction.

Nanoparticles in supported catalysts can give rise to pore blocking and pore constrictions. In **Chapter 6** we introduce DSC of the freezing and melting of confined water and argon physisorption as essential techniques for the quantification of pore blockage. A set of supported catalysts with varying degrees of pore blockage was synthesized using NiO nanoparticles of different sizes and ordered mesoporous silica supports with varying pore diameters. Both DSC and argon physisorption showed to be applicable to an extended range of pore blockages as compared to classical nitrogen physisorption.

Cage silica materials are a unique class of ordered mesoporous materials that consist of spherical cages connected by narrow entrances. **Chapter 7** describes the use of DSC of the freezing and melting of water confined inside the cage materials to quantify the entrance sizes. Although limited by the homogeneous nucleation of water, DSC showed to be sensitive towards a larger range of entrance sizes as compared to physisorption techniques. Furthermore, the entrance size distribution was quantified for the first time.

Chapter 8b

Conclusions & Outlook

The study of nanoconfined phases allows rationalization of supported catalyst preparation. The effectiveness of two precursor loading methods, solution impregnation and melt infiltration was quantified by differential scanning calorimetry. Using cryo-electron tomography the distribution of salt after different drying treatments was visualized. This showed that freeze-drying is essential to obtain homogeneous salt distributions and leads to more uniform nanoparticle distribution after precursor decomposition than conventional drying. Moreover, the nanoparticle distribution was manipulated by different drying treatments that were based on the phase behavior of the precursors. The prepared Fischer-Tropsch catalysts form an excellent starting point for future deactivation studies under industrially relevant reaction conditions.

The study of nanoconfined phases and the use of freeze-drying described in this thesis can be applied to a much wider range of metal precursors and supports than presented here. Freeze-drying is widely applied in the pharmaceutical industry. Therefore, a lot of knowledge on process optimization is available. For example, the melting point of confined hydrated transition metal salts lies higher than for confined transition metal salt solutions. This allows the use of higher temperatures during freeze-drying which would considerably decrease the required drying time. Nevertheless, for successful freeze-drying a fundamental understanding of the nanoconfined phases involved in each synthesis is required, for which DSC is a prime technique. The precursor salt, concentration and solvent as well as pore geometry of the support have large influences on the confined liquid's freezing and melting point depression. The applicability of freeze-drying for supported catalyst preparation can also be expanded to other (oxidic) supports. However, the phase behavior of confined liquids weakly interacting with the support is most suitable to be studied with DSC. For confined liquids with stronger interactions with the support, a large fraction of the confined material will not freeze. For example, γ-Al_2O_3 is a common industrially applied support that has a higher point of zero charge than silica. Therefore, its interaction with positively charged ions in low pH

solutions is stronger. Figure 8.1 illustrates the support effect on the phase behavior of confined $Co(NO_3)_2 \cdot 6H_2O$. Confined within a weakly interacting mesoporous silica support a clear melting peak of the confined phase at ~20 ºC is observed. However, a significantly lower melting enthalpy is released by $Co(NO_3)_2 \cdot 6H_2O$ confined in a γ-Al_2O_3 support with similar pore sizes; this indicates melting of a smaller amount of confined $Co(NO_3)_2 \cdot 6H_2O$. It is postulated that part of the $Co(NO_3)_2 \cdot 6H_2O$ is interacting with the support so strongly that it cannot freeze. This will undoubtedly influence the effect of the precursor loading step and drying on the final metal oxide nanoparticle dispersion and distribution.

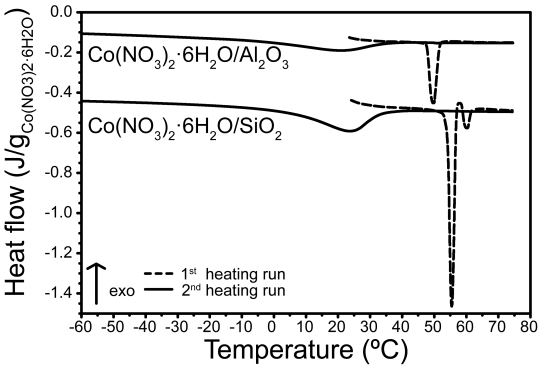

Figure 8.1. DSC recordings of melt infiltration of a mesoporous γ-Al_2O_3 and SiO_2 support with $Co(NO_3)_2 \cdot 6H_2O$. The heat flow is normalized to the amount of $Co(NO_3)_2 \cdot 6H_2O$.

The NO-assisted decomposition method is essential for the preparation of catalysts with controlled nanoparticle distributions using transition metal nitrate precursors and silica supports. Nevertheless, depending on the support-metal salt combination, the calcination atmosphere should be optimized. It is clear that NO also affects the preparation of supported catalysts by freeze-drying and leads to catalysts with higher dispersions as compared to decomposition of freeze-dried catalysts in an inert gas atmosphere. However, the exact mechanism is as of yet unclear. One of the key effects of NO for the decomposition of hydrated transition metal nitrates is the formation of a basic transition metal nitrate intermediate. Surprisingly, during the decomposition of *dehydrated* cobalt nitrate obtained after freeze-drying, this intermediate was also observed using DRIFT. Apparently a small amount of residual water and/or the presence of surface hydroxyl groups are sufficient to form this intermediate. Furthermore, the local dense packing of nanoparticles observed after NO-assisted decomposition of hydrated transition metal nitrates cannot be fully ascribed to the effect of drying. Imaging the distribution of the basic transition metal nitrate intermediate may elucidate this matter. The decomposition of precursor salts can be visualized in-situ with environmental TEM under different gas atmospheres. However, the concentrations of decomposition products, which are known to affect active phase mobility during decomposition, are not representative for catalyst preparation on industrial scale or even lab scale.

In the last two chapters of this thesis, the effect of pore structures on the freezing and melting of water has been discussed. First, with DSC pore blockages in supported catalysts were quantified by the detection of delayed freezing of water in constricted pores. Second, DSC proved to be highly sensitive towards the entrance size of mesoporous cage silica materials. For both applications conventional gas physisorption techniques are available, but DSC provided significant extensions of the range of pore constrictions and entrance sizes that could be detected. These chapters show that DSC is a valuable tool for the characterization of complex mesoporous structures, which hopefully stimulates the further development of theoretical models improving the quantitative character of the analysis. This would enhance the use of DSC as characterization technique but may also be beneficial for the understanding of confinement on catalysis, stabilization of biomolocules and homogeneous nucleation.

In this thesis the synthesis of supported catalysts is rationalized. To this purpose, techniques more common to pharmaceutical science, freeze-drying and DSC, have been essential. Furthermore, principles from physical chemistry such as freezing point depression, homogeneous nucleation and wetting have played dominant roles. Advanced (cryo-)electron microscopy techniques, that find often more application in biology or soft matter and the synthesis of ordered model supports were indispensable. This work showed that catalyst preparation profits from a multi-disciplinary approach.

Chapter 8c

Samenvatting

Katalysatoren zijn voornamelijk bekend van de toepassing in auto's, waar ze schadelijke koolmonoxide en stikstofoxideverbindingen in de uitlaatgassen omzetten in koolstofdioxide, stikstof, zuurstof en water. Naast deze toepassing, spelen katalysatoren een onvervangbare rol in de productie van brandstoffen en chemicaliën. Sterker nog, vrijwel alle moleculen in brandstoffen voor de transportsector zijn in bewerkingsstappen in aanraking gekomen met een katalysator. Overgangsmetalen zoals nikkel en kobalt zijn veel voorkomende vaste stof katalysatoren, waarbij de reactie plaatsvindt aan het oppervlak van het metaal. De activiteit per massa-eenheid wordt grotendeels bepaald door het aantal metaalatomen aan het oppervlak. Daarom worden voor deze typen katalysatoren kleine metaaldeeltjes met afmetingen van 1-10 nanometer (1 nanometer = 1 miljardste meter) gebruikt. Om te voorkomen dat deze nanodeeltjes tijdens de reactie samensmelten of sinteren worden ze afgezet op een dragermateriaal. Deze dragers zijn veelal oxiden zoals silica of alumina met een hoog specifiek oppervlak, typisch 200-700 m^2/g.

Figuur 8.2 illustreert de verschillende lengteschalen waarop het onderzoek naar gedragen katalysatoren plaatsvindt. Figuur 8.2A laat een reactor zien waarin een katalysator zit voor de Fischer-Tropsch reactie. Aan de personen op de foto kan men zien dat het gaat om een reactor van ~20 meter in diameter en enkele tientallen meters hoog. Commerciële katalysatoren worden geproduceerd op voorgevormde katalysatordeeltjes met verschillende vormen en afmetingen in de ordegrootte van centimeters, zie Figuur 8.2B. In Figuur 8.2C zoomen we in totdat de kobaltnanodeeltjes afgezet op een koolstofnanovezel zichtbaar zijn. Dit is de lengteschaal waarop het onderzoek in dit proefschrift zich afspeelt.

Bij het bereiden van deze gedragen katalysatoren zijn een aantal eigenschappen van belang. Ten eerste moeten liefst alle metaaldeeltjes even groot zijn en de grootte moet in te stellen zijn door de bereidingsmethode. Hoe kleiner de deeltjes, hoe meer metaalatomen zich aan het oppervlak bevinden en dus hoe groter de katalytische activiteit per massa metaal. Controle over deeltjesgrootte en deeltjesgrootteverdeling

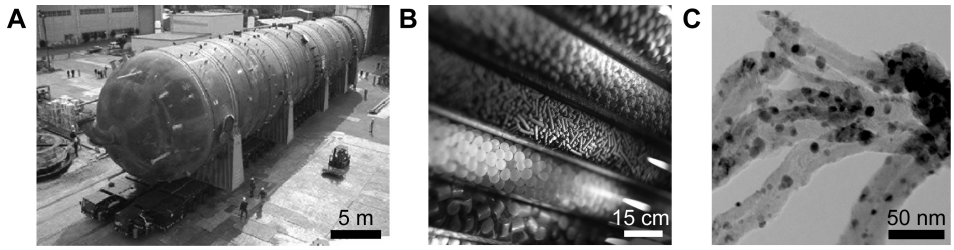

Figuur 8.2. Illustratie van de verschillende lengteschalen die op katalysatoren van toepassing zijn. (A) Reaktor voor de Fischer-Tropsch synthese wordt geïnstalleerd op een Sasol productiesite, aangepast van [1], (B) macroscopische katalysatordeeltjes en (C) kobaltnanodeeltjes op een koolstofnanovezeldrager, aangepast van [2].

is erg belangrijk omdat zelfs een klein aantal grotere deeltjes de totale activiteit sterk kan doen afnemen. Daarnaast zijn er reacties waarbij er een optimum is in the deeltjesgrootte. Ten tweede moeten de deeltjes zo goed mogelijk verspreid zijn over het beschikbare drageroppervlak. Dit betekent dat de afstand tot het dichtstbijzijnde naastgelegen nanodeeltje zo groot mogelijk moet zijn om de kans dat de deeltjes samen kunnen smelten tijdens de reactie te verkleinen. Dit laatste is van essentieel belang om de deactivering van katalysatoren te verminderen. Vooral deze tweede eis vormt het kerndoel van het onderzoek beschreven in dit proefschrift.

Dit onderzoek is vooral toegespitst op katalysatoren voor de Fischer-Tropsch synthese. Bij deze reactie worden langere koolwaterstofketens gemaakt uit koolmonoxide- en waterstofgas. De producten kunnen gebruikt worden als hoogwaardige brandstoffen en smeermiddelen. Normaal gesproken wordt ruwe olie als grondstof voor deze producten gebruikt, maar door de Fischer-Tropsch synthese toe te passen kunnen ook andere koolstofbronnen als steenkool, aardgas of biomassa gebruikt worden. Kobalt is een van de gebruikte katalysatoren voor deze reactie en deeltjes van ~6 nm vertonen een maximale activiteit. De gecontroleerde bereiding van dergelijke katalysatoren met eenvoudige, milieuvriendelijke en kosteneffectieve bereidingsmethode is een uitdaging. Hier gebruiken we gehydrateerde nitraatzouten als uitgangsstof voor de kobalt en silica als dragermateriaal voor de klassieke bereidingsmethode ‘impregneren en drogen’.

Vooralsnog wordt de bereiding van gedragen katalysatoren eerder beschouwd als een kunst dan als een wetenschap en dat terwijl het van essentieel economisch en milieutechnisch belang is om de bereiding goed onder controle te krijgen. In dit proefschrift benaderen we katalysatorbereiding vanuit de fysische eigenschappen van de uitgangszouten en –oplossingen in de poriën van het dragermateriaal. Vloeistoffen die opgesloten zitten in zeer nauwe ruimten vertonen een ander fasegedrag dan dezelfde vloeistoffen zonder ruimtelijke begrenzing. Bijvoorbeeld water in cylindrische poriën met een diameter van ongeveer 8 nm bevriest pas bij -16 ºC in

plaats van bij 0 ºC. Deze vriespuntverlaging geldt ook voor oplossingen begrensd door nauwe poriën, dus ook de uitgangszouten en –oplossingen die gebruikt worden bij het maken van gedragen katalysatoren via impregneren en drogen. Deze eigenschap wordt in dit proefschrift veelvuldig gebruikt om te detecteren hoe de uitgangszout en –oplossing is verdeeld over de poriën van het dragermateriaal. Poreuze silica materialen met geordende poriën en nauwe poriegrootteverdelingen worden gebruikt als modeldragers. Daarnaast maken we gebruik van elektronentomografie, waarbij we een object in 3 dimensies kunnen bestuderen en op de nanometerschaal kunnen vaststellen waar de oplossing, het zout of de metaaldeeltjes zich bevinden.

In **Hoofdstuk 2** wordt met behulp van differentiële scanning calorimetrie (DSC) bepaald hoeveel procent van de poriën van een modeldrager zijn gevuld na een enkele impregnatiestap met water of een waterige zoutoplossing. 85-100% van de poriën bleek gevuld te worden, wat bewijst dat na impregnatie de poriën van het dragermateriaal homogeen gevuld zijn. De verdeling van de oplossing over de poriën van staafvormige modeldragerdeeltjes is in drie dimensies en met nanometerresolutie in beeld gebracht in **Hoofdstuk 3** met behulp van elektronentomografie bij vloeibare stikstoftemperaturen. De verdeling van de oplossing en het afgezette zout over de poriën van eenzelfde dragerdeeltje werd vergeleken na verschillende droogbehandelingen. Dit liet zien dat vriesdrogen noodzakelijk was om een homogene verdeling van het zout te krijgen. Na ontleding van het zout resulteerde dit in een uniformere verdeling van nanodeeltjes dan was verkregen door de conventionele droogmethode toe te passen.

In **Hoofdstuk 4** laten we zien dat begrip van het fasegedrag van een kobaltnitraatoplossing en kobaltnitraatzout gebruikt kan worden om de verdeling van het zout over een commerciële gebruikte silica drager te variëren. Verschillende vriesdroogmethoden werden bedacht op basis van de vriespuntverlagingen van de zoutoplossing en het gehydrateerde zout gemeten met DSC. Na ontleding van het zout werden katalysatoren verkregen met kobaltnanodeeltjes die clusters vormden, zich alleen aan de rand van het dragerdeeltje bevonden of uniform over het hele dragerdeeltje verdeeld waren. Deze katalysatoren waren zeer actief voor de Fischer-Tropsch reactie en kunnen gebruikt worden om het effect van de onderlinge nanodeeltjesafstand op deactivering door samensmelten te meten.

Katalysatorbereiding door smeltinfiltratie wordt besproken in **Hoofdstuk 5** als een alternatief voor impregnatie. Het smelten van kobaltnitraatzout en de gelijktijdige infiltratie van het dragermateriaal konden worden gevolgd met DSC. Na analyse met ook verscheidene andere karakteriseringtechnieken, werd geconcludeerd dat het zout de poriën nagenoeg homogeen vult na infiltratie. Na ontleding van het zout werden zeer actieve katalysatoren voor de Fischer-Tropsch reactie verkregen, die een vergelijkbare kobaltnanodeeltjesverdeling hadden als na impregnatie.

In de laatste twee hoofdstukken wordt de toepassing van DSC besproken om het verlaagde vries- en smeltpunt van water in nanoporiën te meten. In **Hoofdstuk 6** wordt dit principe toegepast om de gedeeltelijke blokkades door nanodeeltjes in de poriën te meten. In **Hoofdstuk 7** wordt DSC gebruikt om de afmeting van de toegang te meten van dragermaterialen met bolvormige poriën. Beide hoofdstukken laten zien dat DSC een toegevoegde waarde heeft ten opzichte van gebruikelijke fysisorptietechnieken met stikstof of argon.

Referenties

[1] *From the Process Engineering to the biorefinery*. 2009 [cited 2011 25 March]; Available from: www.biorefnery.ws/en/bio_btl.php.
[2] J. P. den Breejen, J. R. A. Sietsma, H. Friedrich, J. H. Bitter and K. P. de Jong, *J. Catal.* **2010**, *270*, 146.

Appendices

Appendix A

Appendix A1. List of supporting movies and (cryo-)electron tomography conditions

Figure numbers correspond to the numbers used in **Chapter 3**.

Figure 3.1 (a,b):

Cryo-electron tomography conditions: -65º to 65º with 1º intervals. Magnification 24000x. Defocus -1 µm. Total dose per tilt series: 262 $e^-/Å^2$, two tilt series were acquired per sample.

A movie of the 3D reconstructions obtained by image analysis of the in-situ dried SBA-15 particles is registered under the name:

Figure1_3D-insitu.mov.

Figure 3.2:

Cryo-electron tomography conditions: -65º to 65º with 1º intervals. Magnification 24000x. Defocus -1 µm. Total dose per tilt series: 282 $e^-/Å^2$.

Movies of the full reconstructions are registered under the names:

Figure2a_Conv.mov and *Figure2b_Freeze.mov*.

Please note that the 10 nm sized dark spots are gold fiducials used for alignment.

Figure 3.3:

Electron tomography conditions: -75º to 70º or 75º for CD and FD respectively with 2º intervals. Magnification 29000x.

Figure 3.4:

Electron tomography conditions: -75º to 70º or 73º for CD and FD respectively with 2º intervals. Magnification 29000x.

Movies of the full reconstructions are registered under the names:

Figure4a_NiOconv.mov and *Figure4b_NiOfreeze.mov*.

Please note that the 10 nm sized dark spots are gold fiducials used for alignment.

Appendix A2. Cryo-ET and image analysis for in-situ drying experiment

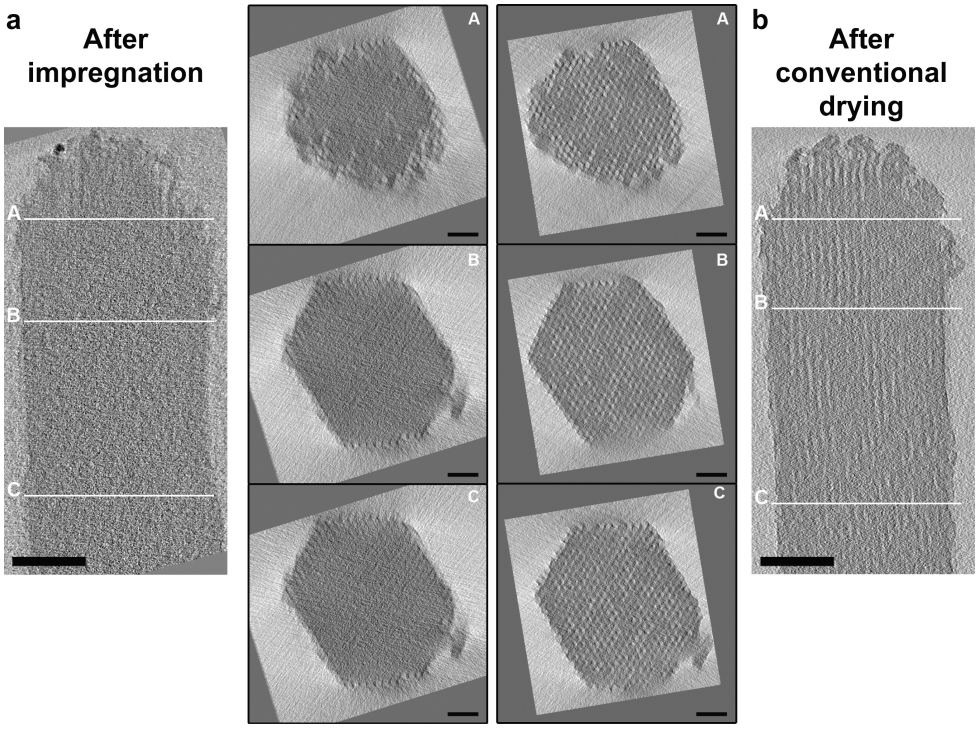

Figure A1. Slices through the reconstructions of the in-situ conventional drying experiment on a single impregnated SBA-15 particle. a, After impregnation with $Co(NO_3)_2$(aq). Scale bar in cross section parallel to the pores: 100 nm, in the slices perpendicular to the pores: 50 nm. b, After conventional drying at 60 ºC. Scale bar in cross section parallel to the pores: 100 nm, in the slices perpendicular to the pores: 50 nm. Numerical cross section parallel to the pores have 0.74 nm thickness. Lines A, B and C indicate positions of 14.8 nm thick slices perpendicular to the pore direction

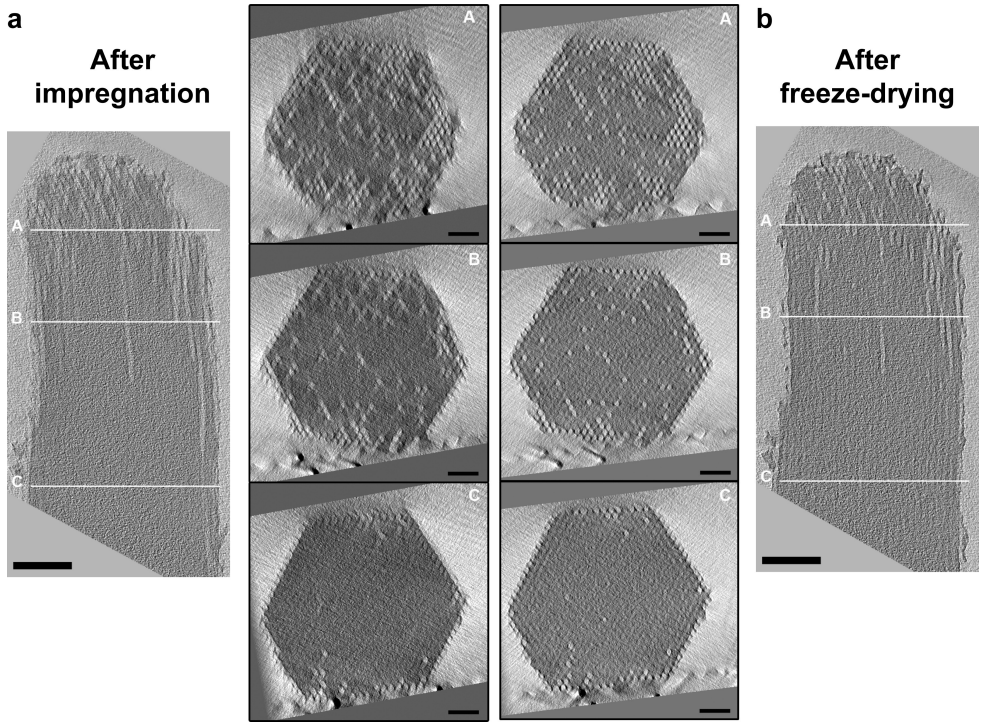

Figure A2. Slices through the reconstructions of the in-situ freeze-drying experiment on a single impregnated SBA-15 particle. a, After impregnation with $Co(NO_3)_2$ (aq). Scale bar in cross section parallel to the pores: 100 nm, in the slices perpendicular to the pores: 50 nm. b, After freeze-drying in the microscope column. Scale bar in cross section parallel to the pores: 100 nm, in the slices perpendicular to the pores: 50 nm. Numerical cross section parallel to the pores have 0.74 nm thickness. Lines A, B and C indicate positions of 14.8 nm thick slices perpendicular to the pore direction

Image analysis was performed on 14.8 nm thick slices perpendicular through the body of the particle, as indicated in Figure A3a. Empty or partially empty pores were detected by a gray value intensity upper limit integrated over 10 nm circular areas fixed on an hexagonal array.[3] For clarity of the 3 dimensional reconstruction, empty pore detections at the rim of the particle were cut-off, as indicated by the hexagonal in Figure A3b.

[3] Crocker, J. C. & Grier, D. G., Methods of digital video microscopy for colloidal studies. *J. Colloid Inter. Sci.* **179,** 298-310 (1996).

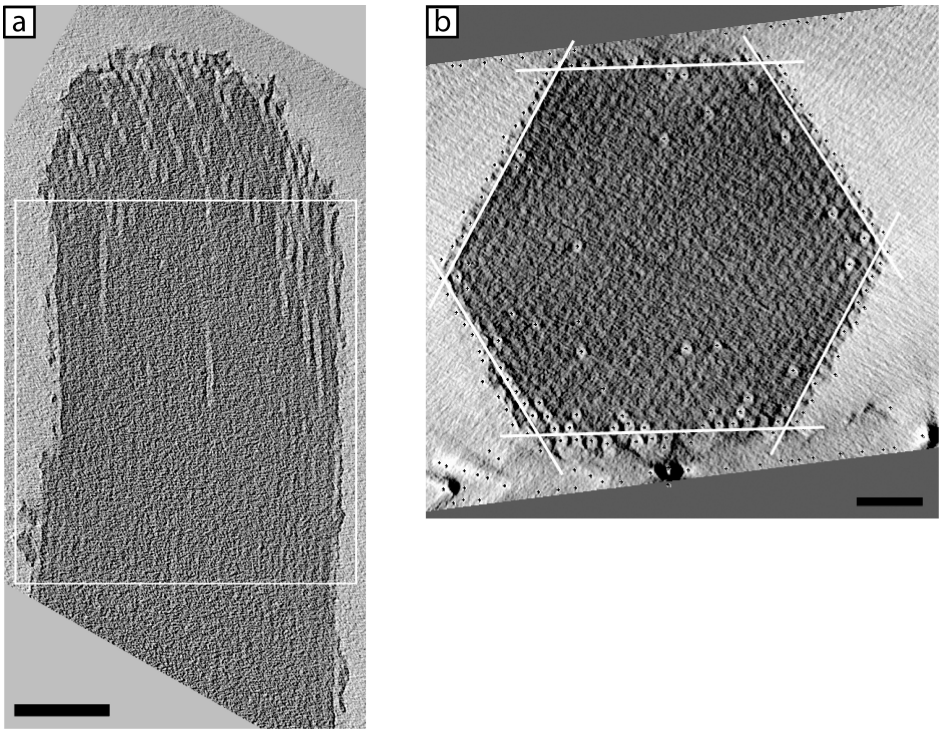

Figure A3. Data selection for image analysis. a, Slice through the reconstruction of $Co(NO_3)_2$/SBA-15 after in-situ freeze-drying. Red box indicates limit of slices selected for image analysis. Scale bar: 100 nm. b, Slice perpendicular through the reconstruction of FD-$Co(NO_3)_2$/SBA-15 showing results of image analysis for open pore detection. Red hexagonal indicates cut-off area for open pore detections. Scale bar: 50 nm

Appendix A3. Cryo-ET reconstructions of lab scale drying experiments

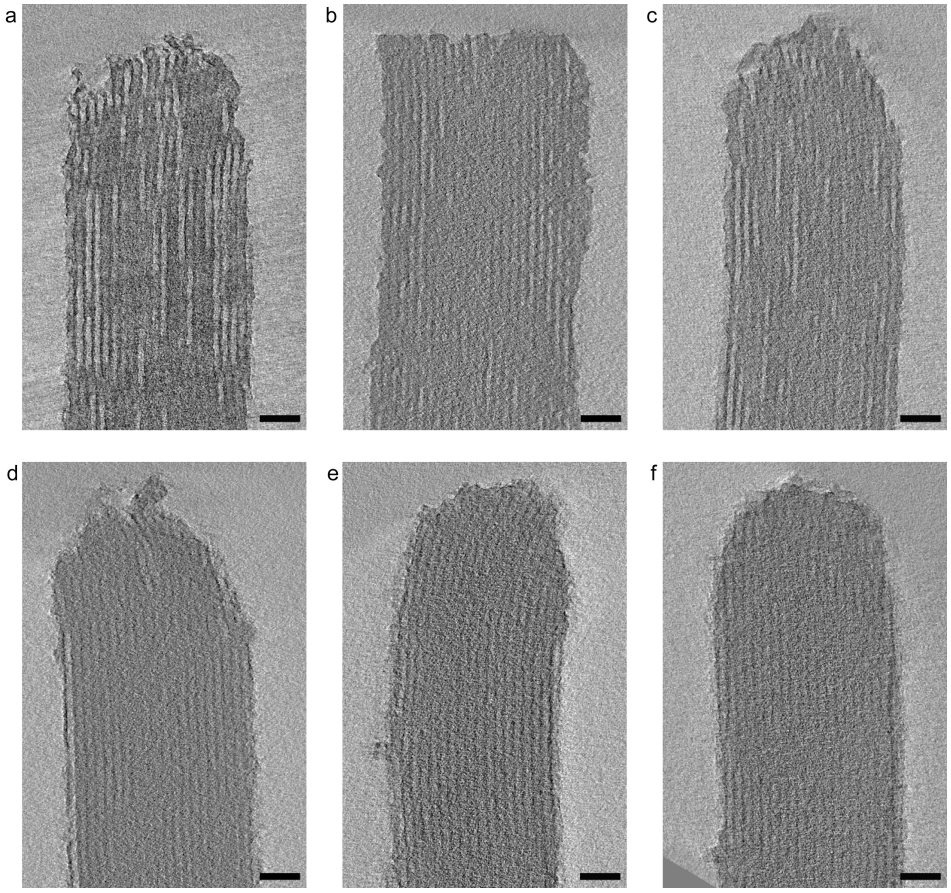

Figure A4. Cryo-electron tomography visualization of $Co(NO_3)_2$ salt distribution on SBA-15 after impregnation and different drying treatments. a,b,c, Prepared on mg scale by conventional drying at 60 ºC. d,e,f, Prepared on mg scale by freeze-drying. a-f, All scale bars are 50 nm.

Appendix A4. Structural characterization with N_2-physisorption for CD and FD prepared catalysts.

Porosity characterization was performed to investigate the effect of the catalyst preparation method on structural integrity of the materials. Samples prepared using SBA-15 batch 3, showed broadening of the pore size distribution and gaps in the silica pore walls. However, this was not representative, as all catalysts prepared from other batches did retain their structural properties. Furthermore, the porous structure of a more industrially relevant commercial silica gel support showed to be

unaffected by conventional or freeze-drying. This shows that freeze-drying does not afflict extensive damage upon the porous structure of the support.

Table A1. Structural characterization of nickel and cobalt oxide catalysts after calcination in a flow of 1% NO/N_2 or N_2 prepared via impregnation and conventional drying (CD) or freeze-drying (FD).[a]

Catalyst[b]	V_{tot}[c] (cm^3/g_{SiO2})	volume loss (% V_{tot}/V_{parent})	S_{BET} (m^2/g_{SiO2})	surface area loss (% S_{BET}/S_{parent})	pore diameter (nm)[d]
Support SBA-15 batch 1	1.18	n.a.	866	n.a.	11.7
Support SBA-15 batch 2	1.10	n.a.	830	n.a.	10.8
Support SBA-15 batch 3	1.10	n.a.	493	n.a.	14
CD-NiO/SBA-15_NO (1)	0.91	23	685	21	11.3
FD-NiO/SBA-15_NO (3)	0.94	14	476	3.4	10.5, 11.7, 13.7
CD-NiO/SBA-15_N_2 (1)	1.04	12	681	21	10.2
FD-NiO/SBA-15_N_2 (3)	1.00	7.9	490	0.55	12.4
CD-Co_3O_4/SBA-15_NO (2)	0.94	15	770	7.2	10.1
FD-Co_3O_4/SBA-15_NO (1)	1.01	14	712	18	10.7
CD-Co_3O_4/SBA-15_N_2 (2)	0.82	25	584	30	10.4
FD-Co_3O_4/SBA-15_N_2 (1)	1.11	6.2	822	5.1	10.2
CD-Co_3O_4/SiO_2-gel	0.78	11	454	-3	7.4[e]
FD-Co_3O_4/SiO_2-gel	0.76	12	451	-2	7.6[e]

[a] N_2-physisorption was performed after drying the samples at 250 ºC for 16 hrs in a flow of N_2. Measurements were performed at -196 ºC (Tristar 2000, Micromeritics), [b] number between brackets indicate batch of parent SBA-15, [c] single point pore volume at relative pressure p/p_0=0.95, [d] average pore diameter determined by NL-DFT calculation on adsorption isotherm, [e] average pore diameter determined by BJH analysis on desorption isotherm.

Appendix B

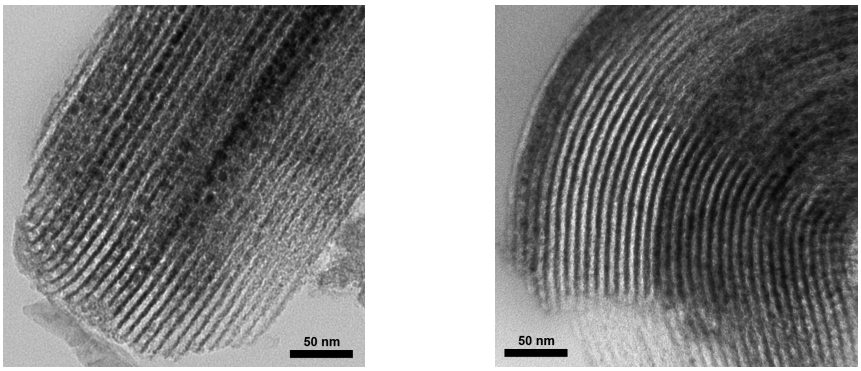

Figure B1. TEM micrographs of Co/S100 (NO calcined) after reduction at 500 ºC, 2 hours and passivation in air (A) and after Fischer Tropsch reaction for 20 hours (B).

Appendix C

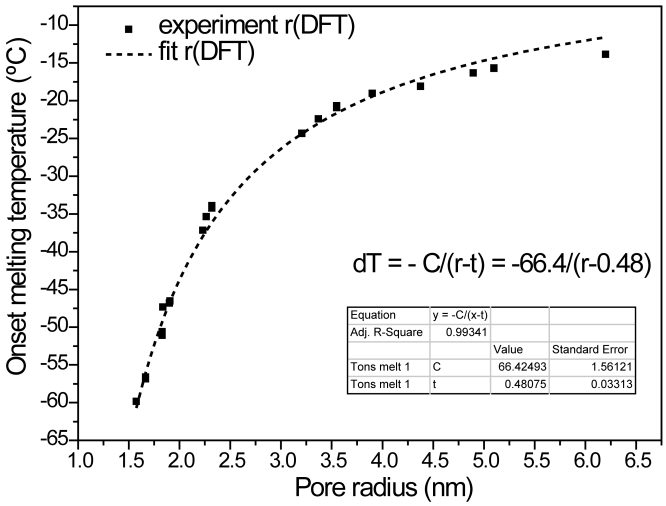

Figure C1. Pore radius dependence of melting point onset of water confined in cylindrical ordered mesoporous silica determined by DSC during heating at 1 ºC/min.

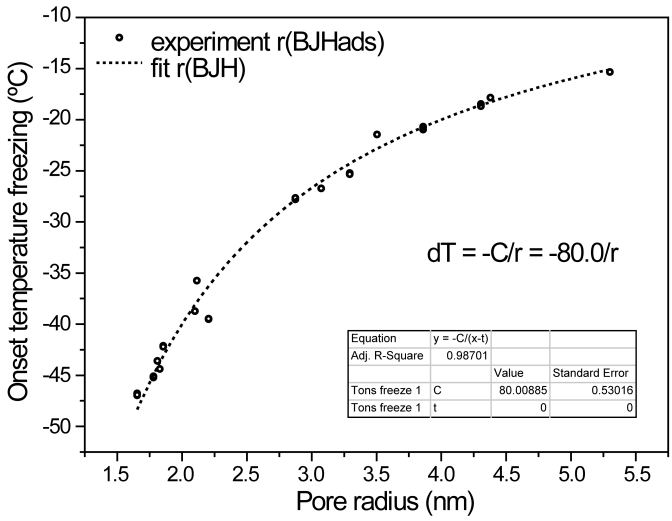

Figure C2. Pore radius dependence of freezing point onset of water confined in cylindrical ordered mesoporous silica determined by DSC during cooling at 1 ºC/min.

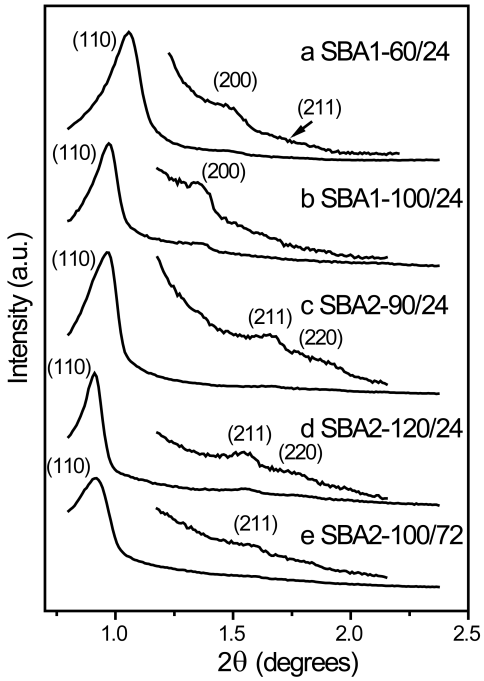

Figure C3. LA-XRD patterns recorded for various SBA-16 silica materials indexed to the *Im-3m* symmetry group confirming structural ordering at the mesoscale: (a) SBA1-60/24, (b) SBA1-100/24, (c) SBA2-90/48, (d) SBA2-120/24, (e) SBA2-100/72.

Appendix C1. SEM characterization of selected SBA-16 and FDU-12 silica materials

The size and morphology of the primary particles of the silica mesostructures were studied by means of scanning electron microscopy (SEM) in a Tecnai FEI XL 30SFEG microscope. The powder samples were covered with a thin conductive layer of *Au*-Pd before observation.

The macroscopic particle morphology of the materials depended on the synthesis gel composition (Figure S4). For SBA-16 materials prepared from gel (1), 2-5 μm rounded polyhedra were observed, while the presence of butanol in gel (2) resulted in large (>10 μm), ill-defined, sharp edged particles. The FDU silicas displayed platelet-like morphology that had occasionally self-organized in hollow spheres, likely templated by small hydrophobic droplets in the synthesis gel formed from an excess of the swelling agent (TMB).

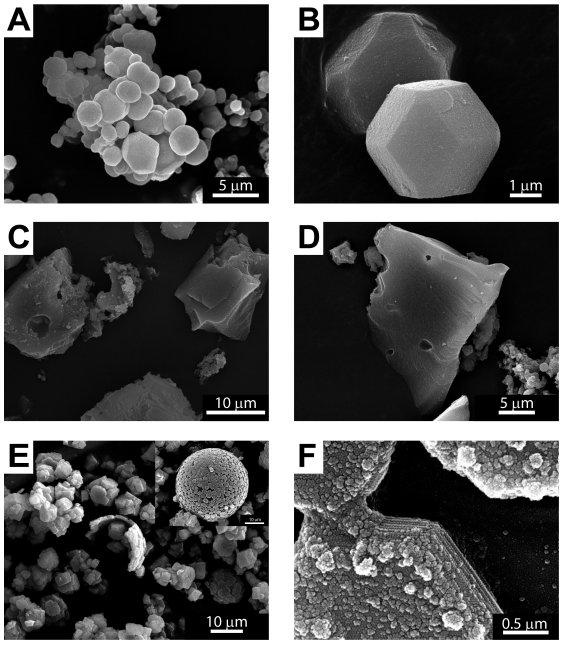

Figure C4. Representative SEM micrographs for SBA1-60/24 (a,b) and SBA2-120/24 (c,d) SBA-16 silicas and FDU-100/48 (e,f) FDU-12 silica.

List of Publications and Presentations

Scientific publications

T. M. Eggenhuisen*, G. Prieto*, H. Talsma, P. E. de Jongh and K. P. de Jong, *'Thermoporometry of Cage Silica for Entrance Size Analysis*', submitted.

T. M. Eggenhuisen*, P. Munnik*, H. Talsma, P. E. de Jongh and K. P. de Jong, *'Freeze-Drying for Controlled Nanoparticle Distribution in Co/SiO_2 Fischer-Tropsch Catalysts'*, submitted.

T. M. Eggenhuisen, H. Friedrich, F. Nudelman, J. Zečević, N. A. J. M. Sommerdijk, P. E. de Jongh and K. P. de Jong, *'Controlling the Aqueous Synthesis of Functional Nanoparticles in Porous Materials*', in preparation.

T. M. Eggenhuisen, J. Zečević, H. Talsma, P. E. de Jongh and K. P. de Jong, *'Quantitative Assessment of Pore Blockage in Supported Catalysts: Comparing Differential Scanning Calorimetry and Physisorption*', *Journal of Physical Chemistry C* **2012**, *116*, 7480.

B. P. C. Hereijgers, T. M. Eggenhuisen, K. P. de Jong, H. Talsma, A. J. M. van der Eerden, A. M. Beale and B. M. Weckhuysen, '*Understanding the Promotion Effect of Lanthanum Oxide on Gold-Based Catalysts in the Partial Oxidation of Methanol by in situ XAFS and DSC Studies*', *Journal of Physical Chemistry C* **2011**, *115*, 15545.

M. Wolters, L. J. W. van Grotel, T. M. Eggenhuisen, J. R. A. Sietsma, P. E. de Jongh and K. P. de Jong, *'Combining Confinement and NO Calcination to Arrive at Highly Dispersed Supported Nickel and Cobalt Oxide Catalysts with a Tunable Particle Size*', *Cataysis Today* **2011**, *163*, 27.

T. M. Eggenhuisen, J. P. den Breejen, D. J. Verdoes, P. E. de Jongh and K. P. de Jong, *'Fundamentals of Melt infiltration for the Preparation of Supported Metal Catalysts. The Case of Co/SiO_2 Fischer-Tropsch Synthesis*', *Journal of the American Chemical Society* **2010** *132*, 18318.

T. M. Eggenhuisen, M. J. van Steenbergen, H. Talsma, P. E. de Jongh and K. P. de Jong, *'Impregnation of Mesoporous Silica for Catalyst Preparation Studied with Differential Scanning Calorimetry*', *Journal of Physical Chemistry C* **2009**, *113*, 16785.

T. M. Eggenhuisen, C. R. Becer, M. W. M. Fijten, R. Eckardt, R. Hoogenboom, and U. S. Schubert,*'Libraries of Statistical Hydroxypropyl Acrylate Containing Copolymers with LCST Properties Prepared by NMP*', *Macromolecules* **2008**, *41*, 5132.

P. E. de Jongh, R. W. P. Wagemans, T. M. Eggenhuisen, B. S. Dauvillier, P. B. Radstake, J. D. Meeldijk, J. W. Geus and K. P. de Jong, *'The Preparation of Carbon-Supported Magnesium Nanoparticles using Melt Infiltration', Chemistry of Materials* **2007**, *19*, 6052.

* Authors contributed equally to the work

Oral Presentations

T. M. Eggenhuisen, P. Munnik, F. Nudelman, H. Friedrich, J. Zečević, N. A. J. M. Sommerdijk, P. E. de Jongh and K. P. de Jong, *'Towards Rational Synthesis of Nanostructured Catalysts using Electron Tomography*', CHAINS, Maarssen, The Netherlands, 28-30 Nov 2011.

T.M. Eggenhuisen, F. Nudelman, H. Friedrich, J. Zečević, N. A. J. M. Sommerdijk, P. E. de Jongh and K. P. de Jong, *'Cryo-Electron Tomography to Visualise Fundamental Processes of Supported Catalyst Preparation*', Europacat X, Glasgow, United Kingdom, 28 August – 2 September 2011.

T.M. Eggenhuisen, F. Nudelman, H. Friedrich, N. A.J.M. Sommerdijk, P.E. de Jongh and K.P. de Jong, '*Fundamental Studies on Supported Co/SiO_2 Catalyst Preparation. Precursor Distribution Visualised with Cryo-Electron Tomography*', Netherlands Association for Microscopy Cryo-workgroup Annual Spring Meeting, Eindhoven, The Netherlands, June 14 2011.

T.M. Eggenhuisen, F. Nudelman, H. Friedrich, N. Sommerdijk, P.E. de Jongh and K.P. de Jong, '*Supported Cobalt Fischer-Tropsch Catalyst Preparation via Freeze-Drying*', 22nd North American Catalysis Society Meeting, Detroit, United States, 5-10 June 2011.

T. M. Eggenhuisen, F. Nudelman, H. Friedrich, J. Zecevic, N. Sommerdijk, P.E. de Jongh and K.P. de Jong, '*Tracing the Precursor Phase during Supported Catalyst Preparation*', Netherlands Chemistry and Catalysis Conference XII, Noordwijkerhout, The Netherlands, Feb 28- March 2 2011.

T. M. Eggenhuisen, F. Nudelman, H. Friedrich, H. Talsma, N. A. J. M. Sommerdijk, P. E. de Jongh and K. P. de Jong, *'Tracing the Precursor Phase during Supported Catalyst Preparation*', American Institute of Chemical Engineers Annual meeting, Salt Lake City, USA, November 7 -12 2010.

T. M. Eggenhuisen, J. P. den Breejen, D. J. Verdoes, P. E. de Jongh and K. P. de Jong, *'Fundamentals of Melt Infiltration for Supported Catalyst Preparation. The Case of Co/SiO_2 for Fischer-Tropsch Synthesis*', American Institute of Chemical Engineers Annual meeting, Salt Lake City, USA, November 7-12 2010.

T. M. Eggenhuisen, F. Nudelman, H. Friedrich, H. Talsma, N. A. J. M. Sommerdijk, P. E. de Jongh and K. P. de Jong, *'Tracing the Precursor Phase during Supported Catalyst Preparati*on', 1st International Workshop of the European Nanoporous Materials Institute of Excellence (ENMIX), Antwerp, Belgium, October 4-5 2010.

J. P. den Breejen, T. M. Eggenhuisen, J. R. A. Sietsma, H. Friedrich, A. M. Frey, J. H. Bitter and K. P. de Jong, *'Design and Synthesis of Maximum Activity Supported Cobalt Fischer Tropsch Catalysts*', Novel Gas Conversion Symposium 9, Lyon, France, May 30-June 3 2010.

T. M. Eggenhuisen, J. P. den Breejen, D. J. Verdoes, P. E. de Jongh and K. P. de Jong, *'Melt Infiltration for Preparation of Cobalt-on-Silica Fischer-Tropsch Catalysts*', Netherlands Chemistry and Catalysis Conference XI, Noordwijkerhout, The Netherlands, March 1-3 2010.

T. M. Eggenhuisen, M. J. van Steenbergen, H. Talsma, P. E. de Jongh and K. P. de Jong, *'Impregnation of Ordered Mesoporous Silica Studied with Differential Scanning Calorimetry*', Netherlands Chemistry and Catalysis Conference X, Noordwijkerhout, The Netherlands, March 2-4 2009.

Poster presentations

T. M. Eggenhuisen, F. Nudelman, H. Friedrich, N. A. J. M. Sommerdijk, P. E. de Jongh and K. P. de Jong, *'Tracing the Precursor Phase during Impregnation and Drying for Supported Catalyst Preparation*', *IZC-IMMS,* Sorrento, Italy, July 4-9 2010**.**

T. M. Eggenhuisen, J. P. den Breejen, D. J. Verdoes, P. E. de Jongh and K. P. de Jong, *'Fundamentals of Melt Infiltration for Catalyst Preparation: Co/SiO_2 Fischer-Tropsch Catalysts*', *International Zeolite Conference* – International Mesoporous Materials Symposium*,* Sorrento, Italy, July 4-9 2010**.**

T. M. Eggenhuisen, F. Nudelman, H. Friedrich, N. A. J. M. Sommerdijk, P. E. de Jongh and K. P. de Jong, *'Tracing the Precursor Phase during Impregnation and Drying for Supported Catalyst Preparation*', Scientific Bases for the Preparation of Heterogeneous Catalysts 10, Louvain-la-Neuve, Belgium, July 11-15 2010.

T. M. Eggenhuisen, J. P. den Breejen, D. J. Verdoes, P. E. de Jongh and K. P. de Jong, '*Fundamentals of Melt Infiltration for Catalyst Preparation: Co/SiO_2 Fischer-Tropsch Catalysts*', Scientific Bases for the Preparation of Heterogeneous Catalysts 10, Louvain-la-Neuve, Belgium, July 11-15 2010.

T. M. Eggenhuisen, J. P. den Breejen, D. J. Verdoes, P. E. de Jongh and K. P. de Jong, '*Co/SiO_2 Fischer-Tropsch Catalysts Prepared via Melt Infiltration*', Novel Gas Conversion Symposium 9, Lyon, France, May 30-June 3 2010.

T. M. Eggenhuisen, M. J. van Steenbergen, H. Talsma, P. E. de Jongh and K. P. de Jong, *'Impregnation of Ordered Mesoporous Silica Studied with Differential Scanning Calorimetry*', Europacat IX, Salamanca, Spain, August 30 – September 4 2009.

Dankwoord

Laat ik bij met de laatste woorden de tekst aan het begin van mijn thesis toelichten. Het eerste concert waar ik heen ben geweest wat ik me kan herinneren was op mijn 12e naar De Dijk. Sindsdien, en na de vele autotochten naar zuid-Frankruik waarop deze cd werd grijsgedraaid, ben ik een groot fan. De tekst die in deze thesis staat klinkt in eerste instantie wat zwaar, maar is eigenlijk een hele positieve boodschap, die wetenschappers door een taaie onderzoeksdag heen kan helpen. Immers: morgen is het allemaal weer anders. En hoe vaak blijkt dat niet het geval te zijn (of niet, maar blijf dan gewoon verder zoeken: wanhoop niet!). Naast deze toelichting is deze plek in het proefschrift aangewezen iedereen te bedanken die via een of andere route aan dit onderzoek heeft bijgedragen. Het onderzoek in deze thesis was zeker niet tot stand gekomen zonder de bijdragen van anderen!

Ten eerste, wil ik mijn promotor, Krijn, bedanken voor de kansen en vrijheden die je me gegeven hebt. Ik heb me in de laatste 4 jaar kunnen en mogen ontwikkelen in alle zelfstandigheid en vrijheid. Je passie voor de wetenschap en interesse voor het onderzoek heeft mij het gevoel gegeven dat je altijd betrokken bleef bij de voortgang. Ik heb met erg veel plezier gewerkt onder jouw begeleiding.

Petra, ik ben ooit begonnen in het onderzoek met jou als begeleider voor mijn bachelorthesis en in de laatste maanden ben ik als postdoc voor jou werkzaam geweest. Het cirkeltje is rond! Ik kan me nog herinneren dat we de eindpresentatie van mijn bachelorthesis gingen doorspreken. Dat was pittig! Maar daarna heb ik nog vaak om je advies gevraagd en dat is niet voor niets. Je inzet, energie, oog voor details en onuitputtelijke doorzettingsvermogen is bewonderenswaardig.

Herre, ik weet niet of je dit voor ogen had, toen 4 jaar geleden dit onderzoeksvoorstel met je werd besproken. De DSC en daarna de vriesdroger hebben hoofdrollen gekregen in dit proefschrift. Oprecht bedank ik je voor de toegang die je me hebt gegeven tot jullie lab en de farmaceutische onderzoekswereld. Niets is leuker dan met je onderzoeksvraag terecht te kunnen bij iemand met een volledig andere achtergrond. De samenwerking was altijd plezierig en ik wil je bedanken voor de

goede adviezen en het meedenken.

Het derde hoofdstuk vormt de kern van dit proefschrift en had niet tot stand kunnen komen zonder de samenwerking met de TU/e. Nico Sommerdijk, bedankt voor de tijd die we op de Titan hebben mogen doorbrengen en voor jouw tijd en energie die je gestoken hebt in het manuscript. Ik heb er veel van geleerd. Heiner, I enjoyed working with you as you always had a different look to experiments. You have an amazing amount of knowledge on the electron microscope and I'm very happy that you shared some of it with me. I wish you all the best in Eindhoven. Fabio, thanks for you skillful help with translating a catalyst preparation research question into a cryo-electron tomography experiment.

Dit proefschrift zou er niet hetzelfde hebben uitgezien zonder de samenwerking met de andere aio's en postdocs van het CatPrep team. Peter, ik heb altijd met veel plezier met je samengewerkt en hoop dat het je lukt om de NO-puzzel volledig te krijgen. Ik wens je veel succes met het gebruiken van de vriesdroger. Jovana, I remember taking the microscopy course with you! We were both, I think, blown away by the amount of information dropped on us. By now you have fully mastered the technique with an eye and care for detail that I will never have. Thanks for the nice conversations and your delicious pancakes. Gonzalo, working with you was effortless and a great pleasure, and I wish you the best for the *future*. Mariska, met jou ben ik aan dit project begonnen en ik wil je bedanken voor alle tips en trucs die je gegeven hebt en voor de vele discussies die we gevoerd hebben.

Ik ben erg blij dat we in onze onderzoeksgroep ook kunnen samenwerken met collega's iets verder weg van ons eigen straatje. Bart, ik ben blij dat ik een kleine bijdrage heb kunnen leveren aan je onderzoek in de vorm van silica's en de DSC. In ruil daarvoor heb ik kunnen delen in je creativiteit, je nuchtere kijk op onderzoek en de wereld en vooral veel gezelligheid. Matti, bedankt dat ik met je mee mocht naar Berkeley, het was zeker een enerverende ervaring. Mooi om te zien dat mensen ondanks stress, frustraties en slaaptekort toch nog wetenschap kunnen blijven bedrijven en ik denk dat de tekst van De Dijk voorin dit proefschrift zeer van toepassing was op de betreffende beamtrip. Johan, bedankt voor al je hulp en het delen van je kennis over de Fischer-Tropsch synthese. Efi and Chieh-Chao, we have collaborated over a distance, and I appreciate your efforts in applying the catalysts I prepared for glycerol hydrogenation and the photocatalytic cleavage of water.

Een onderzoeksgroep als de onze kan niet functioneren zonder de technische staf. Het wordt vaak gezegd, maar kan niet vaak genoeg herhaald worden. Ik wil dan ook alle technische staf en Dymph en Monique bedanken voor hun open deur beleid en bereidheid tot helpen. Mies, ik zou bijna tegen je zeggen: het spijt me. Het spijt me dat ik al die keren naar jouw kantoor kwam lopen met een vraag over de DSC of (nog erger) de vriesdroger. Maar, jouw oneindige optimisme en behulpzaamheid maakte

dat het nooit een probleem was om bij jou aan te kloppen. Ik ben erg blij dat ik met jou heb mogen samenwerken. Hans, ik wil je bedanken voor de gezelligheid bij de microscoop en bewonder je flexibiliteit en inzet om ons aio's te helpen. Hopelijk kom ik je nog eens tegen bij de Driebergenloop.

Harry, je vervult een belangrijke functie binnen de groep. Het is namelijk heel fijn om iemand te hebben waar de deur altijd open staat en waar de drempel om wat voor vraag dan ook te stellen zeer laag is. Bedankt voor alle gezelligheid en gekkigheid.

Tijdens je promotie mag je ook studenten begeleiden en dat heb ik ook met veel plezier gedaan. Dirkjan, Bram, Joep, Anne en Bas: bedankt voor jullie inzet en wetenschappelijke bijdragen! Naast mijn studenten wil ik ook graag mijn oude begeleiders bedanken. Zij hebben een belangrijke invloed gehad op de onderzoeker die ik uiteindelijk ben geworden. Dus: Rudy, Sipke, Warren en Richard, thanks for your interest, enthusiasm, stimulation and time spent on my research projects (which was in some cases a somewhat selfless investment).

I have to thank the group of Inorganic Chemistry and Catalysis as a whole for the great scientific environment it provides. However, the importance of a good atmosphere with fun, coffee, beers on friday nigths, BBQ's, conferences, group outings etc. should not be underestimated. Luckily, our group succeeds to fulfill both tasks, and I greatly enjoyed working in this group. Hirsa, thanks for your company on the conferences in Lyon and Glasgow, it was great spending the time with you, and we should still go and see Iron Maiden together! Thanks to Harry, Anne, Arjan, Rob, Annelie, Ilona, Clare, Peter, Evelien, Piter, Davide, Inge, Bart, Adri, Mariska and Johan for the many enjoyable coffee and lunch breaks. I have been lucky enough to have been in an office my whole PhD, and have had many office mates, whom I all thank for their company and discussions. But, specifically, I would like to thank Ilona and Annelie for disturbing quiet Friday mornings with music and chatter, back in the Wentbuilding. Thanks to Joe, Daniel and Rob for the enjoyable runs and cycling tours.

Na 11 (!) jaar is er voor mij een einde gekomen aan het tijdperk scheikunde in Utrecht. Ik had geen betere plek kunnen kiezen, dat is gebleken tijdens mijn promotie, maar was ook al duidelijk in de jaren ervoor. Bart, Loek, Emiel, Mikal, Jan, Lodewijk, Albert, Marije, Edo en iedereen die samen Proton vormden, bedankt voor de gezelligheid in de afgelopen jaren.

Hier wil ik ook van de gelegenheid gebruik maken om het 3e peleton van de B-cie van het 50 Natresbat te bedanken. Ook al zullen jullie het niet in de gaten hebben gehad, jullie hebben zeker ook bijgedragen aan dit proefschrift. De opkomsten zijn welkome afwisselende, leerzame en (soms fysiek) uitdagende dagen, die ervoor zorgen dat de dagelijkse werkzaamheden leuk blijven. Ik hoop nog lang met jullie te kunnen dienen!

Draak, we gaan al zo lang terug, ik voorzie dat we samen bridgend in het bejaarden tehuis eindigen en ik kijk er nu al naar uit. Het is nooit saai, we kunnen altijd ons (lelijke) zelf zijn en de combinatie witte wijn met thee is tijdloos. Wat je ook gaat doen, waar je ook terecht komt, ik ben trots op je! Lon, jij kan natuurlijk niet ontbreken in het bejaardentehuis, want wat moeten we zonder jou. Sowieso zijn we voorbestemd, aangezien we elkaar al sinds de box steeds weer weten te vinden. Ik wil je natuurlijk bedanken voor de prachtige kaft, maar ook voor al je steun. Je staat altijd voor me klaar (en voor een hele hoop anderen) en dat is onbetaalbaar. Miek, ook jou wil ik bedanken voor de mooie tijden. Ik sta altijd versteld van al je plannen en ideeen, maar ben ook impressed met hoeveel je ervan daadwerkelijk uitvoert. Ik hoop dat er nog genoeg gaatjes in je agenda over blijven om samen een biertje te pakken, te wandelen (danwel gecombineerd met een hardloop-support actie) en voor de Natres.

Als laatste mag ik hier mijn familie noemen. Met trots maak ik deel uit van de negen Eggenhuisen's die Nederland rijk is. En in zo'n familie is elk exemplaar uniek. Claudia en Chantal jullie zijn onmisbaar. Ruben en Feline, ik vertrouw erop dat jullie je volledig inzetten om goede Eggenhuisen-Gijsbertjes te worden. Lieve Broer en Bro, jullie zijn mijn paranimfen bij de verdediging, maar misschien ook wel in het leven. Ik kan me geen betere broers wensen, ik weet dat jullie er altijd voor me zijn. Lieve papa en mama, door jullie heb ik geleerd dat alles kan. Ik nam dat altijd als vanzelfsprekend aan, maar door jullie onvoorwaardelijke steun ben ik nu waar ik ben en wie ik ben.

Tamara

Curriculum Vitae

Tamara Marijke Eggenhuisen was born on September 7th, 1983 in Eindhoven, the Netherlands. After graduating from pre-university education at the van Maerlant Lyceum in Eindhoven, she started her undergraduate studies in chemistry at Utrecht University in 2001. Late 2005, she obtained her Bachelor of Science degree (cum laude) with the thesis entitled "*Preparation and Characterisation of Magnesium/ Carbon Nanocomposites*" under the supervision of dr. P. E. de Jongh and prof. K. P. de Jong. In that same year she started the master program Chemistry and Physics at Utrecht Univerisity. She performed her master's thesis research in the group of prof. W. E. Piers at the University of Calgary in collaboration with the Organic Chemistry and Catalysis group at Utrecht University under supervision of prof. G. van Koten, which resulted in the thesis entitled "*A Long-Known Newcomer in Organoscandium Chemistry: the NCN-Pincer Ligand*". She spent a 6 month intership at Eindhoven University of Technology under the supervision of dr. Richard Hoogenboom and prof. U. S. Schubert on combinatorial polymer synthesis and obtained her Master of Science degree (cum laude) early 2008. Thereafter, she started working as a PhD student in the group of Inorganic Chemistry and Catalysis under the supervision of dr. P. E. de Jongh and prof. K. P. de Jong and the results of that research are described in this thesis. In 2010, Tamara joined the national guard of the Royal Dutch Army, where she now serves as a soldier first class in her spare time.